Astroteilchenphysik

Hardware Integration of the AMANDA into the IceCube Neutrino Telescope and Search for Supersymmetric Particles with the IceCube Neutrino Telescope

DISSERTATION

zur Erlangung des Doktorgrades

Fachbereich C – Mathematik und Naturwissenschaften

Arbeitsgruppe Prof. Dr. Karl-Heinz Kampert und Prof. Dr. Klaus Helbing

Dem Fachbereich Physik vorgelegt von

Andreas Tepe

im

Juli 2009

Contents

Nomenclature

ADC	Analog to Digital Converter.
AGN	Active Galactic Nucleus, current interpretation: super massive black hole in the center of a galaxy actively accreting matter.
AMANDA	Antarctic Muon And Neutrino Detector Array.
ATWD	Analog Transient Waveform Digitizer, stores analog voltages in an array of capacitors.
CLK2ECL	CLocK to ECL, small modules in the TWRDAQ connected to the VME P2 backplanes of the TWR crates, to deliver the 100 MHz clock and the trigger signals to the TWR modules.
CMB	Cosmic Microwave Background, highly redshifted photons left over from proton and electron recombination about 380000 years after the Big Bang.
CMS	Center of Mass System, the system in which the sum of all momenta is 0.
COBE	COsmic Background Explorer, satellite carrying experiments for the exploration of the cosmic microwave background.
dAOM	digitally controlled Analog Optical Modules.
DAQ	Data AcQuisition system.
DESY	Deutsches Elektronen-SYnchrotron, German electron synchrotron.
DMADD	Discriminator and Multiplicity ADDer.
DOM	Digital Optical Module.
DOMHub	A high performance computer reading out a single IceCube string.
DOR	DOm Readout PCI cards, which communicate with the DOMs on a string.
DSB	DOMHub Service Board, a PCI card inside a DOMHub, which receives the time information from a GPS clock and distributes it to the DOR cards inside the DOMHub.
DSP	Digital Signal Processor.
ECL	Emitter Coupled Logic, a current-mode logic, using differential signal transmission.

fADC	flash ADC, ADC, which is storing multiple voltage values in a flash memory.
FIFO memory	First In, First Out memory structure. Always the oldest element of the memory can be requested. Every request deletes the requested element.
FIRAS	Far InfraRed Absolute Spectrometer, experiment mounted on the COBE satellite.
FPGA	Field Programmable Gate Array, a programmable integrated circuit.
GMSB	Gauge-Mediated SUSY Breaking.
GPS clock	clock, which receives very precise time information from the satellites of the Global Positioning System.
GPS2VME	Special VME module reading the time from a GPS clock and delivering the data to AMANDA DAQ.
GRB	Gamma-Ray Burst.
GZK cutoff	A cutoff in the cosmic-ray particle spectrum predicted by Greisen-Zatsepin-Kuzmin.
ICL	IceCube laboratory, a building near the South Pole, which is housing the IceCube DAQ computers.
IRIG	Inter Range Instrumentation Group time code, is a serial bit by bit time coding standard. Several groups differ in the number of synchronization pulses per second. The AMANDA/IceCube integration hardware uses IRIG-B with 100 pulses per second to encode the day of the year, the hour of the day, minutes and seconds.
JEB	Joint Event Builder, builds the IceCube events from the incoming IceCube and AMANDA data streams.
LED	Light Emitting Diode.
LSP	Lightest Supersymmetric Particle. Which SUSY particle is the LSP is highly model dependent. In GMSB models, the LSP is typically the gravitino.
LSP	Lightest Supersymmetric Particle.
LVDS	Low Voltage Differential Signaling, interface standard for high speed data transfer.
M<number>	AMANDA internal nomenclature for a special trigger condition: Simple multiplicity trigger with minimum <number> of hit OMs as trigger threshold.
MAPO	Martin A. Pomerantz Observatory, building at the South Pole housing several scientific experiments.
MMC	Muon Monte Carlo. A software tool, which propagates charged particles through matter. MMC accounts for ionization, bremsstrahlung, photonuclear interactions, electron pair production, Landau-Pomeranchuk-Migdal and Ter-Mikaelian effects, muon and tauon decays and Molière scattering.
MSSM	Minimal Supersymmetric Standard Model.

mSUGRA	Minimal SUperGRAvity.
NIM	Nuclear Instrumentation Module standard. Inter alia, NIM specifies a logic signal transmission standard. The logic states are defined by currents: TRUE $= -12\,\mathrm{mA}$ to $-32\,\mathrm{mA}$, FALSE $= 0\,\mathrm{mA}$.
NLSP	Next to Lightest Supersymmetric Particle.
OM	Optical Module.
OPT2EL	Optical to Electrical converter, converts the electrical IceCube GPS signals into optical signals and the optical trigger signal and SyncPulse from AMANDA into electrical signals.
ORB	Optical Receiver Boards.
OTDR	Optical Time Domain Reflectometer, measures signal run times in optical fibers. An optical pulse is coupled into the fiber, the reflection of the pulse at the end of the fiber is measured. The time delay between sending and receiving delivers the fiber length.
pADC	peak ADC, ADC, which is digitizing only the maximum voltage value of a pulse.
PCI bus	Peripheral Component Interconnect bus, a standard computer hardware interface.
PLL	Phase-Locked Loop, electronic circuit, which is fixing the phasing between two oscillators.
PMT	PhotoMultiplier Tube.
PPS	Pulse Per Second.
RAPCal	Reciprocal Active Pulsing CALibration, method for the synchronization of two clocks.
RS-232	originally for Radio Sector, today for Recommended Standard for a serial interface connection.
SHARC	32-bit floating point DSP produced by Analog Devices. SHARC DSPs of the type ADSP-21060/62 are used for the TWRDAQ VME crate readout.
SM	Standard Model of particle physics.
SPASE-2	New South Pole Air Shower Experiment.
SUSY	SUperSYmmetry, a theory transforming bosonic into fermionic states and vice versa by a supersymmetric transformation.
SWAMP	SWedish AMPlifiers amplifying electrical signals coming from the AMANDA OMs.
SyncMB	SyncPulse MainBoard, an IceCube DOM mainboard, sampling the SyncPulses coming from the GPS4TWR in the AMANDA detector.

SyncPulse	Synchronization Pulse, a periodic signal, which is sent from AMANDA to IceCube.
TCH	IceCube Temporary Counting House, a small heated building containing the first few IceCube DOMHubs and other DAQ systems before the ICL was finished.
TDC	Time to Digital Converter.
ToI	Tensor of Inertia.
TQC	Time Quality Character, the GPS signal quality information: “0” (best), “E”, “A”, “3” and “F” (worst).
TrigMB	Trigger MainBoard, an IceCube DOM mainboard, sampling trigger pulses coming from the AMANDA detector.
TWR	The Transient Waveform Recorder is a VME module containing fADCs and some electronics managing and storing the data coming from the fADCs.
VEV	Vacuum Expectation Value.
VME bus	Versa Module Eurocard, industrial bus standard.
Z-Burst	Decay of a *Z*-boson created in cosmic ray neutrino-antineutrino annihilation.

1

Introduction

Astronomy is one of the oldest, perhaps even the oldest science practiced by humans. Archaeological findings document observations of the sky already 15 to 17 thousand years ago. In the beginning the question addressed to the sky was "What can you tell me about myself?" and not the more modern question "What can you tell me about you?". At times without scientific instruments offering a possibility to understand the intrinsic nature of the lights at the sky, the first question is much more important. The answers to these questions offered the possibility of measuring time and constructing calendars. This more religious point of view allowed for the cultivation of cereals and, as a consequence, the nutrition of a growing population and the first high cultures.

Until the beginning of modern times, the picture of the sky did not change significantly. At first, the knowledge of the mechanics of the solar system compiled by such great people as Nicolaus Copernicus, Tycho Brahe, Johannes Kepler or Galileo Galilei offered a shift to the second question, mentioned above.

After the realization that the objects in the sky have properties which can be measured and understood, also the interest in those objects was kindled. For a long time, the only access to information about planets, stars and other stellar objects was the eye. Even though the usage of the visible spectrum of the light had been optimized due to the usage of telescopes, many properties and even whole classes of objects were, literally, obscured.

When in the end of the 19^{th} and the beginning of the 20^{th} century the nature of electromagnetic waves and the properties of subatomic matter had been discovered by Albert Einstein, Max Planck and many other great scientists, this disadvantage could be eliminated.

Today we know of many windows to the universe. Optical observation is still very important, but further more a wide range of objects have been discovered in additional electromagnetical wave lengths from radio to TeV photons. The discovery of cosmic rays by Victor Franz Hess exploited a new possibility of sky observation: High energy particles. For very high energy cosmic rays, the sources are still unclear. A selection of possible candidates, especially for the expected neutrino component in the cosmic rays, will be given in the first chapter of this thesis. Currently, very popular representatives of particle "telescopes" are the Pierre Auger Observatory in Argentina or the AMANDA and IceCube neutrino detectors at the South Pole.

The several messengers for the observation of the sky have properties which are reducing their worth for answering some kinds of questions, but which are an advantage to solve other ones.

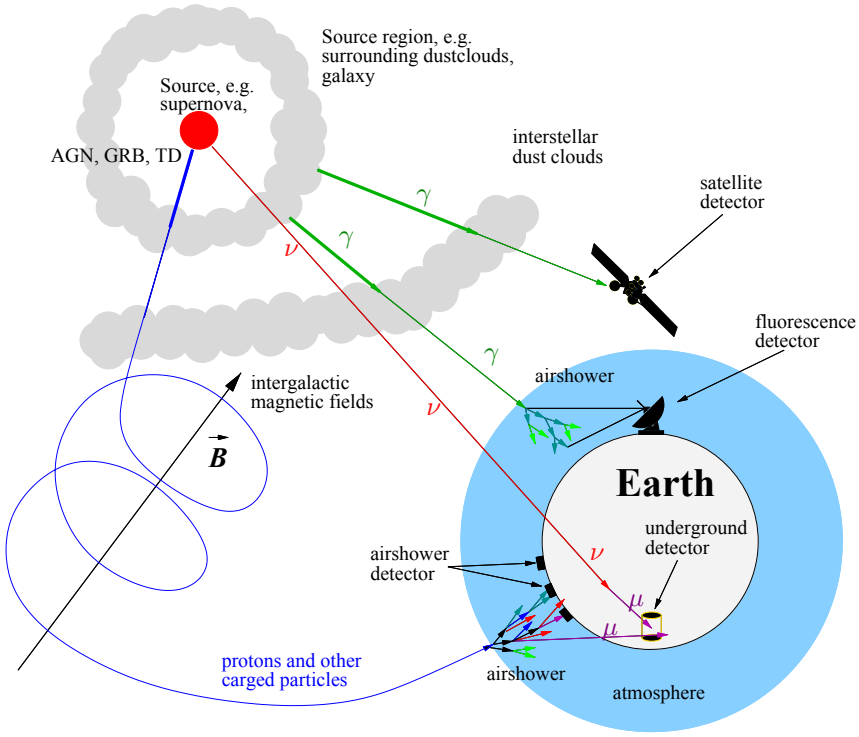

Fig. 1.1: Messengers from Extraterrestrial Objects. Image: [Wag04]

Fig. 1.1 shows a selection of messengers and delivers an impression of their advantages and disadvantages.

Light in form of photons is, as already mentioned, the most obvious way to receive information about the universe. It is not influenced significantly by electromagnetical fields and reaches the "eye" of the observer on a more or less straight line. Unfortunately, many objects like dust or gas clouds are blocking the photons and, accordingly, reduce the range for observations. The charged component of the cosmic rays, mainly protons, can communicate far-reaching information about possible sources. On the other hand, the particles not reaching extremely high energies will be deflected by magnetic fields and the information of the source direction is lost. Neutrinos are the only messengers penetrating every object between the source and the observer without deflection. But the very small cross section for neutrino interactions, puts very high demands on the detectors.

AMANDA and IceCube are searching for neutrinos as part of the cosmic rays, but also as secondary particles from cosmic ray interactions with Earth matter. Neutrino interactions with matter and the detection principles for neutrinos used by AMANDA and IceCube will be explained in Sec. 2.3. Chapter 3 is dedicated to the two experiments.

AMANDA, the predecessor of IceCube, is a neutrino detector with already impressive dimensions. About 690 optical modules carrying photomultipliers for light detection are deployed in depths between about 1500 m to 2000 m into the thick clear ice layer covering the South Pole. The detector volume consists of $15,700,700\,\mathrm{m}^3$ of ice. IceCube is even larger. In its final state it will spread out over a volume of $1\,\mathrm{km}^3$ filled with 4800 optical modules. This is roughly 64 times the size of AMANDA. The IceCube detector array completely surrounds AMANDA. The possibility to use IceCube as a veto for AMANDA events offers new possibilities for doing physics with AMANDA. This is described in Sec. 4.1. Consequently, a joint data taking of AMANDA and IceCube would be an advantage.

The first part of this thesis deals with the hardware integration of the AMANDA detector

into the IceCube data acquisition system. Especially the synchronization of both detectors with an accuracy of better than 10 ns has been a challenge. The necessary hard- and software improvements and measurements showing the reliability of the integration system are presented in Chapter 4.

The primary function of AMANDA and IceCube is to search for neutrinos. But this would not meet the whole range of the capabilities for neutrino detectors. Many groups of scientists inside the IceCube collaboration are working on physics that can be done with AMANDA and IceCube and which does not directly have to do with astroparticle phenomena. The very high energy of cosmic rays offers access to particle physics far beyond the capabilities of current particle colliders. As described in Sec. 5.1, the Standard Model of particle physics cannot solve all problems of modern particle physics. Thus, in the last decades many interesting and promising theories came up to cope with this challenge. One of these theories is supersymmetry (SUSY). A brief introduction to this field of physics is given in Chapter 5.

One prediction of SUSY is the existence of fermionic superpartners to Standard Model bosons and bosonic superpartners to Standard Model fermions. These superpartners have not been discovered yet. Thus, SUSY is not proven. Depending on the parameters of a SUSY model, IceCube should be capable to detect a special type of SUSY particles. The simulation of SUSY induced IceCube events is explained in Chapter 7. The results of the simulation show a special kind of geometrical event signature, making "SUSY events" distinguishable from other IceCube events. A filtering concept and its implementation for the search for SUSY event signatures in the IceCube data stream is introduced in Chapter 8. The short Chapter 6 illustrates possible background signatures and how to avoid them to be passed by the filter.

2

Neutrinos from Cosmic Rays

2.1 Neutrinos and their Properties

Neutrinos are uncharged *fermions*. In the *the standard model of particle physics* (*SM*) neutrinos are members of *lepton families*. One neutrino is always conjugated to one charged lepton. As current experiments are compatible with three different lepton families, three different neutrino types – called *flavors* – are distinguished:

e^-	μ^-	τ^-
ν_e	ν_μ	ν_τ

With the existence of antiparticles to the charged leptons, e^+, μ^+ and τ^+, the existence of the corresponding antineutrinos $\bar{\nu}_e$, $\bar{\nu}_\mu$ and $\bar{\nu}_\tau$ is a demand. This is not excluding the possibility of identical neutrinos and antineutrinos (see below). In case of the electron, the muon and the tauon, the antiparticle can be clearly distinguished from the particle by its charge. This is not possible for the neutrino.

Spin-$\frac{1}{2}$ particles, like neutrinos, are described by the *Dirac equation*[*]

$$\left(i\gamma^\mu \frac{\partial}{\partial x^\mu} - m\right)\Psi = 0, \tag{2.1}$$

where the 4×4 γ-matrices are defined by

$$\{\gamma^\mu, \gamma^\nu\} = 2g^{\mu\nu}\mathbb{1}. \tag{2.2}$$

$\mathbb{1}$ is the 4×4 identity matrix and $g^{\mu\nu} = \mathrm{diag}(1, -1, -1, -1)$. In the so called *Weyl representation*, the γ-matrices are written as

$$\gamma^0 = \begin{pmatrix} \mathbf{0} & \mathbf{1} \\ \mathbf{1} & \mathbf{0} \end{pmatrix} \qquad \gamma^i = \begin{pmatrix} \mathbf{0} & \boldsymbol{\sigma}^i \\ -\boldsymbol{\sigma}^i & \mathbf{0} \end{pmatrix} \quad \text{and} \quad \gamma^5 = \begin{pmatrix} \mathbf{-1} & \mathbf{0} \\ \mathbf{0} & \mathbf{1} \end{pmatrix} \tag{2.3}$$

and the 2×2 *Pauli matrizes* as

$$\sigma^0 = \begin{pmatrix} 1 & 0 \\ 0 & 1 \end{pmatrix} \quad \sigma^1 = \begin{pmatrix} 0 & 1 \\ 1 & 0 \end{pmatrix} \quad \sigma^2 = \begin{pmatrix} 0 & -i \\ i & 0 \end{pmatrix} \quad \sigma^3 = \begin{pmatrix} 1 & 0 \\ 0 & -1 \end{pmatrix}. \tag{2.4}$$

[*]For better readability in this section (only!) $\hbar$ and c are set to 1.

γ_5 is called the *chirality matrix*. It is Hermitian and has the eigenvalues ± 1. The *four-component spinor* Ψ can be split with the help of the two *chiral projection operators*

$$P_L = \frac{1}{2}(1-\gamma_5) \quad \text{and} \quad P_R = \frac{1}{2}(1+\gamma_5) \tag{2.5}$$

into two left- and right-chiral components

$$\Psi = \begin{pmatrix} \Psi_L \\ \Psi_R \end{pmatrix} \tag{2.6}$$

with

$$\begin{pmatrix} \Psi_L \\ 0 \end{pmatrix} = P_L\Psi \quad \text{and} \quad \begin{pmatrix} 0 \\ \Psi_R \end{pmatrix} = P_R\Psi. \tag{2.7}$$

Ψ_L and Ψ_R are 2-component *Weyl spinors*. They are chirality eigenstates with the eigenvalues

$$\gamma_5\Psi_R = +\Psi_R \tag{2.8a}$$

$$\gamma_5\Psi_L = -\Psi_L. \tag{2.8b}$$

Using the Weyl spinors, the Dirac equation 2.1 can be rewritten [Zub04]

$$\left(i\frac{\partial}{\partial x^0} + i\sigma^i\frac{\partial}{\partial x^i}\right)\Psi_R = m\Psi_L \tag{2.9a}$$

$$\left(i\frac{\partial}{\partial x^0} - i\sigma^i\frac{\partial}{\partial x^i}\right)\Psi_L = m\Psi_R. \tag{2.9b}$$

For $m = 0$ the two equations decouple. The resulting equations are identical to the *Schrödinger equation*

$$i\frac{\partial}{\partial x^0}\Psi_{L,R} = \pm i\left(\sigma^i\frac{\partial}{\partial x^i}\right)\Psi_{L,R}. \tag{2.10}$$

The *charge conjugation* operator C connects particle Ψ and antiparticle $\bar{\Psi}$

$$C\left|f(\boldsymbol{x},t)\right\rangle = \eta_C\left|\bar{f}(\boldsymbol{x},t)\right\rangle. \tag{2.11}$$

It transforms a spinor like

$$\Psi \xrightarrow{C} \Psi^C \equiv \eta_C C\bar{\Psi}^T \tag{2.12}$$

with $\bar{\Psi} = \Psi^\dagger\gamma_0$ and $C = i\gamma_0\gamma_2$. C obeys the transformations

$$C^{-1}\gamma_\mu C = -\gamma_\mu^T \qquad C^{-1}\gamma_5 C = -\gamma_5^T \qquad C^\dagger = C^{-1} = C^T = -C. \tag{2.13}$$

From this follows

$$\Psi_L \xrightarrow{C} (\Psi_L)^C = (\Psi^C)_R \tag{2.14a}$$

and

$$\Psi_R \xrightarrow{C} (\Psi_R)^C = (\Psi^C)_L. \tag{2.14b}$$

A *Dirac neutrino* has four degrees of freedom: Ψ_L, Ψ_R, $(\Psi^C)_R$, $(\Psi^C)_L$. Eigenstates of chirality are also eigenstates of charge conjugation

$$\gamma_5\Psi = \lambda\Psi \qquad \Rightarrow \qquad \gamma_5\Psi^C = -\lambda\Psi^C.^* \tag{2.15}$$

*This can be shown with the help of the relations $C^{-1}\gamma_5 C = \gamma_5^T$, $\{\gamma_0,\gamma_5\} = 0$ and $C^T = -C$.

Therefore, the neutrino can be distinguished from the antineutrino by its chirality. Because all inner quantum numbers are identical for neutrinos and antineutrinos – in particular there is no charge –, it is not obligatory to distinguish between them. If the neutrino is its own antiparticle, it will be called *Majorana particle*[*]. The amount of degrees of freedom is reduced to two: $\Psi_L = (\Psi^C)_L$ and $\Psi_R = (\Psi^C)_R$. In nature, only Ψ_L respectively $(\Psi^C)_R$ have been observed. Consequently neutrinos are allowed to be Dirac as well as Majorana particles.

Detailed information about all neutrino properties can be found in [GK07].

2.2 High Energy Cosmic-Ray Neutrinos

To be seen in large ice neutrino detectors like *AMANDA* or *IceCube*, neutrinos have to have a certain minimum energy. For IceCube, the lower threshold lies at about 1TeV for neutrino induced cascades after cuts [Ice01] and for AMANDA, this threshold lies between 10GeV and 50GeV [GHR+07]. As neutrinos only interact weakly, they cannot be accelerated in electromagnetic fields. Consequently, neutrinos with energies above the detector threshold(s) have to be products of decays or interactions of high energy cosmic-ray particles.[†]

2.2.1 Cosmic Rays

After the discovery of the cosmic rays by *Victor Franz Hess*, their energy spectrum and their composition were measured by many different experiments. Today, the cosmic ray spectrum is known from energies of about 10^9 eV up to 10^{20} eV. Below 10^9 eV, the cosmic rays are deflected by the solar wind and the measured spectrum is no longer identical to the interstellar spectrum. Above 10^{20} eV the amount of particles reaching the Earth is so small that it takes a long time to obtain enough statistics to comprehend the spectrum. Even with large detector arrays, like the *Pierre Auger Observatory* [Aug97], unambiguous statements about the shape of the cosmic-ray spectrum at highest energies can only be made after years of data taking. In the following, particles with energies above 10^9 eV are referred to as *high energy cosmic rays* (HECR) and particles exceeding 10^{18} eV as *ultra high energy cosmic rays* (UHECR).

Fig. 2.1: Victor Hess

The differential cosmic-ray energy *flux spectrum* follows a nearly featureless power law

$$I(E) \propto E^{-\gamma} \left(\frac{\text{particles}}{\text{cm}^2 \cdot \text{s} \cdot \text{sr} \cdot \text{eV}} \right) \tag{2.16}$$

stretching out over many magnitudes of energy and flux [PDG08]. γ is called the *spectral index*. A plot containing a collection of cosmic-ray flux measurements from many different experiments is given in Fig. 2.2. Up to 5×10^9 eV the flux reduction due to the shielding by the influence of the sun is visible. From there up to an energy of about 4×10^{15} eV the spectral index equals 2.7 . The region around 4×10^{15} eV is called *the knee*. Behind the knee, the spectral index is changing to $\gamma \approx 3.0$, which can be explained by the assumption that galactic sources cannot accelerate particles to higher energies. Additionally, it is probable that particles with higher energies cannot be bound to our galaxy by its own magnetic field [Ptu01]. γ is constant for energies from the knee to roughly 6×10^{18} eV. Above this energy the spectral index is falling

[*]Ettore Majorana, Prof. of Physics at the University of Naples, ∗ Aug. 5th 1906, missed since Mar. 1938.

[†]This thesis only covers neutrino physics from non terrestrial sources. High energy particle sources on Earth are currently irrelevant for neutrino telescopes at the South Pole.

again. This flattening is called *the ankle*. Two explanations for this feature are discussed. In [Fly94] the ankle is interpreted as a change from galactic to extragalactic cosmic rays in combination with a change of the cosmic-ray composition from heavier to lighter particles. The light extragalactic component, mainly protons, overtakes the heavy galactic part. The second idea is covered by [BGG06]. Here, the ankle is part of a bump caused by protons, which have lost energy due to the *GZK* effect (↗Sec. 2.2.6) [ZK66; Gre66]. They accumulate at energies slightly lower than the GZK threshold and cause a reduction of the spectral index in that area. In recent times, the experiments *HiRes* [HiR08] and the Pierre Auger Observatory [Aug08] observed a steepening of the cosmic-ray spectrum above 4×10^{19} eV. These results are a strong indication for the existence of the GZK effect.

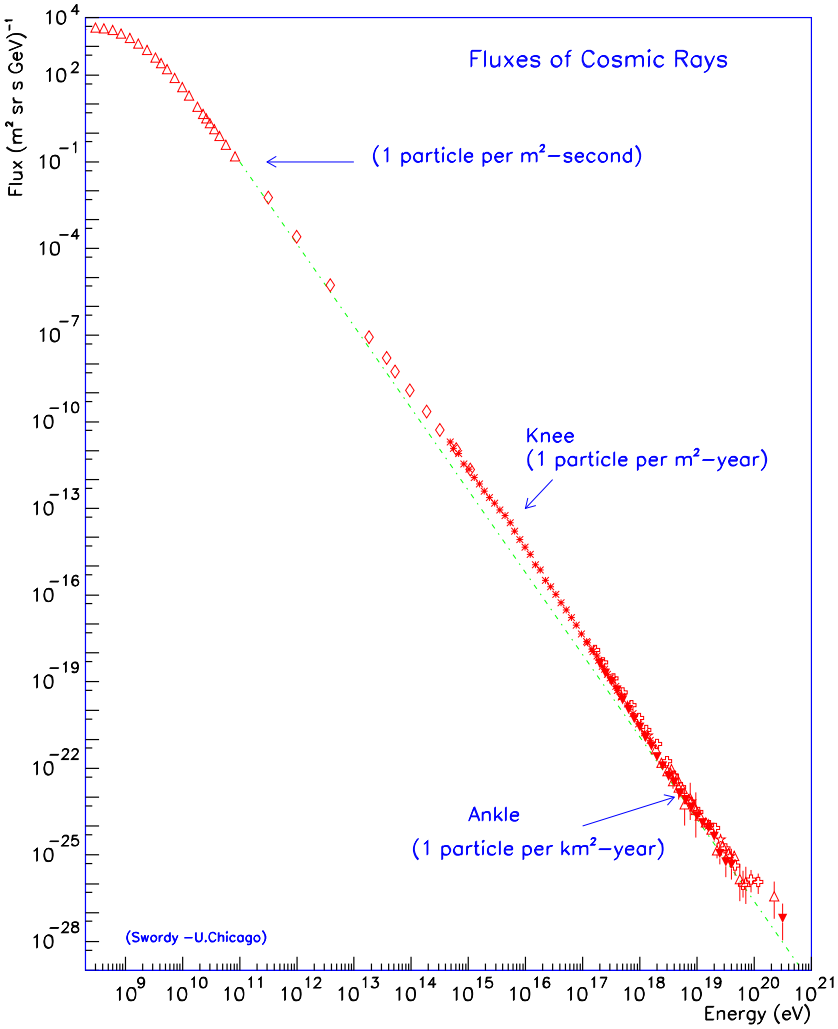

Fig. 2.2: Cosmic-Ray Spectrum. Image: [Swo97]

A good explanation for the highly non-thermal power law spectrum was first found by *Enrico Fermi* [Fer49] with the concept of scattering of particles on moving magnetic clouds. This concept – called *second order Fermi acceleration* – was extended to scattering on shock fronts, moving at relativistic speed through the interstellar medium. This *first order Fermi acceleration* is more efficient [BE87; Web83; Kol07].

The preceding observations and conclusions apply only to charged cosmic rays:

component	fraction
protons	87 %
alpha particles	12 %
electrons	2 %
heavier nuclei	1 %

Photon and neutrino fluxes have been excluded. But the existence of accelerated charged particles is an evidence for high energy neutrinos. A few possible sources of high energy neutrinos are described in the following sections.

2.2.2 The Waxman-Bahcall-Limit

In 1999, *Eli Waxman* and *John Bahcall* calculated an upper limit for diffuse neutrino fluxes especially from sources like AGN (↗Sec. 2.2.4) and GRBs (↗Sec. 2.2.5) [WB99]. In 2001, they validate this limit [BW01]. In the considered sources, neutrino production via photo-meson or $p-p(n)$ reactions is assumed*.

$$\begin{array}{lllll} p+p & \longrightarrow & p+p+\pi^+ + \pi^- & & \\ p+\gamma & \longrightarrow \Delta^+ \longrightarrow & n & +\pi^+ & \\ p+\gamma & \longrightarrow \Delta^+ \longrightarrow & p & +\pi^+ + \pi^- & \\ \hline & & \pi^+ & \longrightarrow \boldsymbol{\nu_\mu} + \mu^+ & \\ & & \pi^- & \longrightarrow \boldsymbol{\bar{\nu}_\mu} + \mu^- & \\ \hline & & & \mu^+ \longrightarrow e^+ + \boldsymbol{\bar{\nu}_\mu} + \boldsymbol{\nu_e} & \\ & & & \mu^- \longrightarrow e^- + \boldsymbol{\nu_\mu} + \boldsymbol{\bar{\nu}_e} & \end{array} \tag{2.17}$$

In this reactions neutrinos are produced in the ratios $\nu_e : \nu_\mu : \nu_\tau = 1 : 2 : 0$. Additionally, the sources have to be optically thin for protons. Thin on this note are sources with a maximum extension of the order of the mean free path of protons (according to the reactions in 2.17). Hence, these sources are also supposed to produce the charged high energy cosmic rays. If first order Fermi acceleration for the protons is postulated, then the measured cosmic-ray spectrum will be compatible with a source spectrum proportional to E^{-2}. $\gamma = 2$ is the lower limit of the spectral index for this acceleration type. With the energy production rate $\dot{\epsilon} \approx 5 \times 10^{44}\,\mathrm{erg\ Mpc^{-3} yr^{-1}}$ in the energy range from $10^{19}\,\mathrm{eV}$ to $10^{21}\,\mathrm{eV}$ [Wax95], it is possible to calculate an overall limit of

$$E_\nu^2 \Phi_\nu < 2 \times 10^{-8} \frac{\mathrm{GeV}}{\mathrm{cm^2\ s\ sr}} \tag{2.18}$$

for the sum over these sources.

2.2.3 *Z*-Bursts

In the classical hot big bang model, neutrinos decoupled from the equilibrium at a temperature of $\mathcal{O}(\mathrm{MeV})$. This was already seconds after the big bang. The momentum p of every neutrino flavor i at temperature T followed a *Fermi-Dirac spectrum* [Wei82]

$$f_i(p) = \frac{1}{\exp\left(\frac{p-\mu_i}{T}\right) + 1}. \tag{2.19}$$

μ_i is the chemical potential of every neutrino flavor. According to [DHS+02] this potential can be neglected.

*Reactions with primary neutrons and intermediate stages with π^0 have been omitted in Eq. 2.17

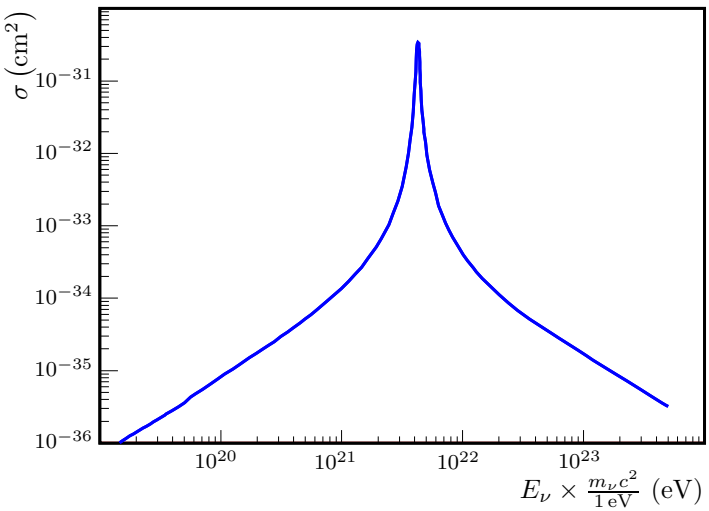

Fig. 2.3: $\nu\bar{-}\nu$ annihilation cross section for Z-exchange in the s-channel as function of the primary neutrino energy $\times\, m_\nu c^2$. Image: [Rou93]

In principle, the evolution of temperature for photons and decoupled neutrinos is the same, and proportional to the scale size R of the universe

$$T \propto \frac{1}{R}. \tag{2.20}$$

Unlike the neutrinos the photons have been reheated by e^+ - e^- annihilation at a later date. This effect can be taken into account by the introduction of a correction parameter

$$\eta = \sqrt[3]{\frac{11}{4}}. \tag{2.21}$$

The temperature of the cosmic microwave background is known to be $T_{\mathrm{CMB}} = 2725 \pm 2\,\mathrm{mK}$ [MFS+99] (↗Sec. 2.2.6). From this the cosmic neutrino background temperature $T_{C\nu B}$ can be calculated to [IH83]

$$T_{\mathrm{C}\nu\mathrm{B}} = \frac{1}{\eta} T_{\mathrm{CMB}} = 1945 \pm 1\,\mathrm{mK}. \tag{2.22}$$

According to this model, the current density of cosmic neutrinos is $n_\nu = 336\,\mathrm{cm}^{-3}$ summed over all neutrino flavors [Zub04].

The only cosmic-ray process sensitive to the neutrino background is the neutrino-antineutrino annihilation at the energy of the Z-boson [Wei82].

$$\nu + \bar{\nu} \longrightarrow Z \tag{2.23}$$

If high energy neutrinos are present, then they should interact with the cosmic neutrino background. This is demonstrated by the neutrino-antineutrino cross section for the Z-exchange in the s-channel, which is plotted in Fig. 2.3.

The resulting Z-boson mainly (69.9 %) decays into hadronic jets. These are producing neutrinos with lower energy than the primary neutrino in a high multiplicity. This process can continue as long as the neutrinos have enough energy for reaction 2.23. Therefore an excess slightly below the Z mass of 91 GeV (in the center of mass system of background and the high energy neutrino) in the cosmic-ray neutrino spectrum is expected. The contribution of the Z-burst process to the neutrino flux is presented in Fig. 2.4.

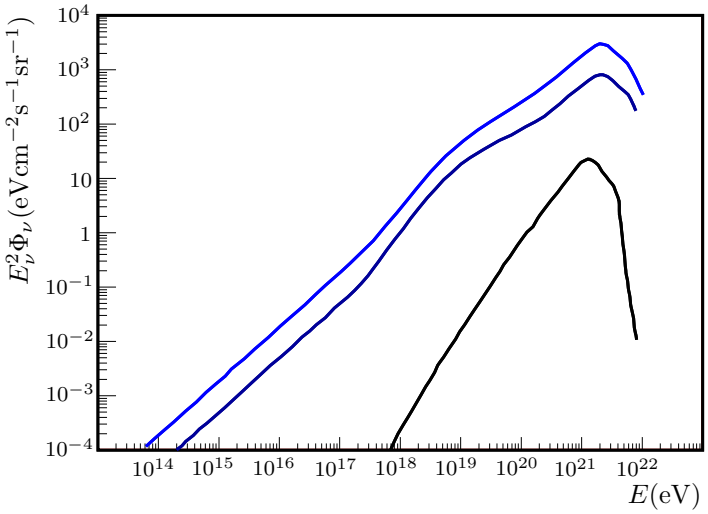

Fig. 2.4: Expected *Z*-burst neutrino fluxes for the three neutrino flavors. Beginning from top: $\nu_\mu + \bar{\nu}_\mu$, $\nu_e + \bar{\nu}_e$, $\nu_\tau + \bar{\nu}_\tau$. Image: [YSL98]

The flux differences between the different flavors is a consequence of the Z-decay. The ratios between the produced charged leptons is dependent on their masses.

2.2.4 Active Galactic Nuclei (AGN)

According to the current knowledge of objects of galactic size, the center of most galaxies contains a *super massive black hole* with a mass of the order of 10^6 to $10^{10} \times M_\odot$. In an *active* galactic nucleus the black hole is in a state of extended mass accretion. This process is associated with the emission of huge amounts of energy. Consequently, AGN belong to the most luminous objects in space. Most radiation emission happens in an area with a size comparable to our solar system. Many objects with different properties can be ascribed to AGN. The most general classification of AGN can be done by their radio emission. *Radio-quiet* AGN usually have no or only a very weak relativistic particle *jet*, which is emitted from the nucleus. *Radio-loud* AGN produce a highly relativistic jet of particles to compensate excessive angular momentum during the accretion process. These jets are believed to be able to produce cosmic rays of the highest energies. The underlying process is first order Fermi acceleration in shock fronts moving through the jet. The particles are bound to the jet region by magnetic fields in the order of a few Gauss produced by the plasma in the jet.

A further subclassification of radio-loud AGN can be done by the angle between the jet direction and the line between the AGN and the observer [UP95]. In this scheme especially the *blazars* are interesting. An AGN is called a blazar if the jet is pointing directly into the direction of the observer (↗Fig. 2.5). If the jets are particle accelerators, these AGN may be seen as cosmic-ray sources. A correlation between the positions of AGNs and the source direction of cosmic rays was found by the Pierre Auger Experiment in 2007 [A$^+$07a].

Commonly pure leptonic and mixed leptonic/hadronic acceleration inside the jets are discussed. The pure leptonic model postulates the acceleration of electrons only, the mixed model, additionally, allows for hadron – mainly proton – acceleration. In the mixed model the high energy protons react with the photon field in the neighborhood of the jet according to photo-meson reaction in Eq. 2.17.

An (outdated) example for a mixed model neutrino flux calculation is given in [HZ97]. Fig. 2.6

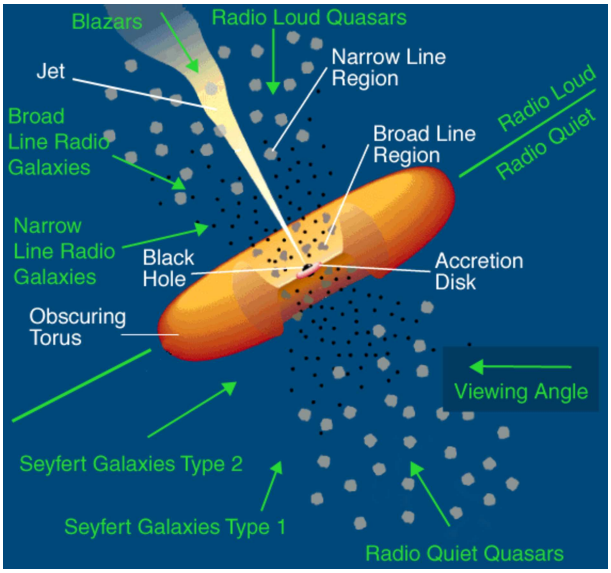

Fig. 2.5: Unified model of active galactic nuclei (AGN). Image: http://www.auger.org

is showing this prediction in comparison to another model from [SDSS92]. Current limits – e.g. from the Baikal neutrino telescope [W+05] – already fall below the expected diffuse neutrino flux. A more detailed calculation with a slightly lower flux can be found in [Bec04].

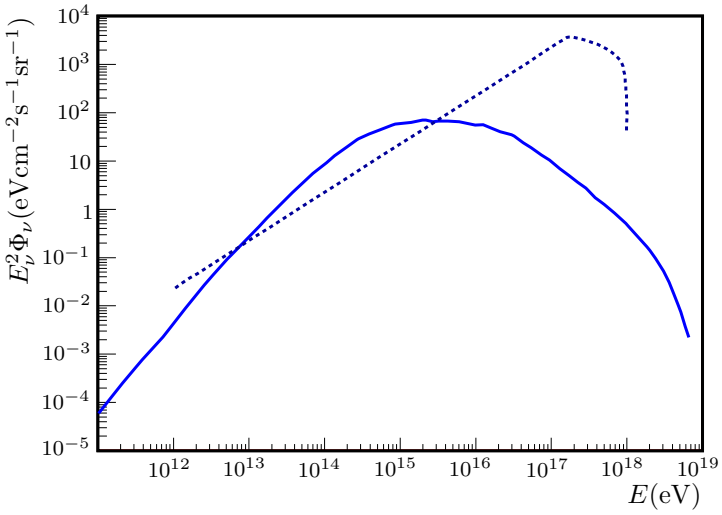

Fig. 2.6: Expected neutrino fluxes from AGN calculated according to two different models. Solid line: ν_μ flux after [SDSS92], dashed line: all flavor ν flux after [HZ97]

2.2.5 Gamma-Ray Bursts (GRBs)

In July 1967, two satellites of the United States of America *Vela* program observed the first gamma ray burst. As the Vela satellites were designed from the US military for detection of illegal atmospheric nuclear weapon tests, the first scientific results have not been published earlier than 1973 [KSO73].

The progenitors of GRBs are still under discussion. The best candidates so far are collapses

of massive stars with a high rotation frequency [Woo93; MW99], millisecond proto-magnetars [TCQ04] and mergers of neutron star binaries or black hole – neutron star systems [JERF99].

Gamma-ray bursts belong to the objects with the highest luminosity in the universe. They are isotropically distributed over the full sky and have high redshifts. Energies of about 10^{44} J are emitted in the γ-ray spectrum within a time of less than a second up to minutes. This short time scale reduces the active volume of the burst to a sphere with a radius $c\Delta t \approx 100\,\text{km} - 1000\,\text{km}$. In this region a *fireball* is expected, in which the high γ-ray density leads to pair production

$$\gamma + \gamma \longrightarrow e^+ + e^-. \tag{2.24}$$

The expansion of the fireball is highly relativistic ($\Gamma_{\text{shock}} = 1/\sqrt{1 - v^2/c^2} > 100$) [KGH01]. This fireball model [Pir99] would predict a thermal photon spectrum to be emitted from the ball. Photons are trapped inside the fireball and their radiation energy will be converted into kinetic energy of baryons, if no further assumptions are made. To explain the measured highly non-thermal photon spectra [CH81; BS99] the fireball shock model is introduced [RM92; MR93]: The energy in the ball is not emitted isotropically, but along jets. Additionally the interaction between the fireball and the interstellar medium is taken into account. If the fireball moves through the interstellar medium, shock waves, which are mediated by chaotic magnetic fields, build up and travel back through the ball. The electrons in the fireball have energies which are high enough that the synchrotron radiation, produced in the magnetic fields, lies in the γ-ray spectrum (↗Fig. 2.7). Therefore, more complicated γ-ray spectra from GRBs can be explained by multiple shocks moving through the GRB fireball.

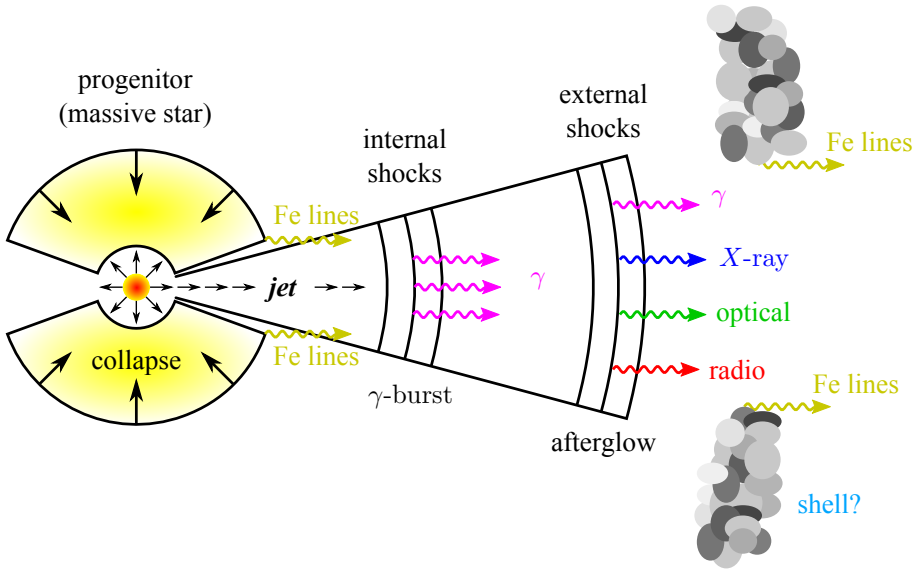

Fig. 2.7: Gamma-ray burst (GRB) fireball shock model. The γ-ray emission happens via synchrotron radiation on shocks, which are mediated by magnetic fields.
Image: [Més01]

The front of the relativistic shock moving into the interstellar medium is appropriate to produce cosmic rays with ultra high energies (up to 10^{20} eV) via first order Fermi acceleration [Vie95]. As GRBs are compact objects, the density of photons (mean energy $E_\gamma \approx 1\,\text{MeV}$) and protons ($E_p > 10^{15}$ eV) is high enough, to convert a fraction of the proton energy into neutrinos via photo-meson production (↗Sec. 2.2.2) [WB97]. The γ-ray spectrum of GRBs follows a broken power law $\Phi_\gamma \propto E_\gamma^{-\beta}$ with $\beta = 1$ for $E_\gamma < E_\gamma^b$ and $\beta = 2$ for $E_\gamma > E_\gamma^b$. E_γ^b, the break energy for the photon spectrum, is derived from the observed GRB spectra [B+93]. If a proton spectrum

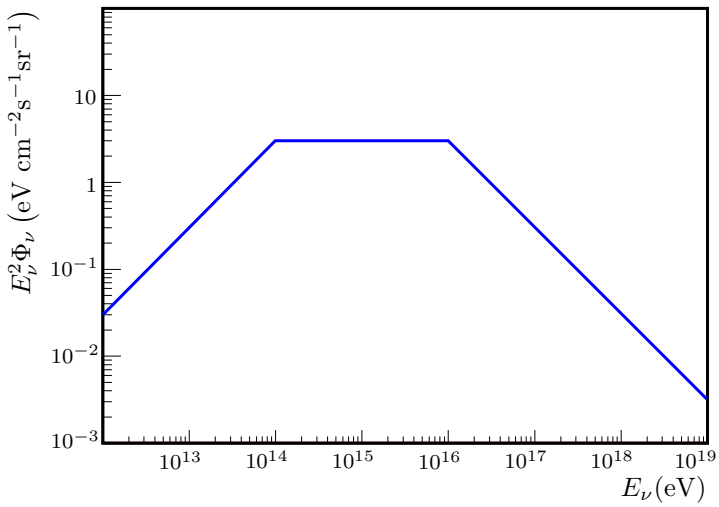

Fig. 2.8: GRB Neutrino Flux. Image: [WB97]

with $\Phi_p \propto E_\gamma^{-2}$ from first order Fermi shock acceleration is assumed, the neutrinos from photomeson production also follow a broken power law with the same spectral indices. The neutrino break energy can be calculated from the γ-ray break energy as

$$E_\nu^b \approx \frac{5}{3} \times 10^{12} \Gamma_{\text{shock}} \frac{1\,\text{MeV}}{E_\gamma^b}\,\text{eV}. \tag{2.25}$$

For the break energy follows, with a given Γ-Factor of about 100, $E_\nu^b \approx 10^{14}\,\text{eV}$.

If the energy of pions and muons is high enough so that also other effects than the adiabatic expansion of the GRB are cooling them down, the resulting neutrino spectrum is getting steeper and from $E_\nu \gtrsim 10^{16}\,\text{eV}$ onwards the flux follows $\Phi_\nu \propto E_\nu^{-3}$.

2.2.6 Greisen-Zatsepin-Kuzmin (GZK) cutoff

According to the *Big Bang Theory* of the universe, electromagnetic waves have been in thermal equilibrium with matter until *recombination* of protons and electrons to hydrogen atoms. The basic process for transfer of kinetic energy was *Thomson scattering* of the photons at the free electrons. Recombination takes place at a temperature of about 3000 K which was reached about 380000 years after the Big Bang. At this time the universe became transparent to light. Today the photons of that time still exist, but due to the expansion of the universe with a very high redshift and wavelengths of about millimeters.

The idea of this *Cosmic Microwave Background* (CMB) was first mentioned by *Georgi Antonowitsch Gamow* [Gam48] supported by the works of *Ralph Alpher* and *Robert Herman* about the genesis of elements. Today's temperature of this radiation was calculated to about 5 K.

The CMB was not found before 1965 and this even only accidentally. The two physicists *Arnold Allan Penzias* and *Robert Woodrow Wilson* were working for the Bell Laboratories. With a large horn antenna radio telescope they tried to receive radio signals reflected by satellites. During calibration work they measured radiation with a temperature of about 3.5 K [PW65]. This "noise" was identified by *Robert Henry Dicke* as the predicted CMB radiation. Dicke made an additional second precise measurement of the CMB [DPRW65].

With the *Far InfraRed Absolute Spectrometer* (FIRAS) aboard the *COsmic Background Explorer* (COBE) satellite the spectrum of the CMB radiation was measured very precisely (Fig. 2.9).

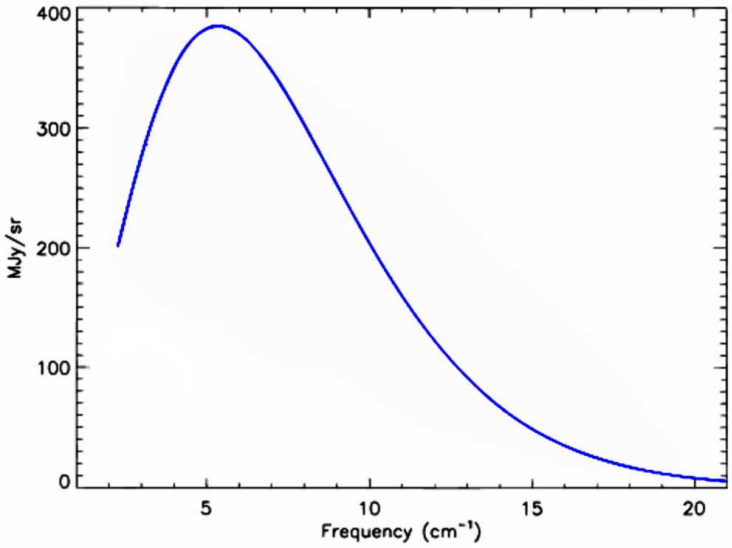

Fig. 2.9: Monopole cosmic microwave background (CMB) spectrum measured by the Far InfraRed Absolute Spectrometer (FIRAS) aboard the Cosmic Background Explorer (COBE) satellite. The fit is lying over the data, the error bars are covered by the line. Image: [FCG+96]

It can be fitted very well with the *Planck function* for the *black body radiation* at a temperature of $T_{\mathrm{CMB}} = 2725 \pm 2\,\mathrm{mK}$ [MFS+99; FM02].

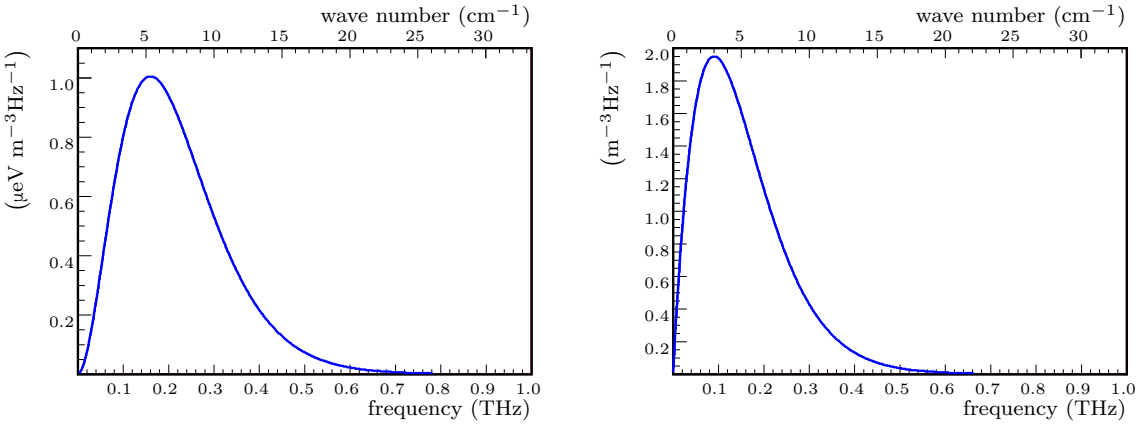

(a) spectral energy density

(b) spectral photon density

Fig. 2.10: Planck's law for CMB temperature $T_{\mathrm{CMB}} = 2.725\,\mathrm{K}$.

With the given spectral energy (Fig. 2.10(a))

$$U_\nu^0(\nu, T) = \frac{2h\nu^3}{c^3} \frac{1}{e^{\frac{h\nu}{k_B T}} - 1} \tag{2.26}$$

and the spectral photon density (Fig. 2.10(b))

$$n_\nu^0(\nu, T) = \frac{2\nu^2}{c^3} \frac{1}{e^{\frac{h\nu}{k_B T}} - 1} \tag{2.27}$$

the absolute photon density

$$\bar{n}_\gamma = \lim_{\nu\to\infty} \frac{1}{\nu} \int_0^\nu n_\nu^0(\nu', T)\mathrm{d}\nu' = (410.4 \pm 0.9)\,\mathrm{cm}^{-3} \tag{2.28}$$

can be calculated [B+03]. Here, ν is the photon frequency. From this follows the mean energy per CMB-photon

$$\bar{E}_\gamma = \frac{1}{\bar{n}_\gamma} \lim_{\nu\to\infty} \frac{1}{\nu} \int_0^\nu U_\nu^0(\nu', T)\mathrm{d}\nu' \approx 0.64\,\mathrm{meV}. \tag{2.29}$$

Three possible interactions with the CMB lead to an energy loss of high energy protons which are assumed to be the major contribution to the cosmic-ray composition at the highest energies (↗Sec. 2.2.1):

(a) Degradation due to the *inverse Compton effect* happens on a timescale of about $10^{20}\gamma^{-1}(m_P/m_e)^3$ s where γ is the relativistic factor for the proton [Hoy65]. For a 10^{21} eV proton this would be ≈ 18 billion years. This is more than the age of the universe and it may be supposed that energy loss of protons due to inverse Compton scattering on the CMB is insignificant.

(b) There is a small contribution to the proton energy loss due to *pair production*. The minimum scale length for energy loss is about half of the *Hubble length* (13.8 billion light years) [Gre66].

(c) Compared to the *photo pion production* the pair production is negligible. The basic concept of photo pion production is already mentioned in Sec. 2.2.2, but here the photons are not part of the astrophysical high energy particle source. The energy of the highest energy cosmic-ray protons is high enough, to produce a Δ^+-*resonance* with the CMB photons:

$$p + \gamma_{\mathrm{CMB}} \longrightarrow \Delta^+ \tag{2.30}$$

The Δ^+-resonance decays

$$\begin{array}{lll} \Delta^+ \longrightarrow n + \pi^+ & \longrightarrow & p + \pi^+ + e^- + \bar{\nu}_e \\ \Delta^+ & \longrightarrow & p + \pi^0, \end{array} \tag{2.31a}$$

and the outgoing proton has lost between about 13 % and 22 % of its initial energy [Gre66]. The mean time $\tau_{p\gamma}$ between reactions of protons with the CMB photons is shown in Fig. 2.11. 10^7 yrs correspond to about 3 Mpc. This is comparable to the diameter of our *local galaxy group*. Taken into account the energy loss at every collision, it is obvious that the volume for sources of detectable high energy protons with energies higher than 2×10^{20} eV is limited. Above this energy a steepening in the cosmic-ray spectrum (↗Sec. 2.2.1) should be visible. The decelerated protons build up a bump in the spectrum just below the resonance energy. The steepening is called *GZK cutoff*, after their predictors *Kenneth Greisen* and *Vadim Kuzmin* and *Georgiy Zatsepin*. A steepening in accord with the prediction has been found by the Pierre Auger Collaboration in 2008 [A+08].

The produced pions in reaction 2.31a decay into muons

$$\begin{array}{l} \pi^+ \longrightarrow \nu_\mu + \mu^+ \\ \pi^- \longrightarrow \bar{\nu}_\mu + \mu^- \end{array} \tag{2.31b}$$

which decay further into electrons

$$\begin{array}{l} \mu^+ \longrightarrow e^+ + \bar{\nu}_\mu + \nu_e \\ \mu^- \longrightarrow e^- + \nu_\mu + \bar{\nu}_e. \end{array} \tag{2.31c}$$

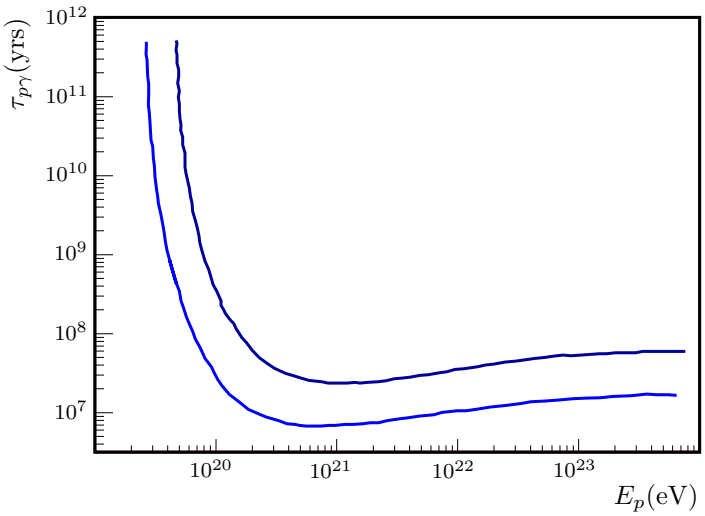

Fig. 2.11: Mean Time Between $\gamma_{\mathrm{CMB}} - p$ Reactions. Image: [ZK66]
Upper line: CMB temperature $T_{\mathrm{CMB}} = 2\,\mathrm{K}$,
lower line: CMB temperature $T_{\mathrm{CMB}} = 3\,\mathrm{K}$.

As each of the latter two decays produce neutrinos, the GZK effect should deliver a contribution to cosmic-ray neutrinos. Detailed calculations [ESS01] of the expected neutrino flux are displayed in Fig. 2.12

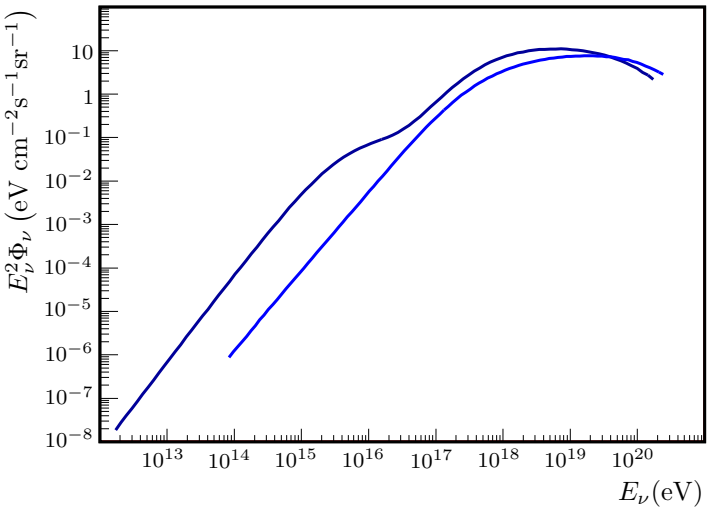

Fig. 2.12: Expected Neutrino Flux from GZK Effect. Top: $\nu_e + \bar{\nu}_e$, bottom: $\nu_\mu + \bar{\nu}_\mu$.
Image: [ESS01]

2.2.7 Topological Defects

During the expansion of the universe, the four forces separated sequentially and developed their natural properties, as they are known today. These processes can physically be described by phase transitions. They happened not smoothly, but in steps at fixed positions in space-time. In

the inflationary period of the universe [BDdS09], not all areas in space-time were coupled causally. This implies that the phase transitions could start at many different regions, without knowing from each other. The result of one phase transition form the properties of the hypersurface of the affected region. The mathematical description of hypersurfaces is done by the definition of topologies. While the universe expanded, the topologies grew and successively met each other. Topologies of different space-time regions do not have to be identical, and the boundary surfaces may persist in a (meta)stable state. These boundaries are called topological defects [Gan03].

The theories for topical defects are numerous. *Domain Walls*, *cosmic strings*, *cosmic textures* or *texture knots* are only a few examples. Some of the defects are not stable. By the decay their inherent energy is set free. The decay channels are not restricted, so also hadronic decay modes are possible. Within hadronic cascades neutrino production is a consequence of meson decay. As an example for the contribution from topological defects to the cosmic-ray neutrino flux, a calculation for the flux due to the collapse of cosmic strings [YDJS97] is presented in Fig. 2.13.

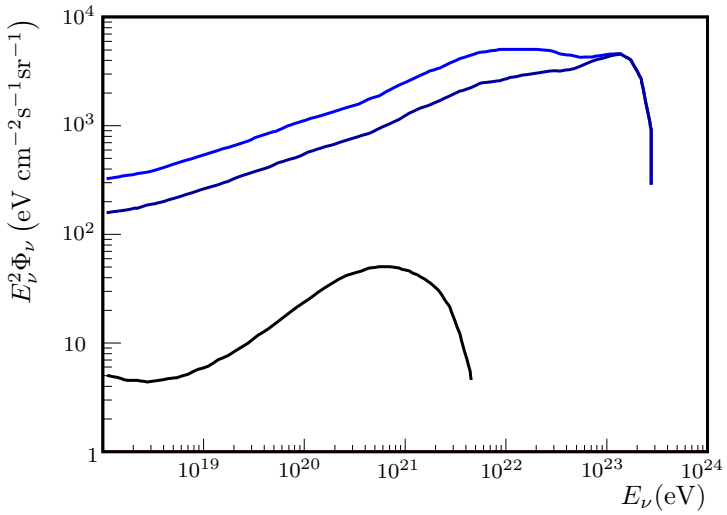

Fig. 2.13: Neutrinos From Cosmic Strings. Calculation of the differential flux from the collapse of cosmic string loops. All neutrino masses are assumed to be 1 eV. From top to bottom: ν_μ, ν_e, ν_τ. Image: [YDJS97]

2.3 High Energy Neutrino Detection

As mentioned in Sec. 2.2, neutrinos are good candidates to be probes for a wide range of astrophysical phenomena. They are not scattered by electromagnetical fields and penetrate matter with nearly no absorption losses. Unfortunately, especially the latter property makes it difficult, to detect neutrinos. Neutrinos interact only weakly and, accordingly, have a very small interaction cross section. In the following two sections, neutrino interactions and the way, how to detect cosmic-ray neutrinos are introduced.

2.3.1 Neutrino Interactions with Matter

Interactions of the types

$$(\nu_\ell \vee \bar{\nu}_\ell) + N \xrightarrow[\mathrm{W}]{} \left(\ell \vee \bar{\ell}\right) + X \tag{2.32a}$$

$$(\nu_\ell \vee \bar{\nu}_\ell) + N \xrightarrow[\mathrm{Z}]{} (\nu_\ell \vee \bar{\nu}_\ell) + X \tag{2.32b}$$

deliver the main contribution to neutrino interactions [GQRS98]. N represents a nucleon in the parton model [GQRS98]. The corresponding differential charged current cross section for an incoming neutrino with energy E_{ν_ℓ} and an outgoing charged lepton with energy E_ℓ is

$$\frac{d^2\sigma}{dxdy} = \frac{2G_f^2 M E_{\nu_\ell}}{\pi}\left(\frac{M_W^2}{Q^2+M_W^2}\right)^2\left[xq + x\bar{q}(1-y)^2\right] \tag{2.33}$$

with

$$\begin{aligned} q &= \frac{u_v+d_v}{2} + \frac{u_s+d_s}{2} + s_s + b_s \\ \bar{q} &= \frac{u_s+d_s}{2} + c_s + t_s. \end{aligned} \tag{2.34}$$

The quark distribution functions q and $\bar{q}$ are dependent on the individual quark distributions u, d, c, s, t, b, which are all functions of the invariant momentum transfer $-Q^2$ and the *Bjorken scaling variable* $x = Q^2/2Mv$. The quark flavor subscripts v and s mark the valence and the see quark contributions. The other parameters of Eq. 2.33 are the energy loss in the nucleon rest frame $\nu = E_{\nu_\ell} - E_\ell$, the relative energy transfer $y = E_{\nu_\ell}/\nu$, the nucleon mass M, the boson mass M_W and the *Fermi constant* $G_F = 1.16632 \times 10^{-5}\,\mathrm{GeV}^{-2}$. The neutral current cross section is given by

$$\frac{d^2\sigma}{dxdy} = \frac{G_f^2 M E_{\nu_\ell}}{2\pi}\left(\frac{M_Z^2}{Q^2+M_Z^2}\right)^2\left[xq^0 + x\bar{q}^0(1-y)^2\right]. \tag{2.35}$$

Here the quark distributions have the chiral couplings

$$\begin{aligned} L_u &= 1 - \frac{4}{3}x_W & L_d &= -1 + \frac{2}{3}x_W \\ R_u &= -\frac{4}{3}x_W & R_d &= \frac{2}{3}x_W \end{aligned}$$

as additional parameters:

$$\begin{aligned} q^0 &= \left(\frac{u_v+d_v}{2} + \frac{u_s+d_s}{2}\right)(L_u^2+L_d^2) + \left(\frac{u_s+d_s}{2}\right)(R_u^2+R_d^2) \\ &\quad + (s_s+b_s)(L_d^2+R_d^2) + (c_s+t_s)(L_u^2+R_u^2) \\ \bar{q}^0 &= \left(\frac{u_v+d_v}{2} + \frac{u_s+d_s}{2}\right)(R_u^2+R_d^2) + \left(\frac{u_s+d_s}{2}\right)(L_u^2+L_d^2) \\ &\quad + (s_s+b_s)(L_d^2+R_d^2) + (c_s+t_s)(L_u^2+R_u^2). \end{aligned} \tag{2.36}$$

$x_W = \sin^2\theta_W = 0.21349(13)$ is the *weak mixing parameter*. For $\bar{\nu}_e, e$ interactions inside the Earth the special case of W^--production at the resonance energy of

$$E_\nu^{res} = \frac{M_W^2}{2m} \approx 6.3 \times 10^{15}\,\mathrm{eV} \tag{2.37}$$

becomes important [GQRS96]:

$$\bar{\nu}_e + e \xrightarrow[W^-]{} \begin{cases} \ell + \nu_\ell & 3 \times (\approx 10.80 \pm 0.09)\% \\ \text{hadrons} & (67.60 \pm 0.27)\% \end{cases}. \tag{2.38}$$

(Decay modes from [PDG08].) In Fig. 2.14, integrated neutrino interaction cross sections for given reactions are plotted. The opacity limit for neutrinos traversing the Earth is derived from the mean free path for neutrino-nucleon interactions

$$\lambda_{\nu,N} = \frac{1}{\sigma_{\nu,N}\cdot N_A}(\text{cm-we}). \tag{2.39a}$$

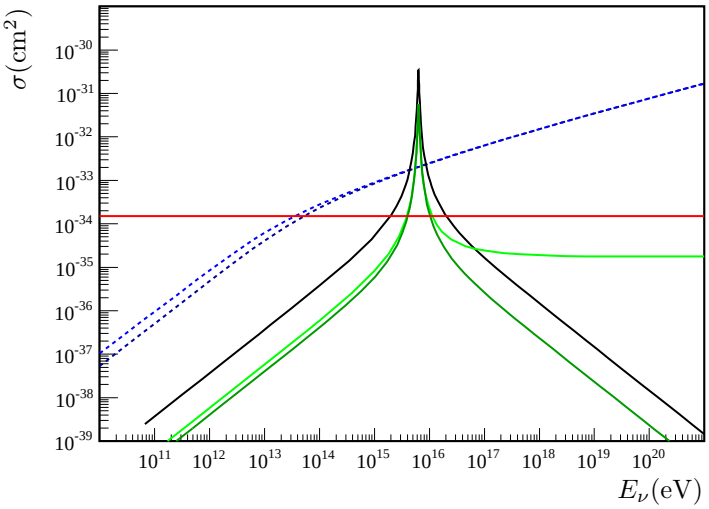

Fig. 2.14: Cross Sections for Different Neutrino Reactions. Non-resonant (dotted line) from top: $\nu_\ell + N$, $\bar{\nu}_\ell + N$; resonant from top: $\bar{\nu}_e + \mathrm{e} \longrightarrow$ hadrons, $\bar{\nu}_e + \mathrm{e} \longrightarrow \bar{\nu}_\mu + \mu$ $\bar{\nu}_e + \mathrm{e} \longrightarrow \bar{\nu}_e + \mathrm{e}$. Horizontal bar: Opacity limit. Under the assumption of this cross section, the Earth diameter equals to the mean free path for the traversing particle. Image: Non-resonant [GQRS98], resonant [GQRS96]

$N_A = 6.022 \times 10^{23}\,\mathrm{mol}^{-1} = 6.022 \times 10^{23}\,\mathrm{cm}^{-3}$ (water-equivalent) is Avogadro's number. For neutrino-electron interactions, Eq. 2.39a has to be modified:

$$\lambda_{\nu,e} = \frac{1}{\sigma_{\nu,e} \cdot (10/18) \cdot N_A} (\text{cm-we}). \tag{2.39b}$$

$(10/18)N_A$ is the number of electrons in one cm^3 of water. Under the assumption of an isotropic density distribution, the *Earth density structure* (Fig. 2.15) can be parameterized like [Dzi98]

$$\rho(r) = \begin{cases} 13.0885 & & -8.8381\,x^2 & & , & 0 & \le r < & 1221.5 \\ 12.5815 & -1.2638\,x & -3.6426\,x^2 & -5.5281\,x^3 & , & 1221.5 & < r < & 3480 \\ 7.9565 & -6.4761\,x & +5.5283\,x^2 & -3.0807\,x^3 & , & 3480 & < r < & 5701 \\ 5.3197 & -1.4836\,x & & & , & 5701 & < r < & 5771 \\ 11.2494 & -8.0298\,x & & & , & 5771 & < r < & 5971 \\ 7.1089 & -3.8045\,x & & & , & 5971 & < r < & 6151 \\ 2.691 & +0.6924\,x & & & , & 6151 & < r < & 6346.6 \\ 2.9 & & & & , & 6346.6 & < r < & 6356 \\ 2.6 & & & & , & 6356 & < r < & 6368 \\ 1.02 & & & & , & 6368 & < r \le & R_{\mathrm{Earth}} \end{cases} \tag{2.40}$$

with $x = r/R_{\mathrm{Earth}}$ and $R_{\mathrm{Earth}} = 6371\,\mathrm{km}$ the radius of the Earth. $[\rho] = \mathrm{g/cm}^3$. A neutrino traveling through the Earth (Fig. 2.16(b)) sees an angular dependent matter thickness. The integration over the density function (Fig. 2.16(a)) along a straight line through the Earth center ($\cos(\theta) = -1$) delivers a thickness of $10.95\,\mathrm{kt/cm}^{2*}$ or $1.1 \times 10\,\text{cm-we}^\dagger$. This value together with Eq. 2.39a delivers the limit. Like illustrated in Fig. 2.14, from an energy of $4 \times 10^{13}\,\mathrm{eV}$ upwards the mean free path for neutrinos inside the Earth becomes smaller than the Earth diameter.

*kt = kilo tonne

†cm-we = cm water-equivalent: $\frac{10.95\,\mathrm{kt/cm}^2}{\rho(H_2O) \approx 1\,\mathrm{g/cm}^3} \approx 11 \times 10^9$ cm-we

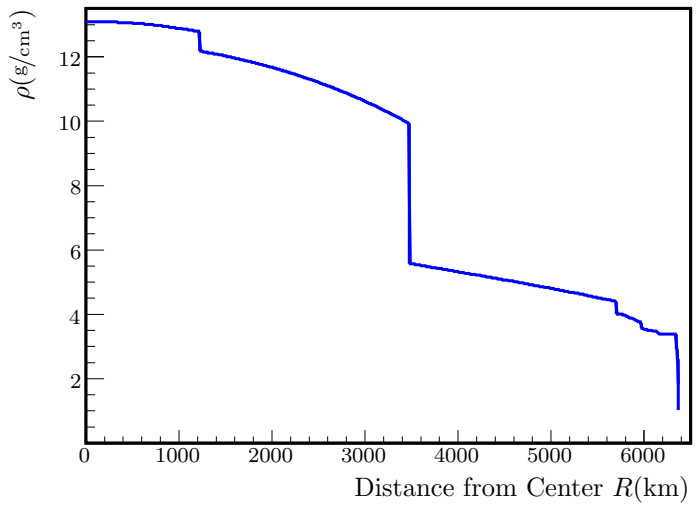

Fig. 2.15: Earth Density Profile.

The small neutrino cross section is used in detectors, to suppress the underground produced by other cosmic rays. The complete Earth is used as a shielding against all other particles. Only neutrinos (with sufficiently low energies) can traverse the Earth and interact in, or near by the detector volume. Inside the detector only events from particles, which had to traverse the Earth are accepted. These events are called *up-going events*.

2.3.2 Neutrino Detection Mechanisms

Neutrino interactions can be observed by their energy deposition in matter (e.g. transfer of kinetic energy into heat) or by interactions of secondary charged particles. Currently, for large ice or water detectors the latter option is common. They detect the light emitted due to continuous energy loss of high energy charged particles inside the detector medium, to back-reference to the properties of the primary neutrino. The further discussion of this section is presuming this kind of detectors.

The reaction 2.32a transfers a neutrino into the charged lepton of its family (↗Sec. 2.1). Besides a hadronic cascade from the primary neutrino-nucleon interaction, individual light signatures for the three possible charged leptons are created inside the detector medium.

Three major mechanisms for light production in matter are excitation and ionization of atoms and emission of fluorescence light due to relaxation, bremsstrahlung and Čerenkov radiation. For high energy particles with $E > 1\,\mathrm{GeV}$, the latter two effects are more important than the ionization.

Bremsstrahlung is a second order process of scattering. All accelerated charged particles emit photons, for example during scattering processes in matter. The energy loss per distance for an electron with energy E is given by

$$\frac{dE}{dx} = -\frac{E}{X_0}. \tag{2.41}$$

X_0 is the radiation length [PDG08]

$$\frac{1}{X_0} = 4\alpha \left(\frac{e^2}{4\pi\epsilon_0 m_e c^2}\right)^2 \frac{\rho N_A}{A} \left\{Z^2 \left[L_{rad} - f(Z)\right] + Z L'_{rad}\right\}, \tag{2.42}$$

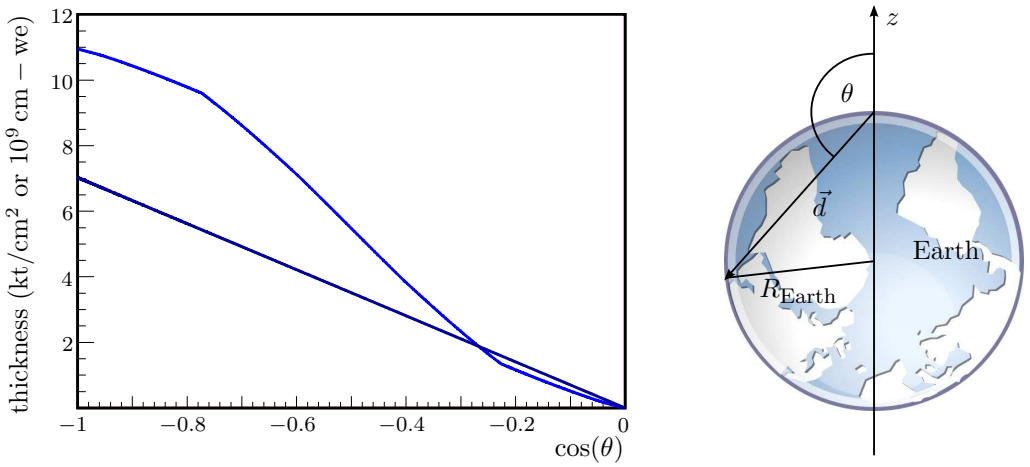

(a) Earth Thickness (b) Definition of Coordinates

Fig. 2.16: Angular Dependence of Earth Thickness. θ is the polar coordinate of the particle flight direction $\vec{d}$. Upper curve: thickness corresponding to Eq. 2.40, lower curve: thickness calculated with a fixed Earth density of $5.515\,\mathrm{g/cm^3}$.

with Avogadro's number N_A, the *fine structure constant* $\alpha = \frac{e^2}{2c_0e_0h} \approx \frac{1}{137}$, and the density ρ, the atomic mass A and the atomic number Z of the traversed matter. The infinite sum $f(Z)$ can be approximated by

$$f(Z) \approx (\alpha Z)^2 \left(\frac{1}{1+(\alpha Z)^2} + 0.20206 - 0.0369(\alpha Z)^2 + 0.0083(\alpha Z)^4 - 0.002(\alpha Z)^6 \right). \quad (2.43)$$

The values for L_{rad} and L'_{rad} are given in Tab. 2.1. Within a distance of X_0 the energy of the

Element	Z	L_{rad}	L'_{rad}
H	1	5.31	6.144
He	2	4.79	5.621
Li	3	4.74	5.805
Be	4	4.71	5.924
Others	> 4	$\ln\left(\frac{184.15}{Z^{1/3}}\right)$	$\ln\left(\frac{1194}{Z^{2/3}}\right)$

Tab. 2.1: L_{rad} and L'_{rad} values for calculation of the radiation length.

electron is reduced to E/e. The radiation length for electrons in water according to Eq. 2.42 is 36 cm. Due to the squared particle mass in the denominator, bremsstrahlung is suppressed by a factor of 43000 for muons. If the emitted photons have an energy of more than $2 \cdot 511\,\mathrm{keV}$, the mass of the electron, e^--e^+-pair production is possible. The created electrons and positrons produce bremsstrahlung on their part. Together, these processes form an *electromagnetic cascade*, which dies out at the *critical energy*

$$E_c \approx \frac{605\,\mathrm{MeV}}{Z + 1.24}. \quad (2.44)$$

For electron energies below E_c, ionization becomes more important than bremsstrahlung.

The shape of the electromagnetic cascade is concentrated along the axis of the primary particle, but also spread out, as multiple Coulomb scattering deflects the charged cascade component. The

radius of the cylinder inside which, on average, 90 % of the primary energy is stored is called the *Molière radius*. It is given by

$$R_M = \frac{X_0 E_s}{E_c}, \tag{2.45}$$

with $E_s = \sqrt{4\pi/\alpha} m_e c^2 \approx 21.2052\,\text{MeV}$ [NJMC66; PDG08].

The light emission of an electronic cascade is - in first order - isotropic and localized. Within an ice or water neutrino detector the electron, which is the secondary particle of a electron neutrino reaction, will produce this kind of signal. It is very likely that the full electron neutrino energy is deposited inside the detection volume.

Vavilov-Čerenkov radiation , often called only Čerenkov radiation, is only emitted, if a charged particle travels through a transparent medium with a speed which is higher than the speed of light inside this medium. The particle polarizes the atoms of the medium which, afterwards, emit electromagnetic waves during relaxation. The interference of those waves is destructive as long as the particle is slow ($\beta < 1/n$). If it exceeds the speed of light the waves from every point on the particle trajectory can interfere constructively on a cone around the trajectory (↗Fig. 2.17). *Pavel Alekseyevich Čerenkov* first documented the effect in 1934, while

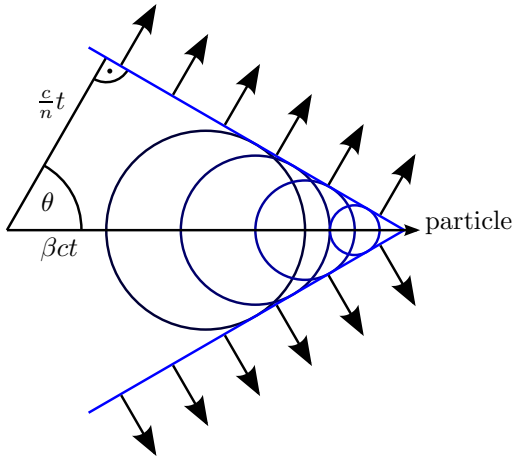

Fig. 2.17: Čerenkov radiation. Illustration of the light emission angle. $\beta = v/c$ is the speed of the particle and n is the refraction index of the traversed medium.

he was working under *Sergey Ivanovich Vavilov*. Three years later, in 1937, *Igor Jewgenjewitsch Tamm* and *Ilja Michailowitsch Frank* delivered the theoretical background for the explanation of the Čerenkov radiation [FT37]. The light emission takes place under an angle of

$$\theta = \arccos \frac{1}{\beta n} \tag{2.46}$$

relative to the trajectory. The energy loss due to the Čerenkov effect can be calculated by the *Frank-Tamm formula*

$$\frac{dE}{dx} = \frac{q^2}{4\pi} \int_{n(\omega)>1/\beta} \omega \mu(\omega) \left(1 - \frac{1}{\beta^2 n(\omega)^2}\right) \mathrm{d}\omega. \tag{2.47}$$

μ and n are the frequency dependent permeability and *refraction index* of the medium. q is the electric charge of the particle. The integration can be done over all wavelengths, for which the threshold condition $n(\omega) > 1/\beta$ is fulfilled. An additional constraint on the integration

boundaries is the demand of polarizability of the medium at the given frequencies. In general, these are the photon frequencies, for which the medium is transparent [Hel09].

For practical applications in particle detectors the Frank-Tamm formula can be modified – under the approximation of frequency-independent refraction index and permeability – with help of the relations

$$\frac{d\omega}{d\lambda} = -\frac{2\pi c}{n\lambda^2} \tag{2.48}$$

and

$$\frac{dE}{dN} = \frac{ch}{\lambda} \tag{2.49}$$

to deliver the number of photons per distance and wavelength:

$$\frac{d^2N}{dxd\lambda} = \frac{\pi\mu cq^2}{hn^2\lambda^2}\left(1 - \frac{1}{\beta^2 n^2}\right). \tag{2.50}$$

Eq. 2.47 shows an increase of the energy loss towards higher frequencies. As ice or water is not transparent for ultraviolet light, only wavelengths between about 300 nm and (because of the reduced emission) 600 nm deliver a significant contribution to a detectable light signal in a detector. The refraction index of ice within this interval can be parameterized by [PW01]

$$n(\lambda) = 1.55749 - 1.57988\lambda + 3.99993\lambda^2 - 4.68271\lambda^3 + 2.09354\lambda^4, \qquad [\lambda] = \mu\text{m}. \tag{2.51}$$

Inside the AMANDA collaboration a fixed refraction index of $n = 1.32$ is used. The energy deposition into photons due to the Čerenkov effect for particles with $\beta \approx 1$ in the given wavelength interval is 765 eV/cm. This is independent of the mass of the charged particle and, therefore, equal for electrons, muons and tau leptons.

Čerenkov radiation is a good option to detect especially the two heavy leptons, the muon and the tauon. Because of their minor light production due to bremsstrahlung, the Čerenkov light offers an alternative light producing process. For the relatively long living muon ($\tau = 2.197 \times 10^{-6}$ s), it is possible to reconstruct the source direction. The Čerenkov radiation is emitted highly anisotropic and homogeneously along the muon trajectory. With the measurement of the arriving time of photons at different positions in the detector, the time and the position of the light emission can be calculated. The angular deviation δ_μ of the secondary muon from the primary muon-neutrino path is [LM00]

$$\delta_\mu = 0.7^\circ \cdot \left(\frac{\text{TeV}}{E_\nu}\right)^{0.7}. \tag{2.52}$$

This good correlation can be used to create a sky map with neutrino events [A+07b].

Tauon signatures are expected to be multi structural. At the tau-neutrino nucleon interaction point, a primary hadronic cascade produces light. The outgoing tau lepton looses energy via Čerenkov light production. The range of the tauon is

$$c\tau\frac{E_\tau}{m_\tau c^2} = c \cdot 291 \times 10^{-15}\,\text{s} \cdot \frac{E_\tau}{1776.84MeV} \approx 5\,\frac{\text{cm}}{\text{TeV}} \cdot E_\tau. \tag{2.53}$$

Consequently, tauons with an energy of about 4 PeV decay after about 200 m. Its decay generates an additional cascade. In the case of a tau lepton crossing the detector, lollipop-shaped light signatures are predicted, where one or both cascades, as well as the Čerenkov light from the path of the tauon are seen in the detector. These events are called *double bang events*.

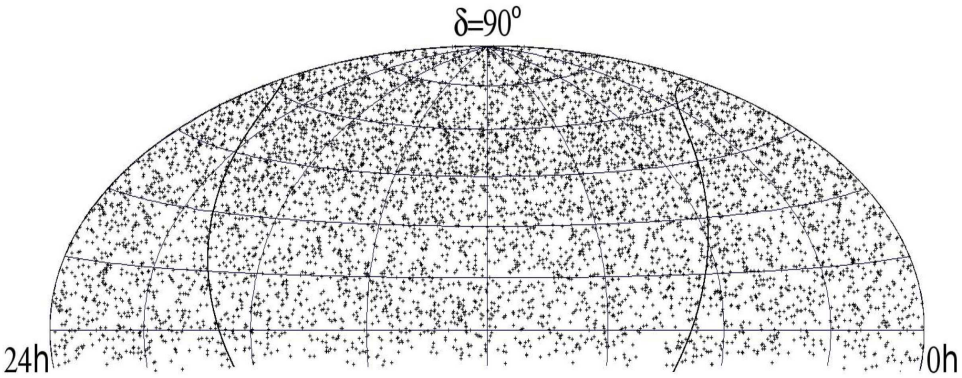

Fig. 2.18: AMANDA Sky Map with data from 2000 to 2006. Image: [A+09b]

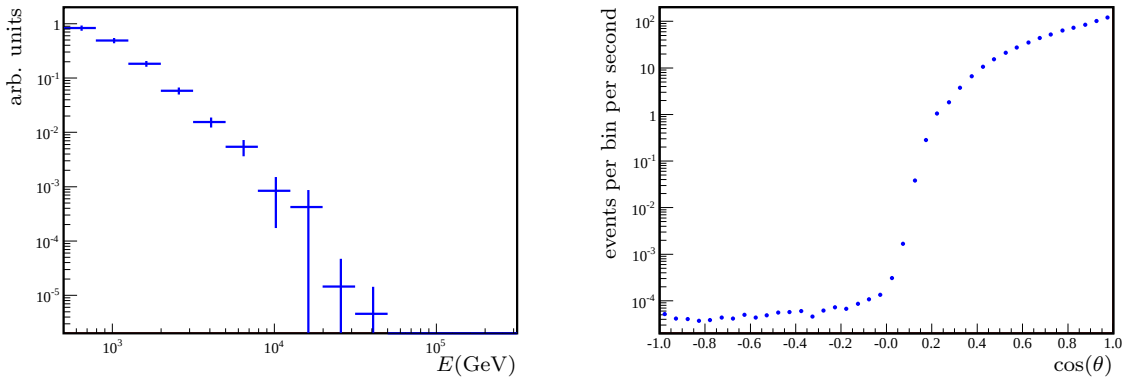

(a) Spectrum

(b) Zenith Angle Dependence

Fig. 2.19: Atmosperic Muon Background. (a) Spectrum of atmospheric muons at the ice surface, measured with AMANDA. Image: [Gee03] (b) Zenith angle dependence of the muon flux in the IceCube detector measured with the 22 string configuration of 2007. Image: [Ber09]

2.3.3 Background for Neutrino Detection

Neutrino detection significantly suffers from background. In case of ice Čerenkov detectors, this background consists of muons produced by interactions of cosmic rays with the atmosphere. These *atmospheric muons* have a high relativistic gamma-factor and can not only penetrate the atmosphere, but also several hundreds of meters of solid matter. The ratio between background atmospheric muons and neutrino induced muons near the detector is about 10^6 [A+02].

Part I

The Hardware Integration of AMANDA into IceCube

3

AMANDA and IceCube

Neutrinos are non charged particles and only weakly interacting. Consequently, their detection is not trivial (↗Sec. 2.3). They cannot be measured directly, but only by their interaction products or – on smaller scales – by missing energy in particle reaction processes. If, additionally, the interest lies in neutrinos with high energies from cosmic rays, particle detectors will have to be very large so that the standard detection methods, which are known from other particle physics experiments, are not applicable.

The two neutrino telescopes AMANDA and IceCube, which are using the ice sheet on the Antarctic continent as detector material, will be introduced in this chapter. As the integration of AMANDA into IceCube is dependent on the accurate timing inside the two detectors, a closer look onto the hardware of the two systems is necessary. Therefore, especially the measurement of time constants and the event timing are described in detail. The illustration of integration itself will follow in chapter 4.

3.1 Detector Principles

There are only few places on Earth where the ice layer is thick enough to offer a sufficient shielding against atmospheric muons, which arrive on the Earth surface, so that neutrino detection is possible at all. Further on, the ice properties have to satisfy additional demands. It has to be free from crevasses, it has to be optically clear enough and, consequently, scattering and absorption length have to be large enough so that light emission from traversing particles is visible over tens to hundreds of meters. The place, where these demands are fulfilled as best as possible, is the ice at the South Pole. Fig. 3.1 shows best fit results for the scattering and absorption lengths λ_e and λ_a of the South Pole ice inside of the AMANDA detector.

Other good reasons to chose the South Pole as a location for an ice Čerenkov neutrino detector are the low ice flow speed of only about 8 m/year and the good infrastructure providing air supply and a well equipped research station.

To detect the Čerenkov light of traversing charged particles, the ice is instrumented with glass spheres (Fig. 3.2), containing *photomultiplier tubes* (*PMTs*). The PMTs use the energy from incoming single photons to produce free electrons. The number of electrons is multiplied in a cascade of charged dynodes to deliver a measurable signal [Ham]. Depending on the internal

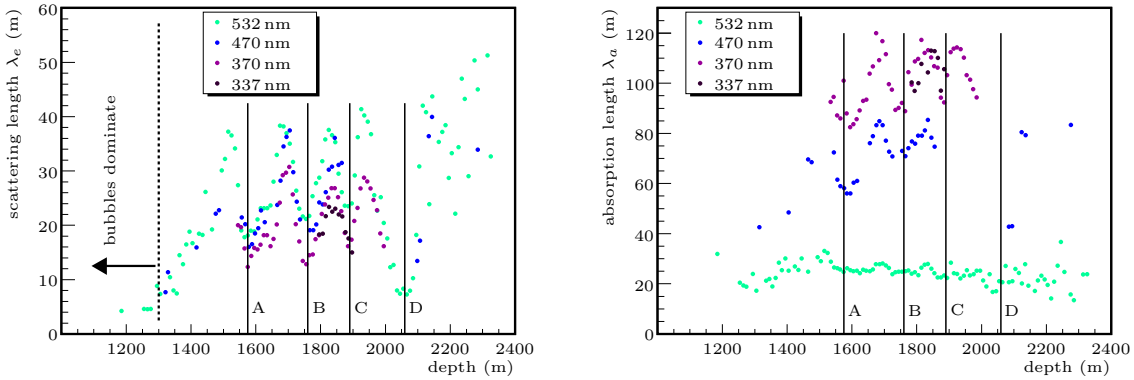

(a) Scattering Length

(b) Absorption Length

Fig. 3.1: Effective Scattering and Absorption Coefficient for ice at the South Pole measured with light sources of the AMANDA detector. The four dips correspond to dust layers of different ages: 38,000 yr (A); 46,500 yr (B); 53,500 yr (C) and 65,000 yr (D) [PWC00; A+95a]. Images: [A+06a]

electronics these spheres are called *optical modules* (*OMs*) or *digital optical modules* (*DOMs*). A hardware connection delivers power to the PMT and the electronics, and transports the signal information to the ice surface. In a "counting house" a *data acquisition system* (*DAQ*) processes the incoming data.

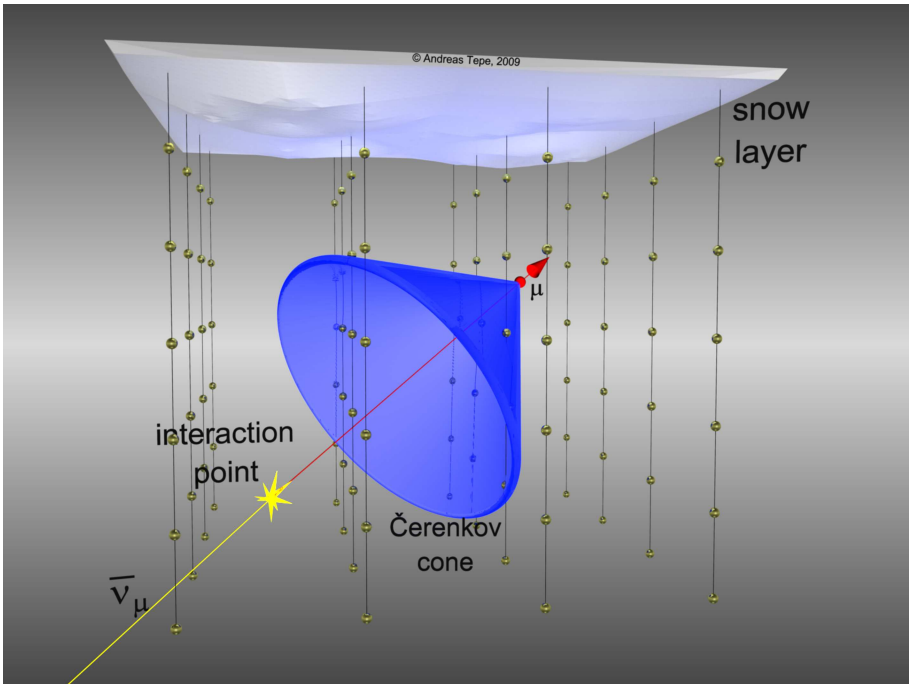

Fig. 3.2: Schematic View of the Detection Principle for an ice Čerenkov detector. Near or inside the instrumented volume a neutrino is interacting with matter. In case of a muon neutrino, the resulting muon traverses the detector and produces Čerenkov light. At a fixed time, this light has traveled a certain distance. The blue cone represents the coherent wave front of the emitted photons at a fixed time.

The drilling of the holes into the ice is done with hot water. A drill head pumps hot water into the ice, the melted water is heated and recycled for drilling. Because ice is a good thermal insulator, the water in a hole stays liquid for many hours. The cable for the surface connection of the glass spheres is lowered into the hole and the spheres are sequentially connected mechanically and electrically to the cable. The deployed combination of cable and glass spheres is called a *string*.

The way of signal handling is different in AMANDA and IceCube. This will be specified in the next sections.

3.2 The AMANDA Neutrino Telescope

The AMANDA telescope – the Antarctic Muon And Neutrino Detector Array – is the first large scale ice Čerenkov neutrino detectors (Fig. 3.3). Because of the innovative concept, many different techniques for signal handling and processing have been tested during installation and operation of the detector.

3.2.1 In Ice

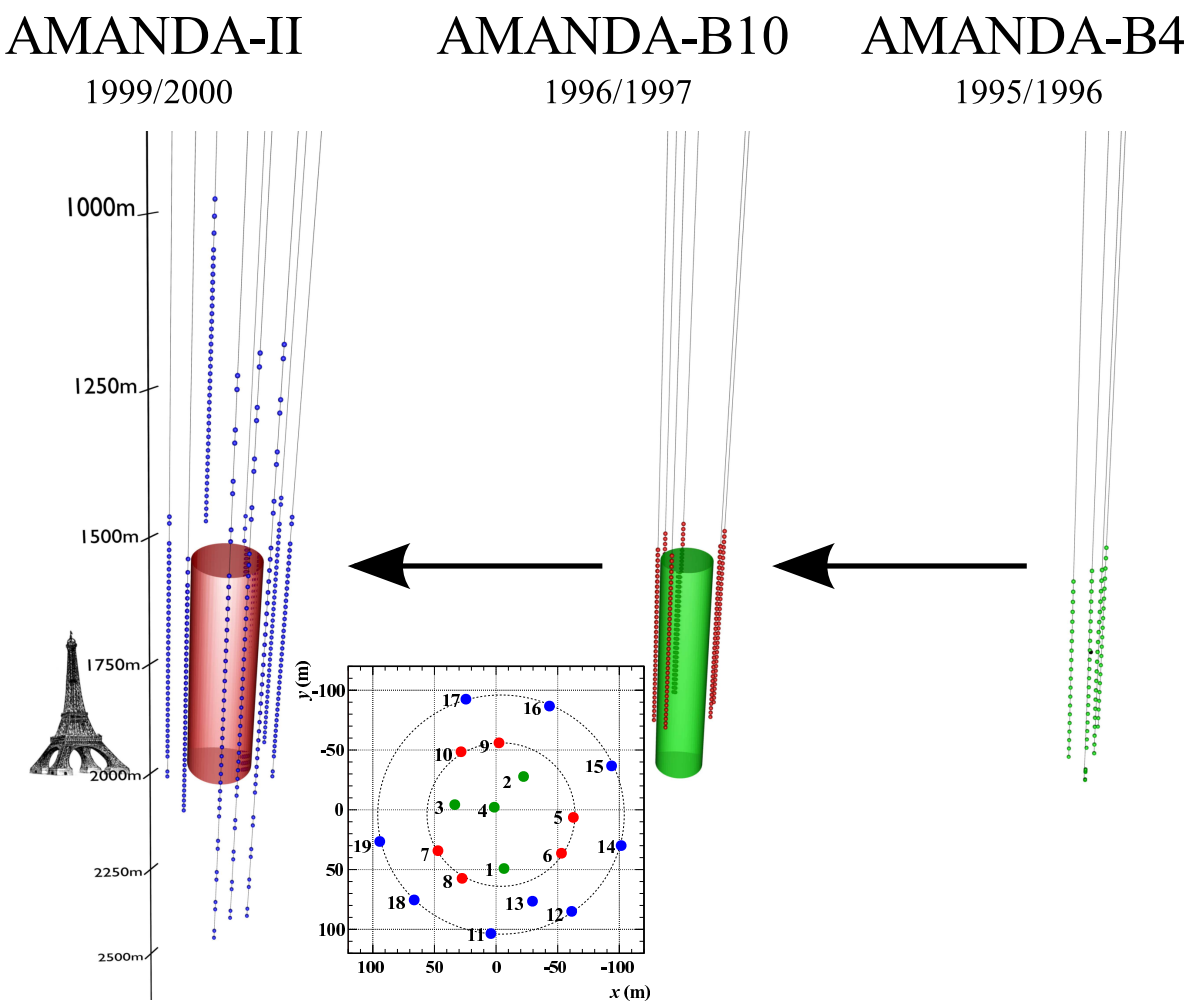

Fig. 3.3: The AMANDA Neutrino Telescope. Depth 0 m is corresponding to the surface. The Eiffel Tower is drawn for comparison.

Physically, the project started in the austral summer season 1993/94, when the four strings of the AMANDA-A detector (not contained in Fig. 3.3) were deployed in a depth between about 800 and 1000 m [A+00]. It turned out that the concentration of bubbles in this depth is high and the light scattering does not allow for accurate track reconstruction [A+95b].

AMANDA-B4 was installed in season 1995/1996. 80 OMs on four strings were frozen into the ice from a depth of 1545 m to 1978 m. The high voltage for the PMTs of string 1 to 4 is produced at the surface and delivered to the OMs via coaxial cables. These cables are also used to transmit the PMT signals to the AMANDA counting house, the *Martin A. Pomerantz observatory* (*MAPO*). Six additional OMs at the bottom of string 4 can also transmit signals over twisted pair cables. For calibration, several subsystems are deployed with the strings:

- 8 LEDs distributed over the full depth and all strings,
- a nitrogen laser on string one at a depth of 850 m,
- three DC halogen lamps with ultra violet light (UV) filters and
- optical fibers with diffuser balls, located near each OM, which are used to lead the light of a neodymium YAG* laser system at the surface into the ice.

In season 1996/97 AMANDA-B4 was upgraded with 216 OMs on 6 strings to AMANDA-B10. The instrumented volume corresponded to a volume of a cylinder with a height of 500 m and a diameter of 120 m. The data transmission is done via twisted pair cables. 1997/98 the first three strings with optical signal transmission technology were installed. 122 OMs have been deployed. AMANDA-II, the final state of the AMANDA detector, was finished in season 1999/2000 with 19 strings and 670 OMs. With the last six strings, two new technologies have been tested. 23 *digitally controlled Analog Optical Modules* (*dAOMs*) and 41 *Digital Optical Modules* (*DOMs*) have been frozen into the ice. The dAOMs are distributed over the strings 17, 18 and 19, whereas the DOMs are only connected to string 18 [KMC+97; Sch02; A+06b].

The different transmission technologies have several advantages and disadvantages. For (analog) signal transmission, the optical fibers turned out, to deliver the best results. The dispersion is very small and signal cross talk, like between electrical cables is only possible in the electronics before or after the optical transmission path. This is the reason, why the dAOM technology is using fibers for analog signal transmission. The high voltage for the PMT is produced locally inside the dAOM and the dAOM functionality is controlled digitally, which is an advantage against the original AMANDA analog OMs. The DOMs have only an electrical connection. Here the PMT pulses are digitized by electronics in the DOM. The digital information is transferred to the surface. This allows for the usage of an electrical connection without the problem of cross talk. Because of the analoge AMANDA data reception, the AMANDA DOMs have an additional analoge tranfer mode to be compatible to the MuonDAQ respectively the TWRDAQ. The digital mode has only been used to verify the transmission technique for IceCube. The very complex electronics of the DOM can be a disadvantage in the ice, but avoiding additional fibers makes the transport and deployment of the DOMs cheaper, than for the dAOMs. This is one of the reasons, why the DOM became the IceCube standard technology.

3.2.2 On Ice

The following descriptions are valid for the AMANDA detector system before the installation of the integration updates! Part of the integration efforts described in chapter 4 is the improvement of several of the described systems.

*neodymium-doped yttrium aluminum garnet (Nd:$Y_3Al_5O_{12}$)

All AMANDA strings come together in the MAPO. Here the high voltage supplies for the analog OMs, as well as the signal handling hardware are deployed. The analog electrical signals are amplified by special fast amplifiers, called *SWAMPs* (SWedish AMPlifiers) and split up. The optical signals are converted to electrical ones by Optical Receiver Boards (*ORBs*) and also split up. The split signals are put into three different systems (Fig. 3.4):

- the Discriminator and Multiplicity ADDer (*DMADD*), which is the trigger building system of the AMANDA detector,
- the *MuonDAQ* system and
- the *TWRDAQ* system.

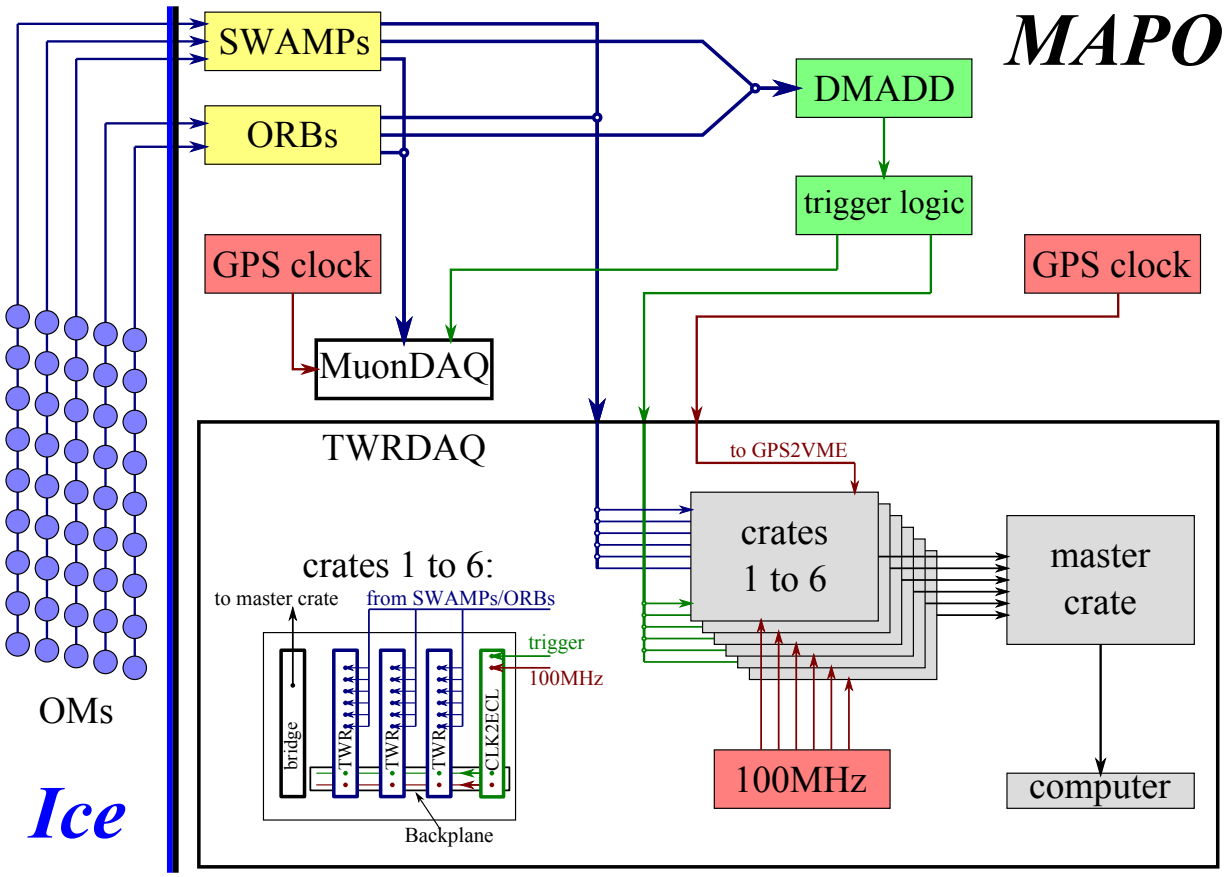

Fig. 3.4: Scheme of the AMANDA DAQ System (before 2006).

The DMADD

discriminates the incoming analog PMT signals [Mar01]. If a signal is low enough*, it passes the internal discriminator threshold. The discriminated pulses take part on the trigger signal building procedure (Fig. 3.5). The DMADD uses the same procedure for different settings of OM combinations and multiplicities. The common setting is the output of three simple† *multiplicity triggers* (M13, M18 and M24) and one *string trigger*, which gives back a trigger signal if a certain

*PMT signals are negative pulses.
†simple means, to add up simply all OM signals.

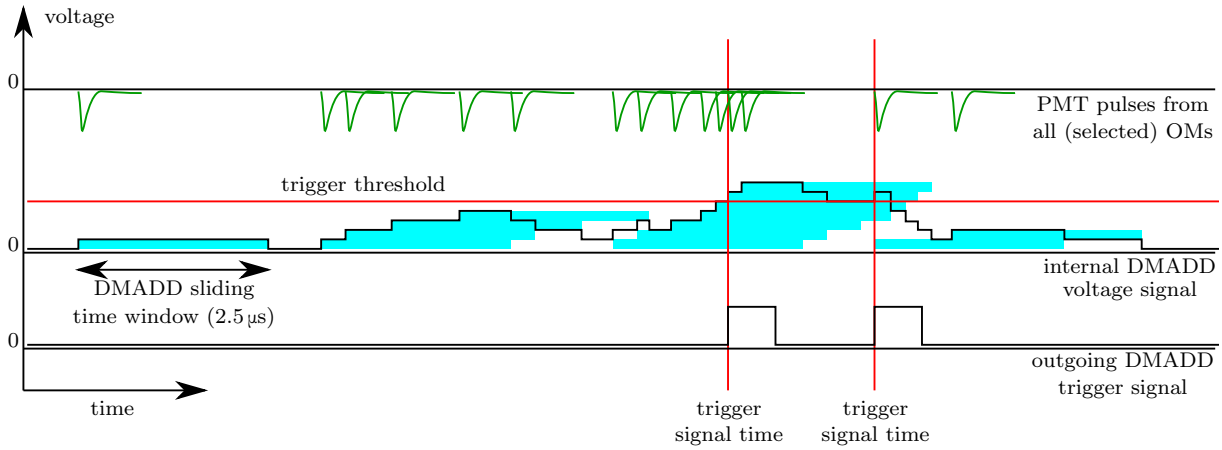

Fig. 3.5: DMADD trigger signal building. Incoming PMT pulses from all (or a set of selected) OMs lead to the generation of a voltage signal with a duration of 2.5 µs (turquoise bars). Additional incoming pulses increase the voltage signal (black line over the turquoise bars). If a selected pulse multiplicity is reached (red horizontal line), the DMADD sends out a trigger signal (lower black line). In this example picture the multiplicity is set to M6.

number of OMs in a row along one string is hit. The trigger rate is a direct consequence of the chosen multiplicity. The lower the multiplicity is, the higher is the trigger rate, because also smaller events with less hits cause a trigger signal.

The MuonDAQ

is the original AMANDA DAQ system. If a trigger signal from the DMADD is received, peak ADCs and fast TDCs read the peak times and heights. The event information is transferred to a computer, which stores it. The MuonDAQ system has a dead time of about 2.2 ms. This is the reason, why the MuonDAQ is triggered by the very high multiplicity trigger of M24. Because the MuonDAQ is not part of this thesis, it will not be explained in detail. For further information see [A+00].

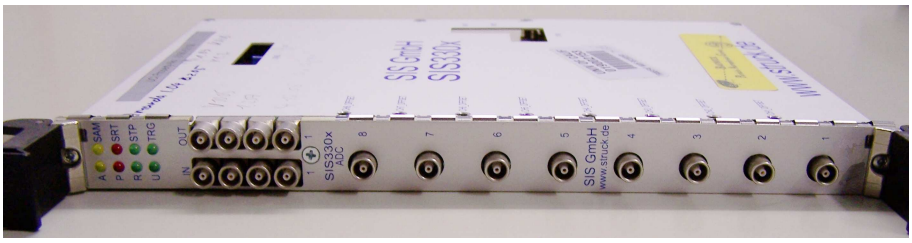

Fig. 3.6: TWR VME Module.

The TWRDAQ

is an AMANDA hardware upgrade, which was installed in the years 2002 to 2004 with several upgrades in the following years [Wag04; Mes06]. Some of the resons for the upgrade are

- the deadtime the MuonDAQ,
- complicated pulse shapes in high energy events, which cannot be resolved with the ADC/TDC combination,

- the low dynamic range ($\lesssim 8$ pulses) of the TDCs [Wag03] and
- a dependency between pulse hight and pulse time.

The new hardware offers the sampling of the full PMT waveforms and not only the peak values: A system with *flash ADCs* (Struck Innovative Systems SIS3300 FADC [Str07]) – called *Transient Waveform Recorders* (*TWRs*) within the AMANDA collaboration – reads out the OM signals, coming out of the SWAMPs and ORBs. Every TWR supports eight input channels (Fig. 3.6). The TWRs continuously read the input voltages and store them into a *ring buffer* structure (Fig. 3.7).

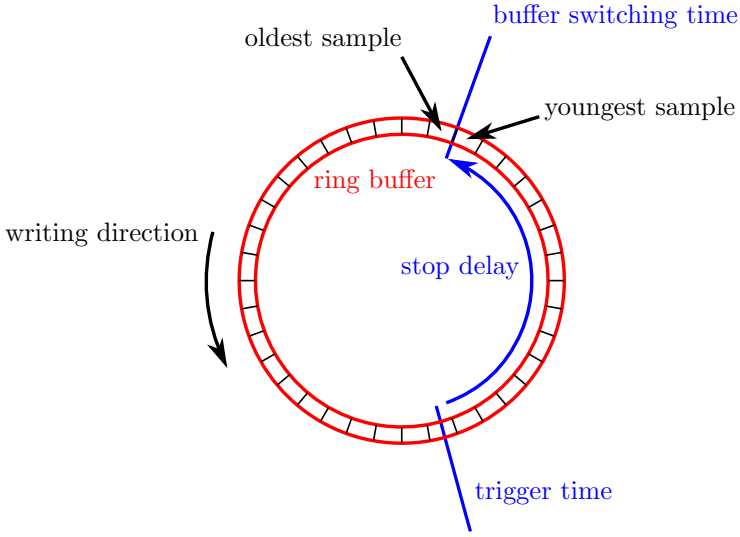

Fig. 3.7: Functional Principle of the TWR Ring Buffers. The buffer samples continuously. With an incoming trigger signal, the stop delay counter is started. After reaching the stop delay time, the complete ring buffer is stored and sampling in another ring buffer is started. The setting of the stop delay allows for time adjustable sampling of signal information before and after the trigger time.

The ring buffers are realized as fixed memory areas on the TWR internal memory banks. With every trigger signal arriving the TWR, the next eight ring buffers (one for every channel) in the memory are used. Always two memory banks are implemented on every TWR. They are configured in an auto switching mode: If one bank is filled up after 128 incoming trigger signals, the bank will be switched (Fig. 3.8). The filled bank is read out while the empty one is filled up again. In this configuration the DAQ system works nearly deadtime free. The TWRs are driven by a 100 MHz clock setting the time bin size to 10 ns. The ADC voltage resolution is 12 bits. One sample value is stored in a 16-bit word. Every ring buffer holds 1024 samples corresponding to 10.24 µs. This can be summed up to

$$8\,\frac{\text{channels}}{\text{triggered event}} \cdot 1\,\frac{\text{ringbuffer}}{\text{channel}} \cdot 1024\,\frac{\text{samples}}{\text{ring buffer}} \cdot 16\,\frac{\text{bits}}{\text{sample}} \cdot 128\,\frac{\text{triggered events}}{\text{memory bank}} \cdot 2\,\frac{\text{memory banks}}{\text{TWR}} = 4\,\frac{\text{MB}}{\text{TWR}}. \tag{3.1}$$

The TWRDAQ has a trigger rate limit of about 250 Hz. With the help of Eq. 3.1 and the assumptions of 13 TWRs per crate and a trigger rate of 250 Hz, the amount of data coming from the TWRs over the backplane can be calculated the following way:

$$2\,\frac{\text{MB}}{\text{TWRmemorybank}} \cdot 13\,\frac{\text{TWRmemorybanks}}{\text{readout}} \cdot \frac{1}{128}\,\frac{\text{readouts}}{\text{event}} \cdot 250\,\frac{\text{events}}{\text{s}} = 50.78\,\frac{\text{MB}}{\text{s}}. \tag{3.2}$$

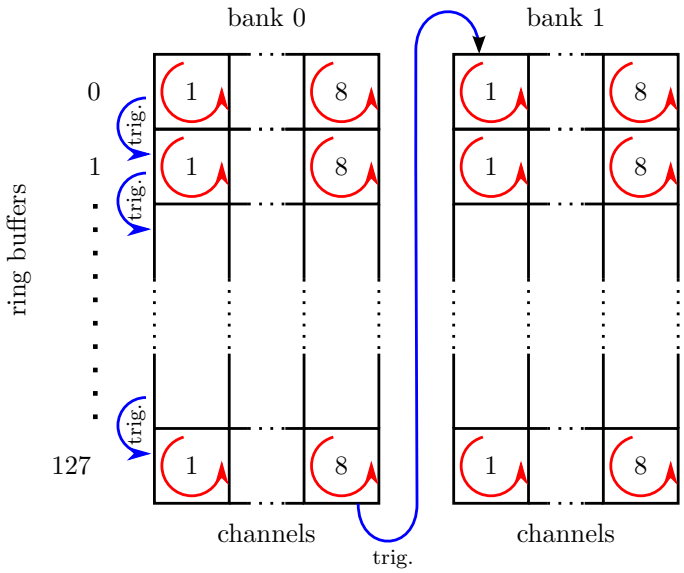

Fig. 3.8: TWR Memory Configuration. Each TWR handles 8 channels. In one of the two memory banks of the TWR, 128 ring buffer contents for each channel can be stored. with the 128th trigger coming, the bank is switched and the filled bank can be read out. If the second bank is filled, the banks are switched back.

The TWR readout and control is done via VME bus architecture. 597 OM channels are read out by 75 TWRs in six TWR crates (Fig. 3.9). A *DSP* (Analog Devices ADSP-21060/62 SHARC DSP) in every crate reads out the waveform information in the TWRs. Additionally, it does a feature extraction: Only significant waveform information in the ring buffer contents is kept, the base line value is stored, but the base line samples are thrown away (Fig. 3.10) [Wag04]. This saves enough bendwidth and disk space to read out and to store all (relevant) TWR data. The DSP is controlled by a software, written in an assembler language, which supports the special abilities of the DSP architecture. Every time the TWR readout software on the DAQ computer is started, the precompiled DSP software is loaded into the DSP memory. After starting the readout, the DSP works autarkically.

The TWR readout software initializes the DSPs and TWRs over a PCI to VME connection (Struck Innovative Systems SIS1100 [Str01]) to the master crate and VME to VME connections (Struck Innovative Systems SIS3100 [Str06]) (Fig. 3.11) to the six TWR crates. It also reads out the DSP memories. The DSPs are hardware upgrades of the VME to VME bridge modules in the TWR crates and do not need an additional VME slot.

The hardware trigger signals coming from the DMADD are distributed to the MuonDAQ and the TWRDAQ. An assembly of NIM electronic modules handles the trigger signal flow to both systems. The following *hardware trigger* signals reach the TWRDAQ:

- M24,
- M18,
- M13,
- string trigger (N hit OMs within a row of M adjacent OMs on one string),
- *SPASE trigger* from the SPASE-2 experiment [D+00],

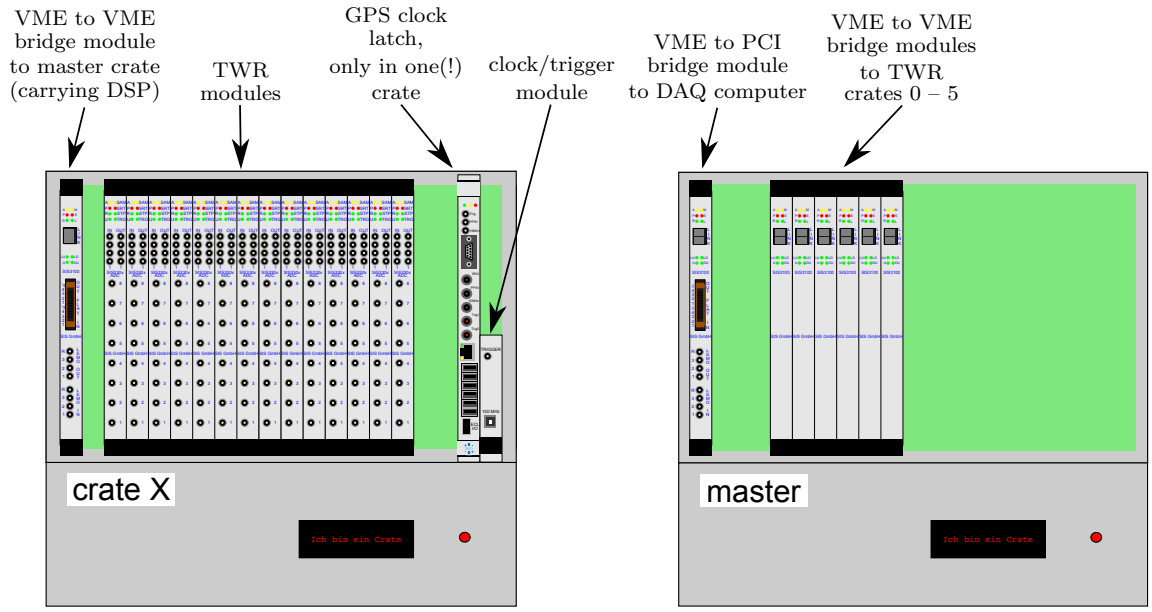

(a) One of Six TWR VME Crates

(b) TWR Master Crate

Fig. 3.9: TWR VME Crate Configuration. A trigger logic distributes the NIM trigger signals to the clock modules in the six TWR crates (Fig. 3.4). The clock module converts the NIM signals to ECL differential signals and distributes them over the VME backplane to the TWRs. Thus, every TWR receives the same trigger signal at the same time. After the TWR internal memory bank switching, the DSP on the bridge in each TWR crate reads out the filled TWR memory banks and stores the data in its own memory. The GPS clock latch is placed in only one of the six TWR crates. It is triggered over the back plane, like the TWRs and read out by the DSP of the corresponding crate. A computer, equipped with a PCI to VME bridge, reads and clears the DSP memories.

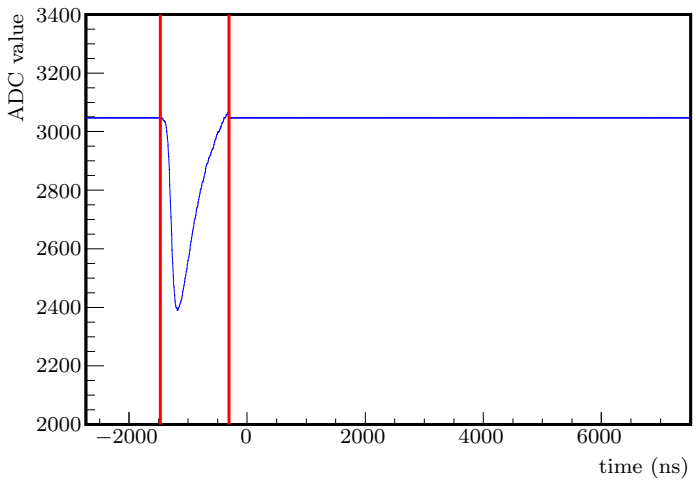

Fig. 3.10: Waveform Data Reduction by Feature Extraction. The DSP cuts away all samples that are not lying below the threshold. The samples outside the red time window are stored as one value. This example shows the already cleaned waveform to illustrate the amount of data size reduction.

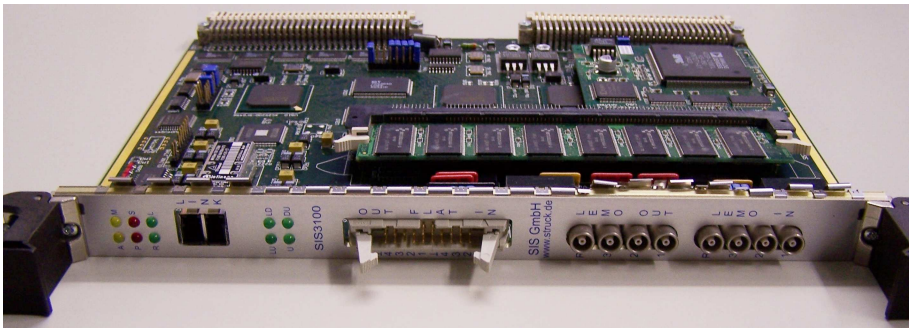

Fig. 3.11: VME to VME Bridge Module.

- *random data (minimum bias) trigger*, which is uncorrelated to physics events in the detector and
- the *laser trigger*, which is used during time calibration measurements with the Nd:YAG laser system.

The signal flow in the *trigger logic* for the TWRDAQ is displayed in Fig. 3.12. All trigger signals are sampled in special TWR channels. This offers the possibility, to differentiate the events by the corresponding trigger signal. In case of trigger signals coming in a fast sequence, it is necessary to block following trigger pulses after the first pulse. This allows for the TWR ring buffers filling up and, consequently, avoiding overlapping time windows. Thus, the minimum veto time is 10.24 µs. If the veto time is chosen close to the sampling time of one ring buffer, the TWRDAQ is nearly dead time free.

Besides the hardware trigger signal, which is triggering the DAQ system, the readout software on the DAQ computer does an additional software triggering. With single PMT noise rates between 320 Hz and 1.1 kHz (for PMTs on the AMANDA-B4 strings) [Wis99], the data rate of a real M13 triggering would be too high, and random coincidences between the PMT signals are likely. Therefore, all M13 triggered events, containing no other hardware trigger, are scanned for special event signatures. The signatures are

- a certain amount of hit PMTs are contained inside a given geometrical detector volume (*volume trigger*) [Mes06], or
- some PMTs recorded sequences of many photons (*fragments trigger*).

If one or both of the signatures are found, the event will be kept, otherwise it will be discarded.

For a detailed description of the TWRDAQ system the study of [Wag04] is highly recommended.

3.2.3 DAQ Timing

Every AMANDA event gets a global timestamp. The time information is delivered by a GPS clock (Symmetricom TrueTime XL) in form of three signals (Fig. 3.13):

- time information string with the current day of the year and the seconds of the day plus a GPS signal quality information (TQC),
- one pulse per second (1PPS) to mark the beginning of a new second,
- a 10MHz signal, phase locked to the 1PPS.

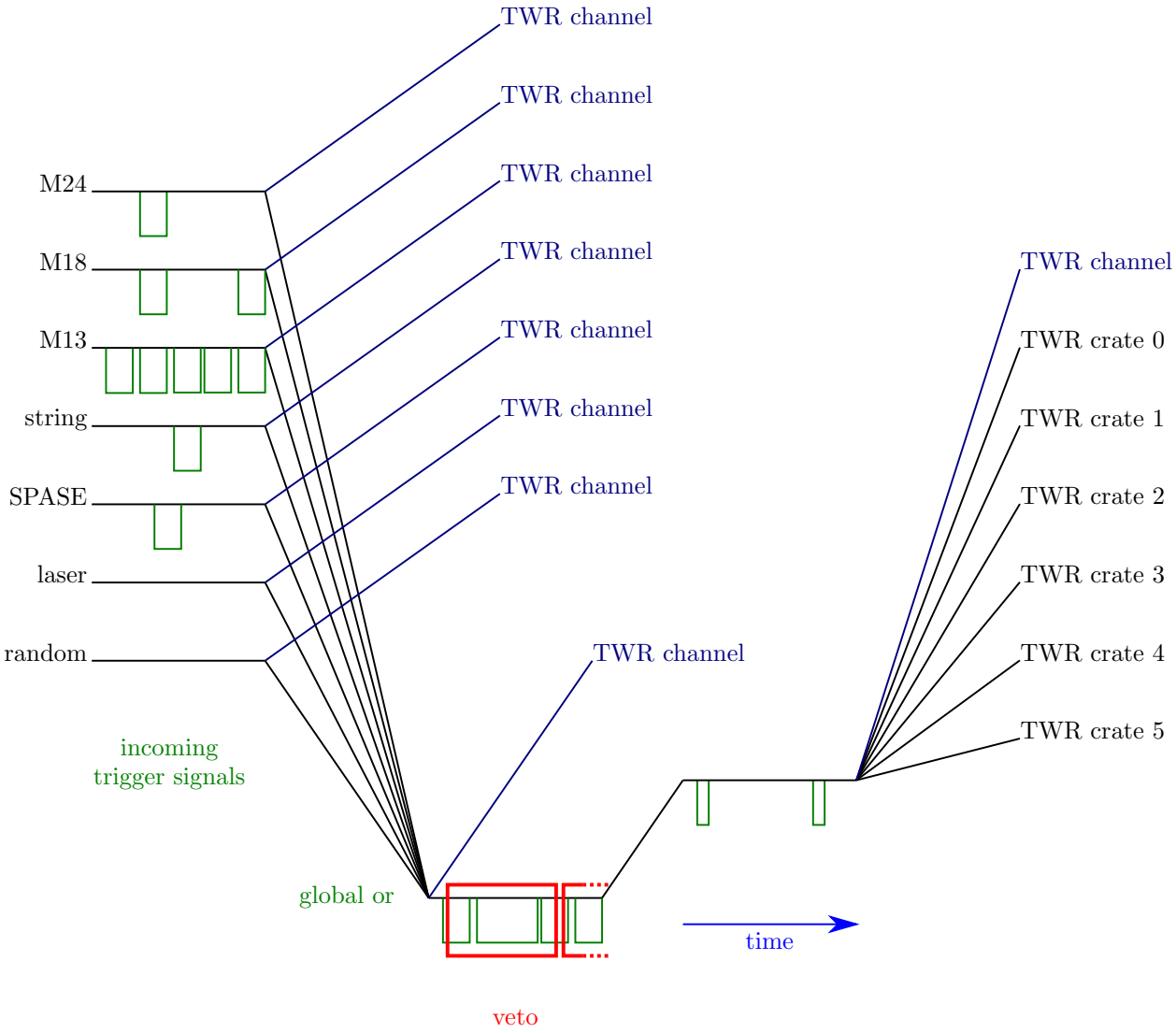

Fig. 3.12: TWR trigger signal way. The hardware trigger signals (green rectangular pulses) arrive at the TWR trigger logic and are split up. On the one hand, all signals are sampled individually in special TWR channels. On the other hand, the signals are merged to a "global OR" trigger, which is also split and fed into a TWR channel. The other copy of the global OR signal is vetoed by a gate generator. The remaining trigger signal pulses are sampled by a TWR channel and sent to the TWR crates to trigger the TWRDAQ.

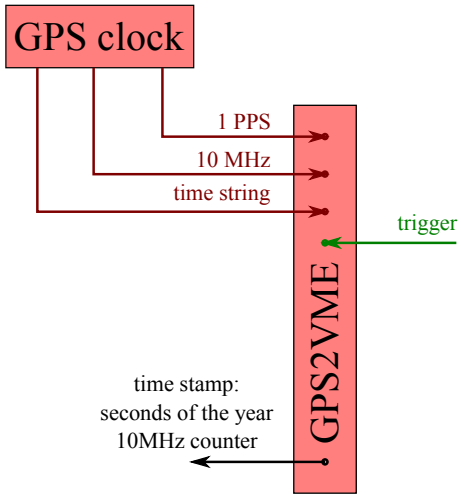

Fig. 3.13: Global Timing of TWRDAQ Events with the GPS2VME Module. The GPS2VME module receives the same trigger signals as the TWRs and stores the time stamp of the corresponding event in its memory. The readout is done over VME together with the readout of the TWRs.

The GPS latch – called *GPS2VME* in the original TWRDAQ setup [Lei03] – receives the GPS clock signals over coaxial cables and a serial (RS-232) connection for the time string. For the VME readout, the incoming information has to be refined. Therefore, every trigger causes the GPS2VME to write the current counter of the 10MHz signal, the current second since the beginning of the year, the year itself, the TQC and the current state of the GPS2VME into an internal FIFO memory. The GPS2VME state is defined by the presence of the necessary clock signals.

One information block is distributed over four 32-bit words. As the VME crates offer a 32-bit data access structure, always four VME cycles are necessary to build up the GPS timestamp information. With every 128 event block, the DSP in the corresponding crate also reads 128 timestamps from the GPS2VME. The timestamps give the global event time. Inside the TWR ring buffer structure (Fig. 3.7), this time corresponds to the trigger time.

For event reconstruction, the trigger time information inside the TWR waveforms is not sufficient. The cable delay from the OM to the TWR input has to be known very precisely. With help of the installed optical fibers, diffusor balls near to every OM and the Nd:YAG laser, a delay measurement with a precision of about $4-7\,\mathrm{ns}$ is possible[A+00]. The signal run time inside the fiber is measured with an Optical Time Domain Reflectometer (OTDR). With the knowledge of all other cable lengths and run times (Fig. 3.14(a)), the signal time delay t_0 of every OM can be calculated:

$$t_{10} + t_{21} - t_{03} - t_{24} = t_{43}, \quad \text{with} \quad t_{ba} = t_b - t_a. \tag{3.3}$$

The indices a and b correspond to the numbered positions in Fig. 3.14(a). Within the MuonDAQ setup, the peak time measurement is done with a ADC/TDC combination. Due to the fixed TDC voltage threshold, the measured time is systematically shifted regarding to the ADC peak time (Fig. 3.14(b)). This shift is inverse proportional to the square root of the peak ADC value U_{ADC}

$$t_{43} = t_0 + \frac{\alpha}{\sqrt{U_{\mathrm{ADC}}}}. \tag{3.4}$$

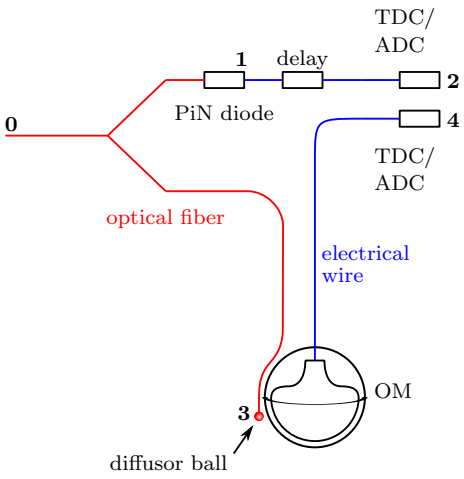

(a) T_0 Measurement

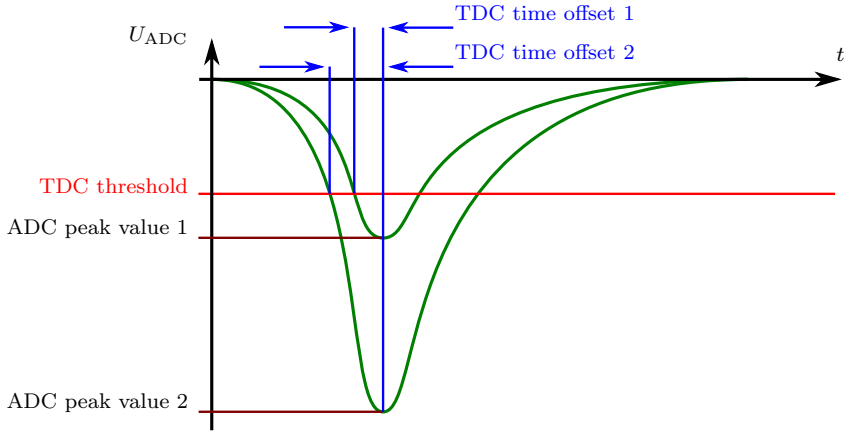

(b) T_0 Offset

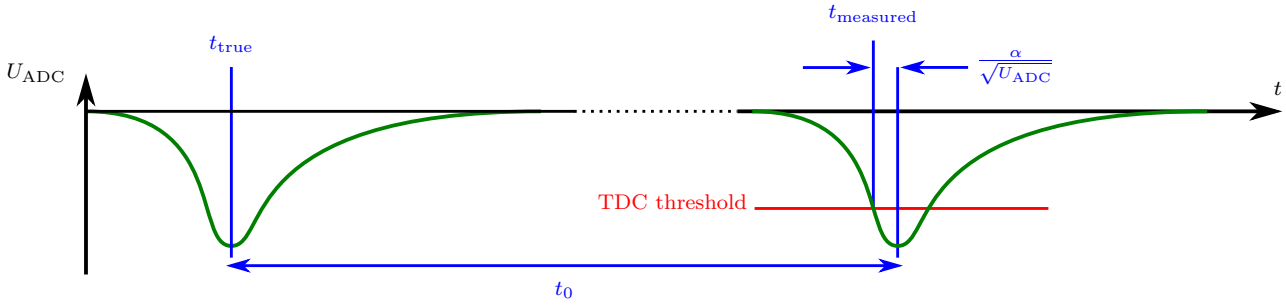

(c) T_0 Offset

Fig. 3.14: OM time calibration. (a) Red: optical fibers, blue: electrical connections. The signal run time from 0 to 3 can be measured with an OTDR. The run time from 0 to 1 has to be measured by hand with a ruler. The dispersion inside the optical fiber is known. The run time from 1 to 2 results from known cable lengths and the adjustable delay. The run time from 3 to 4 is to be determined.
(b) Because the TDC has a fixed voltage threshold for its time measurement, there is an offset between the measured time and the ADC peak value.
(c) How to add up times for determination of signal time inside a OM if t_0 is known (Eq. 3.5).

During the data taking process, the true hit time "inside" a given OM can be calculated to (Fig. 3.14(c))

$$t_{\text{true}} = t_{\text{measured}} - t_0 + \frac{\alpha}{\sqrt{U_{\text{ADC}}}} \tag{3.5}$$

Using the TDC/ADC combination of the MuonDAQ, the proportionality constant α and the signal delay t_0 have to be measured for every optical module.

The TWRDAQ uses a more simple method for the absolute timing of pulses. Here the full waveform allows for a much more accurate timing. For a single isolated pulse, two sample values

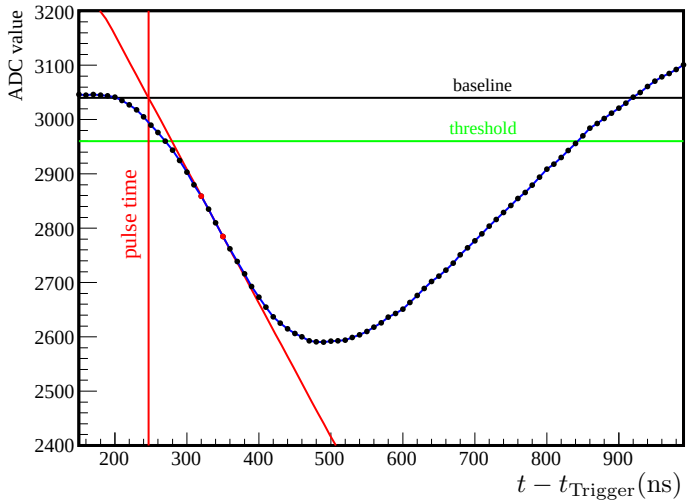

Fig. 3.15: TWR Signal Timing.

around the minimum slope on the leading edge are defining a line (Fig. 3.15). The intersection between this line and the baseline of the corresponding TWR channel gives the time of the pulse [Wag04]. For more complicated waveforms containing additional pulses on the rising edge of previous pulses, the value of the local minimum and not the baseline is used for finding the pulse time.

If the t_0 data for enough OMs is collected, an alternative time calibration method with down-going muons will be applicable [CH01].

3.3 The IceCube Neutrino Telescope

In its final state, the IceCube detector will consist of about 86 strings with 60 DOMs on each string. The geometrically instrumented volume will contain about 1 km^3 of ice (Fig. 3.16).

3.3.1 Detector Principles

Base of the IceCube concept is the AMANDA string 18 with its DOM technology (Fig. 3.17(a)). Like in AMANDA OMs, a PMT is used for light detection. The PMT high voltage is produced inside the DOM. All PMT pulses are sampled directly inside the DOM by a flash ADC and the digital information is sent to the surface.

For digitization the incoming PMT pulse is split. One pulse copy causes a trigger signal, when exceeding a threshold value, the second copy is delayed by a fixed time of 75 ns and triply split. The three identical signals are amplified by values of 16, 2 and 0.25 and given on three Analog Transient Waveform Digitizers (ATWDs). The sampling rate of the digitizers is set to 300 MHz.

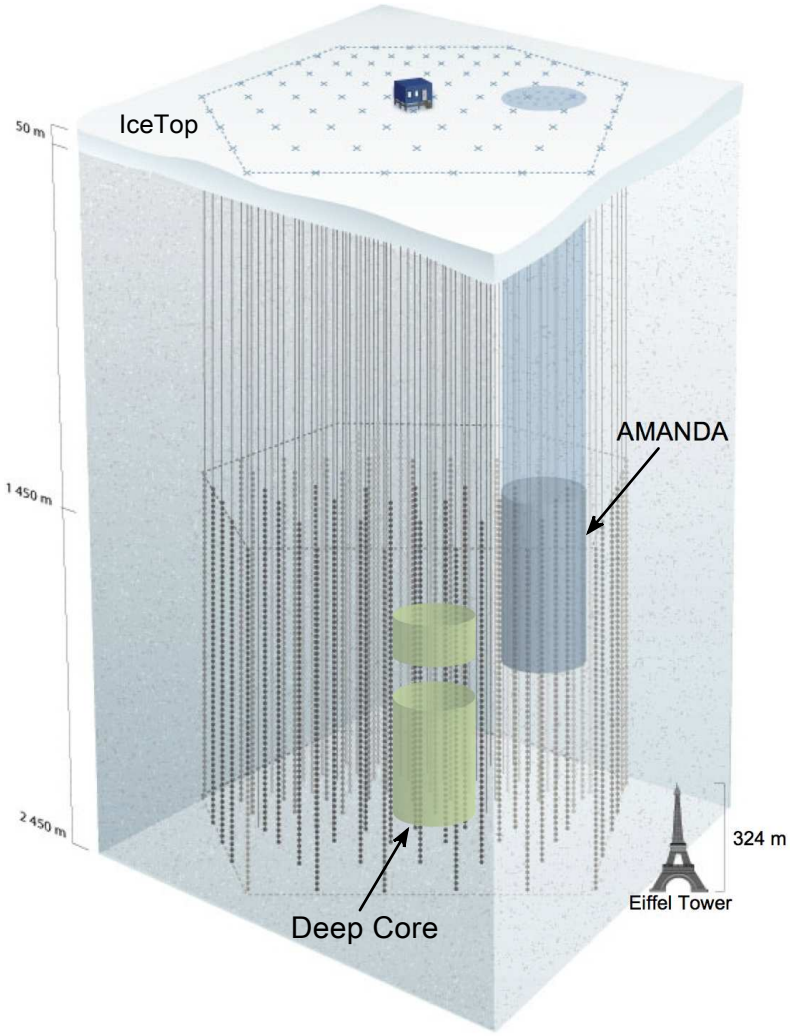

Fig. 3.16: The IceCube Detector. The picture shows the IceCube detector with the nested AMANDA detection volume. The future low energy array *Deep Core* (↗Sec. 4.7.3) will be placed in the bottom middle of the fully deployed IceCube detector.

Every ATWD can store 128 voltage values, corresponding to a recording time of about 400 ns. The readout of the digitizers is done by a 10-bit ADC. As the readout takes a long time (about 0.1 ms), a second set of ATWDs is necessary, to reduce the dead time. If three triggers come in a fast sequence, the system skips the third trigger and the PMT information is refused. An additional fADC, which uses the DOM system clock of 40 MHz, increases the sampling time. The fADC is able to record 256 samples, thus it stores 6.4 µs.

The control unit of the DOM is a FPGA. It manages the operation of the different electronic DOM components and compresses the PMT waveform data. Always the complete waveform information is transmitted to the surface. This puts high demands on the transmission and the surface data acquisition.

The IceCube surface DAQ system is a composition of several high performance computers, which is implemented in a separated building, the *IceCube Laboratory* (*ICL*) (Fig. 3.18). Every string is controlled and read out by a DOMHub computer. Other computers combine and filter the string data. The event trigger information is built in software. Several trigger conditions

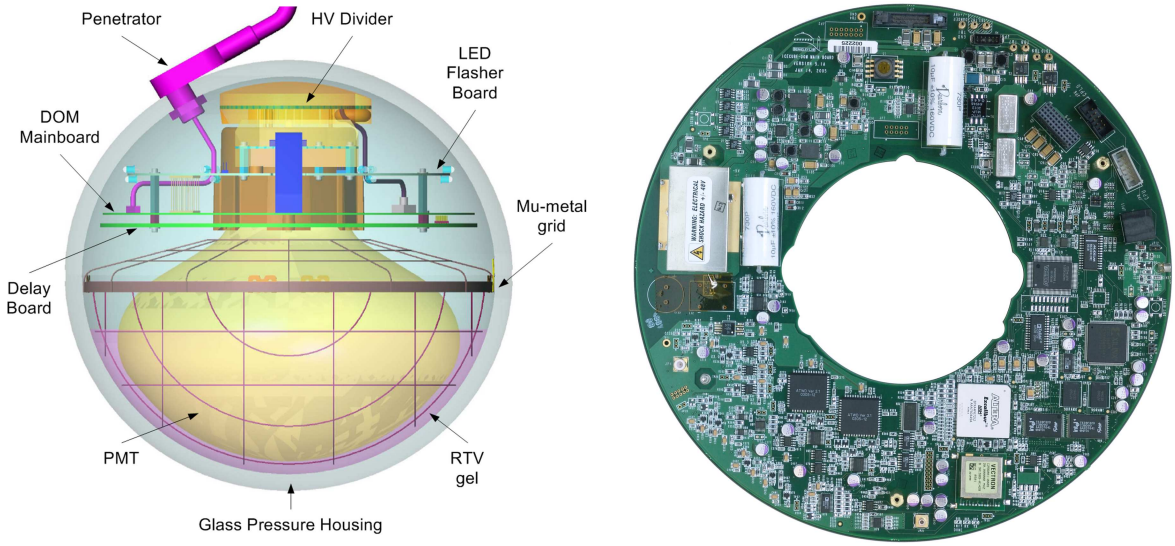

(a) Digital Optical Module (DOM)

(b) DOM Mainboard

Fig. 3.17: Digital Optical Module (DOM) and DOM Mainboard. A DOM can be described as a small standalone photon detector. The high voltage for the PMT is produced inside the DOM. The DOM mainboard is equipped with readout, digitization and communication electronics. A delay board arranges for the arrival of the trigger information before the signal. The LEDs can be used for detector geometry calibrations. A mu-metal grid shields the PMT from the Earth magnetic field. Images: [A+09a]

lead to the recognition of an event inside the data stream [Seo05b].

Because of the DAQ structure of IceCube, it is difficult to get additional hardware signal information into the IceCube data stream. The only access to the data stream is given by the digitizing electronics inside the DOMs. All this electronics is built upon a multilayer board, the *DOM mainboard* (Fig. 3.17(b)). The signal input for the PMT signals can be fed with every other signal, which is sampled and delivered to the IceCube DAQ system. This is very important for the AMANDA/IceCube integration. Further information about the IceCube DAQ system can be found in [A+09a].

3.3.2 IceCube Timing

The IceCube time normal is, like in AMANDA, a GPS clock (Symmetricom ExacTime 6000 OCXO). The clock delivers the 10 MHz phase locked frequency, the 1PPS signal and a time string via a RS-232. It is also possible, to use the *IRIG* format (Inter Range Instrumentation Group time code) for the encoding of the time string. The timing information from the GPS clock is delivered to a GPS fan-out module multiplexing the signals. Every DOMHub houses a DOMHub Service Board (DSB), which receives the timing information from the GPS clock (either directly or via the fan-out). To communicate with the DOMs on the string which is connected to the DOMHub, DOM Readout (*DOR*) cards are used (Fig. 3.19). The DOR cards receive the GPS time from the DSB.

All DOMs themselves carry a high precision 20 MHz temperature-compensated crystal oscillator, which is doubled by a PLL to 40 MHz. A 48-bit frequency counter connected to the 40 MHz acts as a local DOM clock. The DOR clock and the DOM clock are not synchronized. Therefore, the timing relation between the DOM clock and the DOR clock is measured in regular intervals

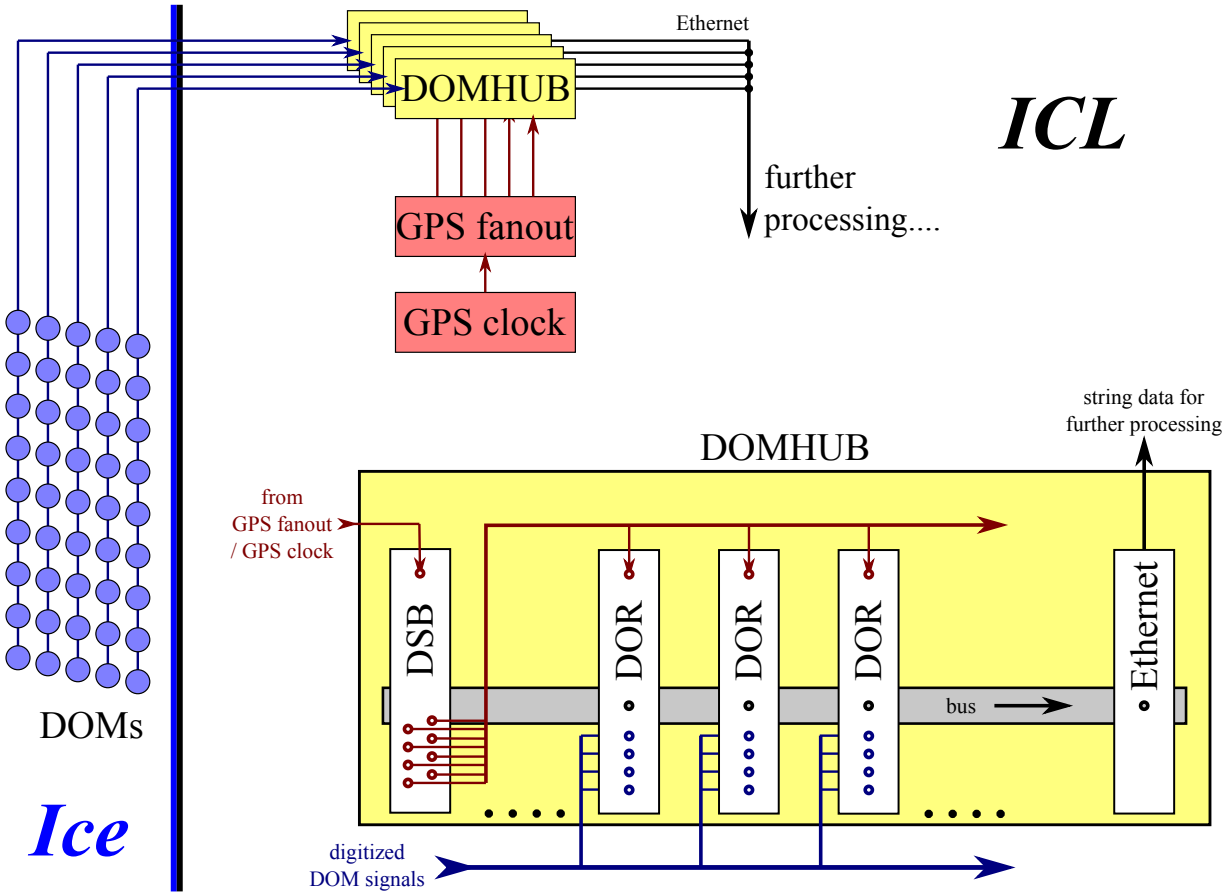

Fig. 3.18: Scheme of the IceCube DAQ System.

of about 5 s. The calibration method is called Reciprocal Active Pulsing Calibration (*RAPCal*) [A+09a]. The RAPCal method uses identical signal sources and receivers on two sides of an electrical connection to measure the time shift between signal transmission and reception. The measurement is done in several steps (Fig. 3.20):

(a) The DOR card sends a very precisely shaped bipolar pulse, which is synchronized to the DOR clock, to the DOM and saves the start time t_1^n of the pulse in units of its clock counter

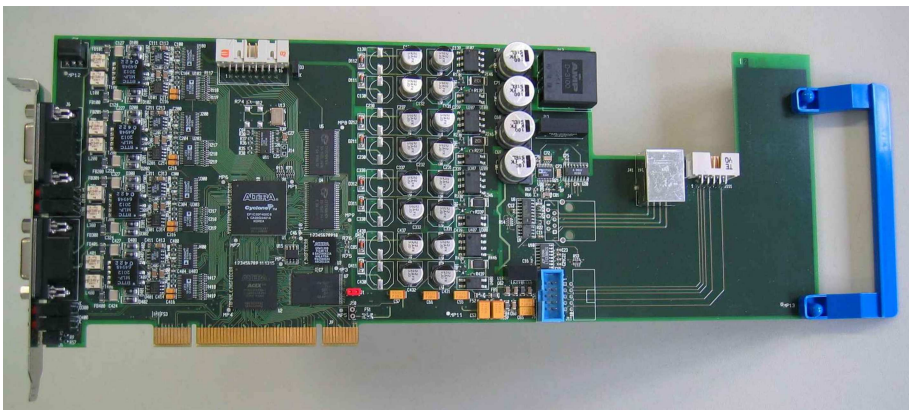

Fig. 3.19: DOM Readout (DOR) card. Image: [A+09a]

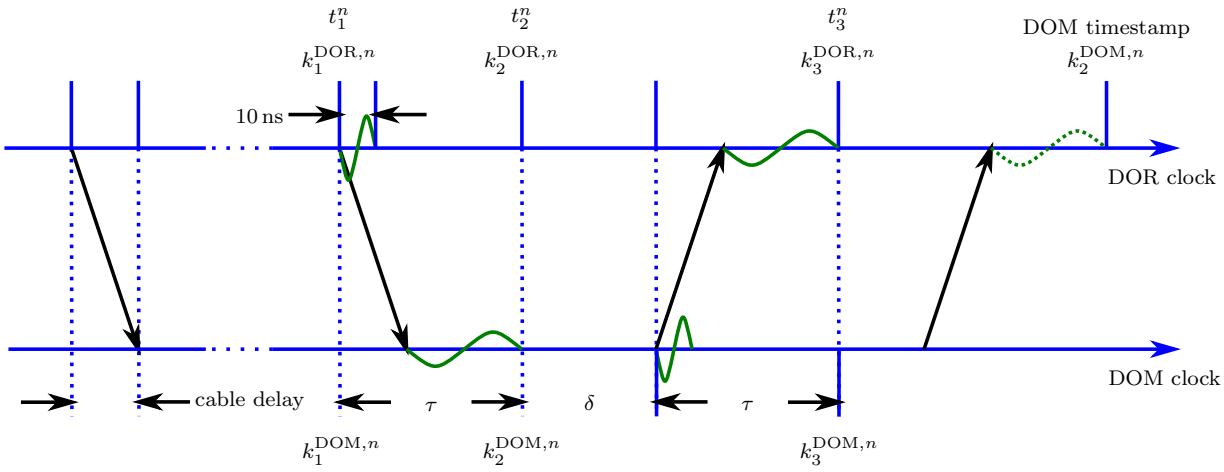

Fig. 3.20: Reciprocal Active Pulsing Calibration (RAPCal). The two time lines illustrate the DOR and the DOM clock. Vertical lines mark the same (physical) time. As the two clocks are floating freely, the values in the clocks corresponding to the same time may differ. The green curves are calibration pulses. They experience dispersion and attenuation while traveling through the cable from the DOR card to the DOM. The dotted curve is the DOM-digitized first DOR calibration pulse. The values t_i are the (GPS) times. $k_i^{\mathrm{DOR,DOM}}$ represent the clock counters of DOR card and DOM at time t_i.

$k_1^{\mathrm{DOR},n}$.

(b) The DOM mainboard receives the pulse and samples it. The last sample of the pulse waveform is timestamped with the local clock counter at the time t_2^n with $k_2^{\mathrm{DOM},n}$. $k_1^{\mathrm{DOR},n}$ and $k_2^{\mathrm{DOM},n}$ are floating against each other.

(c) After the sampling, the DOM waits a fixed time δ, to ensure a cable connection to the DOR card, which is free from interfering signals. Following this short delay the DOM sends a bipolar pulse itself, which is identical to the one, sent by the DOR card.

(d) In the DOR card, the arriving pulse is sampled exactly the same way, as the first DOR pulse was sampled in the DOM. This guarantees the same signal delivering and processing time in each transmission and is called reciprocal symmetry.

(e) The DOR card requests the sampled and locally timestamped waveform from the DOM. The waveform can be used, to verify the reciprocal symmetry, if compared to the DOR waveform sample.

To measure the frequency ratio between the two clocks, the described procedure has to be repeated. The ratio is given by

$$\frac{\nu^{\mathrm{DOR}}}{\nu^{\mathrm{DOM}}} = \frac{t_2^{n+1} - t_2^n}{t_1^{n+1} - t_1^n}. \tag{3.6}$$

The waveform transmission and sampling time can be calculated with the given times to

$$\tau = \frac{(t_3^n - t_1^n) - \delta}{2}. \tag{3.7}$$

It is possible to translate real times $[t] = \mathrm{s}$ into the corresponding clock values $[k] = \mathrm{samples}$ for the DOR and the DOM clock:

$$k^{\mathrm{DOR}} = \nu^{\mathrm{DOR}} \cdot t \quad \text{and} \quad k^{\mathrm{DOM}} = \nu^{\mathrm{DOM}}. \tag{3.8}$$

The values k_1^{DOR}, $k_\delta^{\mathrm{DOM}} = \delta\nu^{\mathrm{DOM}}$, k_2^{DOM} and k_3^{DOR} are known. To calculate k_1^{DOM}

$$t_1 = t_2 - \tau, \quad \text{with} \quad \tau = \frac{1}{2}\left(\frac{k_3^{\mathrm{DOR}}}{\nu^{\mathrm{DOR}}} - \frac{k_1^{\mathrm{DOR}}}{\nu^{\mathrm{DOR}}} - \frac{k_\delta^{\mathrm{DOM}}}{\nu^{\mathrm{DOM}}}\right) \tag{3.9}$$

is needed. Inserting the known values delivers

$$k_1^{\mathrm{DOM}} = k_2^{\mathrm{DOM}} - \frac{1}{2}\left(\frac{k_3^{\mathrm{DOR}}}{\nu^{\mathrm{DOR}}} - \frac{k_1^{\mathrm{DOR}}}{\nu^{\mathrm{DOR}}} - \frac{k_\delta^{\mathrm{DOM}}}{\nu^{\mathrm{DOM}}}\right). \tag{3.10}$$

Now, for every DOM timestamp k^{DOM} at time t the GPS time DOR card timestamp k^{DOR} can be calculated.

$$k^{\mathrm{DOM}} = k_1^{\mathrm{DOM}} + (t - t_1)\nu^{\mathrm{DOM}} \tag{3.11a}$$

$$k^{\mathrm{DOR}} = k_1^{\mathrm{DOR}} + (t - t_1)\nu^{\mathrm{DOR}} \tag{3.11b}$$

can be combined to

$$k^{\mathrm{DOR}} = \frac{\nu^{\mathrm{DOR}}}{\nu^{\mathrm{DOM}}}\left(k^{\mathrm{DOM}} - k_1^{\mathrm{DOM}}\right) + k_1^{\mathrm{DOR}}. \tag{3.12}$$

In principle, also the dispersion caused by the long cable from the DOM to the DOR card can be measured during the RAPCal cycle, but this information is not needed for time calibration or data transmission.

3.3.3 IceCube Data Taking / TestDAQ

Two different DAQ software systems can manage the data taking with the IceCube detector. Besides the DAQ software for standard physics data taking, the so called TestDAQ can be used to operate only parts of the detector, e.g. single DOMs, to obtain special channel data. Here, the hit times are only dependent on the single DOM and not recalculated to the global detector trigger time. It will be shown that this makes the TestDAQ system to a very powerful tool, to observe the AMANDA/IceCube synchronization.

The standard IceCube DAQ does not only provide the detector readout. The resulting data stream is filtered online. All events which contain useful physics information are kept and sent to the northern hemisphere. The decision about which event is useful or not is done by several *online filters*. These software modules are subject to tight restrictions regarding to their event passing rate, because the satellite bandwidth for data transmission is very limited. Furthermore, a monitoring system collects information about the detector state. The monitoring is also done by software modules. They collect the data and store it in histogram form. This way, the detector stability can be observed during the complete uptime. At the end of the next chapter, a monitoring module observing the AMANDA/IceCube timing stability will be introduced.

4

AMANDA/IceCube Integration

This chapter describes the upgrades and modifications done on the AMANDA and IceCube hard- and software and all testing and verification procedures of the upgrades developed within the work for this thesis.

4.1 Motivation

Besides the free availability of 600 additional OMs of AMANDA in the IceCube detector array, several other reasons argue for the integration of AMANDA into IceCube.

4.1.1 Dense Instrumentation

The instrumented volume $V_i \approx 0.0157\,\mathrm{km}^3$ of the AMANDA detector can be approximated by a cylinder with a base radius of 100 m and a height of 500 m. The AMANDA 8″ PMTs (Hamamatsu R5912-2) have a photo cathode diameter of 19 cm and therefore a photosensitive area of $284\,\mathrm{cm}^2$. About 600 AMANDA PMTs are currently delivering good signals. Accordingly, AMANDA has a volume normalized photosensitive area of about $1000\,\frac{\mathrm{m}^2}{\mathrm{km}^3}$.

In its final state, IceCube has an instrumented volume of $V_i \approx 1\,\mathrm{km}^3$. With 60 DOMs on each of the 80 strings the obtained PMT number is 4800. IceCube uses 10″ PMTs (Hamamatsu R7081-20). The photosensitive area of one IceCube PMT is $380\,\mathrm{cm}^2$. This results in a volume normalized photosensitive area of $182\,\frac{\mathrm{m}^2}{\mathrm{km}^3}$.

Due to the denser instrumentation of AMANDA ($38200\,\frac{\mathrm{PMTs}}{\mathrm{km}^3}$) and the higher photosensitive area, the energy threshold for AMANDA is lower, than for IceCube ($4800\,\frac{\mathrm{PMTs}}{\mathrm{km}^3}$). Thus, AMANDA can act as an already running IceCube low energy extension.

A possible further effect of the OM density inside AMANDA, is the higher spacial resolution. This could be used for track identification or even separation in multi track events. In combination with the surrounding IceCube strings, the lever arm for track reconstruction is higher than for AMANDA alone. This allows for a better angular resolution of reconstructed muon tracks, than for AMANDA alone [Res09].

4.1.2 IceCube as Veto

For some physics cases, it is useful to know, where the energy of a particle, which is traversing the detector, is deposited. The location of the starting or stopping point of a particle track can deliver this information. AMANDA is surrounded by IceCube strings (Fig. 4.1). This geometry

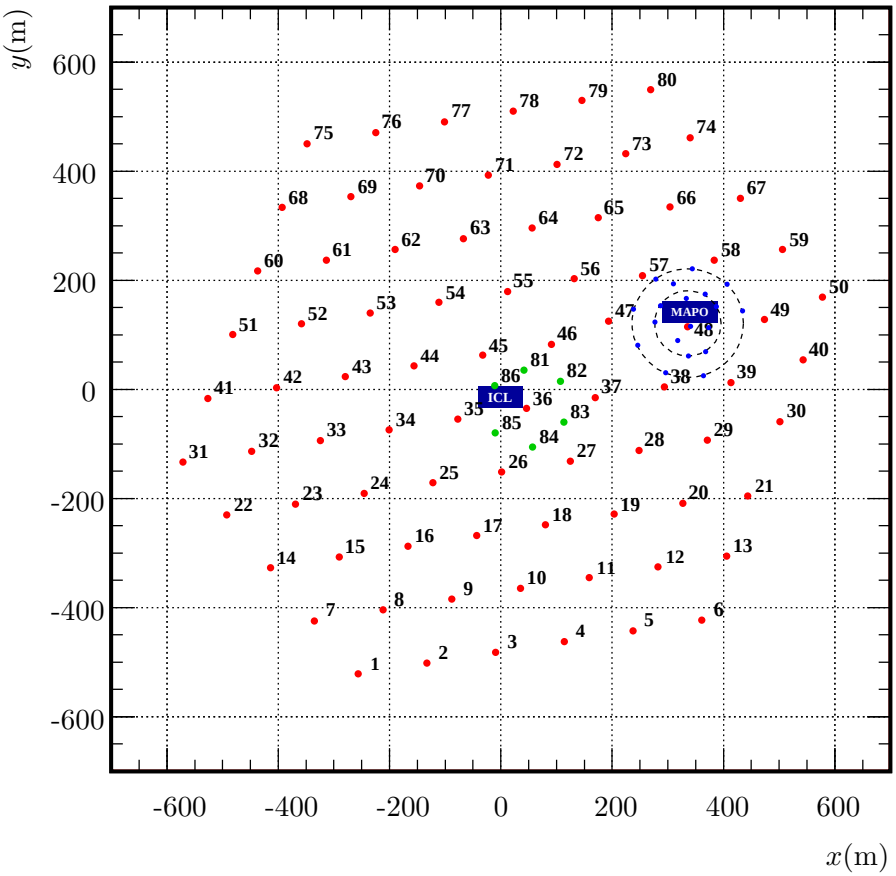

Fig. 4.1: Map of the IceCube Strings. The black concentric rings symbolize the area of the AMANDA detector. In the IceCube strings 81 to 86 belong to the future IceCube Deep Core array. The distance between the two counting houses, MAPO and ICL is about 400 m.

makes it possible, to verify that a charged particle track protrudes from the AMANDA detection volume. If only contained events in AMANDA are wanted, a light signature in the surrounding IceCube strings is a veto condition [GHR+07].

Further on, cascade like events produced by electron or tau leptons can be identified. A cascade on the edge of the AMANDA detection volume can also be interpreted as part of a high energy muon track. The veto capabilities of the surrounding IceCube strings help to determine the particle type.

A possible application is the measurement of the atmospheric muon energy spectrum. Here the energy of atmospheric muons, stopping inside the AMANDA detector, is measured. As the energy loss of muons in air and ice is known, the original energy can be calculated from the deposited energy in AMANDA and the energy loss.

Another application is the low energy analysis of down-going events. These events are normally

background events, but with the vetoing option, AMANDA can look above the horizon. Neutrinos, passing the IceCube strings and interact in the AMANDA detection volume, contribute to the signal. However, a full sky coverage is not possible this way, because the instrumented volume of AMANDA and of IceCube roughly start at the same depth.

4.2 Demands on the Integration System

Because of the different DAQ systems of AMANDA and IceCube, a direct readout of AMANDA by the IceCube DAQ is not possible. It is rather necessary to produce an IceCube and an AMANDA standalone data stream, which are combined at some point of the data processing chain. For the integration AMANDA is regarded as a subsystem of IceCube. Therefore, IceCube needs the AMANDA data stream in a way in which it is possible to integrate the AMANDA event information into the IceCube data stream in real time. Consequently, the AMANDA data has to be converted into the IceCube data format as fast, as the AMANDA detector is delivering its data. The accuracy of the absolute timing within the OM to surface signal transmission of AMANDA is about 5 ns [A$^+$00]. The resolution of the DAQ components inside the IceCube DOMs is $\leq$ 5 ns [A$^+$09a]. The timing accuracy between the AMANDA and the IceCube data stream timestamps has to be in the same order of magnitude. The limit for the synchronization accuracy is set to a value better than 10 ns.

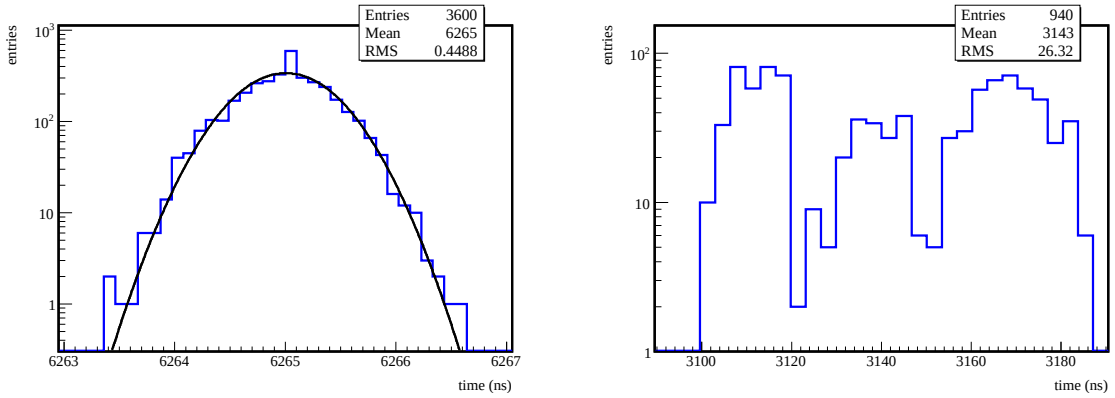

(a) One GPS Clock

(b) Two GPS Clocks

Fig. 4.2: GPS Clock Drift. In the left picture, the 1PPS signal of the IceCube GPS clock sent to the MAPO and back to the ICL is timestamped with the time of the IceCube GPS clock. The right picture shows the times of 1PPS pulses transmitted from the ICL to the MAPO and back, sampled with the source clock of the 1PPS. The duration for both measurements is about 15 min. The two different time scales are a product of different cable lengths for both measurements.

The usage of independent GPS clocks in AMANDA and IceCube is not applicable to achieve this accuracy limit. Measurements show that two GPS clocks have a drift, which is higher than 10 ns. In Fig. 4.2, the arrival times of 1PPS signals measured with GPS clocks are histogramed. The measurement is done with the TestDAQ readout software (↗ Sec. 4.6.2). If only one clock is used to generate the signal, which is then delayed by electronics and long fibers (↗ Sec. 4.3.7) and to measure the arrival time, a narrow (Gaussian) distribution is obtained (Fig. 4.2(a)). Using one clock to produce the 1PPS signal and another one to timestamp it, the arrival time distribution is much broader and not Gaussian anymore (Fig. 4.2(b)). With an RMS of more than 26 ns within only 15 min the minimum demand on the synchronization accuracy is not fulfilled.

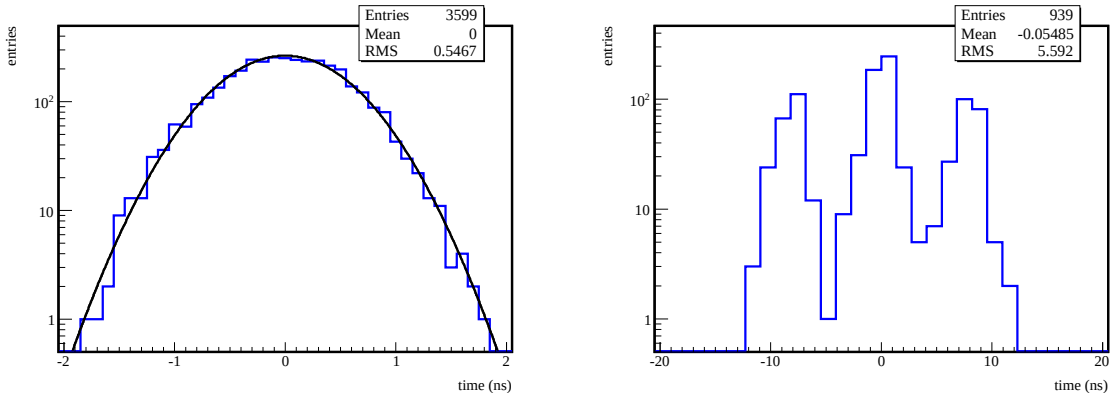

(a) One GPS Clock

(b) Two GPS Clocks

Fig. 4.3: GPS Clock Drift Time Difference. These histograms are based on the two measurements used in Fig. 4.2. Here the time difference between two following 1PPS signals is plotted.

To illustrate the timing fluctuations between the two GPS clocks, the time difference between two following 1PPS signals is plotted in Fig. 4.3. Obviously the 1PPS is switching its time regarding to the beginning of the second in another GPS clock many times during the time of the measurement. This GPS clock drift can be explained. At the South Pole the coverage with GPS satellites is not as good as in more central regions on the Earth. Accordingly, the amount of satellites to choose from is smaller and the error correction for one clock already decreased. If two clocks are operating, it cannot be expected that they use the same satellites. If one clock switches one or more satellites, e.g. because it is falling below the horizon, the other one may still work with its set of satellites. But a satellite switch is causing small timing fluctuations. These fluctuations are not important for one clock (Figs. 4.2(a) & 4.3(a)). If two clocks are operating in parallel, the fluctuations can be measured as a random time drift between the clocks (Figs. 4.2(b) & 4.3(b)).

4.3 Realization of the Hardware Synchronization

As the AMANDA and the IceCube DAQ are installed in different buildings, which are separated by a distance of roughly 500 m, the synchronization of both detectors is not trivial. Ice is a very good insulator. Consequently, objects built on ice have no common ground. A direct electrical connection between buildings at the South Pole always holds the risk of ground loops or – even more problematical – a short circuit of very high electrical potential differences, as the two buildings act like a capacitor. For this reason, it was decided to use already existent optical fiber connections between the ICL and the MAPO for the real time transmission of synchronization signals.

In the following sections, the new hardware components, necessary for the synchronization, are introduced. The complete hardware synchronization scheme (Fig. 4.4) is explained in Sec. 4.3.7.

4.3.1 The GPS Latch GPS4TWR

Heart of the synchronization hardware is the new AMANDA GPS latch [Lei07], which is called GPS4TWR (Fig. 4.5). It replaces the original GPS2VME. The timing information delivered from the GPS4TWR to the AMANDA DAQ is nearly the same as from the GPS2VME module

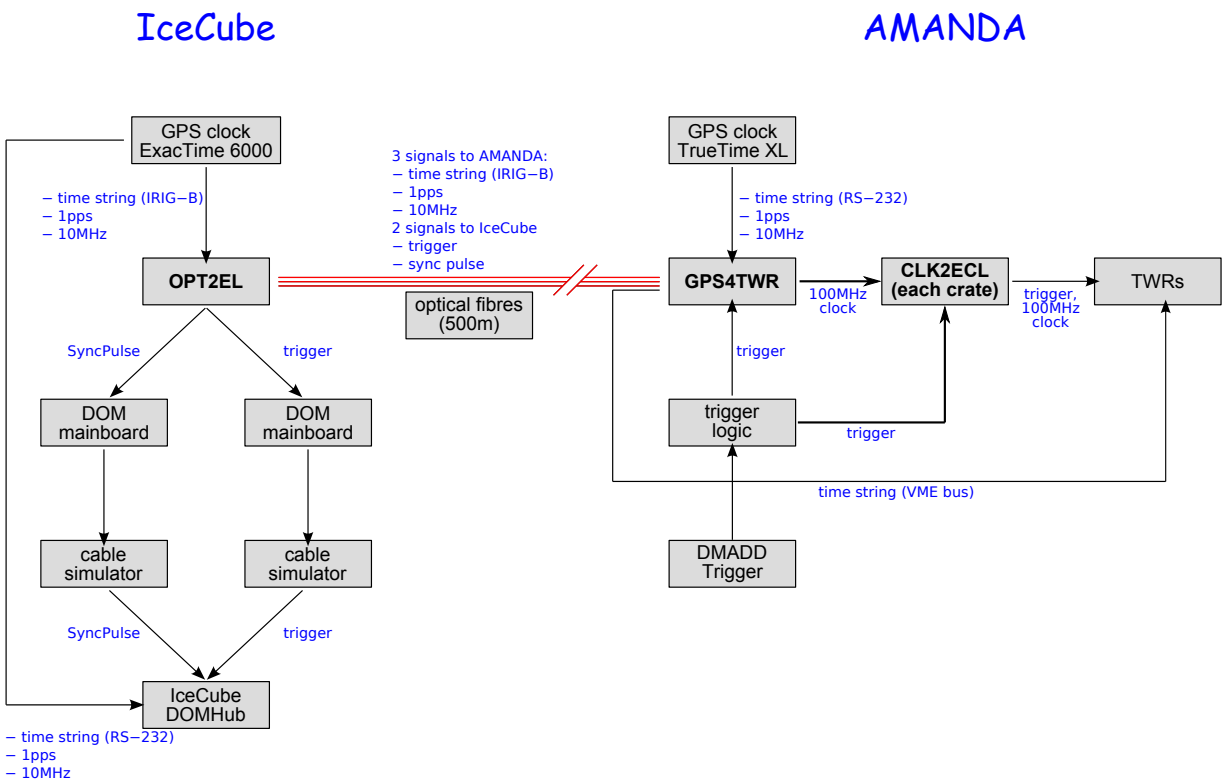

Fig. 4.4: AMANDA/IceCube Hardware Synchronization Scheme. Words in bold letters describe new components. All integration components are explained in the text.

(↗ Sec. 3.2.3). But several upgrades are implemented, to improve the TWRDAQ and to permit the synchronization.

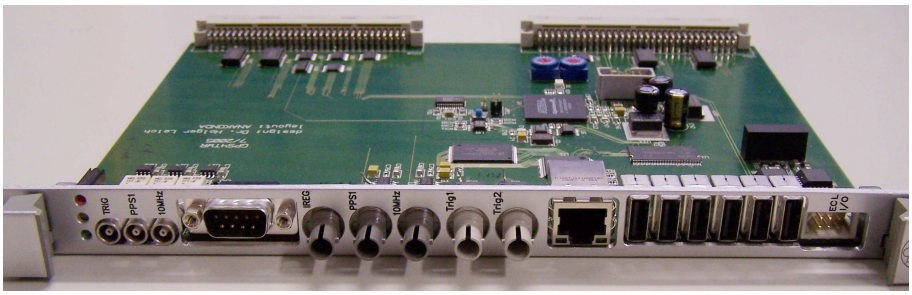

Fig. 4.5: GPS4TWR. Connections from left to right:
3× LEMO connectors: trigger, 1PPS, 10 MHz
Sub-D: time string (RS-232)
3× optical in: time string (IRIG-B), 1PPS, 10 MHz
2× optical out: SyncPulse, trigger
RJ45: Ethernet connection
6× USB-A: 100 MHz out (LVDS)
3× ECL: SyncPulse out, trigger out, n/c.

100 MHz

The GPS2VME only delivered the counter of the 10 MHz signal of the GPS clock. Accordingly, the event timestamping accuracy could not be better than 100 ns. A further disadvantage was the decoupled GPS clock from the 100 MHz driving clock for the TWR modules. The internal TWR counters have been synchronized to each other, but there was no synchronization to the GPS time. The GPS4TWR uses a phase-locked loop (PLL) to multiply the 10 MHz GPS clock frequency by a factor of ten to obtain the 100 MHz TWR clock frequency. This frequency is the new standard for the TWR clock counter. It is distributed to the TWR crates via six low-voltage differential signaling (LVDS) connections.

Electrical and Optical GPS Signal Inputs

To receive the IceCube GPS clock signal via optical fibers, optical to electrical converters are necessary. Three optical inputs convert the 10 MHz, the 1PPS and the time string (delivered in the IRIG-B format ↗ Sec. 3.3.2) into electrical signals. As a backup option, the electrical inputs for the AMANDA GPS clock are still available. The clock switching can be done by setting an internal register of the GPS4TWR. Either a GPS clock input is set fixed forcing the choice of the corresponding clock or the IceCube GPS clock over the optical inputs is set as default. In the latter case, a failure during the data transmission leads to an automated switching to the AMANDA GPS clock.

Trigger and SyncPulse Outputs

Two further options of synchronization between IceCube and AMANDA can be realized with the GPS4TWR. Over two optical outputs, the AMANDA trigger signal and a periodic synchronization pulse, the *SyncPulse*, can be sent to IceCube.

The trigger signal is derived from the signal also triggering the GPS4TWR and the TWRs (Fig. 3.12).

The SyncPulse origin is the 1PPS signal from one of the connected GPS clocks. The 1PPS source clock does *not* have to be the currently used clock input for the event timestamps! It has to be chosen via a register and is fixed. In the following, the SyncPulse is not always the timestamping 1PPS, which is underlined by the different terminology. This feature offers advanced monitoring possibilities, which will be described in section 4.6.

For monitoring reasons, an ECL output delivers the 1PPS also in electrical form (↗ Sec. 4.3.6).

4.3.2 CLK2ECL and the Backplane

The VME standard offers access to the modules inside of a VME crate over two backplanes (Fig. 4.6(c)). One backplane (P1) is standardized. It supports the connected modules with power and manages the data transfer. The second backplane (P2) is freely configurable and is used inside the TWRDAQ to deliver the 100 MHz clock signal as well as the trigger signals to the TWRs. A small clock/trigger module allows for the access to the P2 backplane. For the new 100 MHz distribution from the GPS4TWR this clock/trigger module is replaced by the *CLK2ECL* module (Fig. 4.6(a)). It converts the NIM trigger pulses and the LVDS clock signal into ECL signals. The ECL signals are split and given onto four backplane units. Every unit can supply four TWRs with clock and trigger. This is an improvement regarding to the old backplane, which was a flying wire connection soldered from the left to the right over the complete P2 backplane.

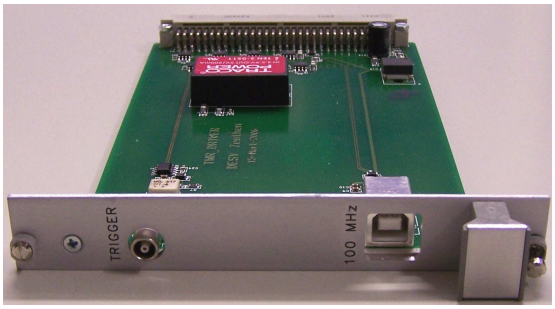

(a) CLK2ECL

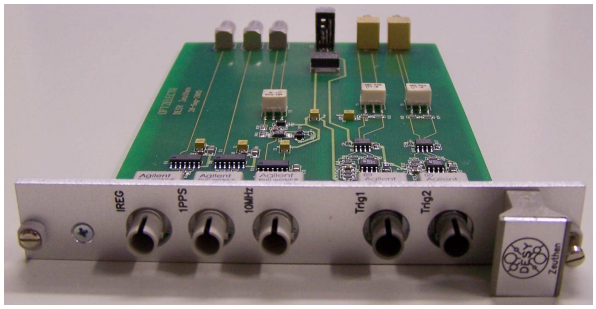

(b) OPT2EL

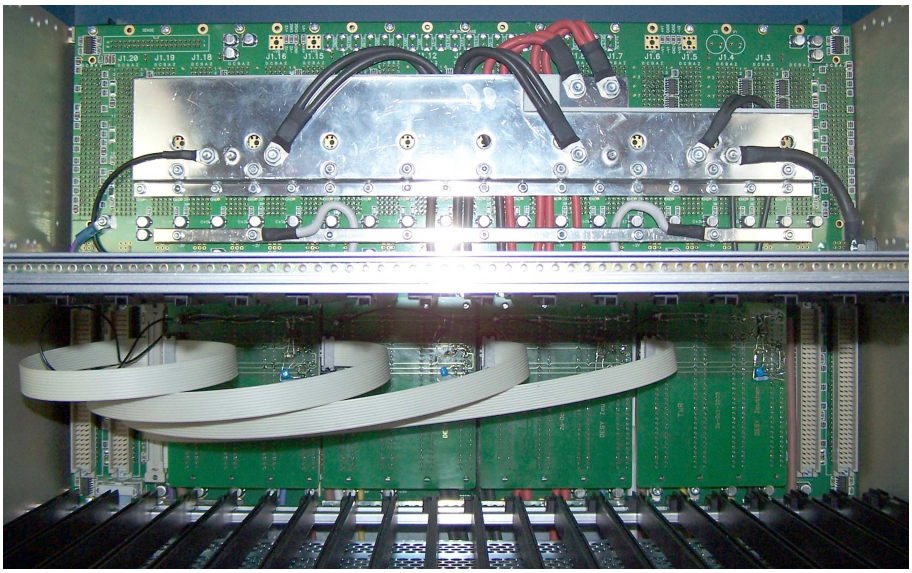

(c) Backplane

Fig. 4.6: CLK2EL, OPT2EL and Backplane.

4.3.3 The Optical to Electrical Converter OPT2EL

The IceCube GPS clock in the ICL delivers only electrical signals. The OPT2EL (Fig. 4.6(b)) converts the electrical IceCube GPS signals into optical signals and the optical trigger signal and SyncPulse from AMANDA into electrical signals. It was developed and produced by the electronics workshop of the DESY Zeuthen.

4.3.4 The AMANDA DOM Mainboards, the Cable Simulator and the AMANDA DOMHub

The AMANDA trigger signals and SyncPulses have to be digitized and given into the IceCube data stream. Incoming signals from the OPT2EL are directly distributed to the "AMANDA DOM mainboards": One mainboard is receiving the trigger signal (*TrigMB*) and the other one is receiving the SyncPulse (*SyncMB*). DOM mainboards cannot be directly connected to the DOR cards in a DOMHub. Some systems (e.g. RAPCal ↗ Sec. 3.3.2) need the dispersion and attenuation of a cable with a length of $\mathcal{O}$(km). The *cable simulator*, a passive combination of resistors, capacitors and inductors, simulates the cable effects. With one simulator, four DOM mainboards can be connected to a DOMHub. Over the cable simulator, the AMANDA mainboards are connected to the "*AMANDA DOMHub*", a DOMHub computer which processes only the incoming AMANDA trigger signals and SyncPulses.

4.3.5 The SyncCrate

For a useful implementation, all components, which are needed for the hardware synchronization in the ICL, are built into a 19″ metal housing, which can be placed into a standard rack. This "SyncCrate" houses the two AMANDA DOM mainboards, the cable simulator and the OPT2EL with its power supply.

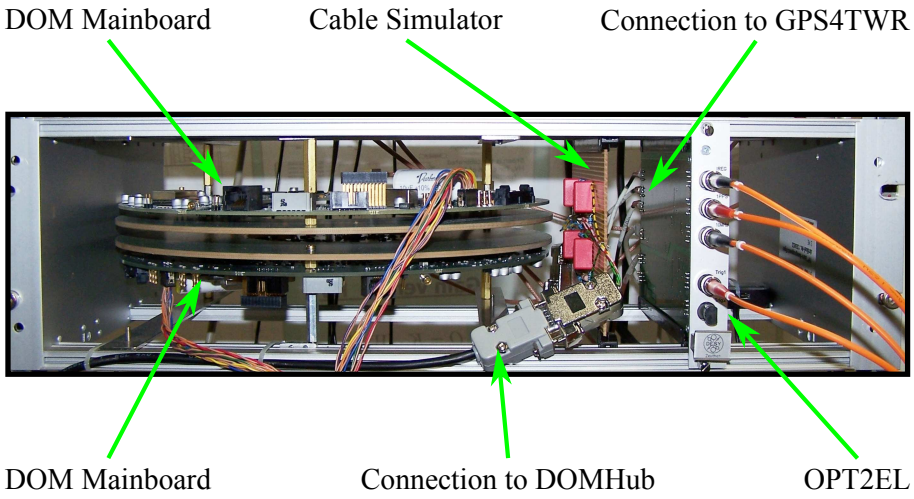

(a) Open SyncCrate in Wuppertal

(b) Built in SyncCrate and AMANDA DOMHub in the ICL

Fig. 4.7: SyncCrate interior and built in view.

4.3.6 The Improved Trigger Logic

Fig. 4.8 shows the improved trigger logic. The former random trigger (cf. Fig. 3.12) is replaced by the SyncPulse from the GPS4TWR.* This new trigger signal does not only deliver minimum

*The ECL signal is converted to NIM before being fed into the logic.

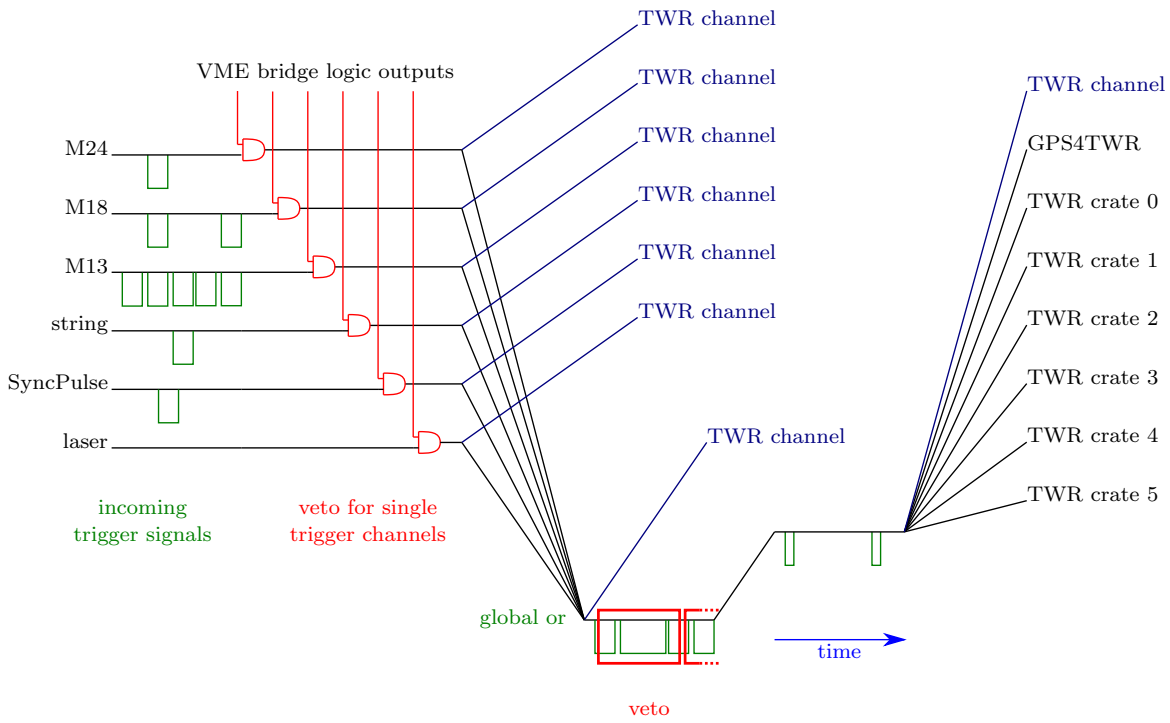

Fig. 4.8: Improved TWRDAQ Trigger Logic.

bias DAQ data with a rate of 1 Hz. If SyncPulse source and GPS clock source are not identical (↗ Sec. 4.3.1), the offset of the timestamp of the SyncPulse events and the beginning of the second, corresponding to the time delivered by the GPS clock, is also a very precise monitoring system for drifts between the AMANDA and the IceCube GPS clock.

The SPASE experiment was switched off, so the trigger is omitted.

The VME bridge modules in the TWR crates feature NIM outputs, which are accessible through VME. With feeding these NIM outputs and the incoming trigger signals into AND gates, the TWRDAQ software can block signals by switching the corresponding bridge output to logical FALSE. This way, the trigger logic is remotely controllable.

4.3.7 The Hardware Synchronization Scheme

The overall scheme is presented in Fig. 4.4. The GPS4TWR receives the GPS time over the optical fibers from the IceCube GPS clock in the ICL. The time offset due to the cable delay has to be measured and monitored. This offset has to be added to the AMANDA timestamps. In case of a failure during the signal transmission, the clock is switched to the AMANDA GPS clock in the MAPO. An 100 MHz clock signal is produced by the GPS4TWR and distributed to the TWR crates. The CLK2ECL modules in the crates transform the clock signal and deliver it to the TWRs over the crate backplanes.

When AMANDA receives a trigger signal, this signal is divided by the trigger logic and passed to the CLK2ECL modules in the TWR crates and to the GPS4TWR. All TWRs get the trigger signal, like the clock signal, over the backplanes. The DAQ readout is done like described in Sec. 3.2.2. Further on, the GPS4TWR is converting the electrical trigger signal to an optical one and sends it to the OPT2EL in the ICL. Here it is converted back to an electrical pulse, which is sampled by the TrigMB. The AMANDA mainboard is read out by the IceCube DAQ system. Dependent on the configuration of the system and the information about the type of the AMANDA trigger (↗ Sec. 4.3.8), the sampled trigger pulse stays in the IceCube data stream

and can be used to synchronize the corresponding AMANDA event to the IceCube data.

The 1PPS signal of one of the GPS clocks is used as SyncPulse. This signal is directly converted to optical by the GPS4TWR, and sent to the OPT2EL. The SyncMB samples the pulse and delivers the digital information into the IceCube data stream. As the SyncPulse is also used as a trigger for the TWRDAQ, several monitoring mechanisms are possible:

- If the other synchronization options fail (e.g. because of broken fibers), the timestamps of the AMANDA SyncPulse events and the AMANDA DOM mainboard, which samples the SyncPulse, can be used to keep up a basic synchronization. This provides a similar accuracy, but requires more capacities during the data merging process.

- The cabling and the electronics cause a delay of the SyncPulse, which is different from the delay of the 1PPS used in the two DAQs to define the beginning of a new second. If the SyncPulse is derived from the 1PPS signal of the IceCube clock, it is sent on a round trip to AMANDA and back to IceCube. The timestamp of the SyncPulse sample in IceCube has an offset to the beginning of the second, which has been defined by the 1PPS of the IceCube GPS clock shortly before. This offset includes the signal conversion, electrical processing in the different devices and the delay due to the transmission through the optical fibers between ICL and MAPO. Thus, it is a very precise measure for annual variations in the optical cable delay. If the clock source and the SyncPulse source differ in the GPS4TWR, these variations can also be measured with the TWRDAQ.*

- Depending on the GPS clock input of AMANDA, a drift between the two GPS clocks can be measured. E.g. if AMANDA runs on AMANDA GPS clock and the SyncPulse source is set to the IceCube GPS clock (Fig. 4.9), the timestamps of the SyncPulse events in AMANDA drift against the beginning of the new second, because the 1PPS signal from the IceCube GPS clock is not synchronized with the 1PPS signal of the AMANDA GPS clock.

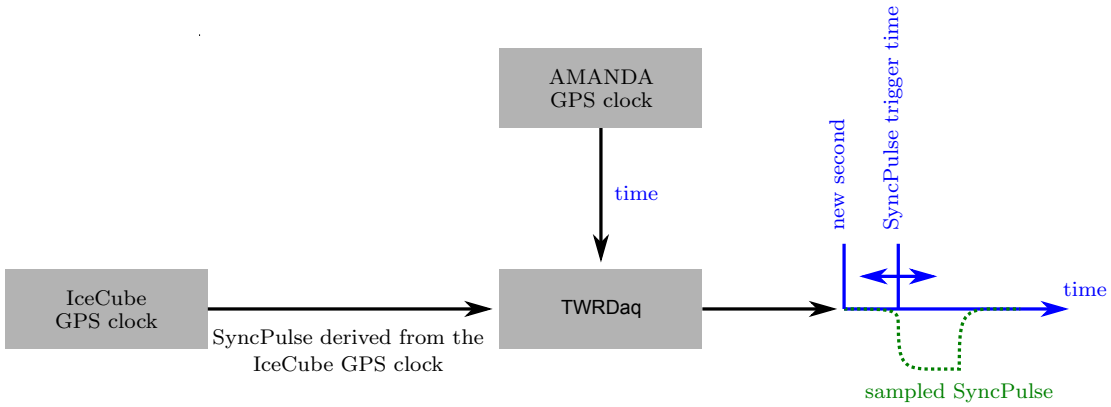

Fig. 4.9: SyncPulse Delay. Example of the SyncPulse delay between the beginning of a new second and the trigger time of the SyncPulse. Here TWRDAQ timing is done with the AMANDA GPS clock and the SyncPulse is derived from the IceCube GPS clock. The delay time may vary due to seasonal effects or a drift between the two GPS clocks.

*If the clock and the SyncPulse source are identical, in AMANDA time, there will be nearly no delay between them.

4.3.8 Software Changes

The software changes for the AMANDA/IceCube integration are not part of this thesis, but will be explained briefly anyway, to allow for a better understanding.

If the TWRDAQ is run in a standalone mode writing out its data for AMANDA only analyses, the necessary changes in the software to support the new hardware situation are marginal. Because of the new 100 MHz timestamping, the data protocol of the GPS4TWR is slightly different. Additionally, the access to the NIM outputs of the VME bridges has to be implemented.

For combined runs, the AMANDA event information has to be transmitted to IceCube. In standalone mode, AMANDA writes out data files, which contain about 10 min of data. IceCube is buffering data for about 30 s. For combined data taking, the output file size of AMANDA is reduced to about 2 s. A system called "*Joint Event Builder*" (*JEB*) grabs the AMANDA files over a standard Ethernet connection and builds merged AMANDA/IceCube events [GHR+07]. Before merging, IceCube needs some information about trigger time and trigger type (M18, string, ...) of the grabbed AMANDA events. Therefore, a software trigger payload with this information is sent to IceCube, every time AMANDA records a valid event [Seo05a]. Depending on the trigger payload, AMANDA events are merged into the IceCube data stream, or rejected.

Because of the cable length, the dispersion in the electrical AMANDA channels is very large. As a result, the waveforms are expanded. The TWR internal sampling rate of 100 MHz delivers a high redundancy for the dispersed electrical channels. Consequently, it is sufficient to store only every second waveform sample (Fig. 4.10). This modification can be part of the DAQ software or of the DSP program.

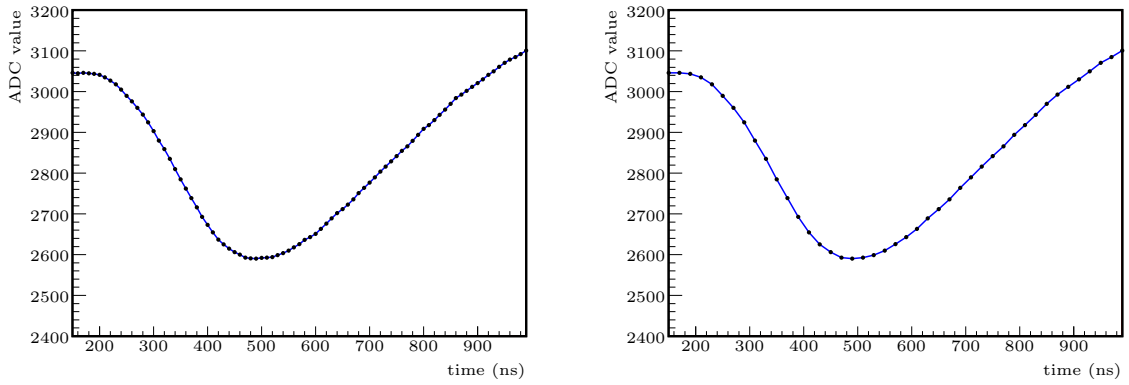

(a) 100 MHz (b) 50 MHz

Fig. 4.10: Sampling Rate Reduction. In both pictures the same waveform is displayed, but in the right one, every second sample is omitted. The reduction of the sampling rate does not affect the data quality.

4.3.9 DSP Software Improvement

The maximum data rate from the TWRs to the DSP in one crate is calculated in Eq. 3.2 to 50.78 $\frac{\text{MB}}{\text{s}}$. This limit is reached when triggering with the M13 multiplicity trigger. The VME data rate capacity is 320 $\frac{\text{MB}}{\text{s}}$ and therefore much more, than the expected maximum data rate. This makes the DSP (↗ Sec. 3.2.2) the bottleneck of the DAQ. A cross compiled program, written in a SHARC specific assembler code is controlling the TWR readout and the feature extraction.

As a part of the work for this thesis, the assambler code has been improved. To disburden the DSP, the sampling rate reduction is implemented into its program. Channels which shall be read

out with reduced sampling rate are marked in a configuration file (mainly all electrical channels). The DAQ software delivers this information to the six DSPs. During readout, the DSP searches for data from those channels and skips every second sample before further processing. Only after this data shortening, the feature extraction is done.

4.4 Synchronization Test System

Before bringing the AMANDA/IceCube integration system to the South Pole, it has to be tested. A realistic test setup is installed at the University of Wuppertal to verify all synchronization hardware components.

4.4.1 Test Hardware

The *Wuppertal Test Setup* provides

- a standard computer, equipped with a DSB and one DOR card, running IceCube DAQ software (TestDAQ),
- two IceCube DOM mainboards,
- a TWRDAQ, based on a standard computer with a PCI to VME bridge, and two bridged VME crates with TWRs and a GPS4TWR,
- OPT2EL cards,
- an ultra-cool freezer with a minimum temperature of $-86\,^{\circ}\mathrm{C}$ (SANYO MDF-492),
- a GPS clock (Symmetricom ExacTime 6000),
- 500 m optical cable (NEXANS UD-0425 1x8 G 62, 5/125 µm), containing 8 multimode fibers.
- a pulse and delay generator (Stanford Research Systems DG535) with an accuracy for the delay of 1500 ps + 25 ppm × delay regarding to the internal time $T0$ and 25 ppm × delay between two delayed outputs [Sta06],
- a 50 MHz frequency generator* (HP/Agilent 8116A) and
- a fast TDC (Caen V488).

By connecting the optical fibers, a fiber length of 4 km can be achieved. The optical fibers used are identical to the fibers connecting the MAPO to the ICL at the South Pole.

4.4.2 Components Test

Before starting measurements, the principle functionality of the synchronization components has to be proven. Therefore, a setup nearly identical to the system at the Pole is build up like in Fig. 4.4. The number of TWR crates is reduced to one and the triggering is done by the pulse generator.

This first test is successful. The AMANDA TWRDAQ reads and samples the trigger pulses, which are also given into some TWR channels. The fiber connection is working, and the timestamps read from the GPS4TWR are valid. The DOM mainboards are read out correctly by the TestDAQ system installed.

*The frequency generator is only used for the TDC linearity calibration

4.4.3 Measurements

For all delay measurements, the DG535 delay generator and the fast TDC are needed. With the setup displayed in Fig. 4.11, the small dynamic range of 90 ns of the TDC can be compensated. Type and length of the pulses, as well as the delay between the outputs are freely adjustable at the delay generator. Standard NIM level pulses with a length of 50 ns are used.

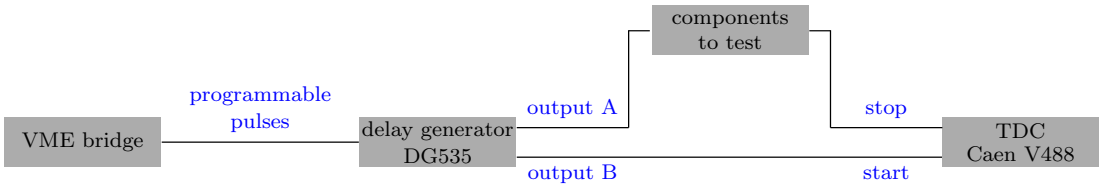

Fig. 4.11: Delay Test Setup. Depending on the components to test, the start and stop signal may have an offset exceeding the dynamic range of the TDC. In this case, output "B" of the DG535 can be delayed very precisely to match the time acceptance of the TDC.

Linearity of the TDC

Before using the TDC, the linear domain has to be found. Therefore, pulses with a period of 100 ns and a width of 50 ns from the DG535 are given onto one of the TDC channels. The time measurement is started by a VME bridge pulse. The bridge pulse initiated by a TDC readout program has a random phase relation to the DG535 pulses. The next following pulse from the DG535 after the start pulse from the bridge stops the TDC. The measured time between the two pulses is read out by the program and stored into a file.

Because of the random phase between start and stop pulse, the measured times are distributed uniformly. This is displayed in Fig. 4.12 for the Caen TDC used. Here, all measured random values are histogramed. The linear area lies between TDC bin 800 and 2200, corresponding to delays from about 18 ns to 40 ns. Outside this window, the TDC timebins do not have all the same size. The bin distribution for the entries in the linear area shows two Gaussian distributions.

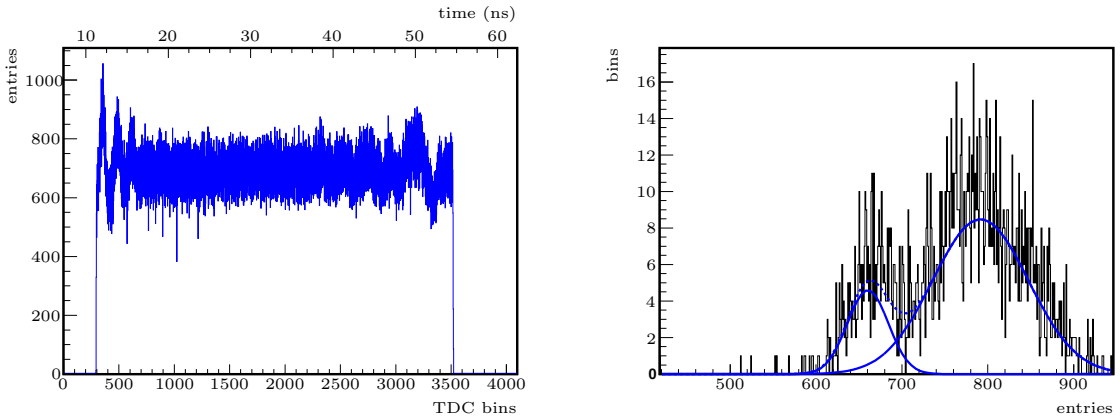

(a) Random Time Distribution

(b) Distribution of Bin Entries

Fig. 4.12: TDC Linearity Calibration. With starting and stopping pulses coming randomly, the linear area of a TDC can be found. A visual interpretation of the left picture shows a linear behavior in a range from bin 800 to bin 2200. In this range, the histogram of the bin entries results in two Gaussian distributions.

Expected is a single distribution. This corresponds to two different bin sizes with a ratio of $792 : 660 = 1.2$. 19 % of the bins belong to the smaller population. As the different bins are distributed uniformly over the complete linear range, it is assumed that the linearity is not violated significantly by the different bin sizes. Thus, this TDC property is ignored below.

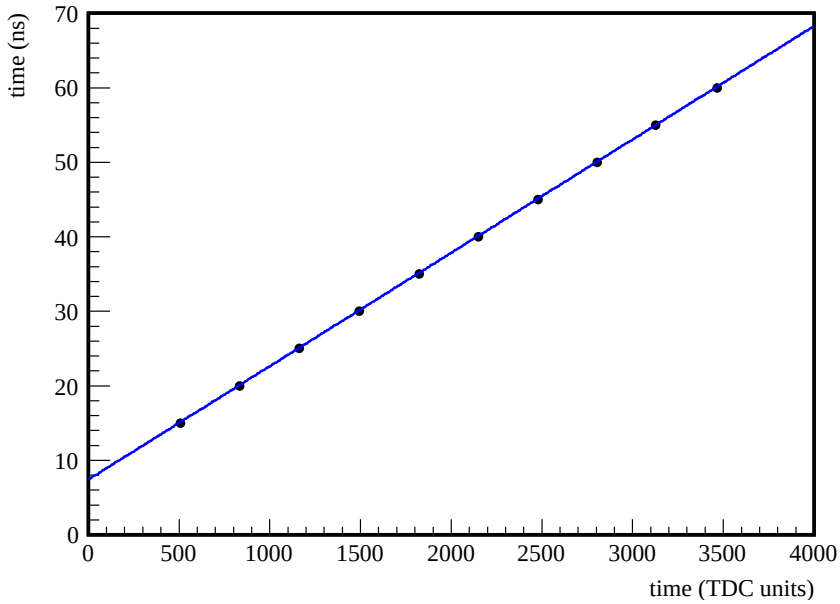

Fig. 4.13: TDC Units to Time Conversion. The errors are not visible at this resolution: $\sigma_{\mathrm{TDC}} \leq 3.1$ and $\sigma_{\mathrm{ns}} \leq 0.06\,\mathrm{ns}$.

Using the setup of Fig. 4.11 without any components and varying the delay between output A and B at the delay generator, the TDC bin to time conversion can be measured. From Fig. 4.13 the relation between the time in nanoseconds and the time in TDC units is derived to

$$t_{\mathrm{ns}} = (15.2199 \pm 0.0111)\ \frac{\mathrm{ps}}{\mathrm{bin}} \cdot t_{\mathrm{bins}} + (7282.35 \pm 23.86)\ \mathrm{ps}. \tag{4.1}$$

Below, the fixed offset is irrelevant because only relative delays are measured.

Cable Delay

For an initial measurement with the optical components, the "components to test" shown in Fig. 4.11 are replaced by the OPT2EL and a variable length of optical fibers. The electrical NIM pulse from the delay generator is fed into the 1PPS input of the OPT2EL. The outgoing light signal is transmitted through the fibers and applied to one of the optical inputs of the OPT2EL. The reconverted electrical signal stops the fast TDC. For every cable length, the delay generator has to be adjusted in a way that the time difference between the two pulses arriving at the TDC is matching its dynamic range. This fixed offset is always added to the result of the TDC time measurement (Fig. 4.14). From the relation of the cable length to the signal time

$$t(s_{\mathrm{cable}}) = (5.0521 \pm 0.0004)\ \frac{\mathrm{ns}}{\mathrm{m}} \cdot s_{\mathrm{cable}} + (90.5958 \pm 0.7380)\ \mathrm{ns} \tag{4.2}$$

a refraction index of 1.5146 ± 0.0001 for the used fiber and wavelength is derived. The fixed offset of about 91 ns is a result of the setup.*

*The internal delay for external trigger signals through the delay generator is already about 85 ns [Sta06].

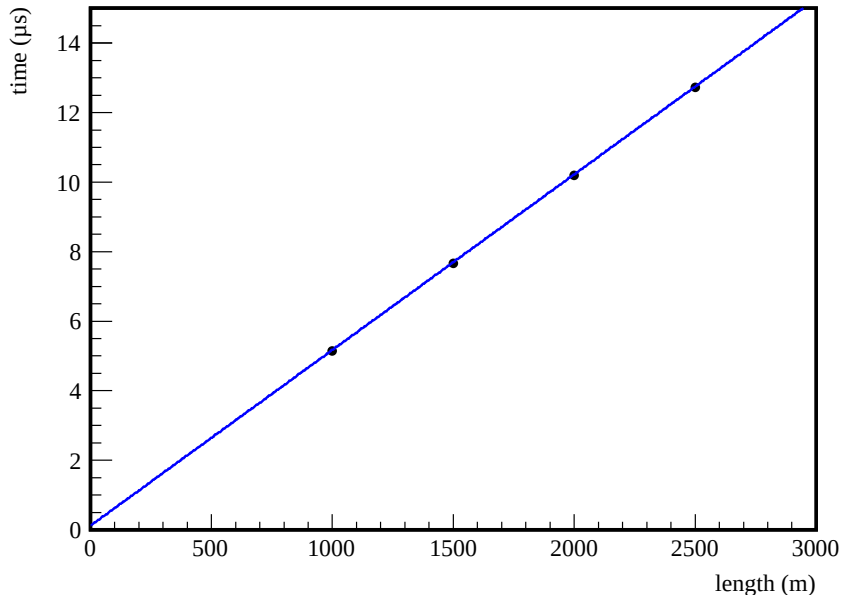

Fig. 4.14: Signal Delay Dependence on the Cable Length. The errors are not visible at this resolution: $\sigma_l \approx 1\,\mathrm{m}$ and $0.12\,\mathrm{ns} \leq \sigma_t \leq 0.70\,\mathrm{ns}$.

Temperature Dependence and Long Term Stability

The temperature deviations in the firn snow layer at a depth of 3 m, which is the estimated depth for cable deployments, can vary over a range of about 10 K [SGB01]. Additionally it is not clear, how the GPS4TWR and the OPT2EL react at a long term usage. To investigate this behavior and the temperature dependence of the signal delay in the optical cables, the "components to test" (Fig. 4.11) are changed to 500 m optical fiber placed inside the ultra-cool freezer. The tests are done over several hours in 10 min intervals. In every interval 10000 delays measurements are done. The measurement for a temperature of $-25\,^{\circ}\mathrm{C}$ is presented in Fig. 4.15. The RMS for every single 10000 delay measurement is not exceeding 0.25 ns. The histogram over every single measurement (Fig. 4.16) shows a strange behavior: The Gaussian distributed delay measurement is placed over a non defined underground. As this underground could not be ascribed to any properties of the used devices, it could not be eliminated. In the following, the peak position of the Gaussian fit function is used as measured value for the delay. To account for the non-Gaussian underground, the RMS of the distribution and not the sigma of the Gauss-fit is used as uncertainty of the measurements. The uncertainty of the temperature is set to a fixed value of $\pm 5\,\mathrm{K}$ because of the deviation during the heating up and cooling down cycles of the freezer. For the determination of the temperature dependence of the signal delay, the measurement for $-25\,^{\circ}\mathrm{C}$ is repeated for 6 further temperatures. The results are shown in Fig. 4.17. Within the needed accuracy, it is possible to fit the graph with a linear function:

$$\frac{\Delta t}{\Delta T \cdot s} = (97.14 \pm 7.65)\,\frac{\mathrm{ps}}{\mathrm{K} \cdot \mathrm{km}}, \tag{4.3}$$

with the delay change Δt, the temperature change ΔT and the length of the fiber s. This value is very low. Accordingly, at the Pole, it is not expected to see major deviations in the signal transmission times due to temperature variations.

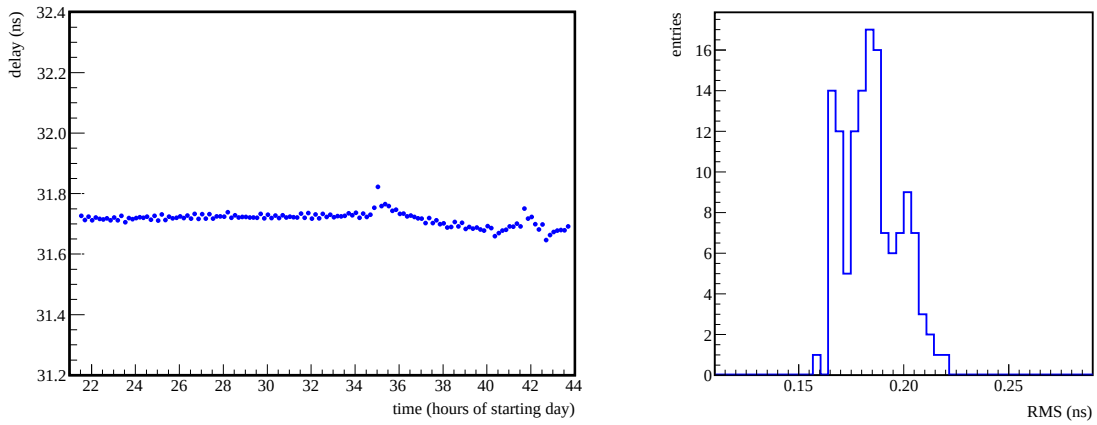

(a) Long Term Stability (b) RMS Histogram

Fig. 4.15: Long Term Delay Measurement of the signal delay over 500 m optical fiber at −25 °C. Left: Every dot represents the mean of 10000 single delay measurements. The larger variations in the delay time from hour 34 onwards is the influence of the air condition of the lab, which was switched on at that time. The RMS values for every dot vary in a range between about 0.16 ns to 0.23 ns. Right: Histogram with the RMS values of the delay distributions.

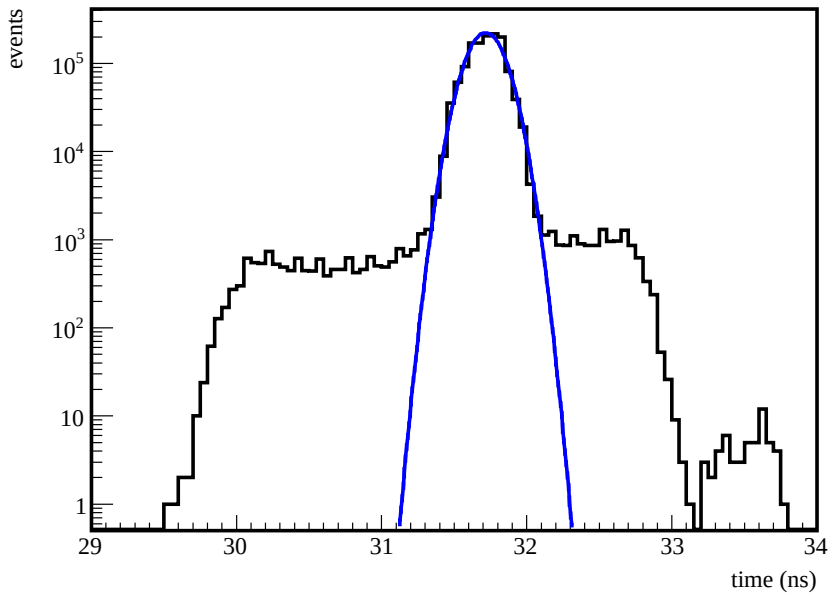

Fig. 4.16: Signal Delay Histogram for a fixed cable length of 500 m and temperature of −25 °C. The non-Gaussian background cannot be eliminated in the measurements. The Gaussian fit is used to determine the measured delay, the RMS of the complete distribution delivers the uncertainty of the measurement.

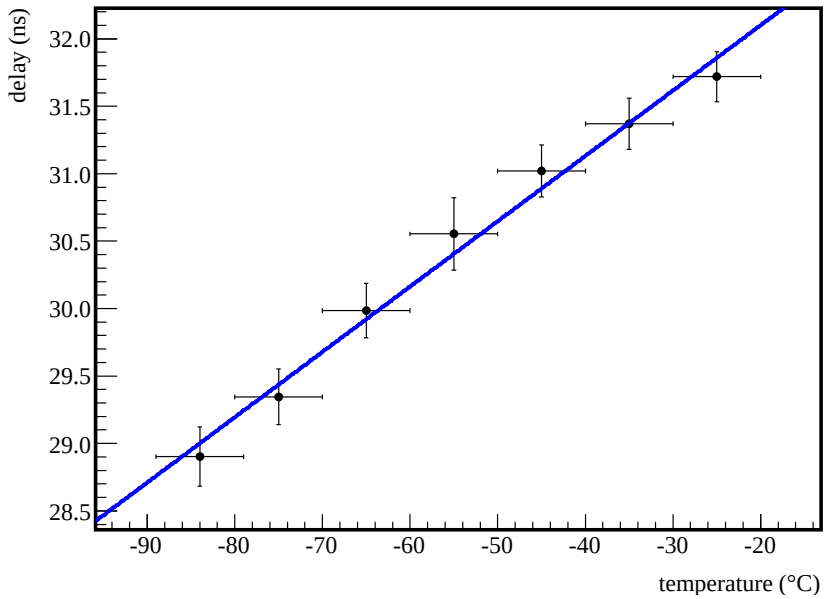

Fig. 4.17: Temperature Dependence of the Signal Delay. The cable length is 500 m.

4.5 Implementation at the South Pole

The implementation of the hardware integration system at the South Pole happened in several steps over three austral summer seasons.

4.5.1 Season 2005/06

The SyncCrate is installed in a DOMHub rack inside a *Temporary Counting House* (*TCH*). The fiber connection to the GPS4TWR is established. The GPS4TWR suffers from a hardware failure and has to be placed into an additional VME crate, which is not containing any other modules. AMANDA timestamping is still done with the GPS2VME, but all TWRs get the 100 MHz clock phase locked to the IceCube GPS clock from the GPS4TWR over new backplanes. The backup solutions, sending trigger signal and SyncPulse to IceCube, are working fine.

The running parts of the system are used, to verify the connection quality. Cable delay measurements are done with TestDAQ (↗ Sec. 4.6.2) and with an oszilloscope.

Status for austral winter 2006			
time stamps	GPS2VME (AMANDA GPS clock)		
100MHz	GPS4TWR (IceCube GPS clock) over new backplane		
AMANDA trigger	M24, M18, string, M13 pretrigger for volume and fragments trigger		
IceCube hardware trigger	AMANDA trigger signal and SyncPulse (only transmission)		
start 06 to Nov. 11th:	SyncPulse derived from IceCube GPS clock		
Nov. 11th to end 06:	SyncPulse derived from AMANDA GPS clock		
software trigger	not implemented, yet		
	line	t(ns)	σ_t(ns)
cable delays	trigger	3267.59	0.29
	SyncPulse	3267.59	0.29
	1pps	3282.46	0.40
	10MHz	3283.50	31.37
	IRIG-B	3282.42	0.39

4.5.2 Season 2006/07

The main GPS4TWR hardware problem is solved.* During TWRDAQ data taking, the GPS clock still cannot be received from the IceCube GPS clock. Directly after starting the TWRDAQ, the GPS4TWR switches from IceCube to AMANDA GPS clock. The TWRDAQ software is modified at the Pole to read out the GPS FIFO directly (not over the DSP) (↗ Sec. 3.2.3). Now the GPS4TWR operates in the master crate. This improves the overall stability of the TWRDAQ significantly, but does not solve the IceCube GPS time reception problem. The status information of the GPS4TWR identifies missing 1PPS signals as the source of clock failures, but the reason could not be found.

The SyncCrate is moved into the ICL. Consequently, the cable delays have to be measured again. The trigger signal and SyncPulse connection are now the most important synchronization systems.

The trigger logic for the TWRDAQ is upgraded (↗ Sec. 4.3.6).

The MuonDAQ is switched off. The trigger signals from the DMADD are still routed through the MuonDAQ trigger logic components.

The AMANDA software is changed to support the JEB system.

*The problem was an internal bad connection to an address line on the VME bus.

Status for austral winter 2007			
time stamps	GPS4TWR (directly switching from IceCube to AMANDA GPS clock)		
100MHz	GPS4TWR over backplane		
AMANDA trigger	M24, M18, string, M13 pretrigger for volume and fragments trigger		
IceCube hardware trigger	AMANDA trigger signal and SyncPulse (derived from IceCube GPS clock) triggering IceCube dependent on the software trigger information		
software trigger	AMANDA trigger payload information sent to IceCube		
	line	t(ns)	σ_t(ns)
cable delays	trigger	3175.25	0.33
	SyncPulse	3175.25	0.33
	1pps	3147.25	0.47
	10MHz	3147.25	0.47
	IRIG-B	3162.25	0.52

4.5.3 Season 2007/08

The GPS4TWR receives thick metal shielding and additional capacitors to remove noise from the power supply lines. It is still not working with the IceCube GPS clock signals. Running the GPS4TWR with the AMANDA GPS clock is now final state. The trigger signal and the SyncPulse deliver a sufficient synchronization for event merging and analysis.

After problems with the old MuonDAQ trigger logic during the austral winter 2007 all MuonDAQ trigger components are removed and the DMADD is connected directly to the TWRDAQ trigger logic.

A VME trigger logic board (TMB) is tested at the pole [Lai07].

The 50 MHz upgrade via DSP program modification is installed. The TWRDAQ can now handle simple trigger multiplicities down to M11. From an alternative point of view, the output file size reduction with M13 trigger multiplicity is about 30 %.*

After the implementetion of the integration upgrades of this season (November), major changes on the AMANDA trigger logic have been done (December/January ?). This is cannot be documented here as no information is available to the author. This makes the use of the TMB impossible for 2008.

*A higher value cannot be achieved. The optical channels, as well as the channels sampling the trigger signals cannot be read out with only 50 MHz, because they do not experience dispersion (↗ Sec. 3.2).

Status for austral winter 2008	
time stamps	GPS4TWR (directly switching from IceCube to AMANDA GPS clock)
100MHz	GPS4TWR over backplane
AMANDA trigger	M24, M18, string, M13 pretrigger for volume and fragments trigger (status before undocumented trigger modifications)
IceCube hardware trigger	AMANDA trigger and 1PPS signal triggering IceCube dependent on the software trigger information
software trigger	AMANDA trigger payload information sent to IceCube
cable delays	identical to 2007

4.6 Synchronization Verification

4.6.1 Absolute Cable Delay between MAPO and ICL

To obtain a value for the temporal offset between signals sent from AMANDA to IceCube, the transit time through the cable and conversion electronics has to be known. The connections

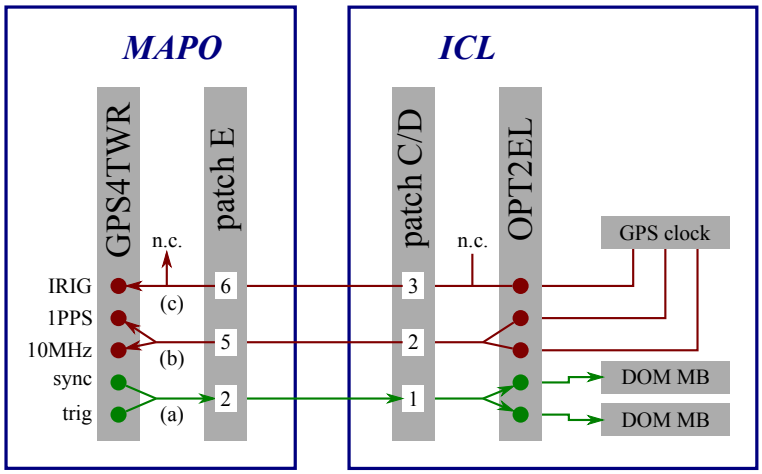

Fig. 4.18: Cabeling 2007. These optical fiber connections are used from 2007 onwards.

between MAPO and ICL after the beginning of 2007 are drawn in Fig. 4.18. The optical fiber structure between the MAPO and the ICL consists of three connections containing two fibers each. It is assumed that the delay in both fibers of each of the connections is identical. Using the OPT2EL in the ICL as "mirror" for signals coming from MAPO, the delay can be measured very precisely (Fig. 4.19). For the measurements, a Tektronix TDS 3054B oscilloscope upgraded with optional advanced analysis module is used. The module delivers statistics output to the measurements. The connections from the optical patch panel with the OPT2EL in the ICL are all identical. The cable lengths of the connections between the patch panel and the GPS4TWR

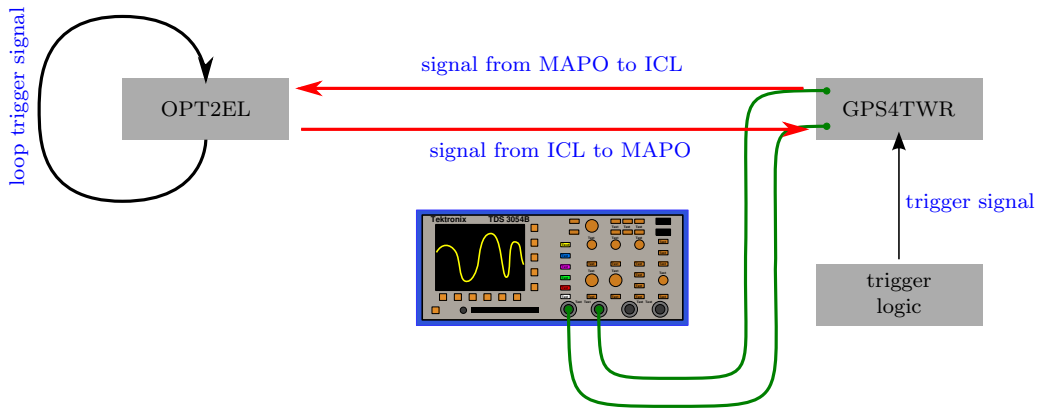

Fig. 4.19: Cable Delay Measurement at the Pole. To obtain a maximum symmetry on the two signal paths from and to the GPS4TWR, the signal delay is measured directly before/after the electrical/optical converters on the GPS4TWR circuit board with an oscilloscope.

in the MAPO are slightly different*. Every cable contains two optical fibers. Three different double fiber cables connect the GPS4TWR with the optical patch panel in the MAPO:

(a) SyncPulse / trigger signal,

(b) 1PPS / 10MHz and

(c) IRIG-B / not connected.

For the first three measurements, cable (a) is used. The delay in the electrical connection of the OPT2EL out- to input is (16.50 ± 0.25) ns. The measured delays are

connection†	round trip‡	one way§
E2 ⇌ C/D 1	(6376 ± 0.4) ns	(3175.3 ± 0.3) ns
E5 ⇌ C/D 2	(6339 ± 0.4) ns	(3161.3 ± 0.3) ns
E6 ⇌ C/D 3	(6368 ± 0.6) ns	(3175.8 ± 0.8) ns

To obtain the delay difference between the first and the other two cables in the MAPO, the first measurement is repeated with cable (b) and (c). The results for the delay differences are (b) (-14.0 ± 0.4) ns and (c) (-13.5 ± 0.4) ns. Accordingly, the cables (b) and (c) are shorter, than cable (a). The final delay values are given in Sec. 4.5.

4.6.2 Observation of the Synchronization Stability with TestDAQ

Besides normal IceCube operations, regular system testing is done. During this tests, the TestDAQ readout software is used. If the two AMANDA mainboards are included in these runs, the SyncPulse can be used, to monitor the precision of the fiber connection. Monitoring data is available for the year 2006 and the first half of 2007. The reception time of the SyncPulse in the SyncMB regarding to the beginning of the second is measured. Typically, the SyncPulse is derived from the IceCube GPS clock, but a few measurements at the end of 2006 are done with the AMANDA GPS clock as SyncPulse source.

*Optical fibers of that type with an appropriate length could not be obtained in Europe.
†These are the labels on the patch panel entries: E (MAPO), C/D (ICL).
‡The scope displays only 4 significant digits.
§The electrical delay for looping the signal at the OPT2EL is substracted.

The figures Fig. 4.20 to Fig. 4.24 show measurements done over several time periods. For every point in the graphs, the arrival times of many SyncPulses are averaged. The arrival time of one SyncPulse is the time from the beginning of a new second, as it is counted in the SyncMB, and the arrival of the SyncPulse in the SyncMB. The error bars correspond to the RMS of the arrival time distribution for one point (↗ Sec. 4.2). The color coding delivers the information about the number of single SyncPulses used for the calculation of one point.

The temperature data has been provided by [KHL+09]. All temperatures are are taken at the surface*, so a slight temporal drift is expected if there is a correlation between the temperatures and the SyncPulse delays. In case of temperature sensitive optical fibers, the bad heat conduction of the snowlayer covering the calbes has to be taken into account.

In the first months of 2006, only a few measurements with TestDAQ have been made. The times displayed in Fig. 4.20 show a negative gradient over the first 100 days of that year. It is possible that this is a temperature effect. The temperature data supports this assumption. The drift of only about 4 ns (Fig. 4.25(a)) is able to affect the synchronization quality.

In August 2006, the SyncPulse arrival time was measured more frequently. The mean arrival time was 6264.4 ± 0.4 ns. Fig. 4.25(b) shows the time distribution. Only a very small spread over less than 2 ns occurs within one month and a temperaure correlation is not visible.

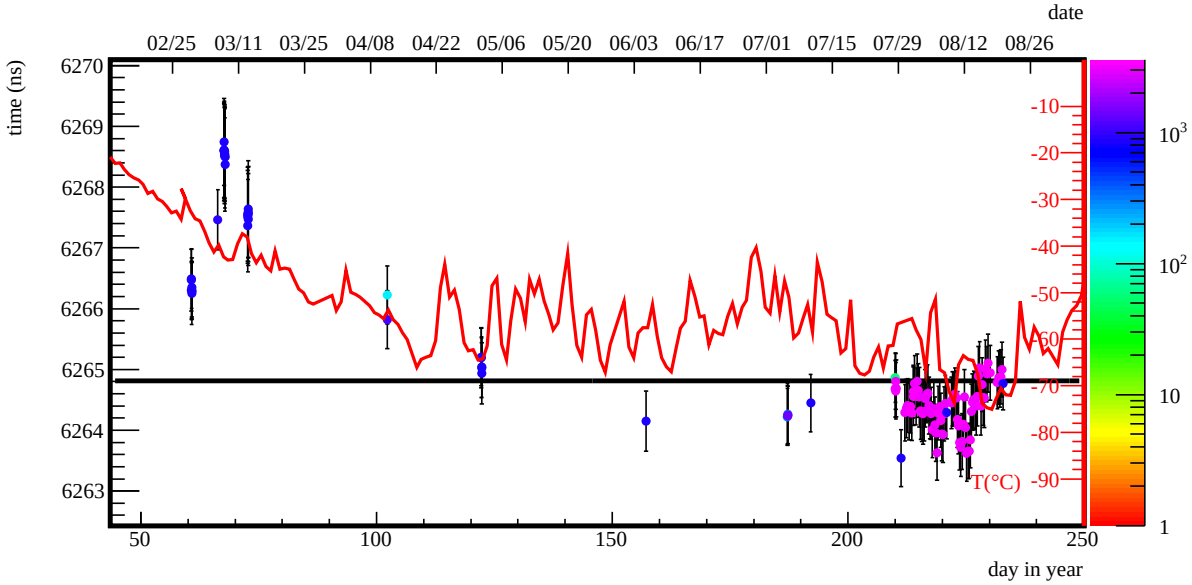

Fig. 4.20: TestDAQ Measurement of the cable delay, Feb.–Aug. 2006. SyncPulse source is the IceCube GPS clock. The color coding represents the number of single measurements for one point.

A firmware upgrade on the DOR cards in August 2006 leads to a different calculation of the absolute time for hits in the DOMs and the SyncPulse arrival time is shifted to 6289.0 ± 0.8 ns. In Fig. 4.22, the results of the time measurements till the end of 2006 are plotted. Here the temperature curve shows similar features like the changes in the delays. From this picture, a temperature dependence can be derived. However, the correlation cannot be found in 2007 (Fig. 4.24). Accordingly, it is very likely that it is a result of the special setup of 2006. In 2006 the IceCube surface hardware was installed in the TCH. It is possible that the small building did not provide a very good insulation. The measured temperature effect, therefore, might be the influence of changing temperatures on the electric integration components inside the TCH.

*The temperature station is located near the "Clean Air Sector" just beyond the new station building.

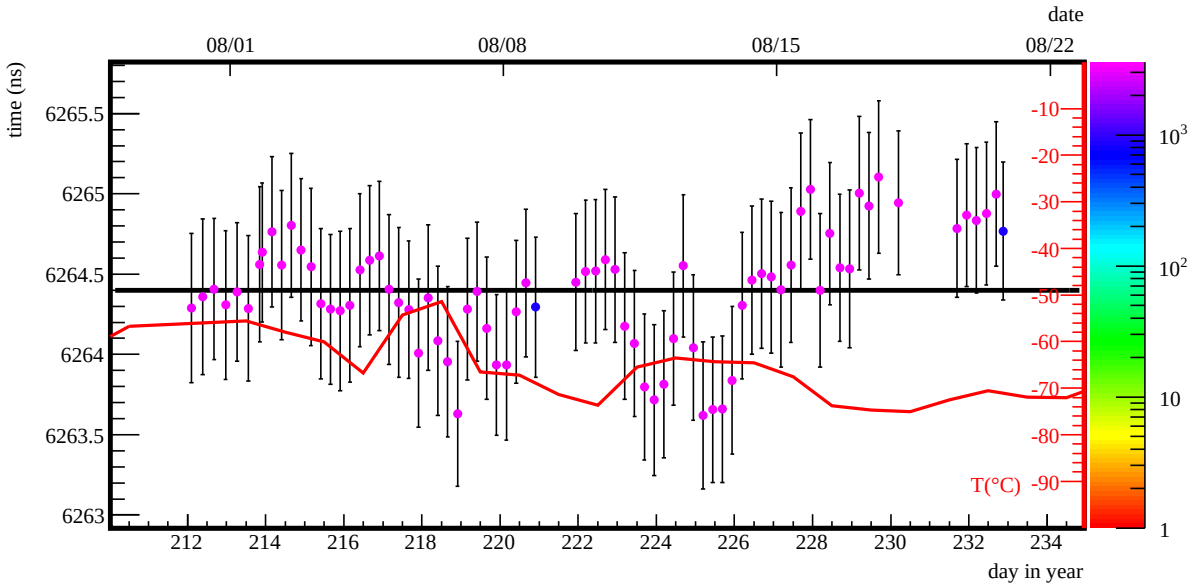

Fig. 4.21: TestDAQ Measurement of the cable delay, Aug. 2006. SyncPulse source is the IceCube GPS clock. The color coding represents the number of single measurements for one point.

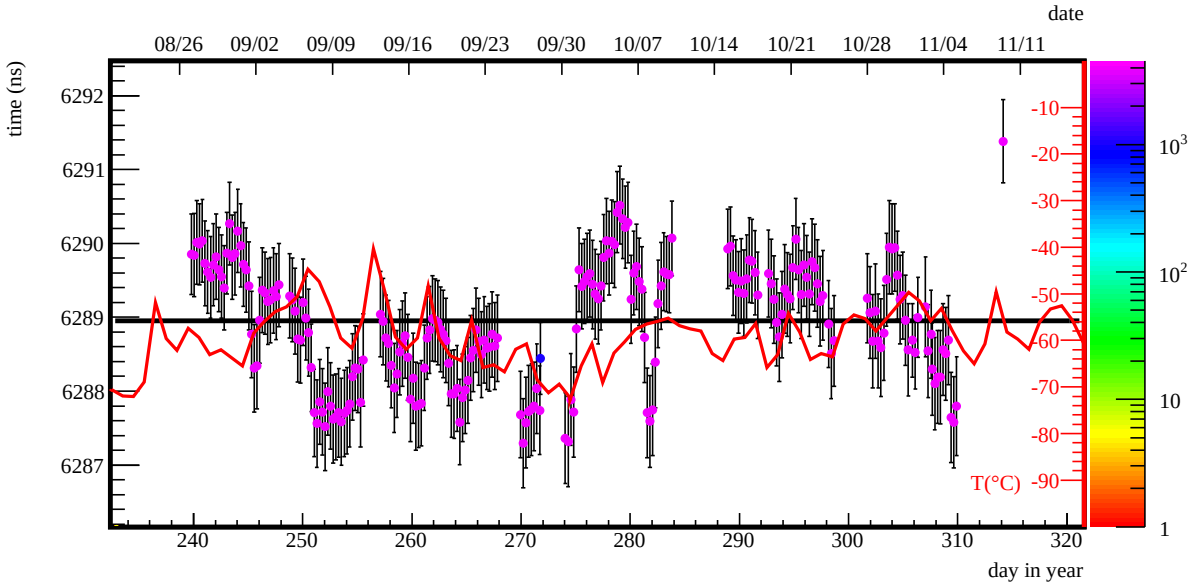

Fig. 4.22: TestDAQ Measurement of the cable delay, Sept.–Nov. 2006. The color coding represents the number of single measurements for one point.

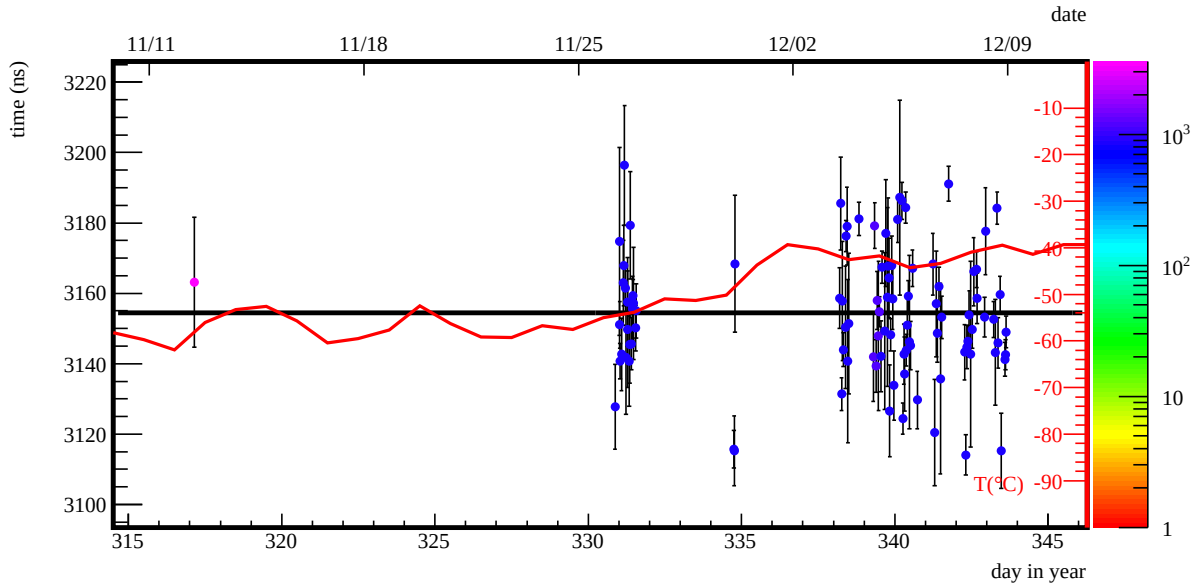

Fig. 4.23: TestDAQ Measurement of the cable delay, Nov. 2006, AMANDA GPS Clock is SyncPulse Source. The color coding represents the number of single measurements for one point.

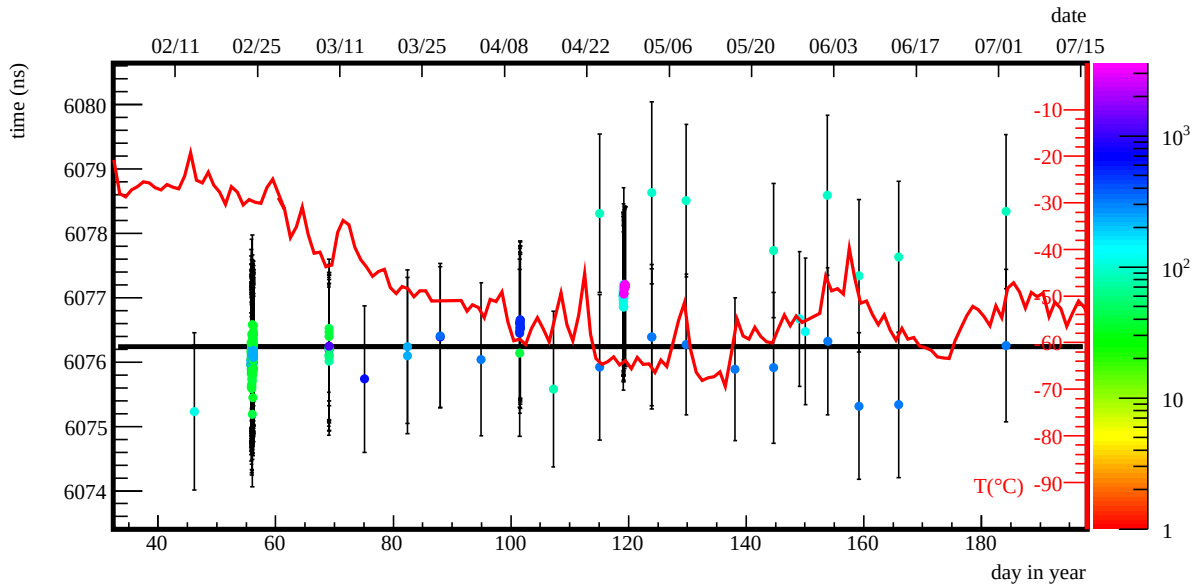

Fig. 4.24: TestDAQ Measurement of the cable delay, 2007. SyncPulse source is the IceCube GPS clock.

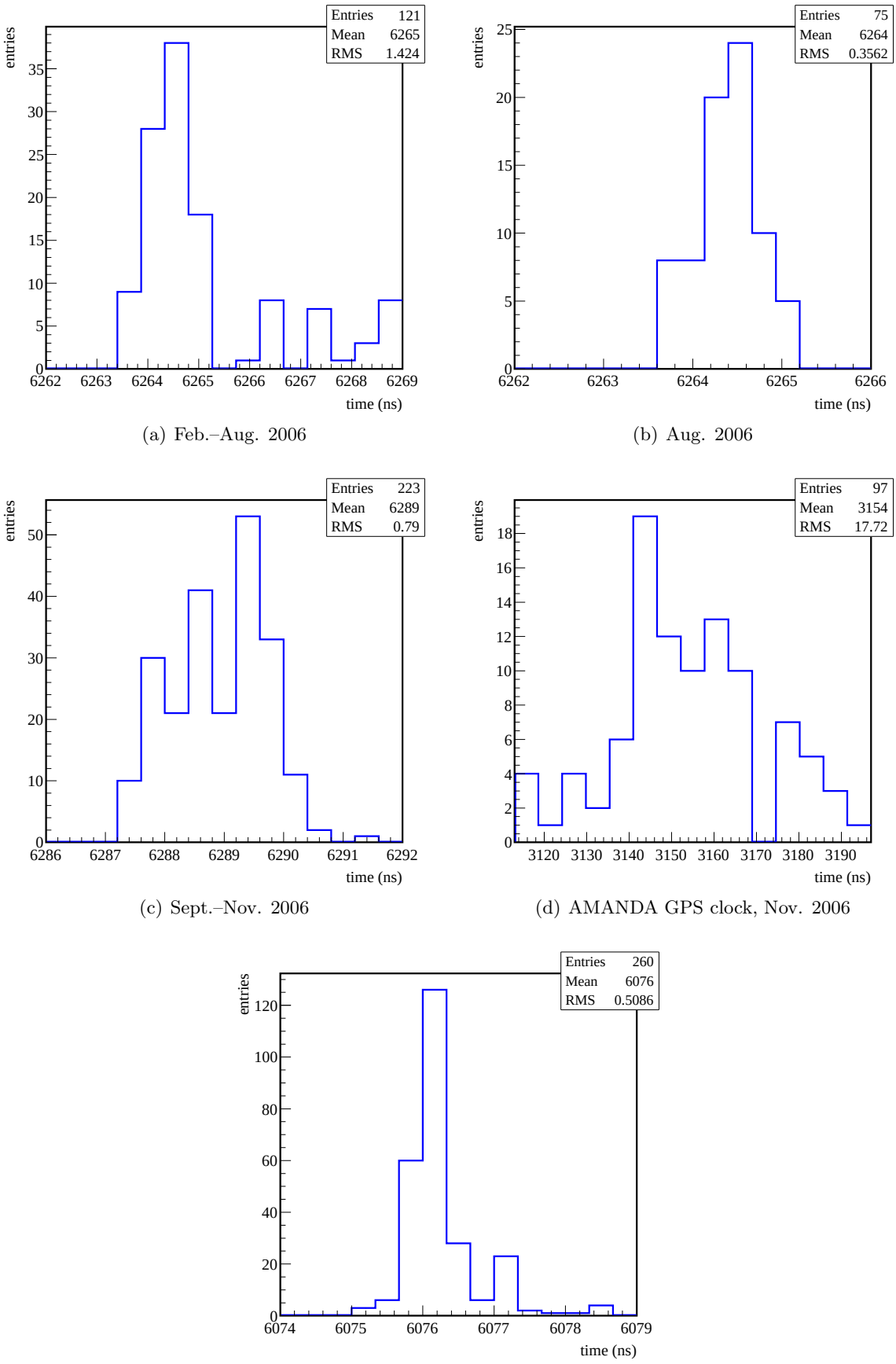

(a) Feb.–Aug. 2006

(b) Aug. 2006

(c) Sept.–Nov. 2006

(d) AMANDA GPS clock, Nov. 2006

(e) Jan.–Jul. 2007

Fig. 4.25: Cable Delay Distributions for the five different time periods with measurements done with the TestDAQ. The Distribution for 2007 contains only measurements after day 45.

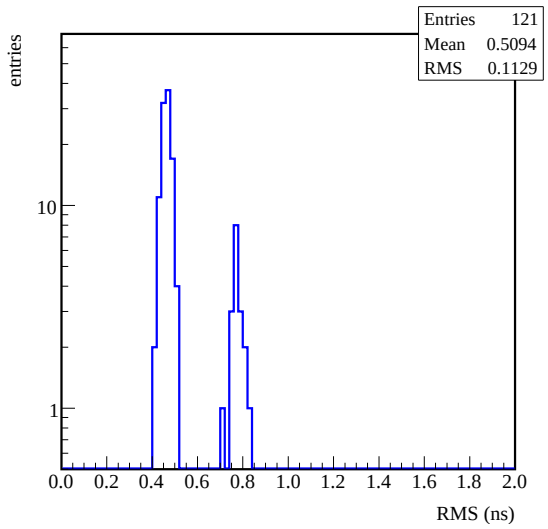

(a) Feb.–Aug. 2006

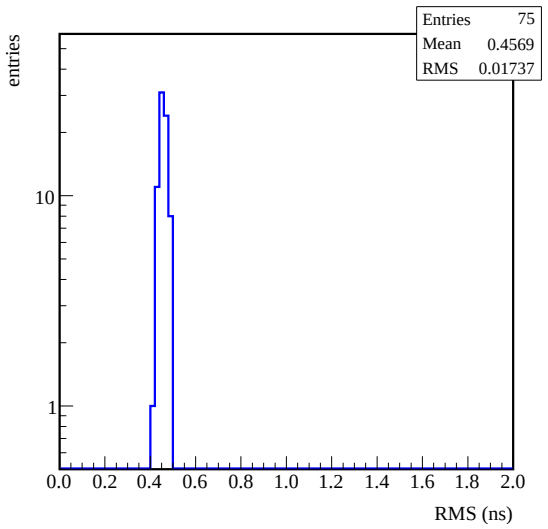

(b) Aug. 2006

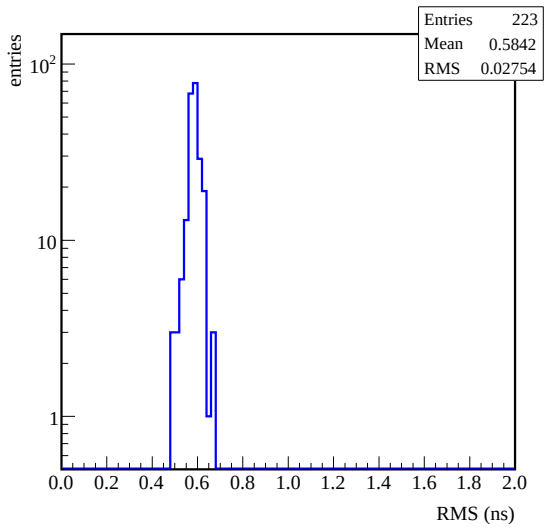

(c) Sept.–Nov. 2006

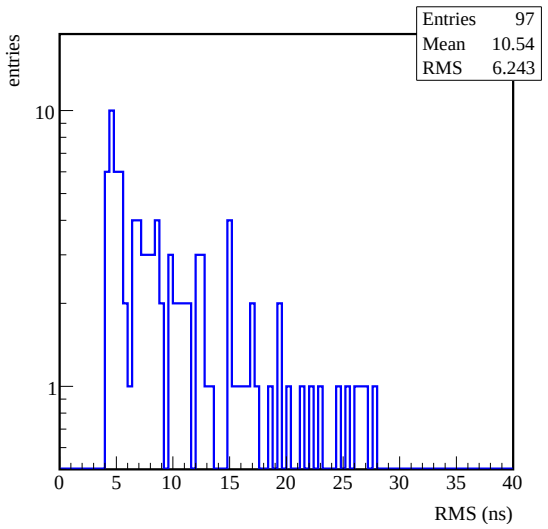

(d) AMANDA GPS clock, Nov. 2006

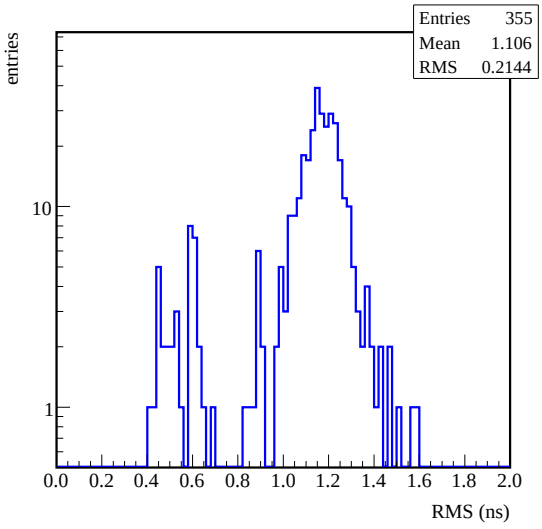

(e) Jan.–Jul. 2007

Fig. 4.26: RMS Values of the Single Cable Delay Measurements for the five different time periods for the measurements done with the TestDAQ software.

At the end of 2006, a few measurements with the AMANDA GPS clock as SyncPulse source have been taken (Fig. 4.23). The arrival time distribution for these measurements is much broader (Fig. 4.25(d)) than for measuring the SyncPulse with the source clock of the SyncPulse. The RMS of more than 17 ns is to high to fulfill the synchronization demands. This proves that running AMANDA and IceCube with two different GPS clocks does not allow for a synchronization of the two outgoing data streams. Only the transmission of the AMANDA trigger signal and its sampling in IceCube provides a sufficient accuracy.

For 2007, TestDAQ measurements are only available until July. The corresponding results are displayed in Fig. 4.24. The falling gradient in the beginning of 2007 is the result of ongoing work at the South Pole during the end of the season. From day 45 onwards, the SyncPulse arrival time stays stable at 6076.2 ± 0.5 ns. From end of April, some measurements done very soon after another show an offset between about 2.5 ns. This is the result of a slightly changed trigger threshold inside the SyncMB during those measurements. The threshold was 1.84 mV for the lower times and 25.01 mV for the higher times.

Fig. 4.26 shows the summed RMS distributions for each of the five measurement periods. In 2006 the RMS values do not exceed 1 ns. The values for the measurements with two GPS clocks are higher. This is the expected behavior and has no influence on the synchronization stability. In 2007, the RMS values slightly rise to values around 1.2 ns. The first peak in the 2007 plot between 0.4 ns and 0.7 ns belongs to the measurements done before day 45 of the year.

4.6.3 AMANDA/IceCube Synchronization Checker

The AMANDA/IceCube synchronization is also observed by the IceCube monitoring system. A special software module, the *AIChecker*, examines eight indicators for the synchronization quality, five of them on two different timescales:

histogram name	histogram description
AMATrigInfo	number and type of AMANDA triggers
AMATrigTimeDiff	time difference between two following AMANDA triggers
AMA1PPSTimeDiff*	time difference of two following SyncPulse triggers in the AMANDA data
AMA1PPSsecDiff*	time of a SyncPulse trigger in the AMANDA data regarding to the beginning of a new second
AMAIceTrigDiff*	TrigMB time minus AMANDA trigger time
TrigMBTimeDiff	time difference between two following triggers in the TrigMB
SyncMBTimeDiff*	time difference between two following triggers in the SyncMB
SyncMBsecDiff*	SyncMB hit time regarding to the beginning of a new second

The AIChecker is applied to already merged AMANDA/IceCube data. Consequently, it does not only detect irregularities in the hardware synchronization, but also all timing errors which have occurred during the merging process. Thus, the AIChecker is not a direct probe for the hardware stability, but delivers important information about the merged data quality.

Below, an example run* is taken, to explain the individual output histograms of the AIChecker. This example is a standard IceCube run and lasts 8 h = 28800 s.

*Two histograms with different temporal resolutions.
*Run 110789: Apr. 08, 2008

AMATrigInfo

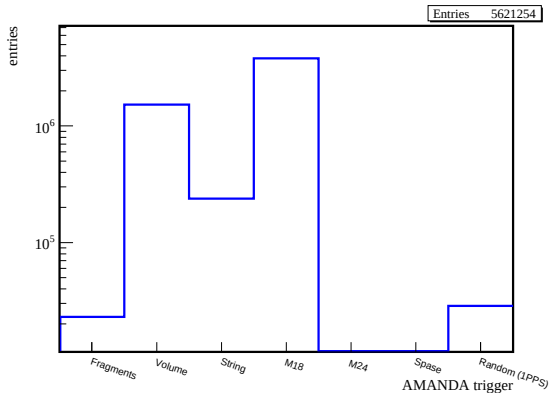

Fig. 4.27: AMATrigInfo Output.

The AMATrigInfo shows the sum of all AMANDA triggers. Events are not counted twice. The hierarchy is as follows:

(a) Laser2 (Secondary laser system, not used anymore.)

(b) Laser

(c) SyncPulse (Former random trigger.)

(d) SPASE (Switched off.)

(e) M24*

(f) M18

(g) String

(h) Volume

(i) Fragments

E.g. if an event is marked with M18 and string trigger, it will be counted as M18.

AMATrigTimeDiff & TrigMBTimeDiff

Here, the time difference of two following trigger signals is histogramed. An exponential distribution is expected. The number of AMANDA events is slightly higher, than the number of hits in the TrigMB. This follows from the different event time frames in AMANDA and IceCube. The IceCube event duration is 40 µs, whereas the AMANDA event duration is only 10.24 µs, defined by the readout window of the TWRs. Accordingly, more than one AMANDA event can be triggered in the time window of one IceCube event. In this case, the two AMANDA events are stored in the IceCube data stream. Up to now, the AIChecker is only counting the first TrigMB hit and ignores all following. This reduces the number of entries in the right plot.

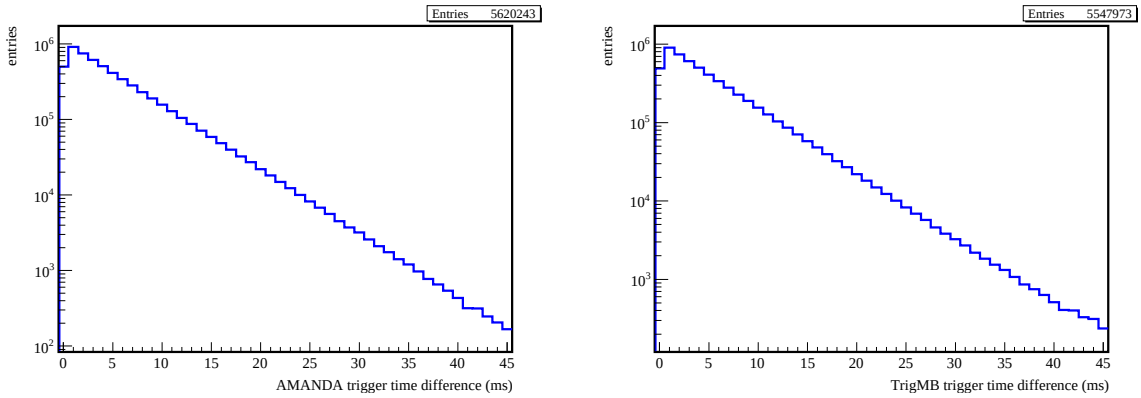

(a) AMATrigTimeDiff (b) TrigMBTimeDiff

Fig. 4.28: AMATrigTimeDiff & TrigMBTimeDiff Output.

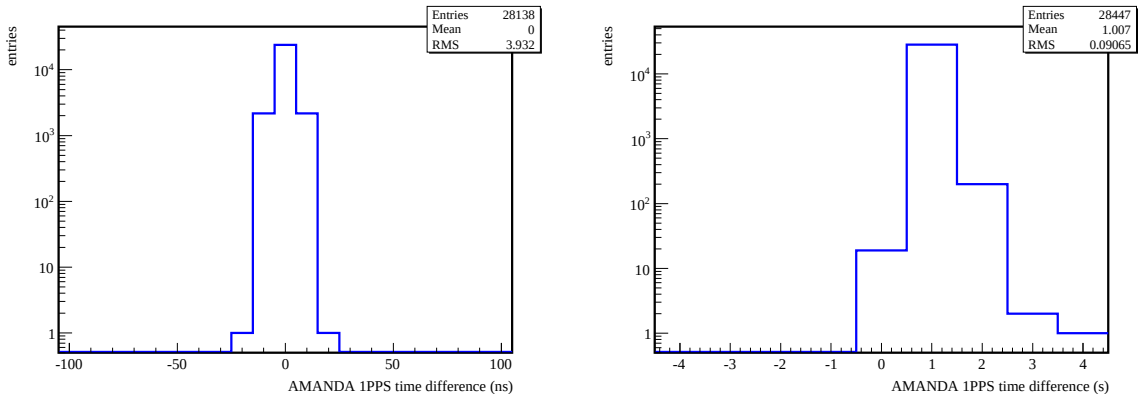

(a) High Resolution (b) Low Resolution

Fig. 4.29: AMA1PPSTimeDiff Output.

AMA1PPSTimeDiff

These two histograms display the time between two sequenced SyncPulse triggers in the AMANDA data. From the values in the high resolution histogram, one second is subtracted. In the left picture the high accuracy of the pulse transmission is visible. An RMS of 5.3 ns falls clearly below the demand of 10 ns.

The low time resolution histogram allows for the conclusion that not all SyncPulses are triggered and sometimes more than the regular SyncPulses lead to a trigger. In the 2008 runs, the SyncPulse source is the IceCube GPS clock. A possible loss of 1PPS signals from the IceCube GPS clock to the GPS4TWR was already mentioned in Sec. 4.5. There are strong evidences that the loss is happening inside the GPS4TWR itself, but this could never be verified. The additional pulses with a time difference smaller than 1 s have to be noise. This number of about 20 time differences has to be divided by two, to get the number of wrong SyncPulse events,* and can be neglected.

Because of the well defined, small window for the SyncPulse time difference, it is possible, to

*Not active in 2008 data because the IceCube software is not capable of handling two multiplicity triggers in the same AMANDA event.

*There is one time difference from a correct SyncPulse to the faulty pulse and one time difference to the next SyncPulse.

sort out noise pulses. SyncPulses from the IceCube GPS clock which are not recognized by the GPS4TWR are a problem for using the GPS4TWR with the IceCube GPS clock. But, as the GPS4TWR is running with the AMANDA GPS clock, this does not affect the TWRDAQ data taking. For the synchronization quality, the loss of about 1 % of the SyncPulses is not critical because the event merging is done by searching for TrigMB hits corresponding to AMANDA triggers.

SyncMBTimeDiff

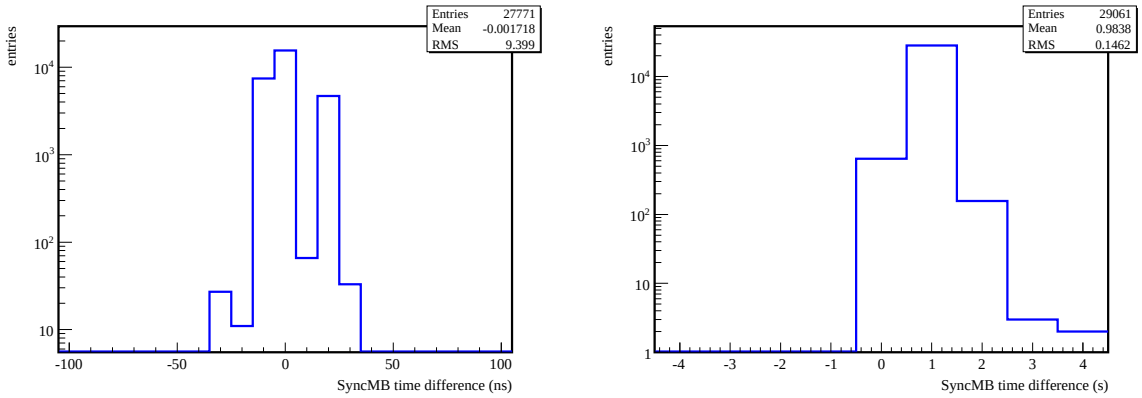

(a) High Resolution (b) Low Resolution

Fig. 4.30: SyncMBTimeDiff Output.

The SyncMBTimeDiff histograms are produced the same way, as the AMA1PPSTimeDiff histograms, but with the time differences of subsequent hits of the SyncMB.

Obviously, more noise events are seen in the SyncMB (entries in bin "0" of Fig. 4.30(b)). This is an effect of the arrangement of the two AMANDA DOM mainboards. In the SyncCrate, they are mounted closely together. Sometimes, this causes crosstalk between the TrigMB and SyncMB. Because a signal in the TrigMB corresponds to an AMANDA event, which is read out, also the two AMANDA mainboards are read out and the SyncMB crosstalk signal stays in the data stream. To quantify the amount of crosstalk, the SyncMBsecDiff histograms (below) can be used.

The crosstalk itself is not lowering the synchronization quality. As explained above, the TrigMB information is more important for the event merging. For the TrigMB, crosstalk from the SyncMB to the TrigMB is not critical, because the TrigMB is also getting a trigger signal (SyncPulse trigger) from AMANDA, every time a SyncPulse is sent.

SyncMBsecDiff

These two histograms show the difference of an incoming SyncPulse signal regarding to the beginning of the second. Dependent on intermediate delays, the SyncPulse, which is derived from the 1PPS signal of a GPS clock, is arriving at a time which is later than the beginning of the second (Fig. 4.9). In 2008, the SyncPulse source is the IceCube GPS clock. Consequently, the SyncPulse is sent to the GPS4TWR in the MAPO and sent back to the ICL, where it is sampled in the SyncMB. The beginning of the second is defined by the 1PPS, which is arriving at the DSB in the AMANDA DOMHub much earlier. The mean time of 6034 ns, derived from the high temporal resolution histogram, corresponds to about the doubled signal transit time between ICL and MAPO.

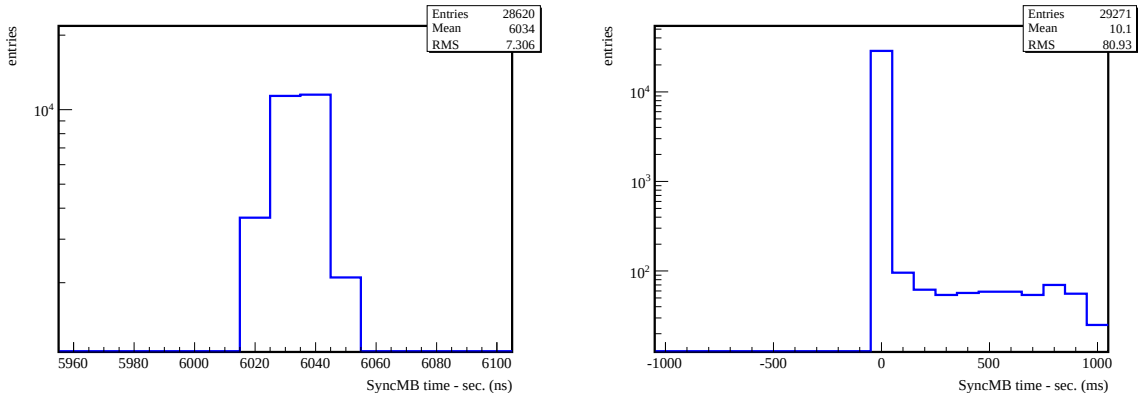

(a) High Resolution (b) Low Resolution

Fig. 4.31: SyncMBsecDiff Output.

The tail to the right side in the low resolution histogram reflects the crosstalk already mentioned above. Regarding to the beginning of the second, only positive entries are possible. Because of the well defined expectation value of the arrival time, the crosstalk samples are easy to identify and to reject.

AMA1PPSsecDiff

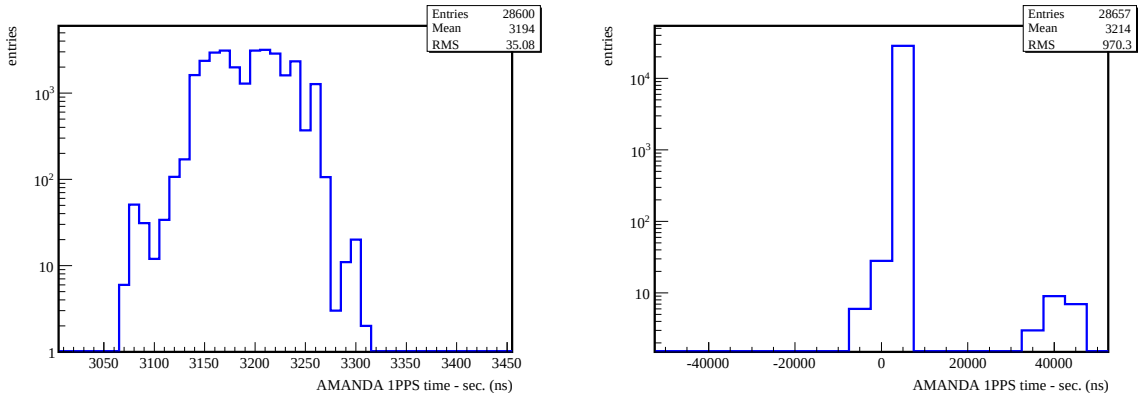

(a) High Resolution (b) Low Resolution

Fig. 4.32: AMA1PPSsecDiff Output.

For the AMANDA data samples, the same analysis as for the SyncMB is possible. The distribution of arrival times regarding to the beginning of the second is broader in the high resolution histogram. This follows from the use of independent GPS clocks. The SyncPulse is derived from the IceCube GPS clock and the beginning of the second is defined by the 1PPS signal of the AMANDA GPS clock. The drift between the two GPS clocks is widening the distribution.

Currently, there is no explanation for the hits around 40 µs seen in the low resolution plot.

AMAIceTrigDiff

The AMAIceTrigDiff histogram is a very good measure for the overall synchronization and data merging quality. If a merged AMANDA/IceCube event is found, the AMANDA TWRDAQ time

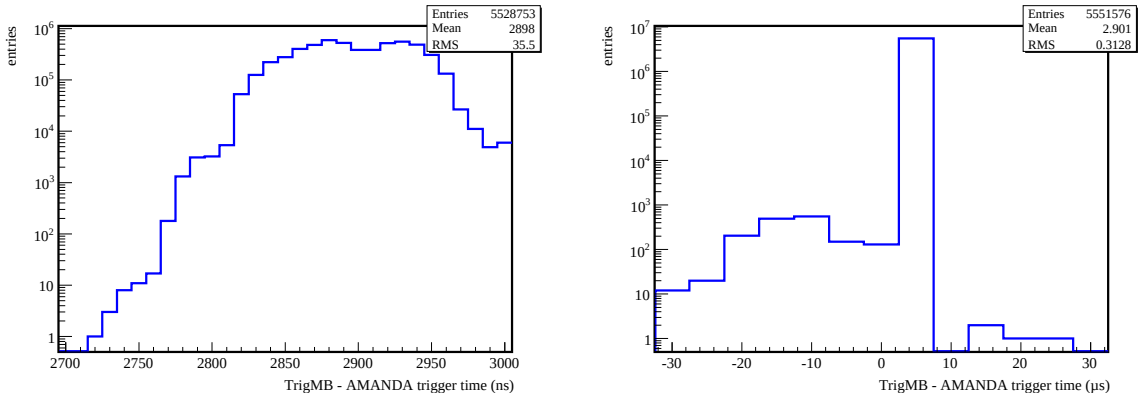

(a) High Resolution (b) Low Resolution

Fig. 4.33: AMAIceTrigDiff Output.

is compared to the IceCube event time. There is no narrow distribution expected, as the trigger building is dependent on the event geometry in AMANDA and IceCube. Accordingly, in the same event the time difference between the two trigger times may differ from event to event. If events are not merged correctly, the offset between the two trigger times is changing. This is visible in the low resolution histogram plot.

4.7 Results

In parallel to the development of the AMANDA/IceCube integration system, many working groups inside the IceCube collaboration have worked on the offline part of the integration. This includes simulation studies about the combined detector performance as well as the development of offline analysis tools, which are able to interprete the taken data. The available *combined data* for the IceCube-22 configuration of 2007 is about 143 days [RGO+09] and about 301 days for IceCube-40 in 2008. This is a very good success of the AMANDA/IceCube hardware integration. Currently, some interesting papers are on the way. A few examples of the ongoing work are given in the next subsections.

4.7.1 Simulation Studies

For the IceCube-22 configuration of 2007 with 22 strings deployed, the effective area for the detection of atmospheric neutrinos has been determined using Monte Carlo simulations [GHR+07]. Within the simulation the muon neutrino channel has been used. The results include all events that pass the online filter level. It is clearly visible (Fig. 4.34(a)) that the combination of AMANDA and IceCube increases the effective area especially for low energy neutrinos. The result is even more notable comparing the resulting expected atmospheric neutrino rate in the detector (Fig. 4.34(b)). Here an increase in the detection rate of about a factor of 10 in the low energy region between 10 GeV and 100 GeV can be observed.

4.7.2 Combined Analysis

An example for the analysis of combined data is given in [RGO+09]. In TeV γ-astronomy many sources with steep energy spectra and low cutoff energies are known. The accelleration mechanisms can be hadronic (↗Sec. 2.2.2) and, consequently, these souces are interresting for

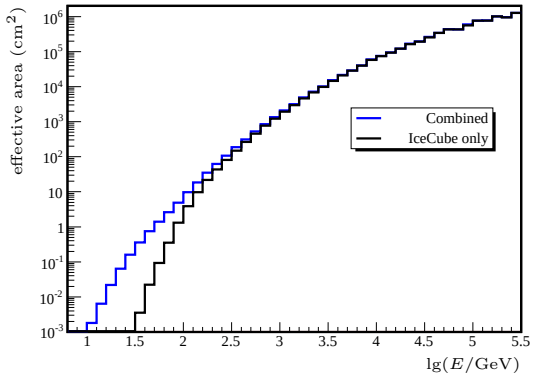

(a) Effective Area for Atmospheric Neutrinos

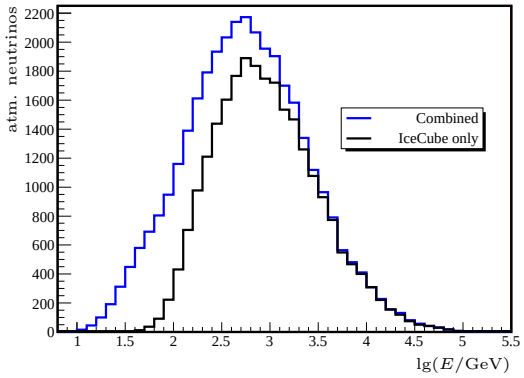

(b) Atmospheric Neutrinos for a Run Period of 200 Days

Fig. 4.34: Effective Area for the Combined AMANDA/IceCube Detector and the expected atmospheric neutrino rates. The simulation is done for AMANDA/IceCube-22. Image: [Res09]

a low energy neutrino detector. The higher sensitivity of a combined detector for events with lower energy directly results in a higher sensitivity for steeper spectra (Fig. 4.35).

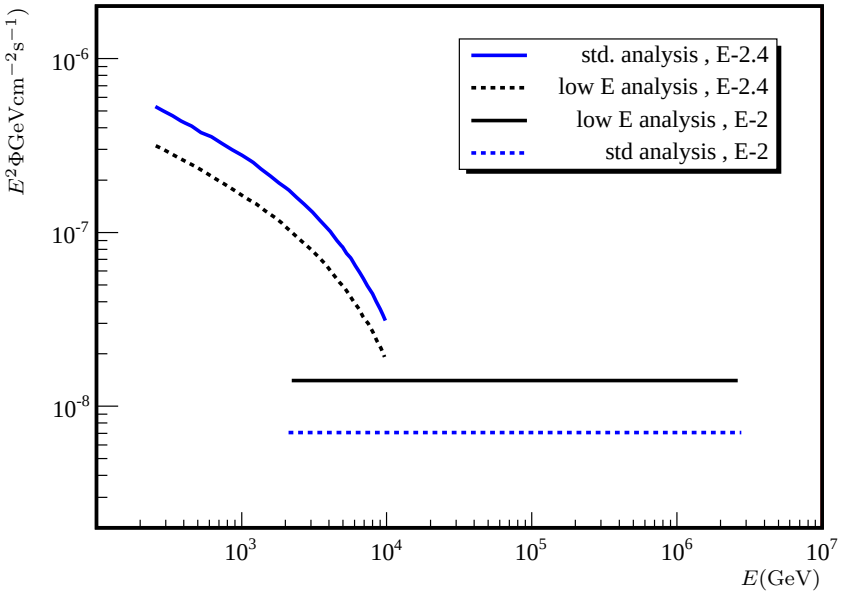

Fig. 4.35: Sensitivity for Low Energy Events of IceCube-22 and AMANDA combined with IceCube-22. For a neutrino flux following a steeper energy spectrum, the combined analysis yields an improved sensitivity. Image: [RGO+09]

In the analysis, four possible high energy neutrino sources have been chosen. Two of them will be discussed here: The crab nebula with an estimated neutrino energy spectrum of

$$\Phi = 3 \times 10^{-7} e^{-E/7TeV} \left(\frac{E}{\text{GeV}} \right)^{-2.4} \text{GeVcm}^{-2}\text{s}^{-1} \tag{4.4}$$

under the hypothesis of hadrons as γ-ray source and Cassiopeia A with an expected neutrino

spectrum of

$$\Phi \propto E^{-2.4}. \tag{4.5}$$

In the data of the combined neutrino detectors, no signal from these sources could be found. So an upper limit on the neutrino flux can be set. The results are given in Fig. 4.36.

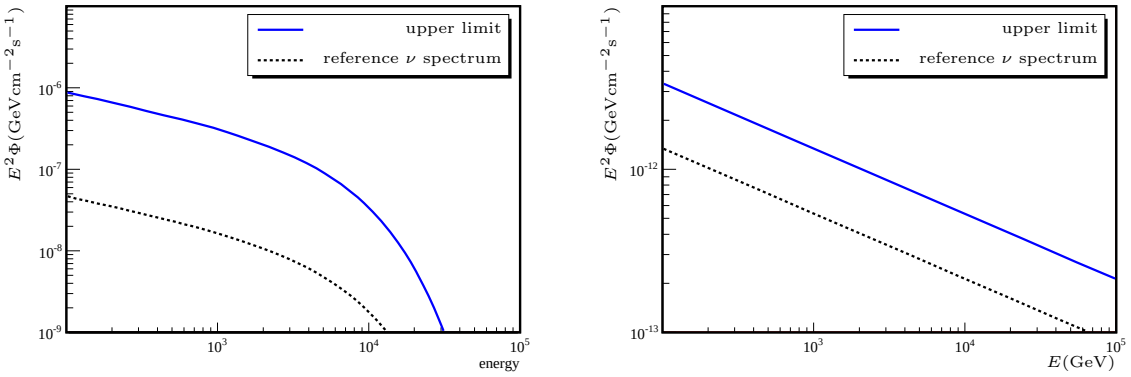

(a) Crab Nebula (b) Cassiopeia A

Fig. 4.36: Neutrino Flux Limits of a Combined Analysis for two possible neutrino sources. Image: [RGO+09]

4.7.3 The Future AMANDA: IceCube Deep Core

The first results of the combined detector have already proven the usefullness of a low energy array within IceCube. Even if the integration of AMANDA into IceCube is a success, several disadvantages cannot be eliminated:

- The local position of the AMANDA detector within IceCube disadvantageous. It is surrounded by only one layer of IceCube strings on one side (Fig. 4.1) and, additionally, inside the top area of IceCube. This makes the veto function of IceCube (↗Sec. 4.1.2) inefficient.
- The AMANDA data is, because of the different hardware, slightly different from IceCube data. This makes combined analyses more difficult.

To remove these disadvantages, a new low energy extension in the bottom middle of the full IceCube detection volume will be installed. This extension is called Deep Core (Fig. 3.16) and consists of 6 strings supporting 60 DOMs each [Res09]. The spacing between the Deep Core strings and the surrounding IceCube strings is 72 m compared to 125 m between the other IceCube strings. The DOM spacing along every Deep Core string is 7 m and for all other IceCube strings 17 m.

Besides avoiding the already mentioned disadvantages of the AMANDA array, a few additional features are provided by Deep Core:

- Due to its deeper position below the ice surface, the shielding against atmospheric muons is improved.
- The ice properties in greater depths are better. It is more transperent, which implies less scattering.

Deep Core will be a condign successor of the AMANDA neutrino telescope. AMANDA has been shut down on Monday, May 11th, 2009 at 3:11am UTC.

Part II

Searching SUSY Matter with IceCube

5

Supersymmetry

The first part of this thesis describes the more technical aspect of working with large detector systems like AMANDA and IceCube. In the second part, the usage of IceCube for doing physics is highlighted. The response on several input signals for detectors of the size and the complexity of a neutrino telescope, cannot be understood by starting at first principles. Only the simulation of known scenarios and the comparison with real data allows for a correct data analysis.

In Chapter 8, a tool for searching supersymmetric particles with IceCube will be introduced. The production of the necessary simulation data is part of this development and will be described in detail in Chapter 7. A very brief explanation of the possible background is given in Chapter 6.

5.1 Why Supersymmetry?

In the last forty years, the standard model of particle physics has been very successful describing many physical phenomena theoretically. Nevertheless, many questions are still open and these questions call for physics beyond the SM. For energies of the order of the Planck mass

$$m_P = \sqrt{\frac{\hbar c}{G}} \approx 1.2 \times 10^{19}\,\mathrm{GeV}, \quad G\text{: gravitational constant}, \tag{5.1}$$

currently no physics model exists. In this energy region, the Compton wavelength of a particle becomes comparable to its Schwarzschild radius.

Some of the open questions are:

- Hierarchy: Why is the Planck mass so large compared to the weak breaking scale? With m_Z, the mass of the Z-boson, one finds

$$\frac{m_Z}{m_P} \approx 10^{-17}. \tag{5.2}$$

- Why do neutrinos have masses? The SM without any further extensions cannot explain neutrinos with masses.

- The radiation corrections to the scalar squared Higgs mass are of the order of Λ_{UV}^2, where Λ_{UV} is an ultraviolet momentum cutoff regulating the loop integral in the corresponding Feynman diagram. As Λ_{UV} is unknown, it should be chosen as at least the energy scale at which new physics becomes important. A natural choice for Λ_{UV} is $\mathcal{O}(m_P)$. The electroweak theory is asking for a Higgs mass of $m_H = \mathcal{O}(m_W)$. The free parameters for calculating the radiation corrections to the Higgs mass have to be set in a way that the corrections nearly eliminate. Why should the parameters in nature be chosen in a way that the large radiation corrections all cancel out?

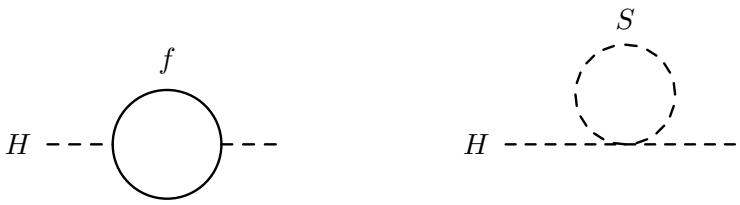

(a) Dirac Fermion f (b) Scalar S

Fig. 5.1: Feynman Diagrams for One-Loop Quantum Corrections to the Higgs squared mass parameter.

For the SM Higgs field the neutral part is a complex scalar H, which has a classical potential

$$V = m_H^2 |H|^2 + \lambda |H|^4 . \tag{5.3}$$

If the Higgs field couples to a Dirac fermion, the corresponding one-loop quantum correction to the situation in Fig. 5.1(a) for the squared mass parameter is

$$\Delta m_H^2 = -\frac{|\lambda_f|^2}{8\pi^2}\Lambda_{\mathrm{UV}}^2 + \cdots \tag{5.4}$$

In case of f is a quark of the SM, Eq. 5.4 has to be multiplied by three to account for the three colors. A heavy complex scalar particle S contributes to the m_H^2 one-loop corrections (Fig. 5.1(b)) as

$$\Delta m_H^2 = -\frac{\lambda_S}{16\pi^2}\left[\Lambda_{\mathrm{UV}}^2 - 2m_S^2 \ln(\frac{\Lambda_{\mathrm{UV}}}{m_S}) + \cdots\right]. \tag{5.5}$$

The comparison of the equations 5.4 and 5.5 shows that the quadratic terms in the mass corrections can cancel out if every fermion state is accompanied by a corresponding scalar [KM82]. For every fermion two scalars are necessary.

5.2 Concept of Supersymmetry

The *supersymmetric theory* (*SUSY*) answers some of the open questions by allocating every SM particle a corresponding supersymmetric particle. The *superpartner* of a SM fermion is a SUSY boson and vice versa. The link between bosonic and fermionic states is the SUSY generator Q:

$$Q\,|\mathrm{Boson}\rangle = |\mathrm{Fermion}\rangle \qquad Q\,|\mathrm{Fermion}\rangle = |\mathrm{Boson}\rangle\,. \tag{5.6}$$

Q is an anticommuting, fermionic spinor and $Q^\dagger$ is also a supersymmetry generator. When N is the number of SUSY generators Q, for simplicity only $N = 1$ supersymmetry is considered here.

Both generators have to satisfy the relations [Mar08; HLS75; CM67]

$$\{Q_\alpha, Q^\dagger_{\dot\alpha}\} = -2\sigma_{\alpha\dot\alpha\mu}P^\mu \tag{5.7a}$$
$$\{Q_\alpha, Q_\beta\} = \{Q^\dagger_{\dot\alpha}, Q^\dagger_{\dot\beta}\} = 0 \tag{5.7b}$$
$$[Q_\alpha, P^\mu] = [Q^\dagger_{\dot\alpha}, P^\mu] = 0. \tag{5.7c}$$

P^μ is the four-component relativistic momentum vector and σ^μ a four-component vector of the Pauli matrices (Eq. 2.4). α and β are the indices of two component Weyl spinors and can have the values 1 and 2. The undotted index indicates a left-handed and the dotted index a right-handed Weyl spinor.

With the transition between bosons and fermions, an irreducible representation of this SUSY algebra, the so called *supermultiplet*, consists of superpartner fermionic and bosonic states. Members of one supermultiplet can be transformed into each other by using combinations of Q and $Q^\dagger$.

Because Q and $Q^\dagger$ commute with P^μ, it also commutes with the squared mass operator $-P^2$. Consequently, all members of one supermultiplet have the same masses. The two SUSY generators also commute with the generators of the SM gauge transformations from which follows that particles of the same supermultiplet have to have the same degrees of freedom in electric and color charge, as well as in weak isospin.

To derive a more general conclusion about the degrees of freedom within a supermultiplet, the operator $(-1)^{2s}$ can be introduced. s is the spin of the particle. The eigenvalue of $(-1)^{2s}$ is -1 when acting on a fermionic and $+1$ when acting on a bosonic state. $|i\rangle$ are the states with the same eigenvalue p^μ of the operator P^μ in a given supermultiplet. According to relation 5.7c, there exist a completeness relation $\sum_i |i\rangle\langle i| = \mathbb{1}$ regarding to Q and P^μ within this subspace. With the help of the completeness relation and the equations 5.7a to 5.7c it can be shown that

$$\sum_i \langle i| (-1)^{2s} P^\mu |i\rangle = 0. \tag{5.8}$$

Using additionally

$$\sum_i \langle i| (-1)^{2s} P^\mu |i\rangle = p^\mu \operatorname{Tr}[(-1)^{2s}] \propto n_B - n_f, \tag{5.9}$$

for the bosonic and fermionic degrees of freedom n_B and n_f follows

$$n_B = n_f \tag{5.10}$$

for a given $p^\mu \neq 0$ within a supermultiplet.

A supermultiplet containing a Weyl fermion (↗2.1), which has $n_f = 2$, must contain two real scalars, which have $n_B = 1$. These scalars can be combined to a complex scalar field. Because of the handedness of the Weyl fermion, supermultiplets of this kind are called *chiral multiplets**. This way, every SM fermion can be allocated a scalar superpartner. The superpartner has the same symbol like the fermion, but carries an additional tilde. The name of the *scalar fermion* is *sfermion* (slepton, squark). E.g., the left-handed electron e_L has the *selectron* $\tilde{e}_L$ as a superpartner. The scalar field has no handedness (spin = 0)! The index L illustrates the handedness of the Weyl fermion of the supermultiplet. Left-handed and right-handed Weyl fermions transform differently in the $SU(2)_L$ group. Therefore, the chiral multiplets with index L are combined to $SU(2)_L$ doublets according to the three families. The chiral multiplets with index R are $SU(2)_L$ singlets.

*Other names are matter or scalar supermultiplets.

The next-to-simplest supermultiplet contains a (massless) spin-1 vector boson. Because of its two helicity states, $n_B = 2$. The superpartner is a (massless) spin-1/2 Weyl fermion. These supermultiplets are called *gauge multiplets* or vector multiplets. The superpartners to the gauge vector bosons carry the ending "-ino". E.g., the *gaugino* to the $W-$ and $B-$bosons are called *winos* and *binos*. Gauge bosons have to transform as their adjoined representations in the gauge group and their superpartners must also. From this follows that the gauginos have the same transformation properties for left- and right-handed components and a further subclassification as for the scalar multiplets is not needed. The spin-2 graviton has a spin-3/2 superpartner, the *gravitino*.

The scalar Higgs boson obviously has to reside in a chiral multiplet, but there is a problem concerning gauge anomalies if there is only one Higgs. One condition for the cancellation of gauge anomalies is [Mar08]

$$\mathrm{Tr}[T_3^2 Y_W] = \mathrm{Tr}[Y_W^3] = 0. \tag{5.11}$$

T_3 is the third component of the weak isospin and Y_W the weak hypercharge. The electric charge can be calculated by

$$Q_{em} = T_3 + Y. \tag{5.12}$$

The traces sum over all left-handed Weyl fermionic degrees of freedom in the theory.

The fermionic superpartner to the Higgs boson carries $Y = 1/2$ or $Y = -1/2$ and builds up a $SU(2)_L$ doublet with $T_3 = 1/2$ and $T_3 = -1/2$. If there is only one Higgs supermultiplet with either $Y = 1/2$ or $Y = -1/2$, Eq. 5.11 cannot be fulfilled since all SM contributions cancel out. The introduction of two Higgs supermultiplets, one for each weak hypercharge solves this problem. Consequently, the $SU(2)_L$ doublet $(\tilde{H}_u^+ \ \tilde{H}_u^0)$ with the charges +1 and 0 form the superpartners to $(H_u^+ \ H_u^0)$, and the $SU(2)_L$ doublet $(\tilde{H}_d^0 \ \tilde{H}_d^-)$ with the charges 0 and −1 form the superpartners to $(H_d^0 \ H_d^-)^*$. The charges are composed according to equation 5.12. The SM Higgs boson is a linear combination of H_u^0 and H_d^0.

Table 5.1 delivers a complete picture over all particles that have been introduced above. All supermultiplets of table 5.1 form the particle content of the so called *Minimal Supersymmetric Standard Model* (*MSSM*).

A special neutral SUSY particle, the *neutralino*, is supposed to be a linear combination of the neutral Higgsinos ($\tilde{H}_u^0$, $\tilde{H}_d^0$) and neutral gauginos ($\tilde{W}^0$, $\tilde{B}^0$). Accordingly, the *chargino* is a composition of $\tilde{H}_u^+$, $\tilde{H}_d^-$ and the two winos $\tilde{W}^\pm$.

In an unbroken SUSY theory, all particle masses in one supermultiplet have to be identical. In this case, SUSY matter already would have been discovered. Currently, no particles exceeding the SM particle spectrum have been found. Therefore, if SUSY is describing nature, it is a broken symmetry and the masses of the SM particle superpartners is higher than the available energy in todays particle collider experiments.

5.3 SUSYs in IceCube

Even if in MSSM the amount of particle types is fixed, many other parameters are variable. On the other hand, several requirements have to be fulfilled to detect SUSY particles with the IceCube detector:

- Only particles that are stable enough to arrive at and to traverse the detector can be seen by IceCube. This sets limits on the necessary mean lifetime.

*The indices are chosen, because the different Higgs fields give mass to either the up-type, or the down-type quarks and the charged leptons.

name	symbol	spin 0	spin 1/2
quarks & squarks	Q_1	$(\tilde{u}_L\ \tilde{d}_L)$	$(u_L\ d_L)$
	Q_2	$(\tilde{c}_L\ \tilde{s}_L)$	$(c_L\ s_L)$
	Q_3	$(\tilde{t}_L\ \tilde{b}_L)$	$(t_L\ b_L)$
	$\bar{u}$	$\tilde{u}_R^*$	$u_R^\dagger$
	$\bar{d}$	$\tilde{d}_R^*$	$d_R^\dagger$
	$\bar{c}$	$\tilde{c}_R^*$	$c_R^\dagger$
	$\bar{s}$	$\tilde{s}_R^*$	$s_R^\dagger$
	$\bar{t}$	$\tilde{t}_R^*$	$t_R^\dagger$
	$\bar{b}$	$\tilde{b}_R^*$	$b_R^\dagger$
fermions & sfermions	L_1	$(\tilde{\nu}_e\ \tilde{e}_L)$	$(\nu_e\ e_L)$
	L_2	$(\tilde{\nu}_\mu\ \tilde{\mu}_L)$	$(\nu_\mu\ \mu_L)$
	L_3	$(\tilde{\nu}_\tau\ \tilde{\tau}_L)$	$(\nu_\tau\ \tau_L)$
	$\bar{e}$	$\tilde{e}_R^*$	$e_R^\dagger$
	$\bar{\mu}$	$\tilde{\mu}_R^*$	$\mu_R^\dagger$
	$\bar{\tau}$	$\tilde{\tau}_R^*$	$\tau_R^\dagger$
Higgs & Higgsinos	H_u	$(H_u^+\ H_u^0)$	$(\tilde{H}_u^+\ \tilde{H}_u^0)$
	H_d	$(H_d^0\ H_d^-)$	$(\tilde{H}_d^0\ \tilde{H}_d^-)$
name		spin 1	spin 1/2
gluon & gluino		g	$\tilde{g}$
W bosons & winos		$W^\pm\ W^0$	$\tilde{W}^\pm\ \tilde{W}^0$
B boson & bino		B^0	$\tilde{B}^0$

Tab. 5.1: Particles of the MSSM. By convention only left handed Weyl fermions are displayed. Consequently, the conjugated of the right-handed Weyl fermions appear in this table.

- The interaction cross section of the SUSY particles with SM particles has to be small enough to avoid absorption inside the Earth.
- The SUSY particles have to be charged because only particles interacting electromagnetically produce Čerenkov light in ice.
- The expected event signature from SUSY particles inside the detector has to be discriminable from those of SM particles.

There are several SUSY models predicting scenarios which satisfy these demands. Consequently, it is useful to search for SUSY matter inside IceCube. Below, short descriptions, in which way some models harmonize with the requirements, will be given.

R-Parity

None of the possible renormalizable terms of the SM Lagrangian violates the baryon B or lepton number L conservation [Ait07]. But, as a consequence of very small non-perturbative electroweak effects, at very high energies B and L can be violated, which might have been relevant at the very early universe.

Supersymmetry, however, allows renormalizable B and L violating terms in the superpotential. The existence of such couplings would enable decay channels for the proton, e.g. $e^+\pi^0$ or $\mu^+\pi^0$. As proton decay has not been observed so far, strict limits on the strengths of the corresponding couplings are set.

The explanation for the very small or non-existent B and L violating terms in the superpotential can be given with an additional parity, the R-parity

$$R = (-1)^{3B+L+2s}, \tag{5.13}$$

where s is the spin of the particle. Every SM particle has $R = 1$ while all SM superpartners carry the R-parity $R = -1$. R is multiplicatively conserved. This enforces even numbers of SUSY particles at every vertex in Feynman diagrams.

R-parity conservation leads to a set of interesting consequences:

- The *lightest supersymmetric particle* (*LSP*) has to be stable.
- The production of SUSY particles in SM particle interactions is only possible in pairs.

This second R-parity consequence is interesting for the SUSY particle detection in IceCube. Due to the high boost, SUSY particles, produced in high energy SM matter interactions inside the Earth (e.g. from cosmic ray neutrinos with a nucleon), would be emitted from the interaction point along two nearly parallel trajectories. For charged particles, a double track signature inside the detector is expected.

5.3.1 SUSY Mass Scales

Without further assumptions it is difficult or even not possible to construct SUSY breaking Lagrangians. Many current SUSY models, therefore, include hidden sectors, which do not interact or interact only very weakly with the visible sector in which, for example, the particles of the MSSM exist. Two theories are very popular: Gravity-mediated SUSY breaking, also called *Minimal Supergravity* (*mSUGRA*) [Nie81], and *Gauge-Mediated SUSY Breaking* (*GMSB*) [GR99].

In mSUGRA, SUSY breaking is introduced by gravity or physics in the region of the Planck scale. In this models, the gravitino is a heavy particle.

More interesting with respect to SUSY detection in IceCube are GMSB models. Here, SUSY breaking is done via new chiral supermultiplets, called *messengers* that couple to the hidden sector, the source of SUSY breaking, and to the particles in the visible sector. These messengers have a vacuum expectation value (VEV) $\langle F \rangle$, which also defines the breaking scale for SUSY. The expected value for $\langle F \rangle$ would be

$$\sqrt{\langle F \rangle} \approx 10^4 \ - \ 10^9 \,\mathrm{GeV}. \tag{5.14}$$

In GMSB, the *Lightest Supersymmetric Particle* (*LSP*) is the gravitino $\tilde{G}$. Provided that R-parity is conserved, all supersymmetric particle decay series will end in the gravitino. The mass of the gravitino is given by [DDRT96]

$$m_{\tilde{G}} = \frac{\langle F \rangle}{\sqrt{3} m_P} \approx \left(\frac{\sqrt{\langle F \rangle}}{100\,\mathrm{TeV}} \right)^2 \cdot 2.5\,\mathrm{eV}. \tag{5.15}$$

The *Next to Lightest Supersymmetric Particle* (*NLSP*) will decay into the gravitino and the corresponding SM particle to the NLSP via

$$\mathrm{NLSP} \longrightarrow \tilde{G} + \text{corresponding SM particle} \tag{5.16}$$

with a decay rate of

$$\Gamma = \frac{\cos^2\theta_W m_{\mathrm{NLSP}}^5}{16\pi \langle F\rangle^2}, \tag{5.17}$$

which translates to

$$c\tau \approx \left(\frac{\sqrt{\langle F\rangle}}{10^7\,\mathrm{GeV}}\right)^4 \left(\frac{100\,\mathrm{GeV}}{m_{\mathrm{NLSP}}}\right)^5 13\,\mathrm{km}. \tag{5.18}$$

For a SUSY braking scale of the order of $\sqrt{\langle F\rangle} > 10^7\,\mathrm{GeV}$ the lifetime of the NLSP grows very fast. Given $\sqrt{\langle F\rangle} = 10^8\,\mathrm{GeV}$ and $m_{\mathrm{NLSP}} = 150\,\mathrm{GeV}$, which is a realistic assumption (↗Fig. 5.2(b)), $c\tau \approx 17000\,\mathrm{km}$. This satisfies the detection demand of a long SUSY particle lifetime.

To obtain an absolute scale for the NLSP mass, the VEVs of the neutral components of the Higgs doublets (↗ Tab. 5.1) are important. Their ratio is written as

$$\tan\beta = \frac{\langle H_u^0\rangle}{\langle H_d^0\rangle}. \tag{5.19}$$

Another parameter to be known is μ. In the MSSM superpotential, it appears in the term $\mu H_u H_d$, which is the supersymmetric form of the SM Higgs mass. Consequently, the value of μ has a great influence on all other particle masses.

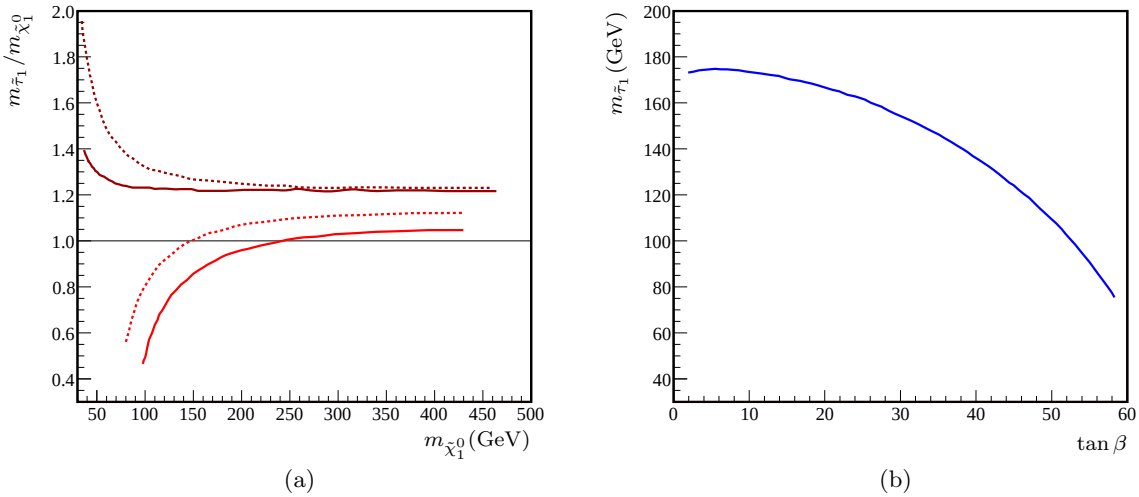

(a) (b)

Fig. 5.2: Masses of $\tilde{\tau}_1$ and $\tilde{\chi}_1^0$. (a) stau mass in comparison to the mass of the lightest neutralino. From top to bottom: $\tan\beta = 2$, $\mu > 0$; $\tan\beta = 2$, $\mu < 0$; $\tan\beta = 45$, $\mu > 0$; $\tan\beta = 45$, $\mu < 0$. (b) stau mass as a function of $\tan\beta$ for $\mu < 0$. (Tree-level results involving several model assumptions.) Images: [BMPZ97]

Dependent on the choice of the parameters, in GMSB the NLSP is the lightest neutralino $\tilde{\chi}_1^0$, the lightest *stau* $\tilde{\tau}_1$ or in some cases the sneutrino [GR99]. $\tilde{\tau}_1$ is a combination of chiral eigenstates $\tilde{\tau}_L$ and $\tilde{\tau}_R$, and forms a mass eigenstate. For smaller $\tan\beta$, $\tilde{\tau}_1$ is nearly the same as $\tilde{\tau}_R$ [Mar08]. To be detected by IceCube, the NLSP has to be charged. Accordingly, the stau is a very good candidate for an observable particle. In Fig. 5.2(a) the ratio between the stau mass and the mass of the lightest neutralino is displayed. For a scenario with $\tan\beta = 45$ the stau mass falls below the neutralino mass over a wide range of possible neutralino masses. To get an impression of the range for the mass of staus, Fig. 5.2(b) shows the stau mass dependent on $\tan\beta$. staus are, like their SM complement, charged particles and, provided, their kinetic energy is high enough, they can be seen in IceCube. If the stau is the NLSP, another detection demand is fulfilled.

5.3.2 stau Radiation Losses

As the stau is charged, it will interact electromagnetically with matter. The energy loss of high energy muons is given by

$$-\frac{dE}{dx} = (a(E) + b(E)E)\,\rho(x), \tag{5.20}$$

where a represents ionization energy loss and b the sum of energy loss due to pair production, bremsstrahlung and photonuclear interactions [PDG08]. The energy loss due to ionization is parameterized by the *Bethe-Bloch formula*

$$-\frac{dE}{dx} = 2\pi N_A r_e^2 m_e c^2 \frac{Z}{A}\frac{z^2}{\beta^2}\left[\ln\left(\frac{2m_e c^2(\beta\gamma)^2 T_{max}}{I^2}\right) - 2\beta^2 - \delta(\beta\gamma)\right]. \tag{5.21}$$

The parameters are

N_A	Avogadro's number,
r_e	classical electron radius,
m_e	the mass of the electron,
$\beta = v/c$	the speed of the incident particle,
γ	its relativistic factor,
I	mean excitation energy of the material,
T_{max}	maximum energy transfer to a free electron,
Z	atomic number of the absorber,
A	atomic mass of the absorber (g/mol),
$\delta(\beta\gamma)$	density effect correction to ionization energy loss.

Equation 5.20 is also valid for stau energy loss [ABC07]. At high values of $\beta\gamma$, the Bethe-Bloch formula can be approximated by

$$a(\beta\gamma) \approx 0.08\,\frac{\text{MeV cm}^2}{\text{g}}\,(17 + 2\ln\beta\gamma). \tag{5.22}$$

In [ABC07] the calculations for the radiative components, summarized in b, can be found. The assumed stau mass is 150 GeV. The results are shown in Fig. 5.3.

In the following, a reproduction of [Alb08a] is done, which is also used in the simulation of staus (↗Sec. 7.2). The combination of the equations 2.40 and 5.20 with the results for b allows for the calculation of the stau travel range inside the Earth. The total energy loss plotted in 5.3 has to be parameterized. Therefore, the double logarithmic plot is divided in three energy windows $E_{\tilde{\tau}_1} < 10^4$ GeV, $10^4\,\text{GeV} \leq E_{\tilde{\tau}_1} < 10^8$ GeV and $10^8\,\text{GeV} \leq E_{\tilde{\tau}_1}$. Afterwards, a linear fit is done for every window:

$$\lg(b) = \xi\lg(E_{\tilde{\tau}_1}) + \chi \quad\longrightarrow\quad b(E_{\tilde{\tau}_1}) = E_{\tilde{\tau}_1}^{\xi}\cdot 10^{\chi}. \tag{5.23}$$

The parameters are [Alb08a]

$$\begin{array}{rrcll} & E_{\tilde{\tau}_1} & < 10^4\,\text{GeV} & : & \xi = 0.2203 \quad \chi = -9.6405 \\ 10^4\,\text{GeV} \leq & E_{\tilde{\tau}_1} & < 10^8\,\text{GeV} & : & \xi = 0.1360 \quad \chi = -9.3179 \\ 10^8\,\text{GeV} \leq & E_{\tilde{\tau}_1} & & : & \xi = 0.1920 \quad \chi = -9.7781. \end{array}$$

To display the stau range inside the Earth, a useful coordinate system has to be found (↗Fig.5.4). The chosen system uses the IceCube detector coordinates as origin. Approximately, this is the center of mass of the IceCube detector. The positive z-axis points to the South. To illustrate the stau range, the stau is starting on the Earth surface and travels directly towards the origin. The angle ϑ defines the direction towards the stau starting point. This is slightly different to [Alb08a], where the stau always starts at the same point on the Earth surface, but travels under

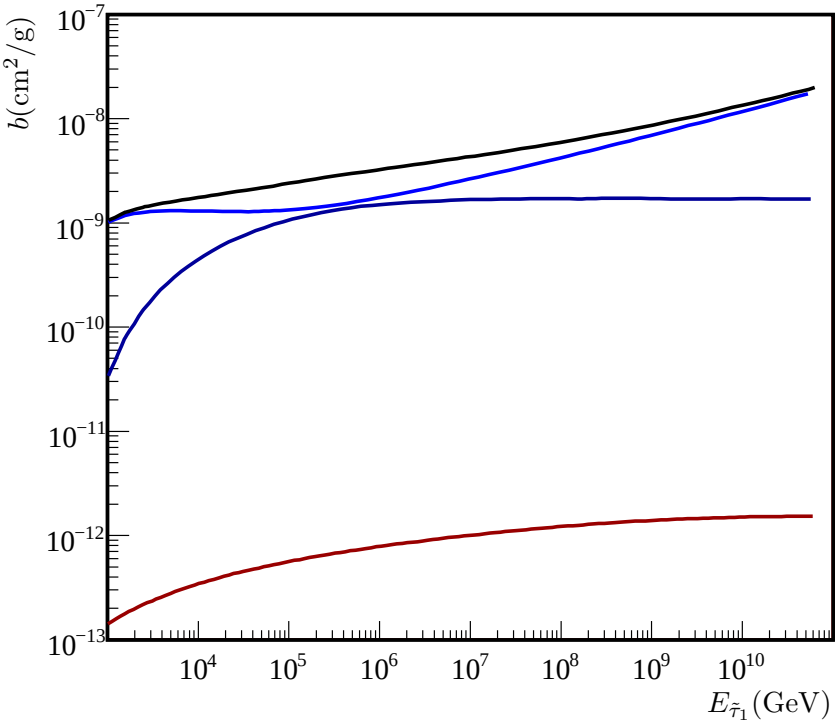

Fig. 5.3: $\tilde{\tau}_1$ Radiative Energy Loss for $m_{\tilde{\tau}_1} = 150\,\mathrm{GeV}$. From top to bottom: total energy loss; photonuclear interactions; pair production; bremsstrahlung. Image: [Alb08a]

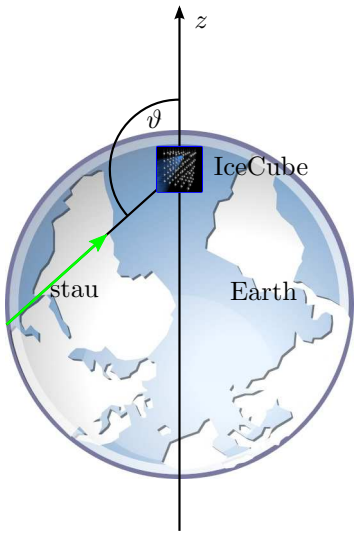

Fig. 5.4: Definition of Coordinates for stau Range Calculation.

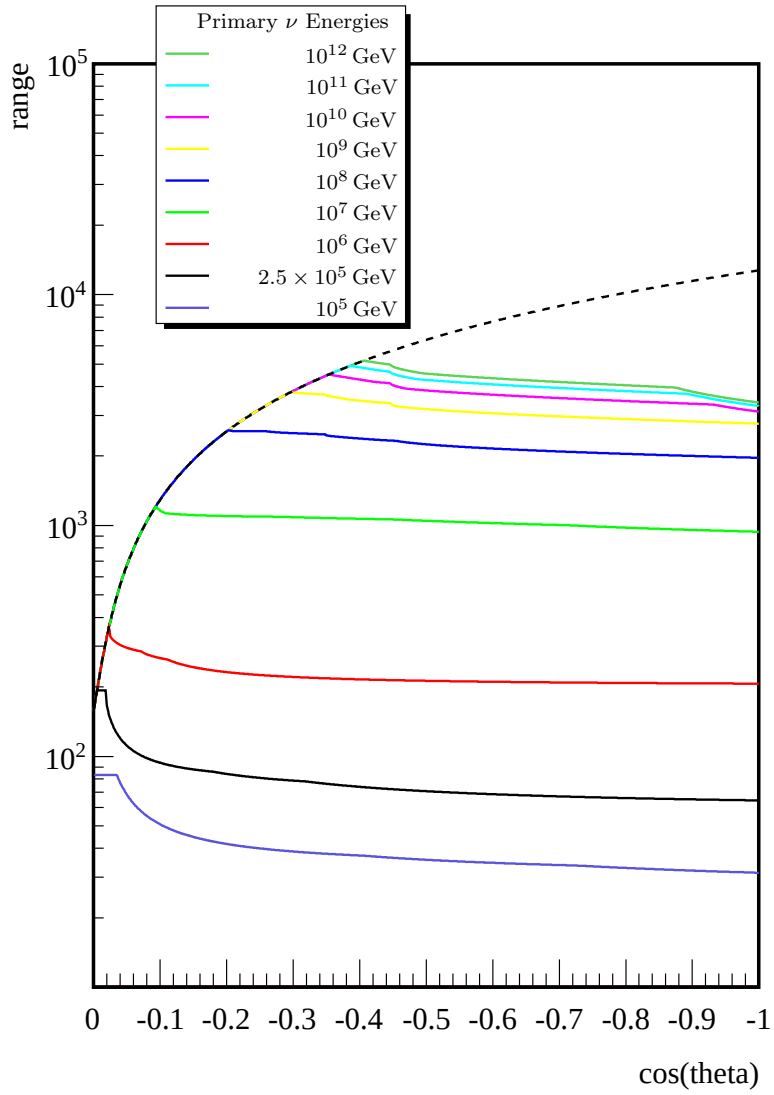

Fig. 5.5: stau Range for Several Energies. The final stau energy is 180 GeV. The given energies are the incident neutrino energies. To obtain the initial stau energies, the given values have to be divided by 6 [Cha08]. The assumed stau mass is 150 GeV. The dotted line represents the distance from the detector to the Earth surface. Image: Reproduction of [Alb08a]

different angles through the Earth. Both procedures deliver the same results. For a given stau energy E_0 at its starting point at the Earth surface, the relation between the travel distance l and the final stau energy E_1 is given by

$$-\int_{E_0}^{E_1} \frac{1}{a(E)+b(E)E}\mathrm{d}E = \int_{l_0=0}^{l} \rho(x)\mathrm{d}x. \tag{5.24}$$

$\rho(x)$ is the Earth density after traveling a distance of x under an angle ϑ from the Earth surface. x is *not* the depth, but the depth is a function of x and ϑ. The left integral is solved numerically with the parameterizations 5.22 and 5.23 for the given limits. This delivers an integrated density value

$$R_E = -\int_{E_0}^{E_1} \frac{1}{a(E)+b(E)E}\mathrm{d}E. \tag{5.25}$$

To obtain the travel distance l, the right integral

$$\int_{l_0}^{l} \rho(x)\mathrm{d}x = R(l) - R(l_0) \stackrel{!}{=} R_E \tag{5.26}$$

is also solved numerically. The integration is done for 10000 supporting points along the full distance from the Earth surface to the detector along the stau trajectory. The calculated points are used to define two spline functions: The first function $R(l)$ is giving back the integrated density value for a given l. The second spline R^{-1} represents the inverted function of R and delivers a length dependent on an integrated density. With these splines, the right side of equation 5.24 can be evaluated:

$$l = R^{-1}\left(R_E + R(l_0)\right). \tag{5.27}$$

The results of these calculations are presented in Fig. 5.5. For several initial energies, the range of staus inside the Earth before falling below a fixed minimum energy of 180 GeV is plotted. To obtain a maximum conformity with [Alb08a], the initial energies are given for incident neutrinos producing SUSY matter inside the Earth. The corresponding stau energy is obtained by dividing the primary neutrino energy by 6 [Cha08].

Even if Fig. 5.5 does not show the more realistic case of an stau produced somewhere inside the Earth, the energy dependent range of the staus becomes apparent. The range of several thousand kilometers for the higher energy staus gains access to a very large volume inside the Earth for the production of staus that can be seen in the detector. Consequently, now all demands for stau detection in IceCube are satisfied.

5.4 Neutrino Induced SUSY Particle Production

The process

$$\nu + N \longrightarrow \tilde{\ell}_L + \tilde{q} + X \tag{5.28}$$

allows for the creation of SUSY matter by SM matter interactions. The always left-handed neutrino can interact in a t-channel reaction either with a left-handed down-type quark (Fig. 5.6) or with a right-handed up-type antiquark. The corresponding Feynman diagrams are shown in

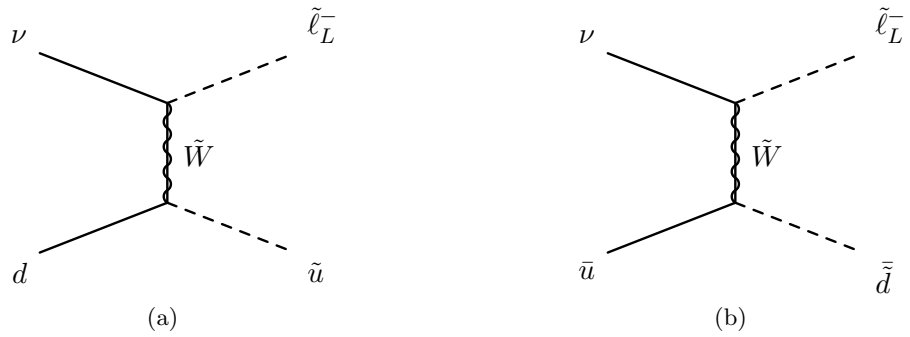

Fig. 5.6: Charged slepton-Creating Neutrino Reactions. Without violation of R-parity, only wino reactions are possible. Image: [ABC07]

Fig. 5.6. The partonic cross sections are

$$\frac{\mathrm{d}\sigma^{(a)}}{\mathrm{d}t} = \frac{\pi\alpha}{2\sin^4\theta_W}\frac{m_{\tilde{W}}^2}{s(t-m_{\tilde{W}}^2)^2} \quad \text{and} \tag{5.29a}$$

$$\frac{\mathrm{d}\sigma^{(b)}}{\mathrm{d}t} = \frac{\pi\alpha}{2\sin^4\theta_W}\frac{tu-(m_{\tilde{\ell}_L}m_{\tilde{q}})^2}{s^2(t-m_{\tilde{W}}^2)^2}, \tag{5.29b}$$

with the Mandelstam variables s, t and u. The total cross sections are calculated in [ABC07] for the wino and left-handed slepton masses $m_{\tilde{W}} = 250\,\mathrm{GeV}$ and $m_{\tilde{\ell}_L} = 250\,\mathrm{GeV}$, and for three different squark masses $m_{\tilde{q}} = 300\,\mathrm{GeV}$, $600\,\mathrm{GeV}$ and $900\,\mathrm{GeV}$. Fig. 5.7 shows the results of

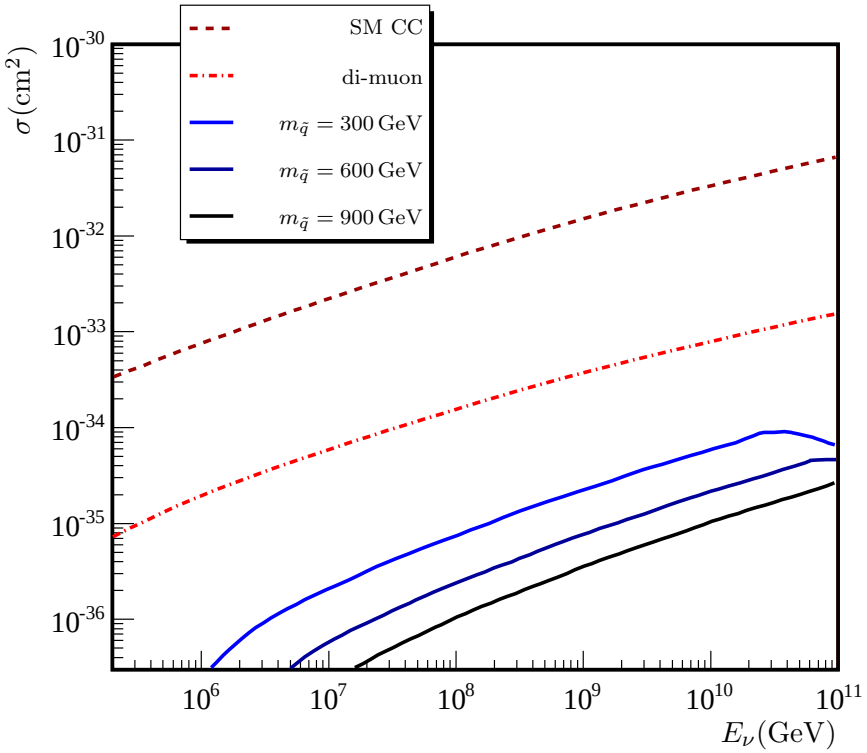

Fig. 5.7: Neutrino Cross Sections for different interactions. Image: [ABC07]

these calculations in comparison with the neutrino SM charged current interaction cross section

(↗Sec. 2.3.1) and the cross section for di-muon production (↗Sec. 6). These cross sections are necessary to simulate the interaction point of the neutrino inside the Earth.

6

Background for stau Detection

The main sources of stau detection background are double muon tracks inside the detector. Because of their relatively small lateral distribution, muon bundles from air showers [GS85; B+89] do not contribute to the background. More critical are muons with a high transversal momentum, so called high p_T muons, in air showers [KC07; Kle08]. These muons, together with the air shower core muon(s), can produce double track events in IceCube. Because of the down-going nature of air shower events, the stau double tracks, which are assumed to be up-going, are distinguishable from the high p_T muon events.

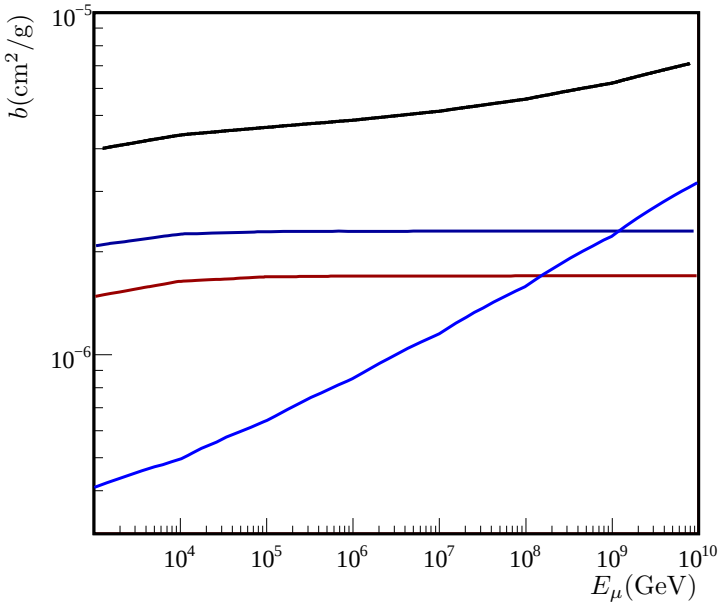

Fig. 6.1: μ Radiative Energy Loss. From top to bottom at low energies: total energy loss; pair production; bremsstrahlung; photonuclear interactions. Image: [ABC07]

A further type of double track events can be produced by charm hadron decay [ABC07]:

$$\nu_\mu + N \quad \longrightarrow \quad \mu^- + H_c^+ \quad \longrightarrow \quad \mu^- + \mu^+ + \nu_\mu + X. \tag{6.1}$$

After the production of a charm hadron by an incident high energy neutrino, it is possible that the hadron decays semi-leptonic with muon emission. If the first reaction additionally results in muon production, two muons on nearly parallel trajectories are emitted. These muons can be seen as double tracks inside the detector.

The range of muons in matter (e.g. bedrock or ice) is much smaller than the range of staus in the same medium. This can be illustrated with the help of Fig. 6.1. The total radiative energy loss of muons is described by a b-parameter which is between 700 and 4000 times larger than the b-parameter for staus (↗Fig. 5.3).

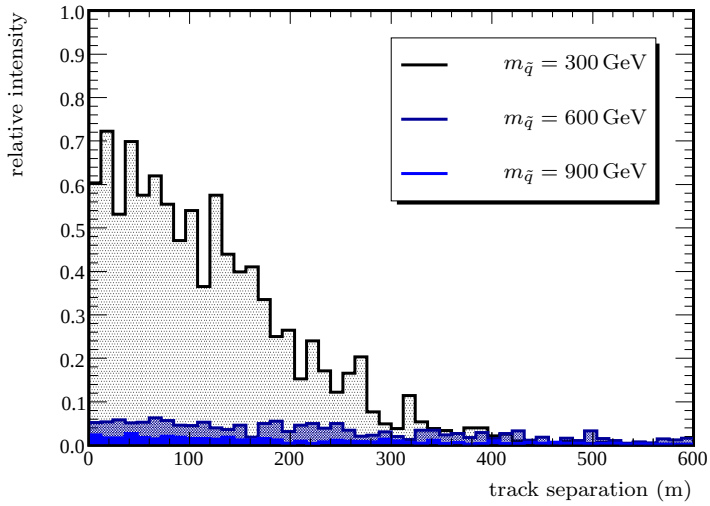

(a) stau Track Separation

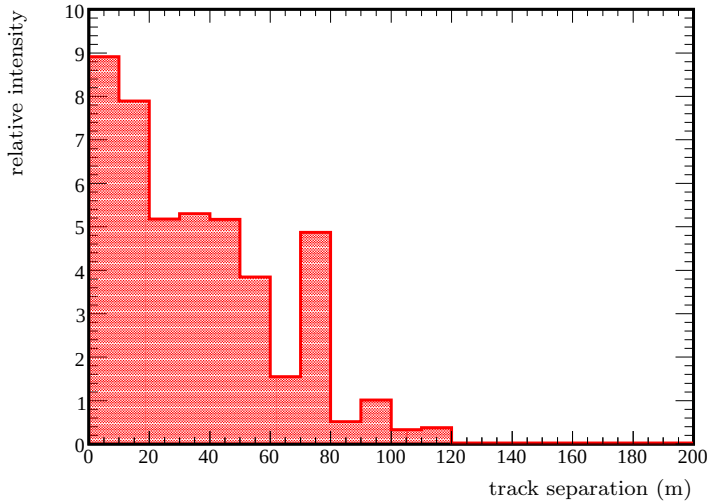

(b) Double-μ Track Separation

Fig. 6.2: Signal and Background Track Separation. Please note the different scales on the x- and y-axes. The stau track separations are calculated for three different squark masses. Images: [ABC07]

This already offers two possibilities for the separation of double muon tracks: By track separation and by light deposition. Due to the higher b-parameter, the light deposition inside the detector is much higher for muons than for staus with the same energy.

The high radiative losses do not allow for a high range of muons in matter. This implies that the muon production has to take place near or inside the detector. Consequently, the separation between muon double tracks is expected to be much smaller than for staus which have traveled a very long distance to the detector.

The theoretical predictions for the track separation inside a km^3-scale detector are presented in Fig. 6.2. The smaller track separation for double muon tracks in the detector is visible. For less than 120 m, the background events clearly dominate, but for larger separations, the staus become more important.

7

Simulation of SUSY Events

For a later analysis of real IceCube data and for the development of a filter searching for stau events in the IceCube data stream, a realistic simulation of stau double track events is needed. In the following sections, the software modules created for this purpose in the context of this thesis are described. Base for the software development is the IceCube software framework "IceTray". IceTray is a collection of classes, written mainly in the programming language "C++". Similar classes within IceTray with respect to their content are arranged in projects. This structure allows for easily writing own projects without the necessity to know the full software package of the IceCube experiment.

All simulations, including IceCube hardware information, use the IceCube-40 geometry of the year 2008. In this configuration, the IceCube detector consists of 40 strings.

7.1 Simulating Simply – The SUSY-simple-gen Module

Often, very special situations are necessary to understand a software system. To set up a first simple simulation the SUSY-simple-gen module is developed. It is omitting many aspects of a realistic simulation in terms of physical correctness, but is including already many practical aspects of double track simulations.

The demands on the SUSY-simple-gen module are:

- The double tracks (at least one of the two particles) have to cross the detector.
- The angle between the tracks has to be variable.
- The source point of the tracks has to be variable, but lying inside the Earth.
- The stau energy has to be variable.

In SUSY-simple-gen, a primary neutrino is created from which the stau properties are derived.

7.1.1 stau Energy

The stau energies $E_{\tilde{\tau}^a,\tilde{\tau}^b}$ are obtained from the primary neutrino energy E_ν by simply splitting it randomly:

$$E_{\tilde{\tau}^a} = \frac{1}{2}E_\nu + RE_{dev} \tag{7.1a}$$

$$E_{\tilde{\tau}^b} = E_\nu - E_{\tilde{\tau}^a}. \tag{7.1b}$$

The parameter E_{dev} is the maximum energy deviation from $E_\nu/2$ and R is uniformly distributed random number between -1 and 1.

For the energy of the primary neutrino, an $E^{-\gamma}$ spectrum with $0 < \gamma < 4$ is used. 4 is an arbitrary choice for the maximum steepness of the spectrum and should cover all physically relevant applications. Minimum energy $E_{\min}$ and maximum energy $E_{\max}$ for the simulated neutrinos are configurable. For $E_{\min} = E_{\max}$ the energy is fixed. The power law energy distribution is produced by using the Monte Carlo method described in App. A.1.

7.1.2 Primary Interaction Point

This point is either fixed or points are randomly distributed over the volume of the Earth.

7.1.3 stau direction

The pointing direction(s) of the stau(s) should cover only a limited volume around the IceCube detection volume, to avoid simulation of tracks which would never be detected.

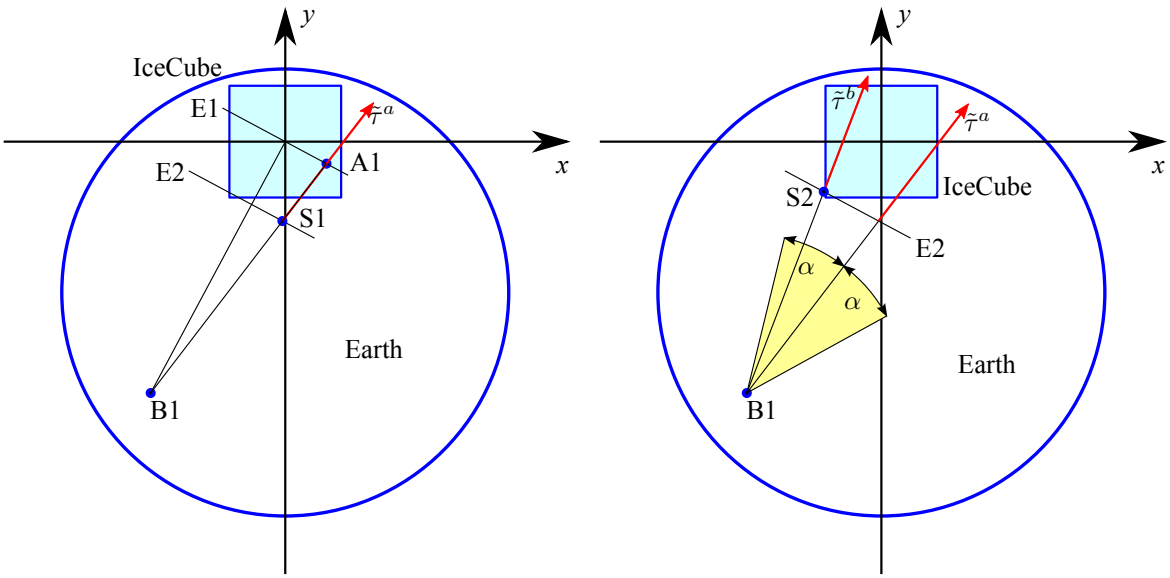

(a) First stau (b) Second stau

Fig. 7.1: SUSY-simple-gen Determination of stau Tracks. Explanation in the Text.

The determination of the stau tracks is done as described in Fig. 7.1. After the interaction point inside the Earth B1 is found, the direct connection between B1 and the origin O of the coordinate system in the center of the IceCube detector is used, to define the plane E1. E1 is lying orthogonally to the vector from B1 to O and is also containing the origin (Fig. 7.1(a)). On this plane, a point A1 is chosen randomly within a maximum distance to the origin. This distance is configurable. The vector from B1 to A1 defines the first stau direction.

It is not wanted to propagate the stau from the interaction point through the Earth to the detector, but let it start within a reasonable distance to the detector. This way, the stau can be directly given to the ice and detector simulation software modules. To find an adequate starting point for the stau, an additional plane E2 is introduced. E2 is defined by the connection between B1 and the origin. The distance of E2 to the origin is a configurable parameter. The starting point of the first stau is the intersection of its direction with E2.

Base of the direction of the second stau is the direction of the first stau. Using the neutrino interaction point B1 as starting point, the direction of the second stau is chosen freely within a cone with the angle α (Fig. 7.1(b)) by using the method described in App. A.2. Like for the first stau, a propagation through the Earth is not wanted. Consequently, a starting point near the detector is needed. Again, the intersection of the track with E2 is used.

The length of both stau tracks is set long enough so that the stau is traversing the complete detector.

7.1.4 Benefit of the SUSY-simple-gen Module

Due to its simplicity the SUSY-simple-gen modules can be used to test the simulation chain from the generation of a charged particle to the triggered events in the IceCube detector. The steps on this way are:

(a) Generation of particle(s) traversing the detector volume.

(b) Propagate particle with the so called *Muon Monte Carlo* (*MMC*) software [CR04], which calculates energy losses and secondary particles. MMC accounts for ionization, bremsstrahlung, photonuclear interactions, electron pair production, Landau-Pomeranchuk-Migdal and Ter-Mikaelian effects, muon and tauon decays, and Molière scattering.

(c) Simulate the amount of light arriving at the PMTs of the detector. The corresponding software module considers also the optical properties of the South Pole ice.

(d) Simulate the PMT response and the characteristics of the DOM electronics.

(e) Simulate the triggering conditions.

If the triggering conditions of the detector are satisfied, the simulated event is stored.

All software modules included in the simulation chain have to be adjusted by parameters. With the help of the SUSY-simple-gen module, the parameter settings can be optimized.

One important question, concerning the stau simulation, is the one for the light deposition inside IceCube. Because of the simple structure of the SUSY-simple-gen module, which is not using any particle specific parameters, like decay rates, mass or energy losses in matter, the generated particle type can be easily changed. Accordingly, the SUSY-simple-gen module allows for the creation of all particle types available in IceTray. To increase the flexibility, the production of two tracks can be reduced to one. This is helpful for the comparison of light emission of particles.

The number of Monte Carlo simulated hits from muons N_{hit}^{μ} compared to those from staus $N_{\text{hit}}^{\tilde{\tau}}$ is plotted in Fig. 7.2. N_{hit} is a good indicator for the light deposition in the detector. Consequently, the question from above can be answered with the help of Figs. 7.2(a) and 7.2(b).

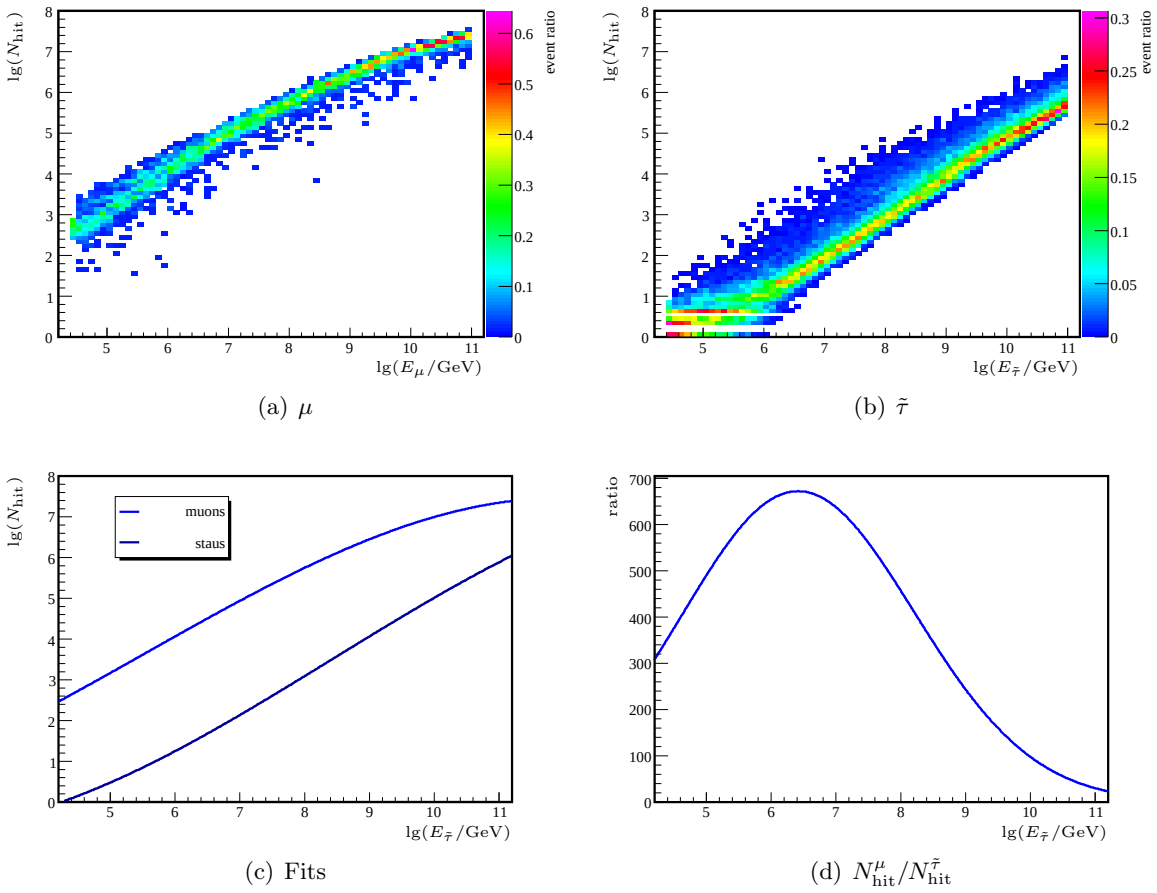

(a) μ (b) $\tilde{\tau}$

(c) Fits (d) $N^{\mu}_{\mathrm{hit}}/N^{\tilde{\tau}}_{\mathrm{hit}}$

Fig. 7.2: Comparison of N_{hit} from μ and $\tilde{\tau}$. The color coding in (a) and (b) shows the number of events in the corresponding bin divided by the integrated number of entries in the corresponding energy bin. This is to remove the spectral shape from the histograms. (c) shows the fits of (a) and (b) with cubic functions. Calculating the non-logarithmic N_{hit}-values from the fits and dividing the results delivers the function plotted in (d).

Both plots have been fitted with cubic functions (Fig. 7.2(c))

$$f(x) = ax^3 + bx^2 + cx + d. \tag{7.2}$$

The fit parameters are

	μ			$\tilde{\tau}$		
a	-8.89×10^{-2}	$\pm$	2.62×10^{-1}	4.51×10^{-2}	$\pm$	4.50×10^{-2}
b	2.22×10^{-1}	$\pm$	1.16×10^{-1}	-7.28×10^{-1}	$\pm$	2.47×10^{-2}
c	1.22×10^{-1}	$\pm$	1.80×10^{-1}	2.02×10^{-1}	$\pm$	4.80×10^{-3}
d	-7.36×10^{-3}	$\pm$	9.05×10^{-4}	-8.00×10^{-3}	$\pm$	2.73×10^{-4}

The ratio $N^{\mu}_{\mathrm{hit}}/N^{\tilde{\tau}}_{\mathrm{hit}}$ (the non-logarithmic values!) is displayed in Fig. 7.2(d). The amount of hits from muon tracks is always exceeding the number of stau track induced hits by more than a factor of 20 over the complete simulated energy range.

7.2 Simulation of double stau tracks with the SUSY-gen Module

SUSY-simple-gen only provides a basic double track simulation without physical background. Even if the SUSY-gen module is still under construction, many important features exceeding the possibilities of SUSY-simple-gen are already implemented and will be presented in the following subsections.

Within this work, the processes at the interaction point of the primary neutrino are simulated in a simplified way. The correct calculations would go beyond the scope of this thesis and will be done during the ongoing work on this topic. The simplifications are

- assumption of direct production of two $\tilde{\tau}_1 \approx \tilde{\tau}_R$,
- ignoring structure functions of the nucleon, only using the nucleon mass,
- usage of the $\nu + N$ SM interaction cross section (Fig. 2.14) instead of the different cross sections for chargino interactions. Fig. 5.7 shows that the SM and SUSY cross section curves are aligned in parallel over a wide energy range. In this region, the usage of the SM interaction cross section only leads to a flux renormalization.

7.2.1 Generation of the Neutrino Flux

The neutrino flux arriving at the Earth is assumed to be isotropic. Only neutrinos potentially creating staus arriving at the detector are interesting to simulate.

To archive an isotropic neutrino flux, the neutrinos are assumed to come from a sphere around the Earth. Every neutrino starts at an arbitrary point A on the sphere (Fig. 7.3(a)), which is described by the radius R of the sphere and the polar coordinates ϑ and φ. R has to be larger than the Earth radius R_{Earth}. The IceCube detector is located at a depth d_{det} below the Earth surface.

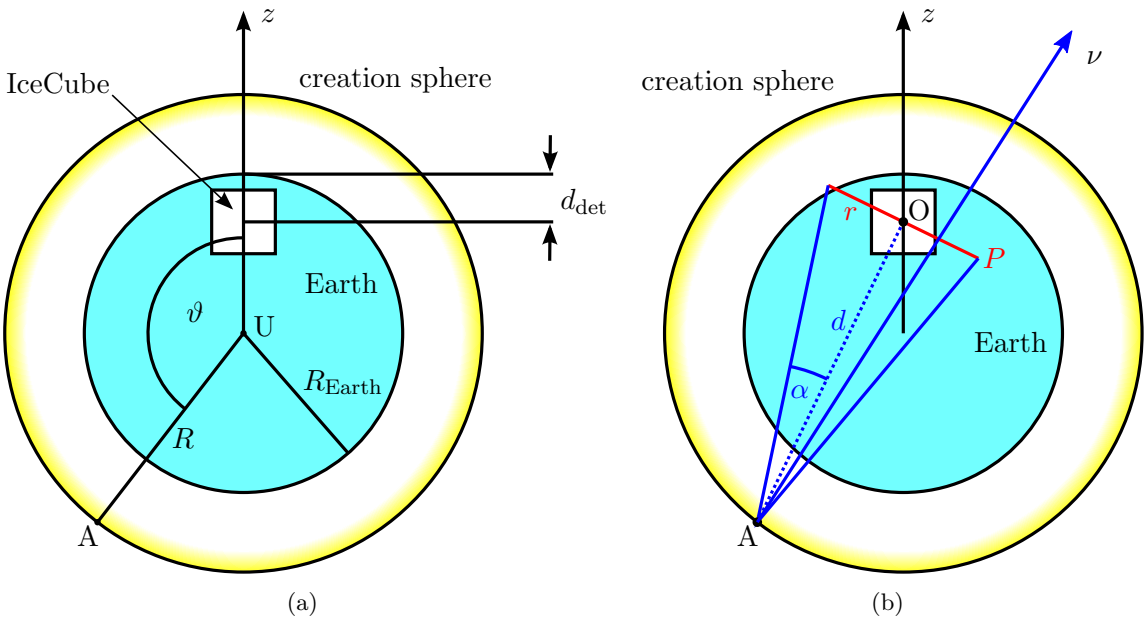

Fig. 7.3: Illustrations for Neutrino Generation. Explanations in the text.

Only neutrinos that have the potential to produce double tracks arriving the detector shall be simulated. This can be achieved by the demand that the neutrino trajectory has an intersection with a circular plane P with radius r. P is defined by having the connection between O and A

as normal vector and including the center of the detector O (Fig. 7.3(b)). The distance between point A and the detector is called d. Consequently, the allowed solid angle for every neutrino is dependent on the value of ϑ defining A. φ is arbitrary in this context.

The solid angle Ω is given by

$$\Omega = \int_0^{\alpha} \int_0^{2\pi} \sin(\alpha') \mathrm{d}\beta' \mathrm{d}\alpha' = 2\pi \left[1 - \cos(\alpha)\right]. \tag{7.3}$$

W.l.o.g., it can be assumed that α' and β' describe spherical coordinates during the integration. α is defined by

$$\tan(\alpha) = \frac{r}{d}. \tag{7.4}$$

d follows from the law of cosines:

$$d^2 = R^2 + (R_{\mathrm{Earth}} - d_{\mathrm{det}})^2 - 2R(R_{\mathrm{Earth}} - d_{\mathrm{det}}) \cos(\vartheta). \tag{7.5}$$

The amount $N(\vartheta)$ of valid neutrinos starting at point A on the creation surface is proportional to the portion Ω of the full sphere 4π, which is then given by the unbeautiful formula

$$\begin{aligned} N(\vartheta) &\propto \frac{\Omega(\vartheta)}{4\pi} \\ &= \frac{1}{2}\left[1 - \cos\left(\arctan \frac{r}{\sqrt{R^2 + (R_{\mathrm{Earth}} - d_{\mathrm{det}})^2 - 2R(R_{\mathrm{Earth}} - d_{\mathrm{det}}) \cos(\vartheta)}}\right)\right]. \end{aligned} \tag{7.6}$$

To simulate this distribution the method described in App. A.3 is used. The only parameter to be chosen with care in this method is the radius r of the plane through the detector. The radius of the creation sphere R is more or less arbitrary as long as it is larger than the Earth radius. For $r = 500\,\mathrm{m}$ and $R = R_{\mathrm{Earth}} + 1\,\mathrm{km}$, Eq. 7.6 is plotted in Fig. 7.4.

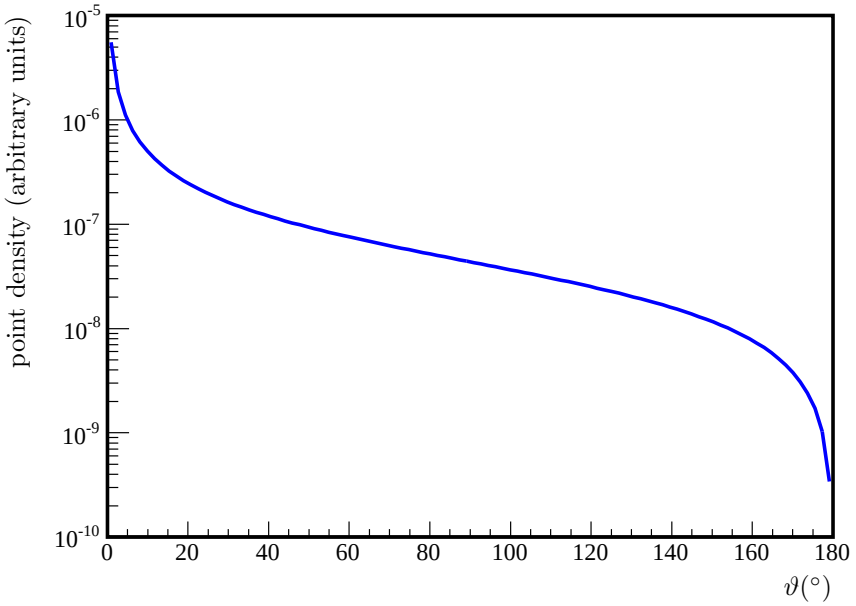

Fig. 7.4: Plot of Eq. 7.6 for $r = 500\,\mathrm{m}$ and $R = R_{\mathrm{Earth}} + 1\,\mathrm{km}$.

After the point on the creation sphere is found, the neutrino direction is chosen. The direction is limited by the cone defined by the neutrino starting point and the circular plane P through the IceCube detector. Within this cone, the direction is chosen randomly using a uniform distribution.

The energy distribution of the primary neutrinos follows the method in Sec. 7.1.

7.2.2 Generation of the Neutrino Interaction Point

Now, as the starting point of the neutrino on the creation sphere and the direction of the neutrino trajectory is found, the interaction point inside the Earth has to be simulated. The number of particles interacting while traversing matter

$$\frac{\mathrm{d}N}{\mathrm{d}x} = -N\sigma\frac{\rho(d)}{m_N} \tag{7.7}$$

is dependent on the number of particles N, the interaction cross section σ with the targets in the medium and the particle density $\rho(d)/m_N$ in the medium. ρ is given by Eq. 2.40 and is a function of the depth regarding to the Earth surface. The particles forming the traversed matter are nucleons with mass m_N. Solving Eq. 7.7 by separation of variables delivers

$$N(l_0, l) = N(l_0)\exp\left(\frac{\sigma}{m_N}\int_{l_0}^{l_0+l}\rho(d)\mathrm{d}d\right), \tag{7.8}$$

where the depth d is a function of l and ϑ. l is the distance, the particles are traveling through the medium. l_0 is the starting point of the "propagation" and $N(l_0)$ is the amount of particles starting at position l_0. The amount of particles can also be translated by the probability of one particle not having interacted until reaching the distance l. The probability at the starting point l_0, consequently, is 1. The integration has to be done along the neutrino path. The starting point $l_0 = 0$ lies on the Earth surface. If $\vec{a}$ is the vector pointing from the detector center to the neutrino starting point on the creation sphere (Fig. 7.5(a)), $\vec{b}$ the vector from the Earth center to the detector center, $\vec{c}$ the direction of the neutrino trajectory and $\vec{R}$ the vector pointing on the starting point on the Earth surface, which has to be found, the starting point is defined by

$$\vec{s} = \vec{b} + \vec{a} + x\vec{c}. \tag{7.9}$$

In combination with the demand

$$\vec{R}^2 = \left(\vec{b} + \vec{a} + x\vec{c}\right)^2 \tag{7.10}$$

x is calculated to

$$x = -\left(\frac{\vec{a}\vec{c}}{\vec{c}^2} + \frac{\vec{b}\vec{c}}{\vec{c}^2}\right) \pm \sqrt{\left(\frac{\vec{a}\vec{c}}{\vec{c}^2} + \frac{\vec{b}\vec{c}}{\vec{c}^2}\right)^2 - \left(\vec{a}^2 + \vec{b}^2 - \vec{R}^2 + 2\vec{a}\vec{b}\right)}. \tag{7.11}$$

The "$-$" sign delivers the x-value x_{min} for the entrance point of the neutrino into the Earth and the "$+$" sign the x-value x_{max} for its exit.

Every value l in

$$\vec{t} = \vec{s} + l\frac{\vec{c}}{c} \tag{7.12}$$

with $0 < l < x_{max} - x_{min}$ and $\vec{t}$, the neutrino trajectory through the Earth, a depth

$$g(l) = \vec{b}^2 + \vec{s}^2 + 2\vec{b}\vec{s} + l^2 + \frac{2l}{c}\left(\vec{s}\vec{c} + \vec{b}\vec{c}\right) \tag{7.13}$$

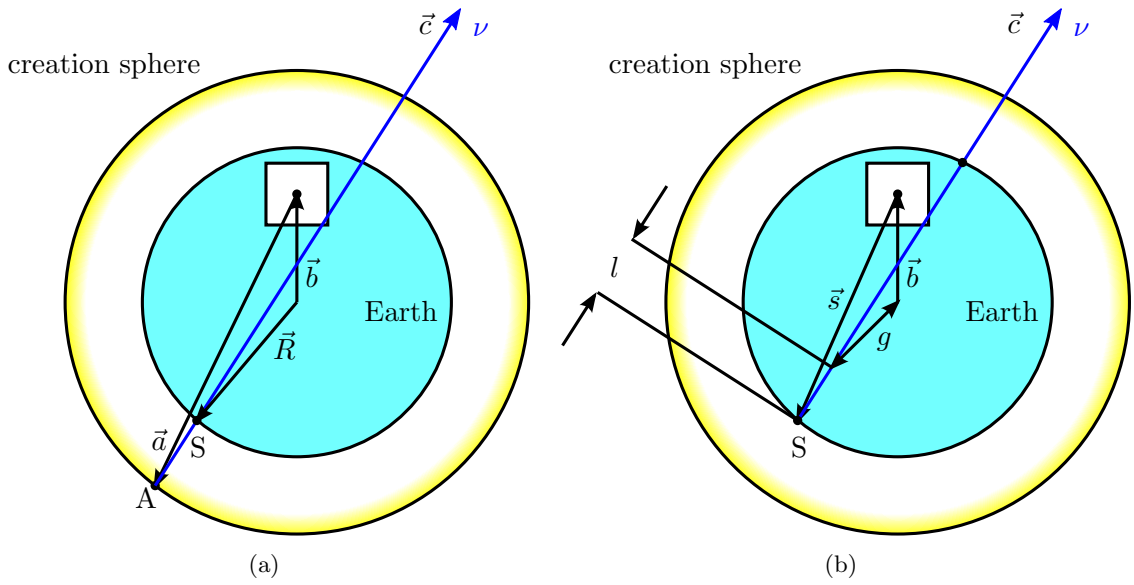

Fig. 7.5: Illustrations for Neutrino Generation. Explanations in the text.

to the Earth center can be assigned (Fig. 7.5(b)). Accordingly, the depth $d(l)$ is given by

$$d(l) = R_{\text{Earth}} - g(l). \tag{7.14}$$

With the help of Eq. 7.8, a random interaction point can be simulated.

The input neutrino energy spectrum for all simulations done with the SUSY-gen module for this thesis follows the Waxman-Bahcall-Limit (↗Sec. 2.2.2) with a spectral index of $\gamma = 2$. The slope of the energy distribution is -0.94 ± 0.33, which is the expected value (↗App. A.4). For a fixed neutrino energy the cross section σ is a constant. The complicated integration over the Earth density dependent on the track distance l has to be done numerically for every neutrino starting point S and every neutrino direction $\vec{c}$. The final Monte Carlo simulation is done according to the method described in App. A.3. If a neutrino is passing the Earth or detector volume without interaction, a completely new neutrino with new start parameters will be simulated. The resulting distance distribution is plotted in Fig. 7.6(b).

The distribution of the zenith angle ϑ of the interaction point seen by the origin coordinates of the IceCube detector peaks at $\cos\vartheta = -0.1$ (Fig. 7.6(c)). Thus, most interaction points are lying in a belt with a z-coordinate slightly below 0 around the detector. Even if Eq. 7.6 suggests an excess of neutrinos coming from $\cos\vartheta \lesssim 1^\circ$ (↗Fig. 7.4), the small neutrino cross section makes the neutrinos interacting after passing the detector. But these events are refused. At $\cos\vartheta = -0.1$ the large amount of neutrinos coming from this direction compensates the low interaction probability best.

The interaction probability inside the Earth is exponential over a wide range of depths (Fig. 7.6(d)). The excess at small depths can be explained with the belt around the detector where a large fraction of events come from. At large depth the plot is deformed by the fact that neutrinos passing the Earth center before interacting, contribute to the bin contents of smaller depths. Because of the few entries above a depth of 5000 km, this effect is not significant.

7.2.3 stau Generation

As mentioned above, the generation of the two staus is done in a very simplified way in the version of the SUSY-gen module topical during the writing of this thesis.

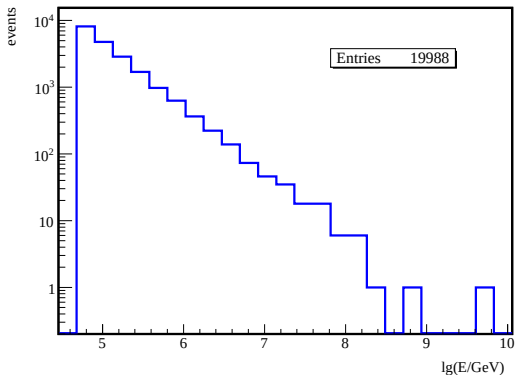

(a) Primary Neutrino Energy

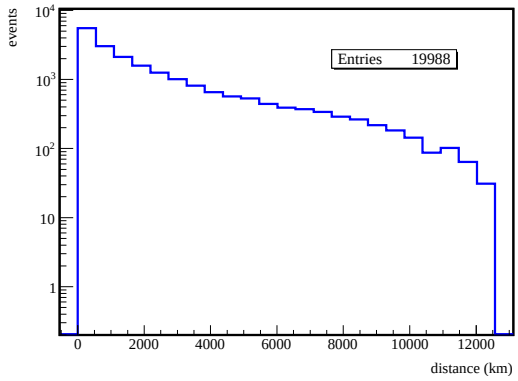

(b) Distances of Interaction Points to the Detector

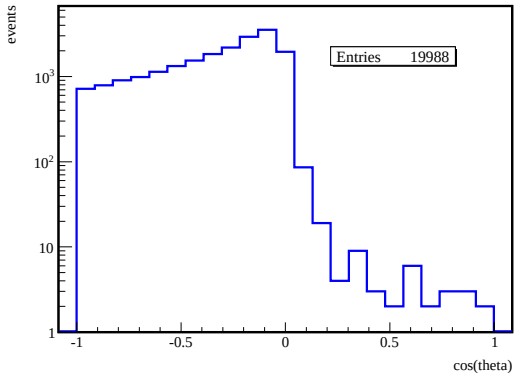

(c) Zenith Angle of the Interaction Point

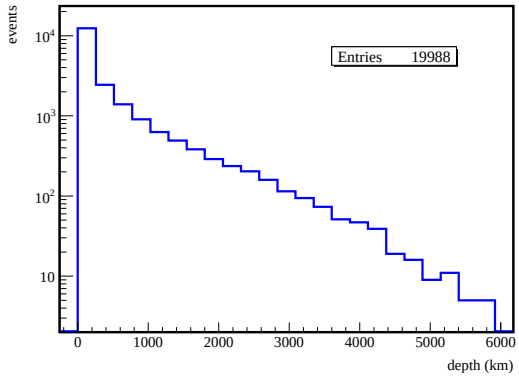

(d) Depth of the Interaction Point Inside the Earth

Fig. 7.6: Properties of the Interaction Point Without Restrictions.

At the interaction point a nucleon is assumed to be the target of the incident neutrino. Neutrino and nucleon are boosted into their center of mass system (CMS) (↗App. B.1). The nucleon rest mass is set to $m_N = m_p = 0.938\,\text{GeV}$ and the neutrino is assumed to be massless. The complete available energy in the CMS is converted to directly create two right-handed staus. The energy not converted to stau mass is given to the staus as kinetic energy. The trajectory of the two staus in the CMS is arbitrary but antiparallel.

Using Eq. B.12 and inserting a uniform distribution in $\cos(\vartheta)$ (↗App. A.2) delivers the simulation results of Fig. 7.8(a). For some neutrino energies the angular distribution is plotted in 1D histograms. This is presented in Fig. 7.8(b). It is clearly visible that the amount of events with smaller angle of beam spread is increasing for higher neutrino energies.

After boosting the staus back into the lab frame (the rest frame of the Earth), the angle α between their trajectories and the distance of the interaction point to the detector determine the track distance inside the detector. The definition of the track distance is explained in Fig. 7.7. The correct angular distribution is very important for the double track simulation. In this simple generation scheme ignoring the nucleon structure and neglecting the neutrino mass, the maximum angle between the two staus in the lab frame is only dependent on the mass of the nucleon and the mass of the two generated particles (↗App. B.2). The resulting distributions for α for several incident neutrino energies are plotted in Fig. 7.8(a).

The correct handling of the neutrino interaction is done in [ABC07]. Those results are not used in this thesis and are subject of the ongoing work on this topic. The energy dependent angular distributions, presented in App. C, have been provided by [Alb08b].

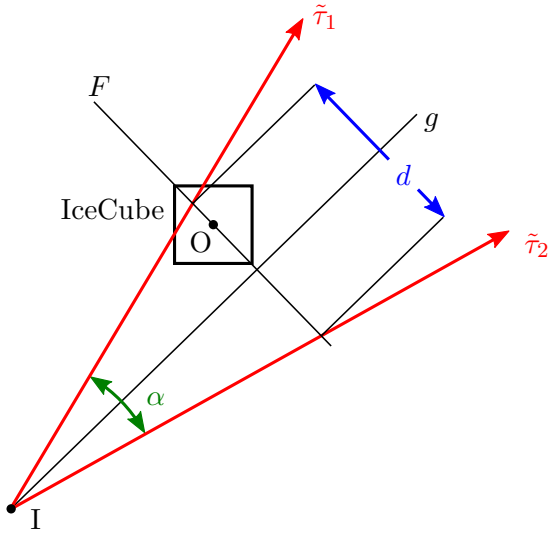

Fig. 7.7: Definition of the Track Distance. The bisecting line g between the two stau trajectories $\tilde{\tau}_1$ and $\tilde{\tau}_2$, starting at the interaction point I, together with the origin of the IceCube detector coordinates O, define the plane F. The track distance d is given by the distance of the intersection points of the two trajectories with F.

Without any further restrictions, the distance distribution shown in Fig. 7.9 of the two staus at the detector is obtained. The distance is defined as described in Fig. 7.7. This distribution is very broad and most of the double tracks will not cross the IceCube detection volume. Consequently, it is useful to accept only events with both stau tracks traversing the detector.

This restriction changes also all distributions displayed in Fig. 7.6. The new distributions are presented in Fig. 7.10. The most obvious change can be observed in the distance of the interaction points to the detector (Fig. 7.10(b)). Using the same algorithm for the angular distribution as before, the interaction point has to move towards the detector to have both stau tracks inside. This significantly reduces tracks coming from the bottom and produces something like a belt of interaction points around the detector at values of ϑ around $90\,^\circ$ (Fig. 7.10(c)). Consequently, the available amount of matter between the detector and the surface is reduced and the depth of the interaction point inside the Earth is decreased. Fig. 7.10(d) displays the position of the interaction point inside the Earth without taking into account the direction of the incident neutrino. Therefore, in the small depths also interaction points below the detector from neutrinos traversing the Earth are summed up like in (Fig. 7.6(d)).

An interesting result is the decrease of the neutrino spectrum for neutrinos producing double stau tracks arriving the detector. The input neutrino spectrum is still $\propto E^{-2}$. The resulting logarithmic histogram Fig. 7.10(a) has a slope of -0.69 ± 0.16 corresponding to a spectral index of -1.69 ± 0.16. This slight flattening results from the connection between the neutrino energy and the distribution of the beam spread between the two staus (Fig. 7.8(a)). If the neutrino energy is high, the beam spread becomes smaller and the traverse of both stau tracks through the detection volume more likely.

When applying the demand of two stau tracks passing the detector, the track distance distribution presented in (Fig. 7.11) is the result. In this histogram also geometrical effects of the special shape of the detection volume are visible for larger track distances. Distances of more than one km are only possible when both staus hit opposite corners of the hexagonal shaped volume (Fig. 3.16) of IceCube.

Before starting a simulation, the influence of the stau energy onto the detector response has to

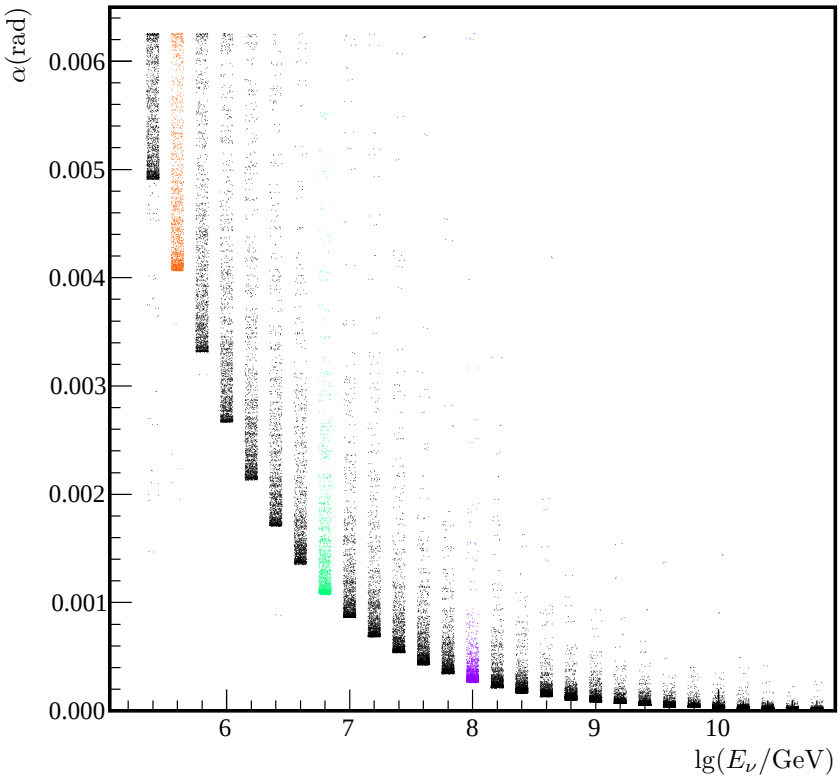

(a)

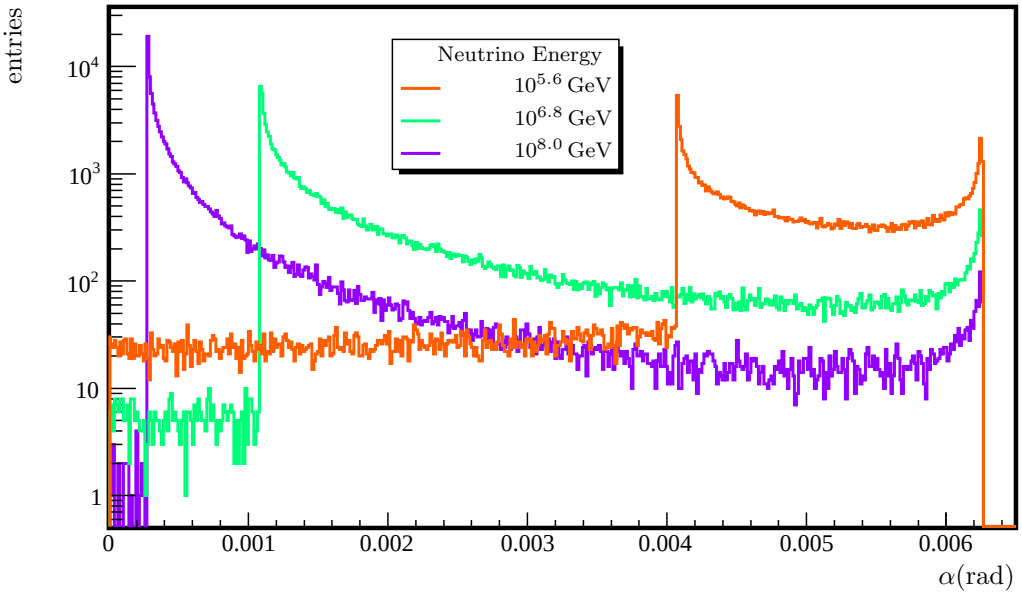

(b)

Fig. 7.8: Distribution of the Angle of Beam Spread between two stau trajectories created with the method described in the text. (a) The incident neutrino energies are varied between $10^{5.4}$ GeV and $10^{10.8}$ GeV. (b) 1D histograms for a sample of three different incident neutrino energies.

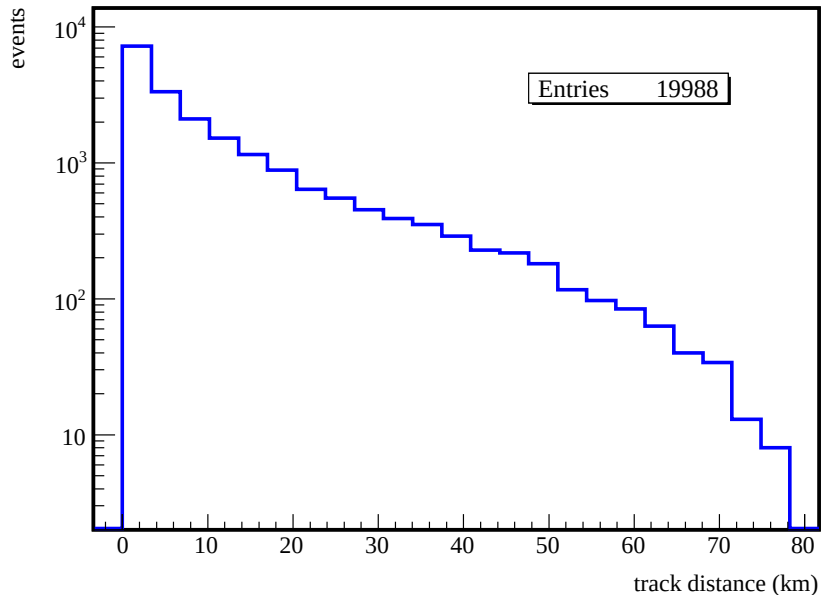

Fig. 7.9: stau Track Distance Without Restrictions.

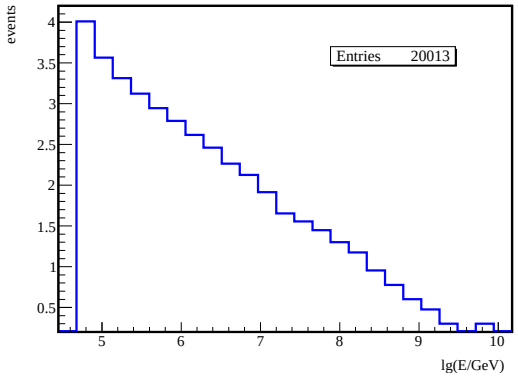

(a) Primary Neutrino Energy

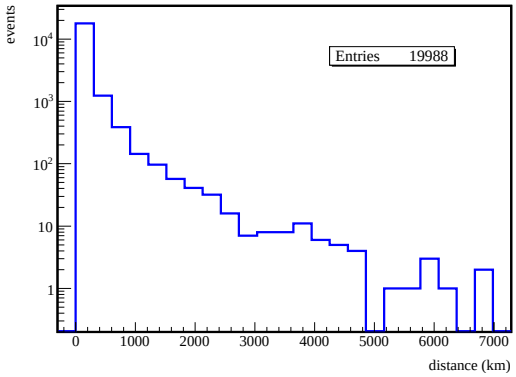

(b) Distances of Interaction Points to the Detector

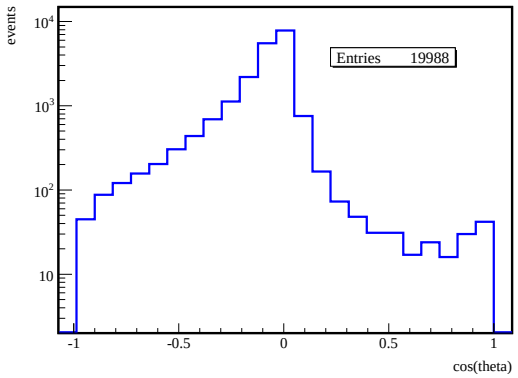

(c) Zenith Angle of the Interaction Point

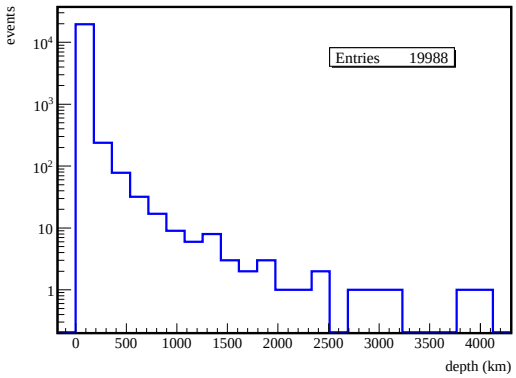

(d) Depth of the Interaction Point Inside the Earth

Fig. 7.10: Properties of the Interaction Point under the demand of two staus traversing the IceCube detector.

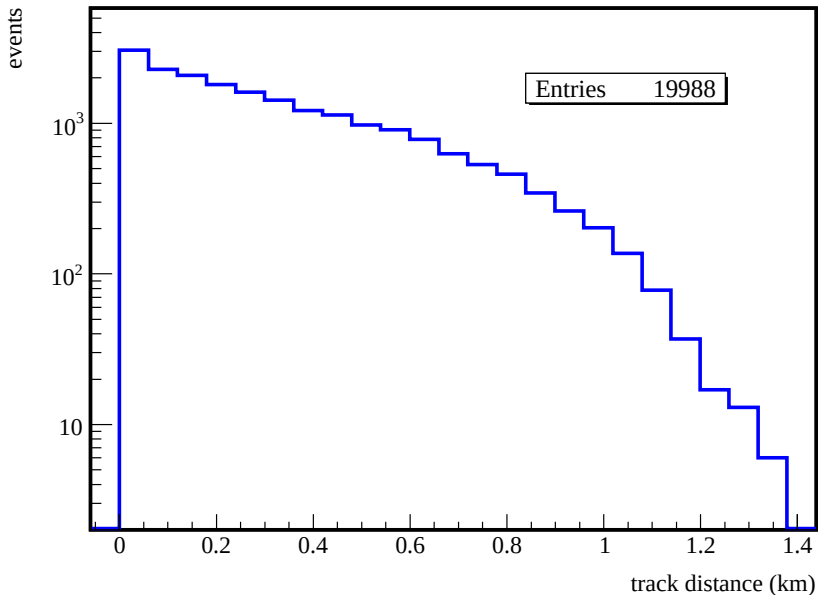

Fig. 7.11: stau Track Distance including the demand of both tracks traversing the detector.

be investigated. Not every stau is producing enough light to be seen in the detector. To increase the efficiency, it is useful to limit the stau production at lower energies. The sum of the energy of the staus at the positions S1 and S2 (Fig. 7.1) near the detector without further restrictions is displayed in Fig. 7.12. The technical realization of the simulation software limits the minimum kinetic energy to 1 GeV. Accordingly, the first filled bin in the histogram contains all staus pairs that have lost all their kinetic energy on the way to the detector and can be neglected. The reason for the reduction to lower energies visible from about $10^{4.5}$ GeV to $10^{2.75}$ GeV lies in the geometrical restrictions for the stau double tracks. Because both tracks have to traverse the detector volume they have to come from points relatively near to the detector. This results in the already mentioned belt at ϑ-angles of about 90 °. Thus, most of the staus only traverse less than 500 m of the Earth. These staus did not have enough time to lose much of their energy due to radiation losses and end up in the higher energy bins of Fig. 7.12.

Two terms are important for the understanding of the IceCube data: The number of *hit DOMs* and the number of *hits*. A hit DOM is a DOM that has reported activity. Normally this is the case when photons have been recognized by the PMT of the DOM. Every time a DOM reports activity, this is called a hit. Within one IceCube event, a hit DOM denotes one or more hits. Consequently, the number of hits is always equal or lager than the number of hit DOMs

$$N_{\text{hit}} \geq N_{\text{ch}}. \tag{7.15}$$

More generally, the number of hit DOMs is also called number of hit channels. Thus, for this value N_{ch} is used.

N_{hit} is a good measure for the light in the detector. In Fig. 7.13 the number of hits dependent on the energy of staus traversing the detector is plotted. Here the software simulation chain produces secondary particles and propagates light through the ice to the DOMs. The hits correspond to the photons arriving at the PMT. Simulations of the response of the detector hardware are not included here. The plot suggests a power law relation between the two variables. Obviously, from stau energies of $10^{3.5}$ GeV onwards, photons arrive at the IceCube DOMs.

The final decision of the minimum stau energy for a full simulation has to be done using the

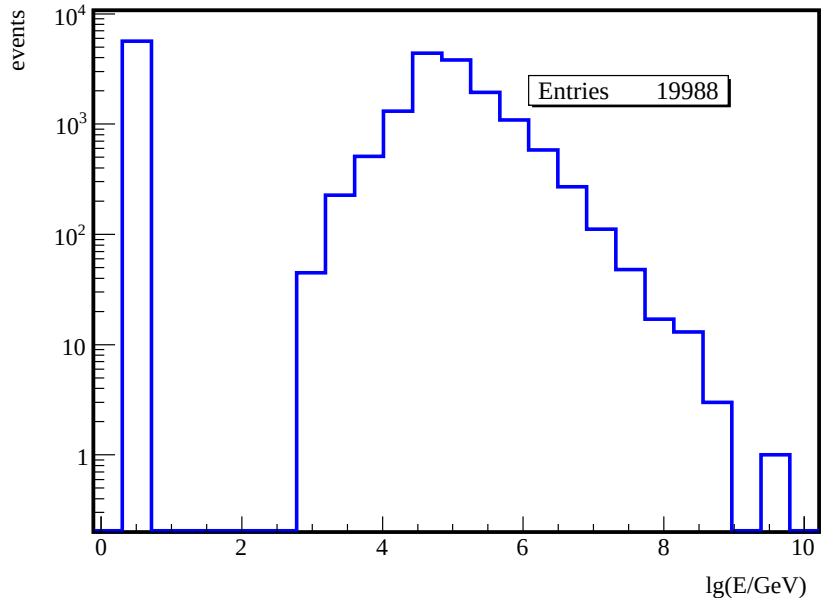

Fig. 7.12: stau Energy near the Detector including the demand of both tracks traversing the detector.

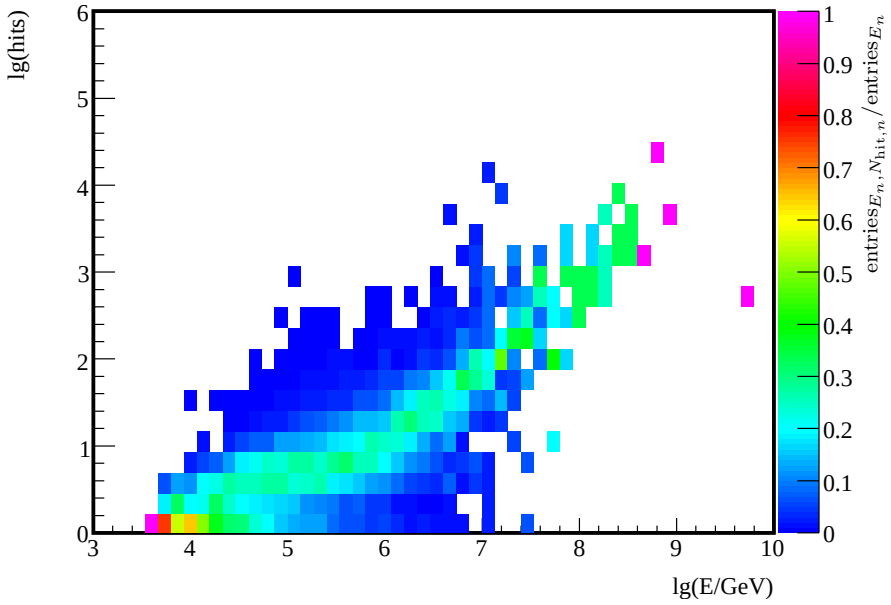

Fig. 7.13: Correlation Between stau Energy and N_{hit}. The bin color represents the number of entries in the bin divided by the number of all entries in the corresponding energy bin. This removes the shape of the stau energy spectrum from the histogram.

number of hit DOMs. Currently, IceCube uses a threshold for a simple majority trigger of 8 hit DOMs within a period of 5 µs. This limit should be reached by the incident staus. Fig. 7.14 shows the hit DOM distribution dependent on the stau energy. All events causing hits in less

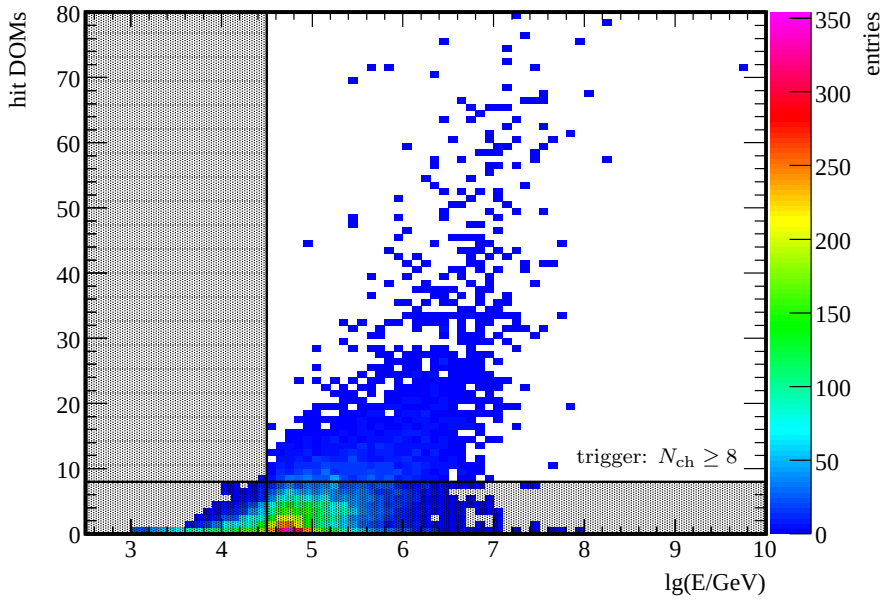

Fig. 7.14: Correlation Between stau Energy and N_{ch}. The trigger condition is achieved when 8 DOMs have been hit within a time window of 5 µs.

than 8 DOMs will be rejected, as the trigger condition is not achieved. Below an stau energy of $10^{4.5}$ GeV nearly no events reach this condition. For the simulation of events for testing a possible stau filter algorithm, the minimum stau energy at the stau starting points near the detector therefore is set to $10^{4.5}$ GeV. Simulated events with stau energies below this value will be rejected and not put into the further simulation chain.

Under this additional precondition, the initial distributions for the neutrino spectrum and the interaction point characteristics are changing again. The resulting distributions are plotted in Fig. 7.15.

The final stau track distance distribution is given in Fig. 7.16 and the final stau energy distribution can be found in Fig. 7.17.

All modules used in the simulation chain and their parameters are summarized in App. D.

The resulting files of the simulation act as testing material for the stau double track filter which will be introduced in the next chapter.

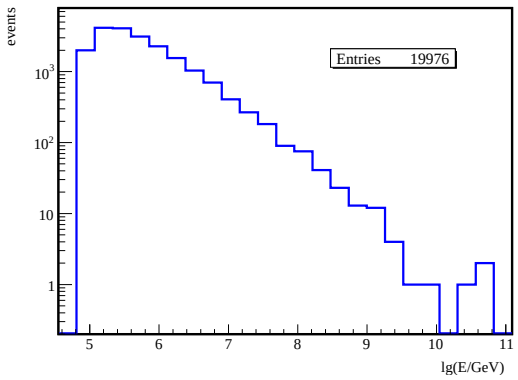

(a) Primary Neutrino Energy

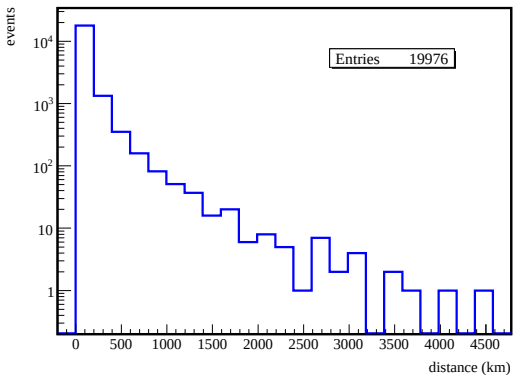

(b) Distances of Interaction Points to the Detector

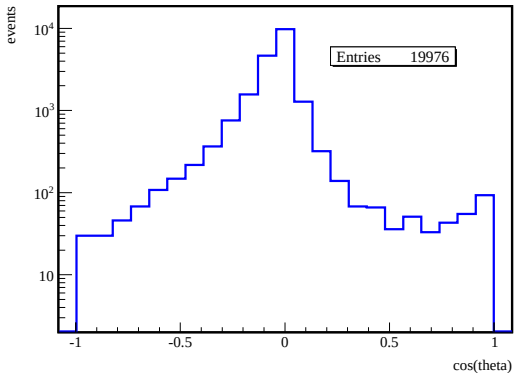

(c) Zenith Angle of the Interaction Point

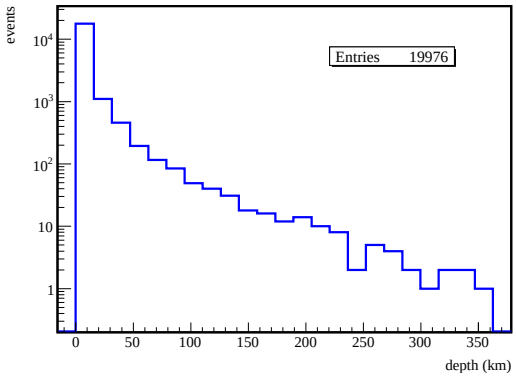

(d) Depth of the Interaction Point Inside the Earth

Fig. 7.15: Properties of the Interaction Point under the demand of a resulting minimum stau energy of $10^{4.5}$ GeV.

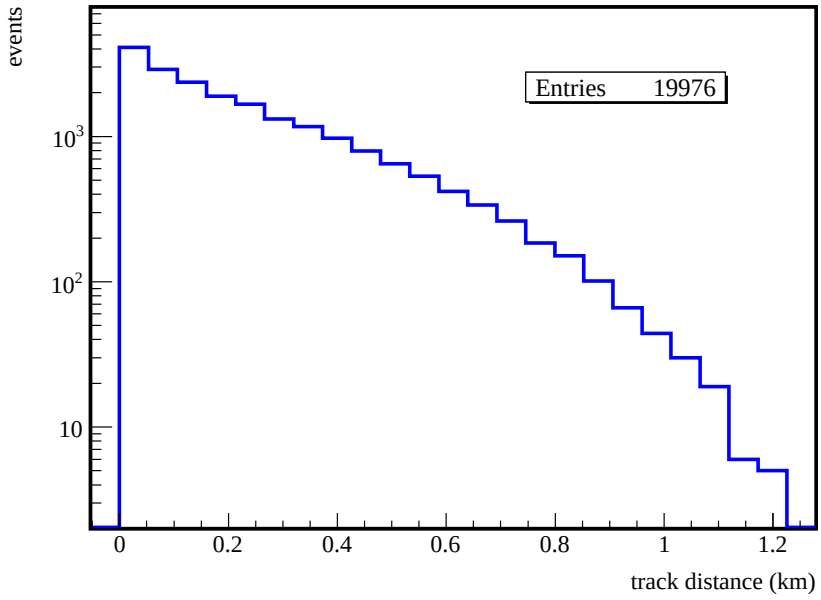

Fig. 7.16: Final stau Track Distance Distribution including the demand of both tracks traversing the detector and a minimum stau energy.

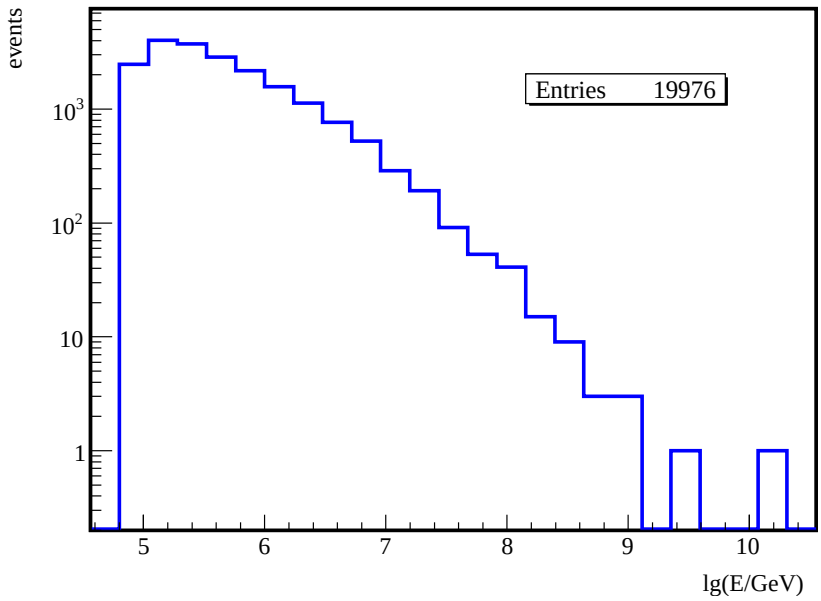

Fig. 7.17: Final Distribution of stau Energy Near the Detector including the demand of both tracks traversing the detector and a minimum stau energy of $10^{4.5}$ GeV.

8

Searching for SUSY events

The majority of IceCube neutrino events are caused by atmospheric neutrinos [Gee02; Kel09]. These neutrinos are generated in cosmic ray interactions with the atmosphere. Normally, they traverse the Earth without any effect. But for those neutrinos interacting inside the Earth, there is a small probability that the interaction takes place near the IceCube detector. If this is a charged current interaction, the resulting charged lepton can be detected. The expected signatures are described in Sec. 2.3.2. The muons, which create long traces inside the detection volume, are very important for IceCube. Because of the aligned signature of muon events, the direction of the primary neutrino can be calculated, and the creation of an event sky map is possible. Consequently, IceCube events are scanned for muon signatures. The *MuonFilter*, an online filtering module, is responsible for sorting out corresponding events. This online filter has the highest transparency of all online filters running at the South Pole. Therefore, a new filter searching for different signatures has to be tested for two things:

- Is it transparent to events, not passed by the MuonFilter?
- Does it find a useful subsample of the events passed by the MuonFilter?

To develop an stau filter for which one of the two questions is true, criteria have to be found which separate stau events from other IceCube events.

8.1 Filter Description

The most obvious difference between a neutrino induced SM lepton and a SUSY matter reaction is the double track structure of the produced SUSY particles. In case of long living staus, the double tracks can be detected by IceCube. The corresponding *geometric event signature* differs from the signature of single tracks. This is the central event feature that will be used by the *SUSYFilter* which is developed during the work for this thesis.

The general idea is to calculate the *tensor of inertia* (*ToI*), using the hit positions as discrete "masses". The ToI for discrete masses m_i is given by

$$I = \sum_i m_i \begin{pmatrix} y_i^2 + z_i^2 & -x_i y_i & -x_i z_i \\ -y_i x_i & x_i^2 + z_i^2 & -y_i z_i \\ -z_i x_i & -z_i y_i & x_i^2 + y_i^2 \end{pmatrix} \tag{8.1}$$

If one DOM is hit more than once, the same hit position is counted as often as the DOM is hit. The mass m_i in the context of hits in DOMs can be translated as the electric charge delivered by the hit PMT. Within this thesis, the origin for the coordinates for the calculation of the ToI is always set to the center of mass of the hits.

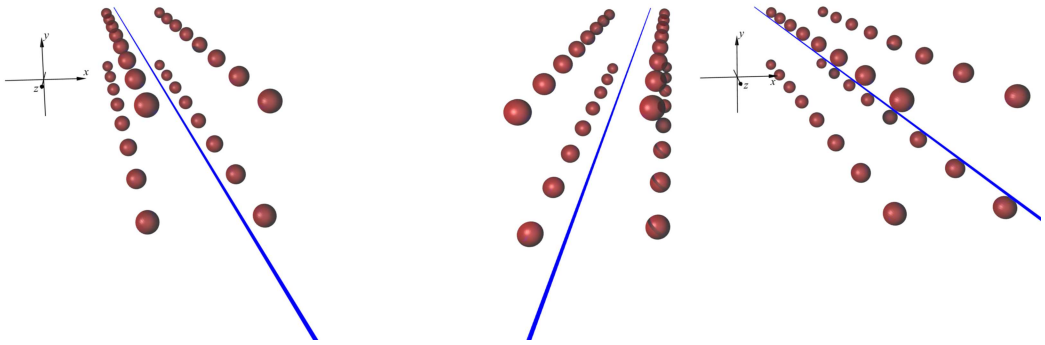

(a) Single Track (b) Double Track

Fig. 8.1: Example Hit DOM configurations to explain the results of the tensor of inertia calculation.

Given the example situation plotted in Fig. 8.1(a). Here all toy DOMs have the same distance of 10 units. The resulting ToI is

$$I_1 = 32 \cdot \begin{pmatrix} 550 & 0 & 0 \\ 0 & 550 & 0 \\ 0 & 0 & 50 \end{pmatrix}. \tag{8.2}$$

Physical information can be gained out of the *eigenvalues* and the *eigenvectors* of the ToI. The eigenvalues are called momenta of inertia for an object rotating around the corresponding eigenvector and the center of mass. The eigenvalues and eigenvectors are obtained by diagonalization of the ToI [Fis97]. In this simple case, the diagonalization is not necessary anymore. Because of the chosen geometry, the eigenvalues are the diagonal elements and the eigenvectors the axes of the coordinate system.

Obviously, the eigenvalues belonging to the axes with the smallest expansion (x and y) of the hit distribution are larger than the one belonging to the z-axis. This is a first useful result.

The same calculation can be done for the example given in Fig. 8.1(b). The ToI then changes to

$$I_2 = 64 \cdot \begin{pmatrix} 550 & 0 & 0 \\ 0 & 775 & 0 \\ 0 & 0 & 275 \end{pmatrix}. \tag{8.3}$$

The distribution of the mass along the y- and z-axis does not change, but the amount of mass is doubled. Consequently, the eigenvalue for the rotation around the x-axis is increased by a factor of 2. The moment of inertia simply doubles. The situation along the other axes is more complicated. The largest eigenvalue belongs to the eigenvector along which the geometrical hit distribution has the lowest expansion. In this case, the mean distance of hits to the rotation axis has the highest possible value. In Fig. 8.1(b) this is the eigenvalue belonging to the rotation around the y-axis.

For the further discussion, it is useful to give unique names to the eigenvectors and eigenvalues. The eigenvalues will be numbered beginning with the smallest

$$\lambda_1 \leq \lambda_2 \leq \lambda_3 \tag{8.4}$$

and the corresponding eigenvectors will carry the same numbers $\vec{x}_1$, $\vec{x}_2$ and $\vec{x}_3$. In the given examples the eigenvectors are $\vec{x}_1 = \vec{e}_z$, $\vec{x}_2 = \vec{e}_x$ and $\vec{x}_3 = \vec{e}_y$.*

Obviously, The two examples are not chosen by chance. In the first case, a single track like hit signature is adumbrated and the second example shall demonstrate the hit distribution of a double track. By looking at the two eigenvectors with the lowest hit expansion, $\vec{x}_2$ and $\vec{x}_3$, a characteristic shape becomes visible. Defining a plane perpendicular to the eigenvector with the highest hit expansion $\vec{x}_1$ (this is a plane expanded by $\vec{x}_2$ and $\vec{x}_3$)

$$P: \quad \vec{x}_1 \cdot \vec{r} = 0, \tag{8.5}$$

the double track delivers an oval hit distribution (Fig. 8.2(b)) and the single track a round one (Fig. 8.2(a)) when projecting all hits on this plane, respectively an oblate or prolate geometry in three dimensional space. For the round distribution holds $\lambda_2 \sim \lambda_3$ and for the oval $\lambda_2 < \lambda_3$. Consequently, the comparison of λ_2 and λ_3 is a candidate for an indicator for double stau events.

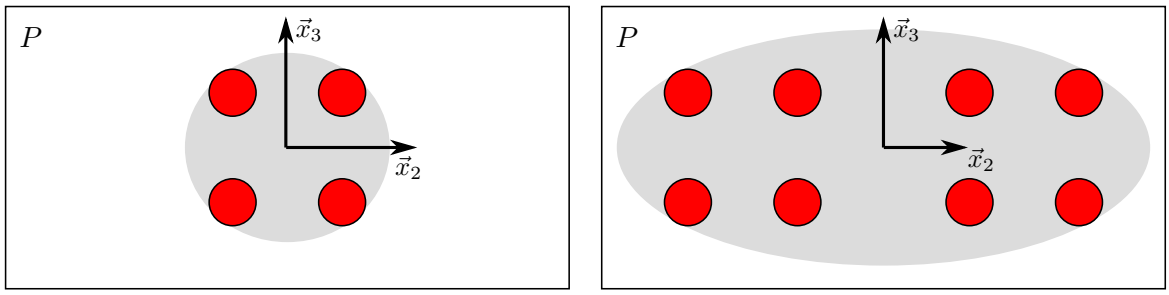

(a) Single Track (b) Double Track

Fig. 8.2: Schemes of the Projected 2D Hit Distributions.

The availability of the ToI main axes in form of the eigenvectors allows for an alternative concept. After the projection of all hits onto one of the eigenvectors, the extension of the hit distribution along this eigenvector can be expressed with the help of the standard deviation of the hit distribution

$$\sigma_i = \sqrt{\frac{1}{N_{\text{hit}} - 1} \sum_{j=1}^{N_{\text{hit}}} \left(y_j^{(i)} - \bar{y}^{(i)} \right)^2}. \tag{8.6}$$

The real number $y_j^{(i)}$ is the position of projection of hit j along the eigenvector i. The offset is arbitrary as it cancels out in Eq. 8.6. In this case, the numbering of the σ_i is beginning at the largest σ-value because of the coupling to the eigenvectors. Accordingly, the comparison of σ_2 and σ_3 delivers a possible criterion for event filtering. In this case, the three sigma values are $\sigma_1 = 23.28$, $\sigma_2 = 5.08$ and $\sigma_3 = 5.08$ for the single track and $\sigma_1 = 23.09$, $\sigma_2 = 15.94$ and $\sigma_3 = 5.04$ for the double track.

To use the ToI for filtering, the events put into the SUSYFilter have to be cleaned. There are several event signatures and properties that make the filter ineffective. The event cleaning is described in the next section. The cleaning mechanisms are part of the SUSYFilter module and will be applied to the data directly before using the ToI filtering algorithm.

*In the first example, $\vec{x}_2$ and $\vec{x}_3$ can be permuted.

8.2 Event Cleaning

The ToI filtering method has several weak points. To avoid events without double tracks passing the filter, it is useful to reject all events not satisfying several minimum demands. These demands are listed here.

8.2.1 Number of Hit DOMs

The minimum requirement for the useful calculation of a ToI is a sufficient large number of supporting points. Consequently, the number of hit DOMs N_{ch} has to be higher than a minimum number. The chosen value is 8. This is also the default trigger level for the simple majority trigger.

8.2.2 Number and Position of Hit Strings

If all hits in an event occurred only along one or two strings, it is not possible with the ToI method to find out whether detected light results from one or two tracks. This is also the case for next neighbor strings. The minimum number of strings, therefore, is set to $N_{\mathrm{string}} \geq 3$ and the maximum distance of all hit strings to all other hit strings has to be at least $d_{\mathrm{string}}^{\mathrm{max}} \geq 150\,\mathrm{m}$, which safely covers the distance of 125 m between two strings in IceCube.

8.2.3 Track Direction

The most important filtering is the rejection of down-going muons. A very simple method providing a basic down-going rejection is also provided by the SUSYFilter module. Here the hit timing becomes important. Every hit has a hit time t_i. If every hit position of one event is projected onto the z-axis of the IceCube coordinate system and the resulting position z_i is plotted against the corresponding hit time t_i, graphs, like the ones presented in Fig. 8.3, are the outcome. The z-axis points to the South. Accordingly, the slope s_z of linear fit through the points can be used for deciding whether the event is down-going ($s_z < 0$) or up-going ($s_z > 0$). The Čerenkov light cone from a charged particle, which is traversing the detector perfectly horizontally, can cause hits in every depth. The mean times from hits measured above and below, but at the same distance to the particle trajectory, are identical. This, in general, results in a hyperbolic shape when plotted into a graph like Fig. 8.3. Consequently, the linear fit is parallel to the abscissa and has a slope of 0.

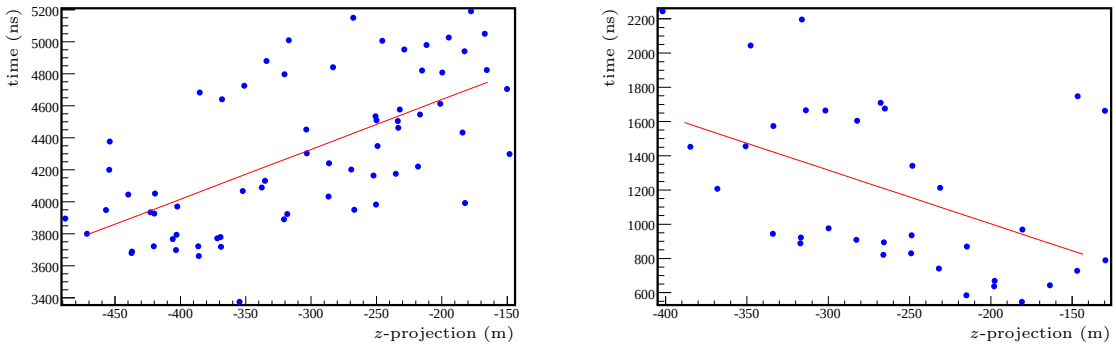

(a) up-going (b) down-going

Fig. 8.3: z-Projection vs. Hit Time. Pictures from simulated stau events.

The projections in Fig. 8.3 have slopes of $s_{up} = 3.12\,\mathrm{ns/m}$ and $s_{down} = -3.14\,\mathrm{ns/m}$. In Fig. 8.4, double stau events generated with the SUSY-gen module are plotted against their ϑ-angle.* Because of the source point distribution of the stau tracks around the detector, also

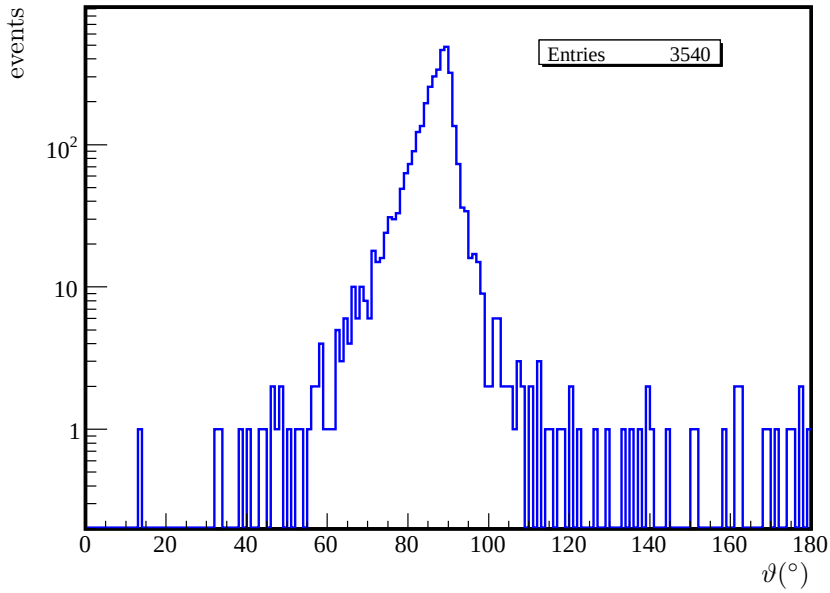

Fig. 8.4: ϑ-angle of Incident stau Tracks.

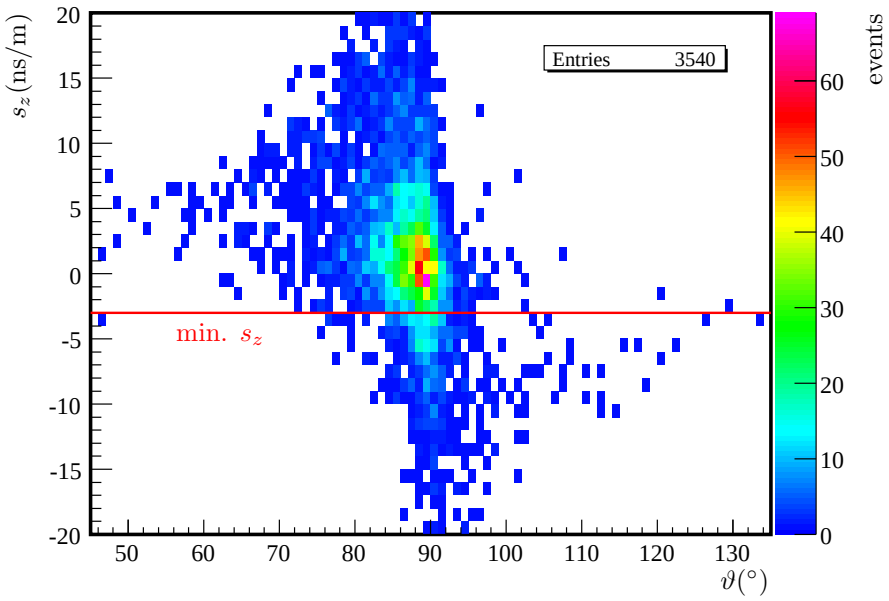

Fig. 8.5: Correlation between Time Projection and stau ϑ-angle. The events contain double stau tracks generated with the SUSY-gen module.

*A vector with $\vartheta = 0\,^\circ$ points along the z-axis towards the South (up-going). If two stau tracks are simulated, the ϑ-angle results from the bisecting line.

the stau track direction peaks at a ϑ-angle of about 90 °. This makes it difficult to find a good value for the minimum slope of the linear fit. Comparing ϑ with s_z (Fig. 8.5) a cut demand can be found. The chosen minimum for s_z is $-3\,\mathrm{ns/m}$. A value lower than 0 is a compromise. It is cutting away 9.8 % of the events which have ϑ-angle of less than 90 ° and which are fulfilling the prior cleaning demands, but 42.1 % of those with $\vartheta \geq 90\,°$. The plot of the data from simulated atmospheric muon events in Fig. 8.6 shows a rejection of 87.2 % over all events that are passing the former event cleaning algorithms.

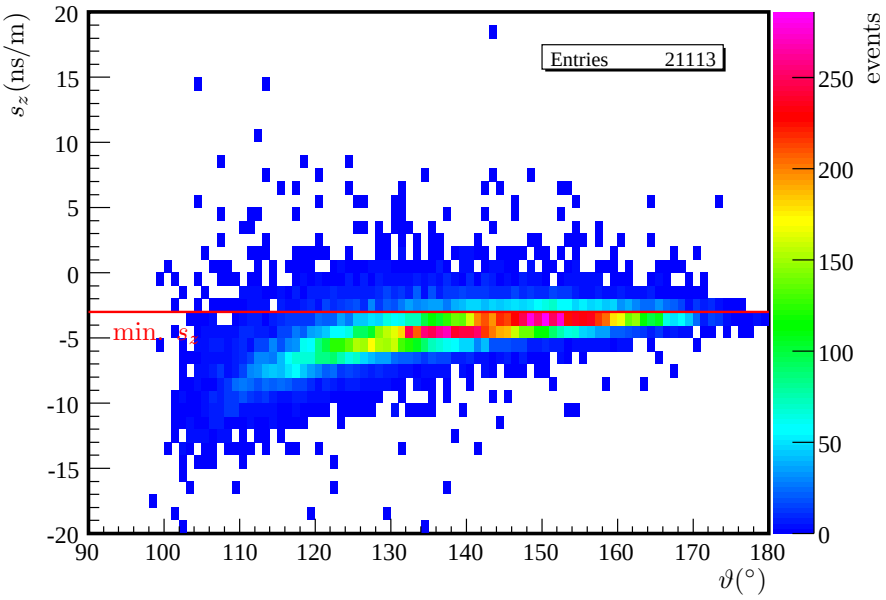

Fig. 8.6: Correlation between Time Projection and stau ϑ-angle for Background Data. The events are generated in an IceCube mass production of atmospheric single muons (data set 1313).

8.2.4 Flatness

This and the following cleaning options already use features of the ToI. Accordingly, the ToI and the resulting eigenvalues and eigenvectors have to be calculated to allow for using the cleaning options.

Tracks hitting only strings lying in the same plane always cause a two dimensional hit DOM distribution. These events always would be recognized as double tracks by the SUSYFilter. In this case, the value σ_3 becomes very small. A very easy way to avoid single track events being recognized as double track events because of only hitting strings lying in a row is to limit the minimum value of σ_3. A useful value should be large enough, to cover variations of the DOM positions along each string. For the event cleaning a value of $\sigma_3 \geq 4\,\mathrm{m}$ has been chosen.

8.2.5 Sphericity

In the context of geometrical event cleaning, also the other extreme situation can occur: An event can have a spherical extension. In this case, the directions of the eigenvectors of the ToI are not providing any information. Possible candidates for events of this shape are charged current ν_e interactions (↗Sec 2.3.2) and hadronic cascades produced by neutral current neutrino scattering. As it turns out during the testing procedures of the SUSYFilter, this test does not

provide a better filtering result. Consequently, the sphericity check is switched off in the current SUSYFilter version.

8.2.6 Event Causality

As mentioned above, the smallest eigenvalue belongs to the eigenvector with the largest geometrical event extension. If the particle direction is lying in parallel to the eigenvector $\vec{x}_1$, the speed of the particles along this vector can be calculated. The principle of the speed calculation is the same as in Sec. 8.2.3, but the projection axis is changed from the z-axis to the axis defined by $\vec{x}_1$. The maximum speed of the particle(s) will be limited by the speed of light. The corresponding slope is

$$s = \frac{1}{v} \quad \text{with} \quad |s| > \frac{1}{c} = 3.33564\,\text{ns/m} \equiv s_c. \tag{8.7}$$

A typical situation caused by a two track induced event is given in Fig. 8.7. In this situation, the

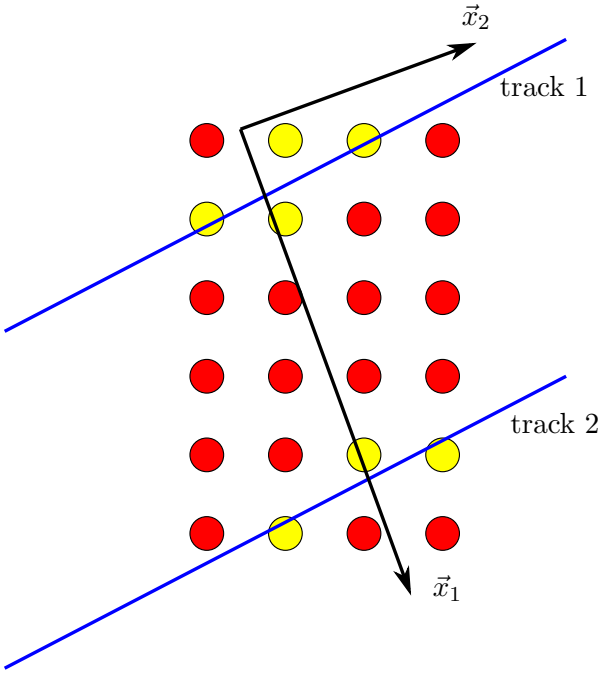

Fig. 8.7: (Pretended) Violated Event Causality. The circles represent optical modules. Red modules are not hit, yellow modules have been hit by photons emitted along one of the particle tracks.

eigenvector $\vec{x}_1$ would not point along the particle trajectories. If the two tracks result from an stau pair, the hit times in both hit clusters are nearly identical. The s-value consequently falls below s_c. For particle tracks in parallel to $\vec{x}_1$, this violates causality.

The use of this information can be discussed controversially. In a first approach, events showing this behavior have been rejected because of the undefined geometrical behavior along the other eigenvectors. Taking a closer look, the extension along the eigenvectors $\vec{x}_2$ and $\vec{x}_3$ is not disturbed by the direction of the eigenvector $\vec{x}_1$. The specific oblate shape of double track induced events is still detectable by the ToI filter method. Accordingly, the check for the event causality is not done for event cleaning.

8.2.7 External Event Processing

Before entering the SUSYFilter module, the generated events are passing a few other modules taking care of the data quality and doing some basic data processing. These modules are listed and explained in App. E.

8.3 Filter Settings

When looking for intelligent filter settings, the criteria for the decision whether the filter is effective or not have to be found. In the context of double track events, two special parameters deserve closer attention:

- The track distance and
- the number of hits produced by every track.

If the track distance is small compared to the distance of DOMs in the detector array, the hits from the individual tracks cannot be resolved. In this case, the double track would look like a single track and a rejection is useful.

An identification of a double track can only be done if a minimum number of hits is caused by each of the two tracks.

8.3.1 Dataset

With the SUSY-gen module 29995 events according to the settings in App. D have been produced. The reduction of the amount of valid events due to the five quality cuts $N_{\text{ch}} \geq 8$, $N_{\text{string}} \geq 3$, $d_{\text{string}}^{\text{max}} \geq 3$, $s_z \geq -3\,\text{ns/m}$ and $\sigma_3 > 4\,\text{m}$ is plotted in the Figs. 8.8. The cuts deliver

value	demand	remaining	%
generated		29995	100.00 %
N_{ch}	≥ 8	4313	14.38 %
N_{string}	≥ 3	3662	12.21 %
d_{string}	$\geq 150\,\text{m}$	3540	11.80 %
s_{up}	$\geq -3\,\text{ns/m}$	2962	9.87 %
σ_3	$\geq 4\,\text{m}$	2719	9.06 %

The remaining 2719 events are used to optimize the SUSYFilter parameters.

8.3.2 Configuring the Filter

Two relations are interesting to discriminate between single and double tracks:

$$r_\lambda = \frac{\lambda_3}{\lambda_2} \text{ and } r_\sigma = \frac{\sigma_2}{\sigma_3}. \tag{8.8}$$

The quality of the settings for r_λ and r_σ can be measured by comparing the amount of single track events and double track events passing the filter applying the cleaning cuts. A perfect filter would pass all double track events while all single track events are rejected. In a more realistic scenario, this behavior is dependent on the event geometry. The track distance has to be large enough so that both tracks produce hits in different regions of the detector and the amount of hits from each single track has to be high enough to achieve a distribution having a flat shape. The Figs. 8.9(a) and 8.9(b) show the distributions of the two different ratios.

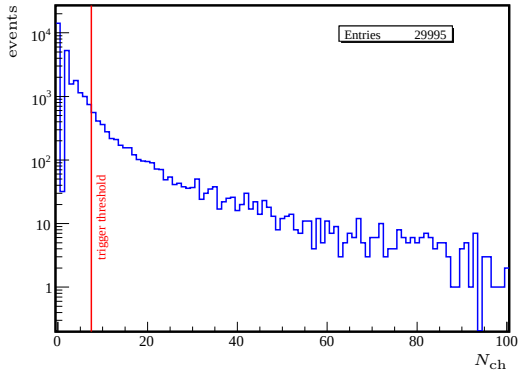

(a) $N_{\mathrm{ch}} \geq 8$

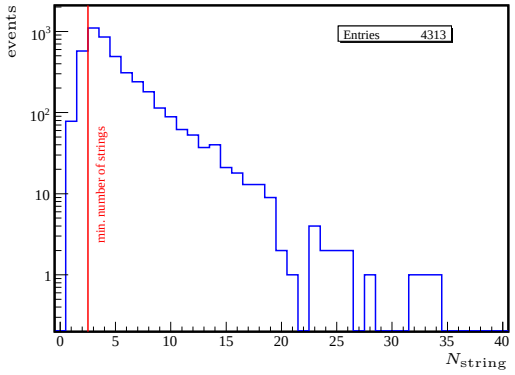

(b) $N_{\mathrm{string}} \geq 3$

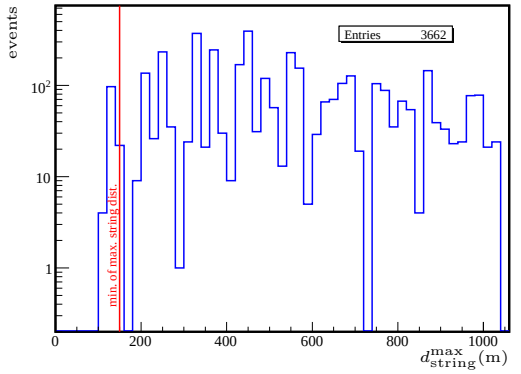

(c) $d^{\mathrm{max}}_{\mathrm{string}} \geq 150\,\mathrm{m}$

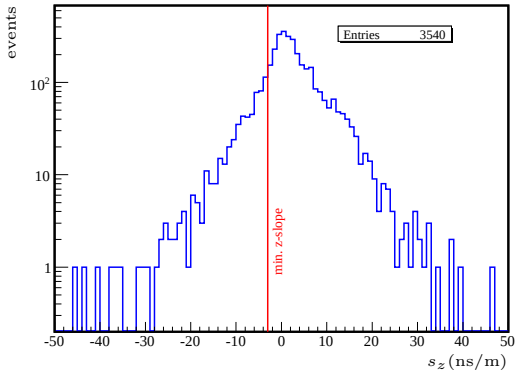

(d) $s_z \geq -3\,\mathrm{ns/m}$

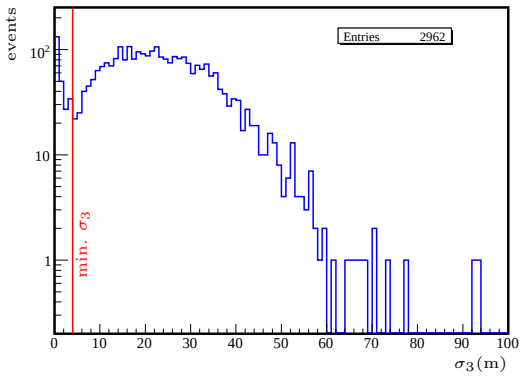

(e) $\sigma_3 \geq 4\,\mathrm{m}$

Fig. 8.8: Event Cleaning. The plots show the reduction of the amount of data due to event cleaning. The cuts are done from (a) to (e). Always only the events passing the former cut are added to the next histogram.

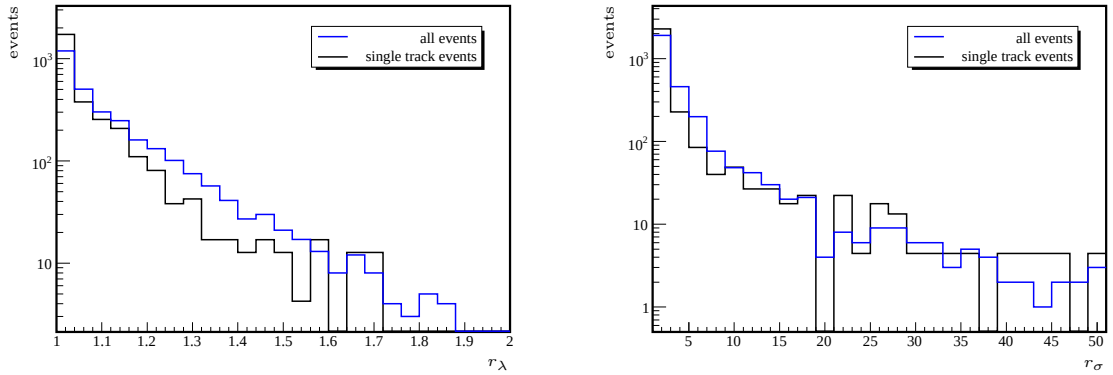

(a) (b)

Fig. 8.9: Possible Parameters for Event Discrimination. The number of single tracks in the data sample is scaled to the number of entries of the complete sample.

In Fig. 8.10(a) and 8.10(b) the variables r_λ and r_σ are related to the track distance and the amount of hit DOMs caused by every single stau track. Both figures show a similar behavior. With a rising amount of hit DOMs per track, the correlation between the discrimination values r_λ and r_σ and the track distance becomes more obvious. In this thesis, the optimization of the cut parameters $r_\lambda^{\min}$ and $r_\sigma^{\min}$ is done only by eye. The values $r_\lambda^{\min} = 1.15$ and $r_\sigma^{\min} = 2.5$ have been chosen.

For comparison, these cuts can now be applied to double tracks with only one stau producing hits. The corresponding histograms are shown in Fig. 8.11. In the case of $r_\lambda \geq 1.15$, the cut removes 84.4 % of the single particle traces and in the case of $r_\sigma \geq 2.5$ 82.1 %.

Including the event cleaning with the settings described above, the SUSYFilter delivers the following results for double stau events satisfying the demand $N_{\text{ch}}^{\min}/\text{track} \geq 4$:

double track definition	$\boldsymbol{N}_{\textbf{events}}$	**param.**	$\boldsymbol{N}_{\textbf{passed}}$	$\boldsymbol{N}_{\textbf{passed}}/\boldsymbol{N}_{\textbf{events}}$
$N_{\text{ch}}/\text{track} \geq 4$	1942	r_λ	431	22.2 %
		r_σ	577	29.7 %
		$r_\lambda \wedge r_\sigma$	317	16.3 %
		$r_\lambda \vee r_\sigma$	691	35.6 %
+ track distance $\geq 150\,\text{m}$	841	r_λ	337	40.1 %
		r_σ	485	57.7 %
		$r_\lambda \wedge r_\sigma$	288	34.2 %
		$r_\lambda \vee r_\sigma$	534	63.5 %

For all stau events, also those with less hit DOMs per track, the event reduction within the different filtering steps is plotted in Fig. 8.12.

The filter performance dependent on the track distance using the two parameters r_σ and r_λ is shown in Fig. 8.13. The more stringent r_λ filtering increases the filter performance for small track distances. The r_σ filtering is transparent for nearly all large track distances.

These are very promising results. Now, The SUSYFilter has to be applied to non-stau data to ascertain its effectivity in event rejection.

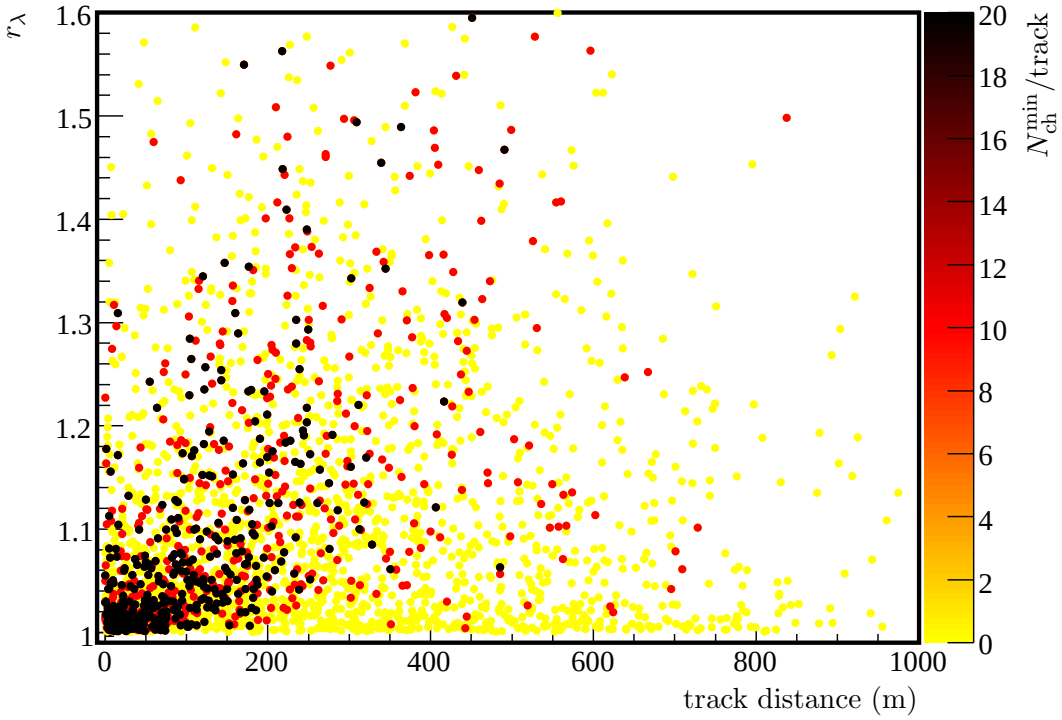

(a) $r_\lambda = \lambda_3/\lambda_2$

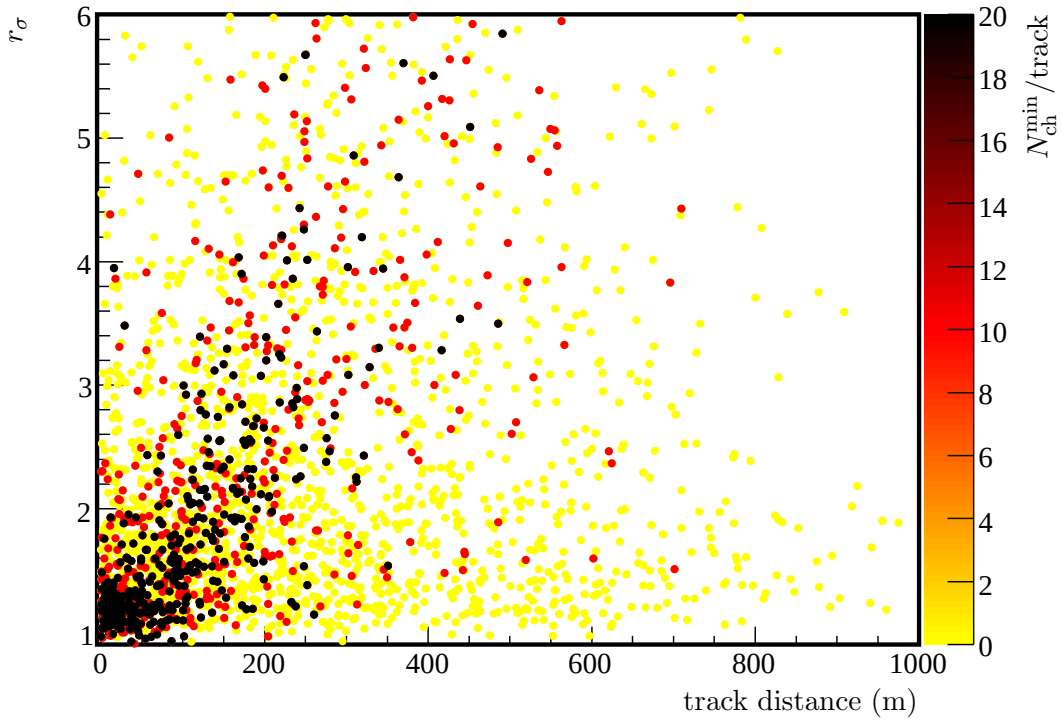

(b) $r_\sigma = \sigma_2/\sigma_3$

Fig. 8.10: Possible Parameters for Event Discrimination. Plotted are the ratio r_λ and r_σ against the track distance. The color coding represents the number of minimum hit DOMs $N_{\mathrm{ch}}^{\mathrm{min}}$ caused by each of the two stau tracks. In both figures, three different values for $N_{\mathrm{ch}}^{\mathrm{min}}$/track have been chosen: $N_{\mathrm{ch}}^{\mathrm{min}}$/track = 0, 10 and 20.

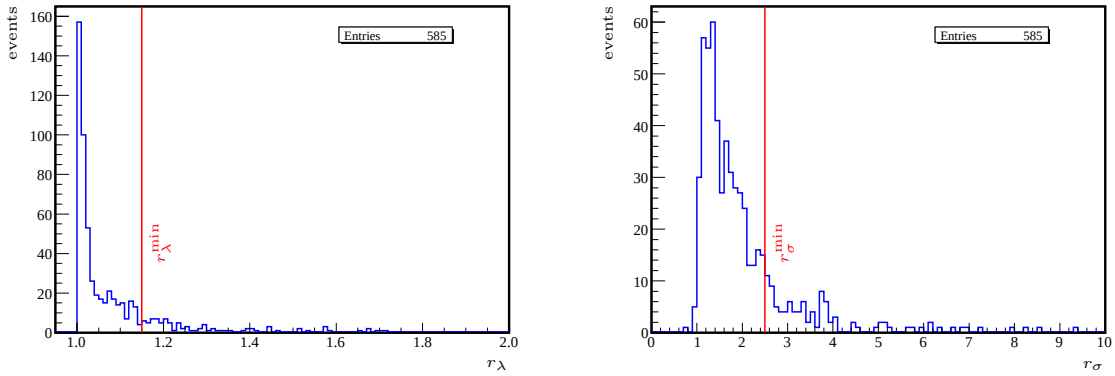

(a) $r_\lambda = \lambda_3/\lambda_2$ (b) $r_\sigma = \sigma_2/\sigma_3$

Fig. 8.11: Event Discrimination Parameters Applied on Single stau Tracks.

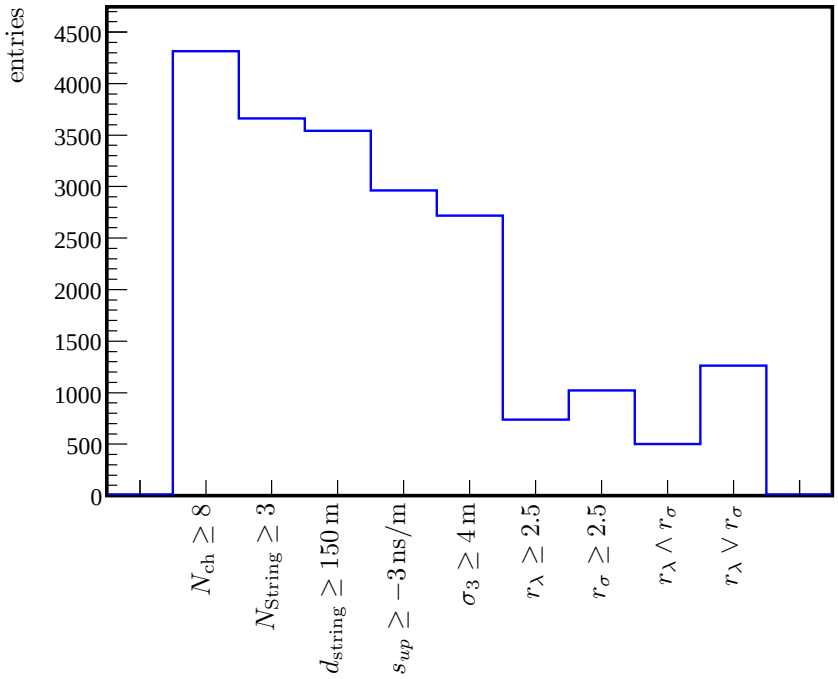

Fig. 8.12: Plot of the Filter Steps Applied to Double stau Track Data.

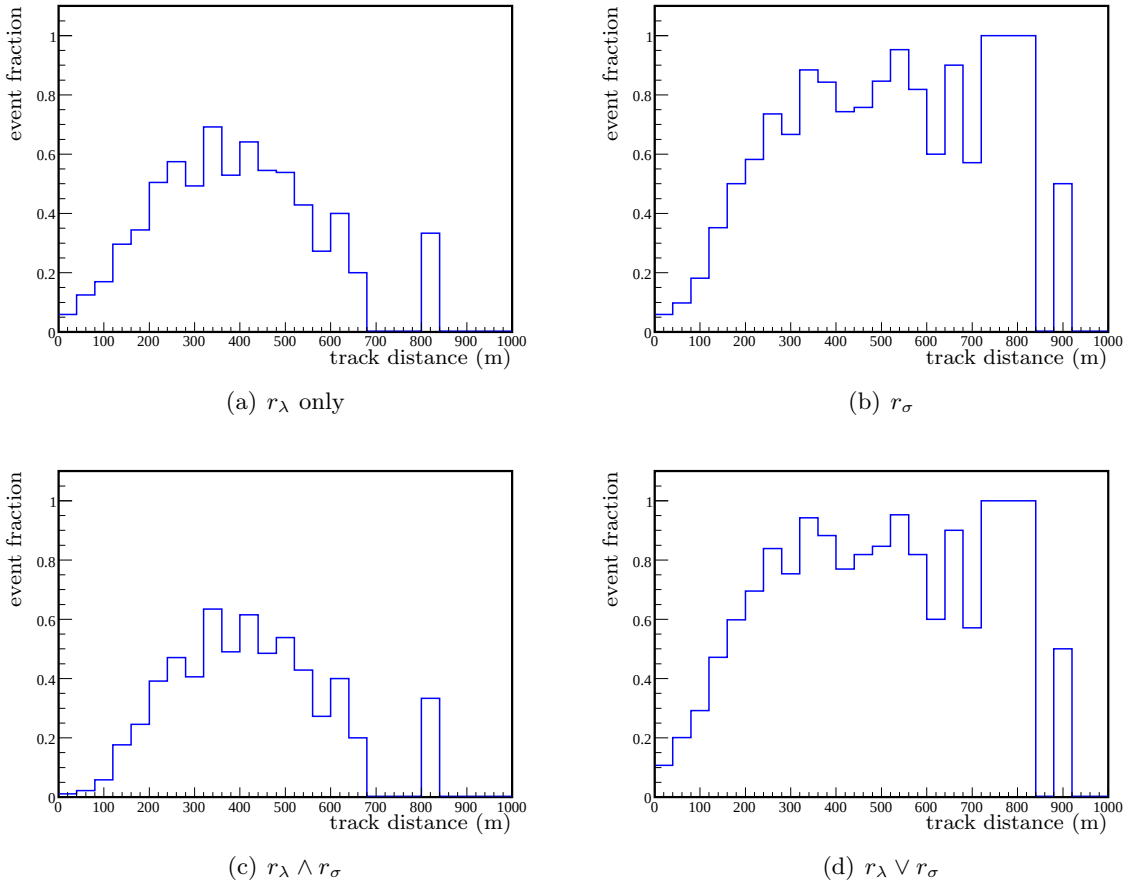

(a) r_λ only (b) r_σ

(c) $r_\lambda \wedge r_\sigma$ (d) $r_\lambda \vee r_\sigma$

Fig. 8.13: Filter Performance for Double stau Tracks. In this plots only double tracks with $N_{\text{ch}}/\text{track} \geq 4$ are counted.

8.4 Applying the SUSYFilter

The response of the SUSYFilter to double stau data is known, now. But it is also important to know the passing rates for other event types. The SUSYFilter is applied to three different data sets:

- down-going single muons*,
- atmospheric double coincident muons† and
- unfiltered real data from the South Pole.‡

For all data sets, the corresponding plots of the filter response are given in Fig. 8.14.

8.4.1 Down-going Muons

On the one hand, these events deliver the highest contribution to the sum of all IceCube events. The event rate in the simulation data is set to about 1050 Hz. On the other hand, the atmospheric

*Dataset 1313: IC40+TWR CORSIKA-in-ice single muon, polygonato model with unweighted spectrum of Hoerandel, using AHA07v2 photon tables. Angular range of $0^\circ < \vartheta < 89.99^\circ$ and $600\,\text{GeV} < E_{\text{prim}} < 10^{11}\,\text{GeV}$

†Dataset 1360: IC40+TWR CORSIKA-in-ice double coincident, polygonato model with unweighted spectrum of Hoerandel, using AHA07v2 photon tables. Angular range of $0^\circ < \vartheta < 89.99^\circ$ and $600\,\text{GeV} < E_{\text{prim}} < 10^{11}\,\text{GeV}$

‡Run 111310: July 15$^{\text{th}}$, 2008

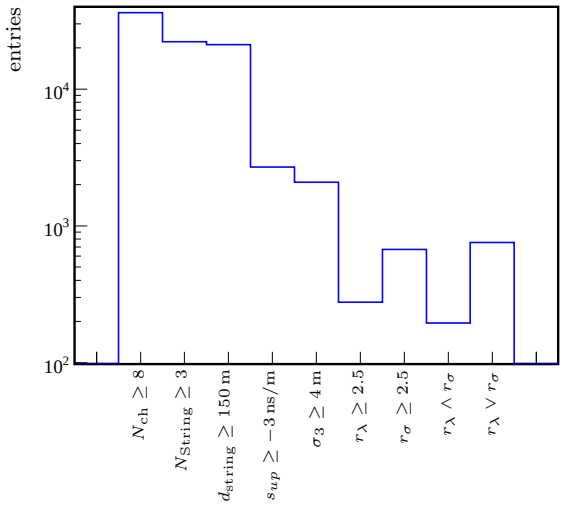

(a) Single Down-going Muons

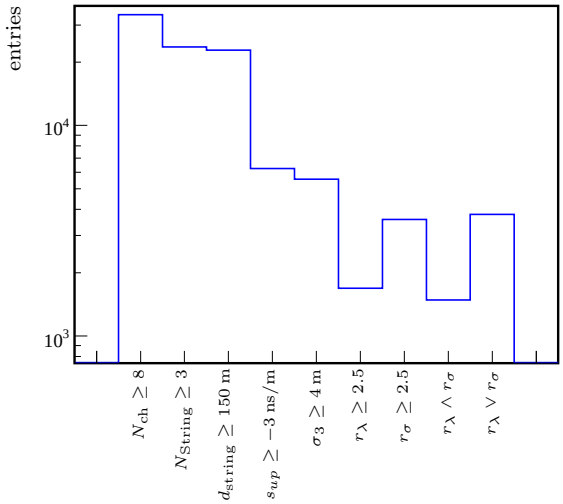

(b) Double Coincident Atmospheric Muons

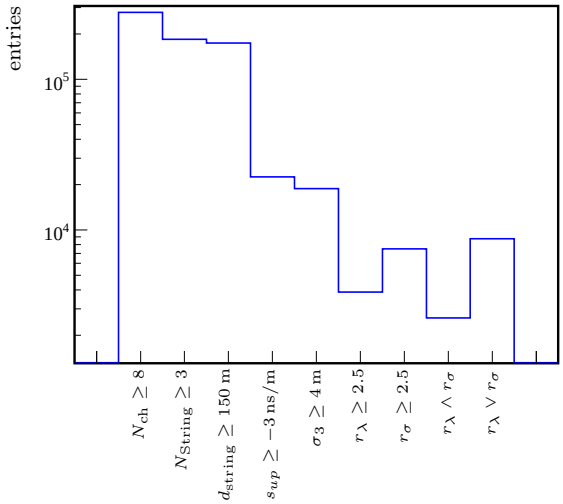

(c) Real Data

Fig. 8.14: Filter Steps for Several Data Sets.

muon events are not of interest in the context of stau double track filtering. Consequently, none or at least only a very small fraction of these events are allowed to pass the SUSYFilter. The application onto the simulated single muon data set delivers the following results for the several combinations of r_λ and r_σ filtering:

N_{events}	param.	N_{passed}	relative	rate
45678	r_λ	277	0.60 %	6.30 Hz
	r_σ	674	1.48 %	15.54 Hz
	$r_\lambda \wedge r_\sigma$	195	0.43 %	4.52 Hz
	$r_\lambda \vee r_\sigma$	756	1.66 %	17.43 Hz

These values are comparable to the passing rate of the MuonFilter of 12.22 Hz for this data set.

8.4.2 Coincident Atmospheric Muons

The detection volume of IceCube is large enough to have significant statistics of traversing muons from coincidental air showers. Normally, a coincidence consists of not more than two air showers in the same event.* The resulting muons can produce event signatures on which the SUSYFilter is sensitive. Therefore, the amount of passed double coincidence events is important to know. The filtered event numbers are

N_{events}	param.	N_{passed}	relative	rate
39341	r_λ	1687	4.29 %	5.79 Hz
	r_σ	3583	9.11 %	12.30 Hz
	$r_\lambda \wedge r_\sigma$	1485	3.77 %	5.09 Hz
	$r_\lambda \vee r_\sigma$	3785	9.62 %	12.99 Hz

This is significantly higher than for the single muon data set. Because of the lower rate of coincident events of about 135 Hz, the passing rate is similar to the passing rate for single muon events. Again, the passing rates are similar to the rate of the MuonFilter of 10.62 Hz.

8.4.3 Real Data

The final decision about the filter settings can only be done after the application on real data. The event rate of the chosen data sample is 1119.302 Hz. If the passing rate is too high, the SUSYFilter cannot be used as an online filter at the South Pole. The numbers obtained with the current settings are

N_{events}	param.	N_{passed}	relative	rate
336095	r_λ	3863	1.15 %	12.87 Hz
	r_σ	7497	2.23 %	24.97 Hz
	$r_\lambda \wedge r_\sigma$	2603	0.77 %	8.67 Hz
	$r_\lambda \vee r_\sigma$	8757	2.61 %	29.16 Hz

The passing rate of the MuonFilter using this data sample is 1.74 % corresponding to a data rate of 19.43 Hz. As the MuonFilter is the most important physics filter applied at the Pole, it

*Currently, even simulation mass productions for three coincident muons are available.

performs a relatively weak event rejection. An additional filter searching for very special physics should not exceed a passing rate of about 1 Hz. Accordingly, the current filter settings are not restrictive enough.

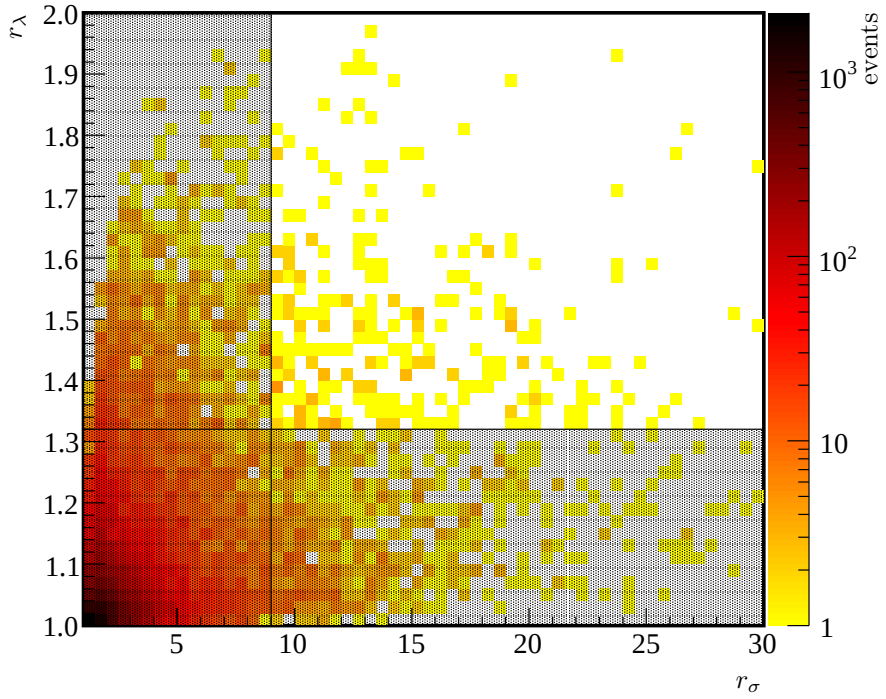

Fig. 8.15: Refinement of the Filter Parameters.

A possible new choice of parameters using the combined $r_\lambda \wedge r_\sigma$ filtering can be made with the help of Fig. 8.15. To achieve a passing rate of 1 Hz, only about 300 events are allowed to pass the SUSYFilter. Using r_λ and r_σ nearly symmetrically for event filtering, the corresponding values are $r_\lambda \geq 1.32$ and $r_\sigma \geq 9.0$. These values cause a reduction of the amount of detected stau events from the generated double stau track data set to only 1.0 %. This is not enough for searching an exotic data signature.

A different way is to search for staus in the events passed by the MuonFilter.

8.5 Online or Offline Filtering

A very good reason not to use the SUSYFilter online at the Pole has already been given in the last section. This is not automatically a disadvantage. The offline event processing is not as time critical as online filtering. Consequently, an offline filter is not such a subject to restrictions as an online filter. If other filters, like the MuonFilter, pass a significantly high amount of double tracks, the search with the SUSYFilter can be done offline. The application of the MuonFilter to the generated data set with double staus delivers the result plotted in Fig. 8.16. Like for the other performance plots using the double stau data, also here $N_{\text{ch}}/\text{track} \geq 4$ is a demand for events being counted. Obviously, the MuonFilter cuts away double tracks with a high track separation. This is expected for a filter searching for single muon tracks. The amount of events passing both, the Muon- and the SUSYFilter, is displayed in Fig. 8.17. The number of 317 events passed by the SUSYFilter in the $r_\lambda \wedge r_\sigma$ only setup is reduced to 245 events passed by Muon-

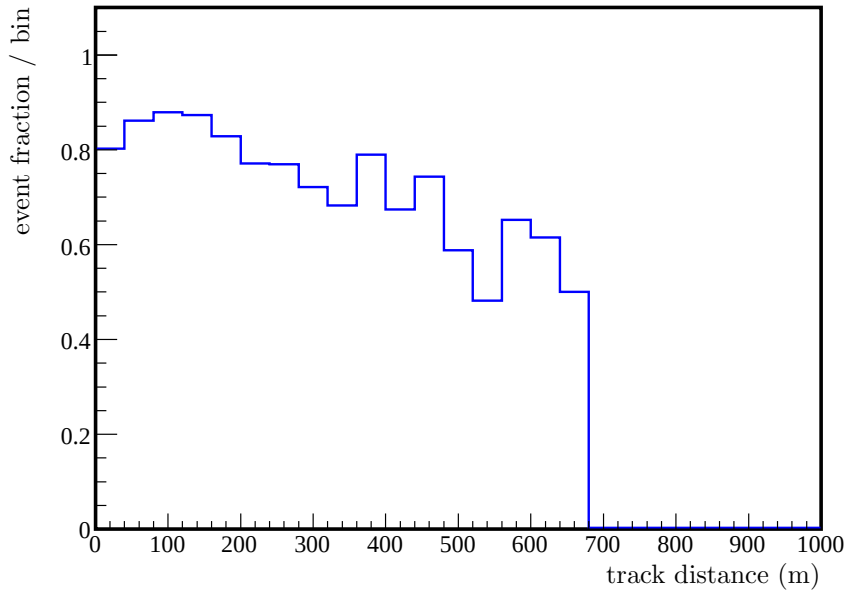

Fig. 8.16: Double stau Tracks Passing the MuonFilter.

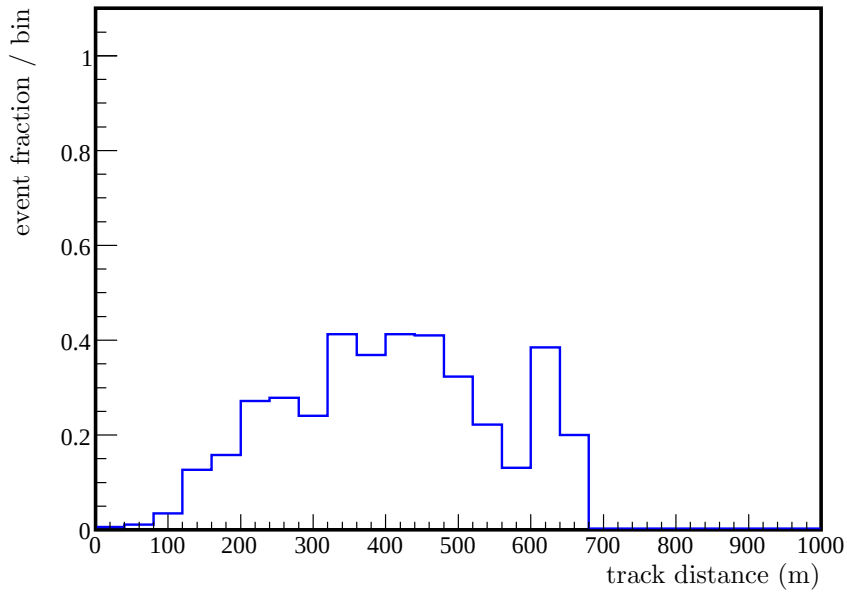

Fig. 8.17: Double stau Tracks Passing the Muon- and the SUSYFilter.

and SUSYFilter. This is a reduction of 22.7 %. The same analysis can also be done for the other filter settings. The results are

double track definition	**param.**	$N_{\text{passed}}^{\text{SUSY}}$	$N_{\text{passed}}^{\text{SUSY+Muon}}$	**reduction**
N_{ch}/track ≥ 4	r_λ	431	346	19.72 %
	r_σ	577	442	23.40 %
	$r_\lambda \wedge r_\sigma$	317	245	22.71 %
	$r_\lambda \vee r_\sigma$	691	543	21.42 %
+ track distance $\geq 150\,\text{m}$	r_λ	337	264	21.66 %
	r_σ	485	361	25.57 %
	$r_\lambda \wedge r_\sigma$	288	221	23.26 %
	$r_\lambda \vee r_\sigma$	534	404	24.34 %

An event reduction between about 20 % to 25 % for the different filter settings due to the prior usage of the MuonFilter is much less than the event reduction caused by the adjustment of the minimum values of the parameters r_λ and r_σ for the possible use of the SUSYFilter as an online filter. Consequently, the usage of the SUSYFilter in this configuration as an offline filter will deliver the best filtering performance.

9

Résumé and Outlook

The present thesis joins several aspects of the work with the neutrino telescopes AMANDA and IceCube. It starts with the work on the base hardware and finishes with a software module for analyzing the data stream coming from the detectors. Below, the results of this work and the ongoing activities in the fields covered by this thesis will be summarized.

From the beginning, AMANDA has been an impressive enterprise, which resulted in the largest neutrino telescope on Earth. The proven abilities of AMANDA have made it an important instrument for physicists. IceCube exceeds the abilities of AMANDA in many areas, but there are questions which cannot be answered with analyses of the IceCube data, alone. The TWR upgrade of 2002 to 2004 allowed for an integration of the AMANDA system into the IceCube DAQ. This integration has now been finished and the first results of this productive fusion are available.

The first part of this thesis deals with the hardware aspects of the AMANDA/IceCube integration. It describes the necessary hardware upgrades for the synchronization of the two detectors, as well as changes in the readout software. The results of measurements proving the quality of the synchronization system have been presented.

The hardware integration system consists of two major upgrades – one on the AMANDA and one on the IceCube side. The only available connections between the buildings housing the AMANDA DAQ (MAPO) and the IceCube DAQ (ICL) are optical fibers. The transmission of non-standard signals, i.e. not digital data of computer networks, requires non-standard hardware, which was developed by DESY Zeuthen.

On the AMANDA side, a new GPS latch – the GPS4TWR – manages the time stamping of AMANDA events. Additionally, the GPS4TWR is the interface to the optical signal transmission from and to IceCube. On the one hand, it receives its time information either from a GPS clock inside the MAPO or a GPS clock in the ICL via optical fibers. The GPS clock time information consists of three signals: A time string, containing the information of the day and the second of the day, a 1PPS signal indicating the exact beginning of a new second, and a 10 MHz signal counting in 100 ns steps from the beginning of a new second. On the other hand, the GPS4TWR sends two different synchronization signals in form of short pulses to IceCube. The two signals are the AMANDA hardware trigger signal, which is also initiating the AMANDA DAQ readout and the event time stamping, and a periodic signal with a frequency of one second. The latter signal is derived from the 1PPS pulse of one of the two available GPS clocks. Accordingly, this periodic

transmission delivers valuable information about the quality of the hardware synchronization.

On the IceCube side, a bidirectional optical to electrical converter – the OPT2EL – does the transformation between the electrical components in the ICL and the optical fibers to the MAPO. It obtains the information from the IceCube GPS clock to send it to AMANDA and receives the AMANDA trigger and synchronization signals. The only ways to inject hardware signals into the IceCube DAQ system are the DOM mainboards. Normally, those boards handle the pulses from the photomultipliers inside the IceCube DOMs. Due to the integration hardware upgrades, two additional boards, which process the AMANDA signals, are connected to the IceCube DAQ. All ICL components of the synchronization system are assembled in a 19" crate, called SyncCrate.

Before the installation at the South Pole, all components have been tested in Wuppertal. Additionally, a measurement of the temperature dependence of the optical fiber transmission has been performed. The result of

$$\frac{\Delta t}{\Delta T \cdot s} = (97.14 \pm 7.65)\,\frac{\mathrm{ps}}{\mathrm{K} \cdot \mathrm{km}}, \tag{9.1}$$

with the delay change Δt, the temperature change ΔT and the length of the fiber s, leads to the assumption that temperature effects on the transmission stability are negligible.

During the installation and testing of the synchronization system at the South Pole, the clock signal transmission from IceCube failed, but measurements with the AMANDA synchronization signals have proven an excellent reliability of the system without the usage of the GPS signal transfer. Two kinds of measurements have been performed: Short term measurements over periods of a few minutes to seconds and long term analyses using the results of the short term measurements. The results of the short term measurements show RMS values of less than 1.4 ns for the delay due to the transmission trough the optical fibers. The delay deviation over a few months is stable within about 4 ns. A general temperature dependence could not be found. The accuracy limit has been set to a value better than 10 ns. Accordingly, the implemented synchronization system safely satisfies the minimum requirements for a stable synchronization of AMANDA and IceCube.

Even though AMANDA has been switched off in May 2009, the combined data, taken in 2007, 2008 and 2009, is analyzed by several IceCube work groups. Studies about contained tracks or interesting astrophysical objects seen above the horizon have been performed or are on the way. Additionally, the presently existing results helped for planning the new IceCube low energy upgrade "DeepCore". Because of its geometry, this dense instrumented array in the center of IceCube is expected to deliver data with an even higher quality than the AMANDA/IceCube combination.

The second part of this thesis is focusing on the data from IceCube. The possibility of doing physics additionally to the original purpose of a neutrino telescope is a fascinating field, because the very high energies of cosmic rays permits particle reactions inaccessible to modern large scale colliders experiments.

One theoretical model beyond the Standard Model of particle physics is supersymmetry. Dependent on the model parameters, two long living staus from a neutrino reaction with standard matter inside the Earth are expected. These charged supersymmetric particles can cause a Čerenkov light signature comparable to those of charged heavy leptons, but with less light intensity. The double track signatures of SUSY particle induced events are distinguishable from other IceCube events.

During the work for this thesis, a complete simulation software module, creating stau double tracks in IceCube, has been developed. A filtering module, searching for stau double tracks inside the IceCube data stream, has been produced using the generated simulation data.

The simulation includes an isotropic neutrino flux assumption with a power law energy spectrum. Furthermore the interaction point is created using a Monte Carlo method including the

Earth density profile and the energy dependent neutrino interaction cross section for standard matter interactions. The generation of the angles between the two staus is done in a simplified way. The incident neutrino and the target nucleon are transformed into their center of mass system (CMS). The complete available energy in the CMS is distributed to stau masses and kinetic energies. The stau directions in the CMS are arbitrary but anti-parallel. The transformation back to the rest frame of IceCube delivers the angle between the two particles. The energy loss of the staus due to ionization and radiation losses while traveling through the Earth to the detector is calculated also considering the Earth density profile. At a point near the detector, the propagated staus are delivered to the IceCube simulation software modules that are generating the detector response.

The resulting IceCube event data is used to develop the filtering module for stau tracks and for its fine tuning. The so called SUSYFilter is based on a tensor of inertia (ToI) calculation using the geometrical distribution of hit DOMs. After the diagonalization of the tensor, the eigenvalues and eigenvectors of the ToI are available. The eigenvectors are the main axes of the tensor and the eigenvalues are the moments of inertia along the main axes.

The geometrical structure of a double track event has a more oblate shape, while single tracks are more prolate. This can be seen either in the ratio of the two largest eigenvalues or in the ratio of the two smallest geometrical hit distribution along the main axes. Both ratios have to exceed a certain value to deliver a minimum probability for an stau double track event.

Both filtering concepts have been analyzed independently and in combinations. The result is a statement on the best field of application for the SUSYFilter. The decision of using the module as an online filter running at the South Pole, or a filter applied on already filtered data available in the northern hemisphere has to be made. The best performance of the SUSYFilter is expected to be achieved when used as an offline filter. The already operating online filter modules, especially the MuonFilter module, are already transparent to a significant amount of double stau tracks. The final transparency in a chain of Muon- and SUSYFilter is reaching 20 % to 40 % for stau track separations between 200 m and 650 m. This is much compared to a value of only 1 % of all double tracks, when adjusting the SUSYFilter to deliver passing rates of about 1 Hz in the application on real detector data. This low passing rate is a demand for the implementation of a new filter module at the South Pole.

The ongoing work in this field is spread over several tasks. An extension of the simulation software for double tracks should include a correct handling of the angular distribution between the generated staus. Further on, it is possible to think about a more effective filtering module. This can only be achieved by the invention of a new algorithm for doing the event classification. Even if events are found by a filtering software, methods for the analysis of this event class are not available yet. These challenges will have to be met in the future.

Appendix A

Monte Carlo Simulation

In Chapter 7 many situations occur where random number distributions are needed that are not available via standard software packages. Here, the generation of arbitrary distributions from uniform distribution will be described. At this, the focus lies more on the practical implementation, than on the theoretical background. At first, the random number generation for an analytically solvable problem, using the example of a power law, will be explained. In a second section, numerical methods are used, to derive a special random number distribution.

A.1 Generation of a Power Law Energy Spectrum

Over many orders of magnitude in energy, the CR particle spectrum follows a power law (↗ 2.2.1)

$$I(E) = kE^{-\gamma} \left(\frac{\text{particles}}{\text{cm}^2 \cdot \text{s} \cdot \text{sr} \cdot \text{eV}} \right). \tag{A.1}$$

To obtain this spectrum between the energies E_0 and E_1 from a uniform distribution, the following steps are necessary. The different steps are illustrated in Fig. A.1 for $\gamma = 0.5$ and $k = 2$ with arbitrary units.

(a) Integrate the spectrum beginning at E_0

$$\Phi(E) == \int_{E_0}^{E} kE'^{-\gamma} \mathrm{d}E' = \frac{k}{1-\gamma} \left(E^{1-\gamma} - E_0^{1-\gamma} \right) \tag{A.2}$$

and calculate $\Phi(E_1)$. (Fig. A.1(b))

(b) Invert $\Phi(E)$ (Fig. A.1(c))

$$E(\Phi) = \left(\frac{1-\gamma}{k} \Phi + E_0^{1-\gamma} \right)^{\frac{1}{1-\gamma}}. \tag{A.3}$$

(c) Replacing Φ with uniformly distributed values between 0 and $\Phi(E_1)$ delivers the wanted distribution for the values of E. (Fig. A.1(d))

Attention! For $\gamma = 1$, the given results are not valid, but the procedure to obtain the correct distribution is the same.

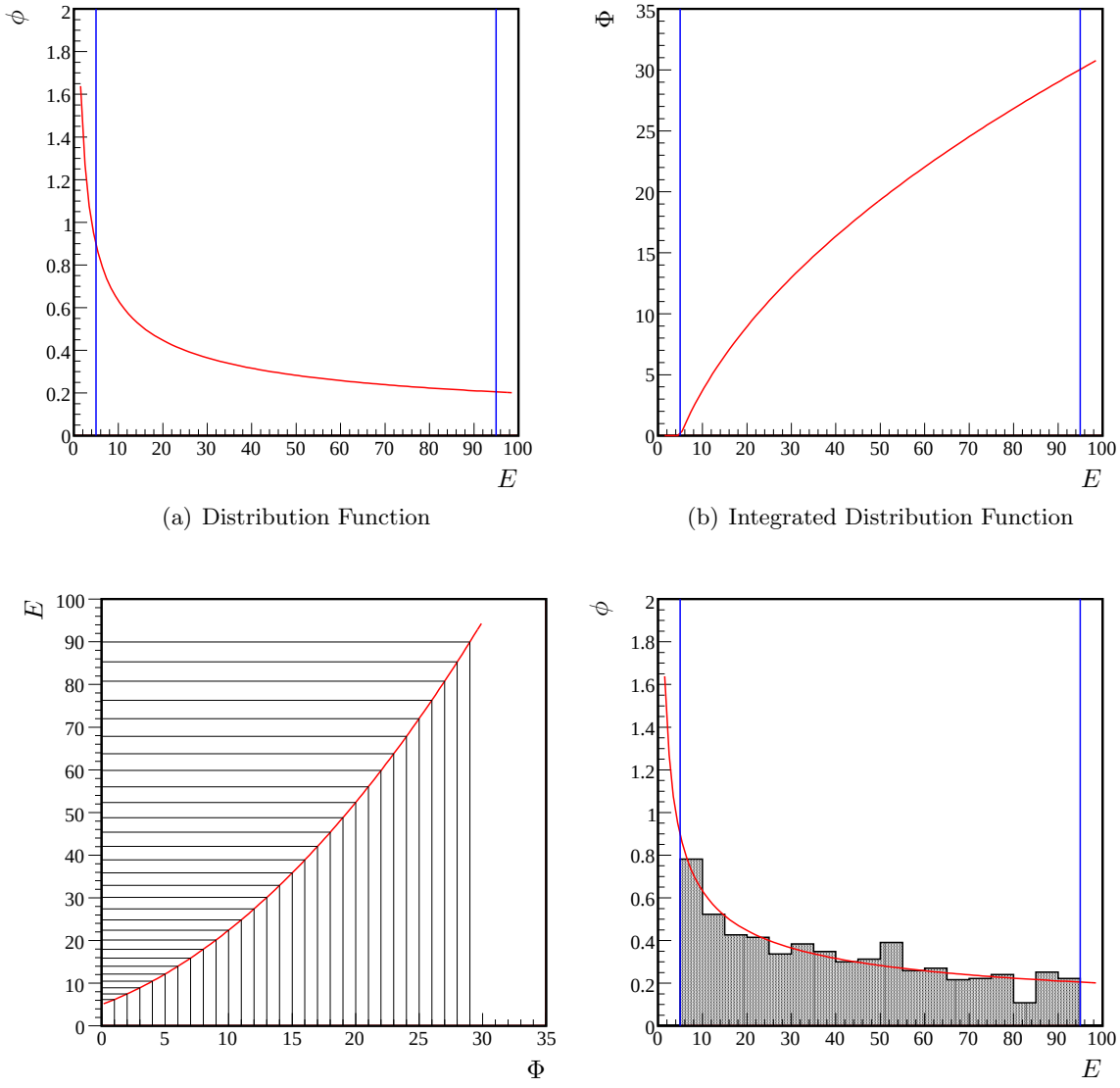

(a) Distribution Function

(b) Integrated Distribution Function

(c) Inverted Integrated Distribution Function

(d) Resulting Distribution

Fig. A.1: Demonstration of Monte Carlo Method used in this thesis. The given distribution function (a) is integrated within the needed interval (b) and inverted (c). Inserting a uniform distribution into the inverted function delivers a distribution according to the original distribution function (d).

A.2 Generation of an Equal Point Distribution on a Sphere

Because of its relevance, the simulation of a homogeneous point density on a sphere will also be demonstrated. This is equivalent with the demand that the point density n/s on a ring with the length s around the surface described by an angle ϑ is constant for every angle ϑ (Fig. A.2). ϑ is one component of the spherical coordinates (r, ϑ, φ). The length s of the ring is given by

$$s = 2\pi r \sin(\vartheta). \tag{A.4}$$

With $n/s = k$ the demand can be formulated as

$$n(\vartheta) = 2\pi k r \sin\vartheta. \tag{A.5}$$

A distribution described by this equation can be obtained like above by integration

$$N(\vartheta) = \int_0^{\vartheta} n(\vartheta')\mathrm{d}\vartheta' = 2\pi k r(1 - \cos\vartheta) \tag{A.6}$$

and inversion

$$\vartheta = \arccos\left(1 - \frac{N}{2\pi k r}\right). \tag{A.7}$$

The maximum value for N is $N(\pi) = 4\pi k r$. A uniform distribution for N inserted into Eq. A.7 is translated to the correct distribution for ϑ for an equal point distribution on a surface. The φ coordinate is arbitrary and can be set as a value from a uniform distribution between 0 and 2π.

The argument of the arccos in Eq. A.7 can have values between -1 and 1. Because of the linear dependence of the parameters in the argument, it is allowed to rewrite Eq. A.7 to

$$\vartheta = \arccos(U) \tag{A.8}$$

with U being a uniform distribution with values between -1 and 1.

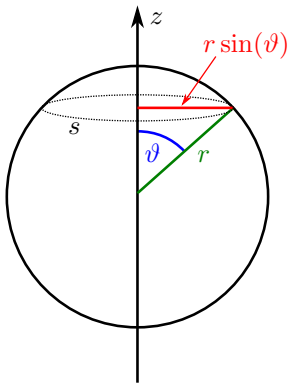

Fig. A.2: Simulating an Equal Point Distribution on a Sphere Surface

A.3 Generation of an Arbitrary Distribution

If the integral of a function is not available analytically, the integration has to be done numerically. In this work a spline function is used, to interpolate between the integral supporting points.

If $y(x)$ is the distribution function, the integration is done for n supporting points like

$$Y_i(x_i) = Y_{i-1}(x_{i-1}) + \int_{x_{i-1}}^{x_i} y(x)\mathrm{d}x \tag{A.9}$$

for $0 < i < n$ and $Y_0(x_0) = 0$. Given a range of $x_{min} = x_0 < x_i < x_{n-1} = x_{max}$ in which randomly distributed values are wanted, equally distant x_i are calculated by

$$x_i = \frac{x_{n-1} - x_0}{n-1} \cdot i + x_0. \tag{A.10}$$

The spline function can directly be defined as the inverted integral distribution function by using the supporting points mirrored at the bisectrix of the first quadrant

$$(x_i|Y_i) \rightarrow (Y_i|x_i). \tag{A.11}$$

Replacing Y, the variable of the spline, by values between 0 and $Y(x_{n-1})$ from a uniform distribution delivers the needed distribution according y.

A.4 Power Law Distribution in Double Logarithmic Plot

A special remark has to be done regarding to the plots of power law distributions. Because of their wide range of values, often over many orders of magnitude, power law distributions are mostly plotted with double logarithmic scales (Fig. A.3). Double logarithmic histograms with

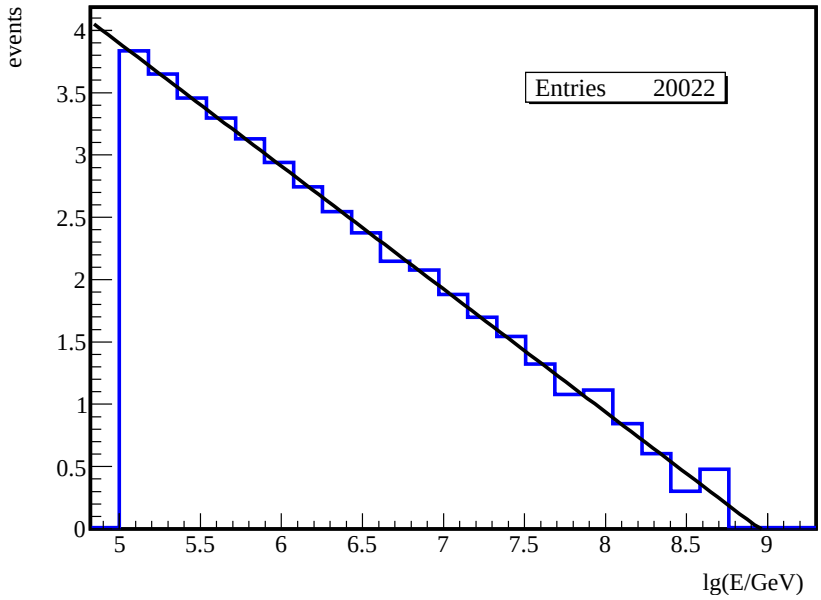

Fig. A.3: Example for a Power Law Distribution. The events contributing to this histogram are generated according to $\dot{\Phi} \propto (E/\mathrm{GeV})^{-2}$

events distributed this way show a different slope than the distribution function used for the event generation. This will be demonstrated here.

Values generated according to the power law distribution

$$f(x) = a \cdot x^b \tag{A.12}$$

shall be put into a histogram with equidistant bins on a logarithmic x-axis:

$$\lg x_{n+1} - \lg x_n = \Delta \tag{A.13}$$

with $\Delta = \text{const}$ for every x_n and x_{n+1} describing the left and right edge of the same bin in the histogram. From this follows for the bin edges

$$x_{n+1} = 10^{-\Delta} x_n. \tag{A.14}$$

The number N of entries* in one bin between x_n and x_{n+1} is given by the integral

$$N_n = \int_{x_n}^{10^{-\Delta} x_n} a \cdot x^b \mathrm{d}x. \tag{A.15}$$

This can be evaluated to

$$N_n = \frac{a}{1+b} \left(10^{-\Delta(1+b} - 1\right) x_n^{1+b}, \tag{A.16}$$

*The discrete example is chosen because of its relevance in this thesis.

for all $b \neq 1$. In a double logarithmic plot the slope s of the resulting linear distribution is

$$s = \frac{\lg N_n - \lg N_m}{\lg x_n - \lg x_m} = b + 1. \tag{A.17}$$

This result differs by +1 from the slope of the distribution function

$$\lg f(x) = \lg \left(a \cdot x^b \right) = \lg a + b \cdot \lg x \tag{A.18}$$

in a double logarithmic plot.

Appendix B

Particle Generation in the Center of Mass System (CMS)

In this Chapter, the calculations for creating two particles with equal masses from a neutrino-nucleon interaction are done. These calculations do not include nucleon structure functions and reduce the problem only on relativistic kinematics. The neutrino mass is considered to be $m_\nu = 0$.

B.1 Transformation to the CMS

In the lab frame the relativistic momentum vectors of the neutrino and the nucleon are given by

$$\text{nucleon:} \quad p_N^\mu = \begin{pmatrix} E_N/c \\ p_{x,q} \\ p_{y,q} \\ p_{z,q} \end{pmatrix} = \begin{pmatrix} E_N/c \\ 0 \\ 0 \\ 0 \end{pmatrix} \tag{B.1a}$$

$$\text{neutrino:} \quad p_\nu^\mu = \begin{pmatrix} E_\nu/c \\ p_{x,\nu} \\ p_{y,\nu} \\ p_{z,\nu} \end{pmatrix} = \begin{pmatrix} E_\nu/c \\ 0 \\ 0 \\ p_\nu \end{pmatrix}. \tag{B.1b}$$

W.l.o.g., the z-axis of the lab frame is chosen in parallel to the classical neutrino momentum vector and therefore $p_{z,\nu} = p_\nu$ and $p_{z,q} = p_q = 0$. The two relativistic vectors can be Lorentz

transformed:

$$\begin{pmatrix} E'_N/c \\ 0 \\ 0 \\ p'_N \end{pmatrix} = \begin{pmatrix} \gamma(E_N/c - \beta p_N) \\ 0 \\ 0 \\ \gamma(p_N - \beta E_N/c) \end{pmatrix} = \gamma \begin{pmatrix} E_N/c \\ 0 \\ 0 \\ -\beta E_N/c \end{pmatrix} \tag{B.2a}$$

$$\begin{pmatrix} E'_\nu/c \\ 0 \\ 0 \\ p'_\nu \end{pmatrix} = \begin{pmatrix} \gamma(E_\nu/c - \beta p_\nu) \\ 0 \\ 0 \\ \gamma(p_\nu - \beta E_\nu/c) \end{pmatrix} = \gamma \begin{pmatrix} E_\nu/c - \beta p_\nu \\ 0 \\ 0 \\ p_\nu - \beta E_\nu/c \end{pmatrix} \tag{B.2b}$$

The CMS is defined by the disappearing sum of the classical momenta

$$p'_N + p'_\nu = 0, \tag{B.3}$$

from which follows with the approximation $m_\nu \approx 0$

$$\beta \approx \frac{E_\nu}{E_N + E\nu}. \tag{B.4}$$

The available energy in the CMS

$$E'_{tot} = E'_N + E'_\nu \tag{B.5}$$

is obtained by inserting β and

$$\gamma = \frac{1}{\sqrt{1-\beta^2}} \tag{B.6}$$

into the corresponding lines of the Lorentz transformations Eqs. B.2a and B.2b:

$$E'_{tot} = \sqrt{E_N^2 + 2E_N E_\nu}. \tag{B.7}$$

The limit for double particle production with a particle mass m therefore is

$$E'_{tot} \geq 2mc^2 \Longrightarrow E_{\nu,min} = \frac{2m^2c^4}{E_N} - \frac{E_N}{2}. \tag{B.8}$$

The momentum p of one of the two produced particles is given by

$$p' = \sqrt{\left(\frac{E'_{tot}}{2c}\right)^2 - m^2c^2}. \tag{B.9}$$

The new particles are emitted antiparallely in the CMS with the angles ϑ and $180\,^\circ + \vartheta$ regarding to the original neutrino direction. W.l.o.g., the plane containing the vector of the neutrino momentum and the two momenta of the new particles may be the x-y-plane (Fig. B.1). The relativistic momentum vectors then look like ($E'_{\tilde{\tau}_1} = E'_{\tilde{\tau}_2} = E'$)

$$p_1^{\mu\prime} = \begin{pmatrix} E'/c \\ p'_{x,1} \\ 0 \\ p'_{z,1} \end{pmatrix} = \begin{pmatrix} E'/c \\ p' \sin(\vartheta) \\ 0 \\ p' \cos(\vartheta) \end{pmatrix} \tag{B.10a}$$

$$p_2^{\mu\prime} = \begin{pmatrix} E'/c \\ p'_{x,2} \\ 0 \\ p'_{z,2} \end{pmatrix} = \begin{pmatrix} E'/c \\ -p' \sin(\vartheta) \\ 0 \\ -p' \cos(\vartheta) \end{pmatrix}. \tag{B.10b}$$

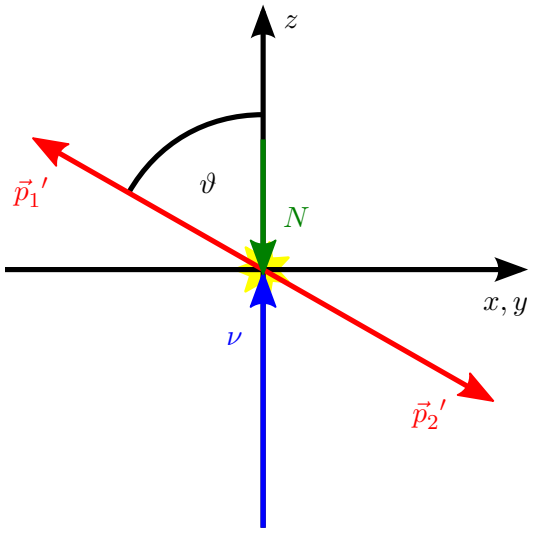

Fig. B.1: Relativistic Particle Generation in CMS.

B.2 Transformation to the Lab Frame

Conversion back to the lab frame delivers

$$p_1^\mu = \begin{pmatrix} E_1/c \\ p_{x,1} \\ 0 \\ p_{z,1} \end{pmatrix} = \begin{pmatrix} \gamma\left(E'/c + \beta p'_{z,1}\right) \\ p'_{x,1} \\ 0 \\ \gamma\left(p'_{z,1} + \beta E'/c\right) \end{pmatrix} = \begin{pmatrix} \gamma\left(E'/c + \beta p' \cos(\vartheta)\right) \\ p' \sin(\vartheta) \\ 0 \\ \gamma\left(p' \cos(\vartheta) + \beta E'/c\right) \end{pmatrix} \tag{B.11a}$$

$$p_2^\mu = \begin{pmatrix} E_2/c \\ p_{x,2} \\ 0 \\ p_{z,2} \end{pmatrix} = \begin{pmatrix} \gamma\left(E'/c + \beta p'_{z,2}\right) \\ p'_{x,2} \\ 0 \\ \gamma\left(p'_{z,2} + \beta E'/c\right) \end{pmatrix} = \begin{pmatrix} \gamma\left(E'/c - \beta p' \cos(\vartheta)\right) \\ -p' \sin(\vartheta) \\ 0 \\ \gamma\left(-p' \cos(\vartheta) + \beta E'/c\right) \end{pmatrix}. \tag{B.11b}$$

From these formulae, the angle α between the two created particles in the lab frame can be calculated:

$$\alpha(\vartheta) = \arccos\left(\frac{\vec{p}_1 \vec{p}_2}{|\vec{p}_1|\,|\vec{p}_2|}\right). \tag{B.12}$$

α as a function of ϑ is plotted in Fig. B.2 for $E_N = m_p c^2 = 0.938\,\text{GeV}$, $m = 150\,\text{GeV}$ and several neutrino energies. With these parameters, the minimum neutrino energy is $E_{\nu,min} = 47960\,\text{GeV}$. The maximum for α is not dependent on the neutrino energy, but only on the mass of the target and the generated particles.

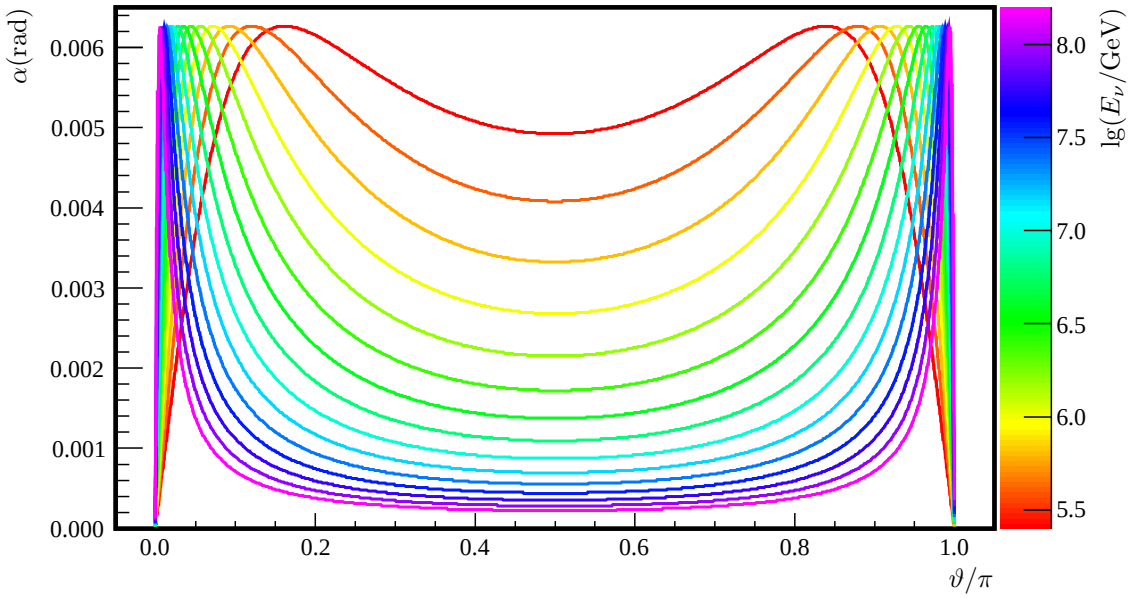

Fig. B.2: Angle Between Two Particles generated in the CMS for several incident neutrino energies.

Appendix C

Correct Treatment of the Neutrino Interaction

The results of a detailed calculation including the generation of a squark and a left-handed slepton according to Fig. 5.6, the correct consideration of the nucleon structure and the decay of the produced primary particles have been given to the author in [Alb08b]. The corresponding plot is presented in Fig. C.1(a). The corresponding 1D histograms showing the angle of beam spread distributions for the same three neutrino energies as in Fig. 7.8(b) are plotted in Fig. C.1(b). Obviously, a correct treatment of the physical processes of the neutrino interaction and the decay of the outgoing SUSY particles leads to a much narrower distribution of the angle α. Consequently, more double track events inside the IceCube detector from interactions happening in a greater distance to the detector are expected than for the currently used simple generation of two staus in the neutrino-nucleon CMS.

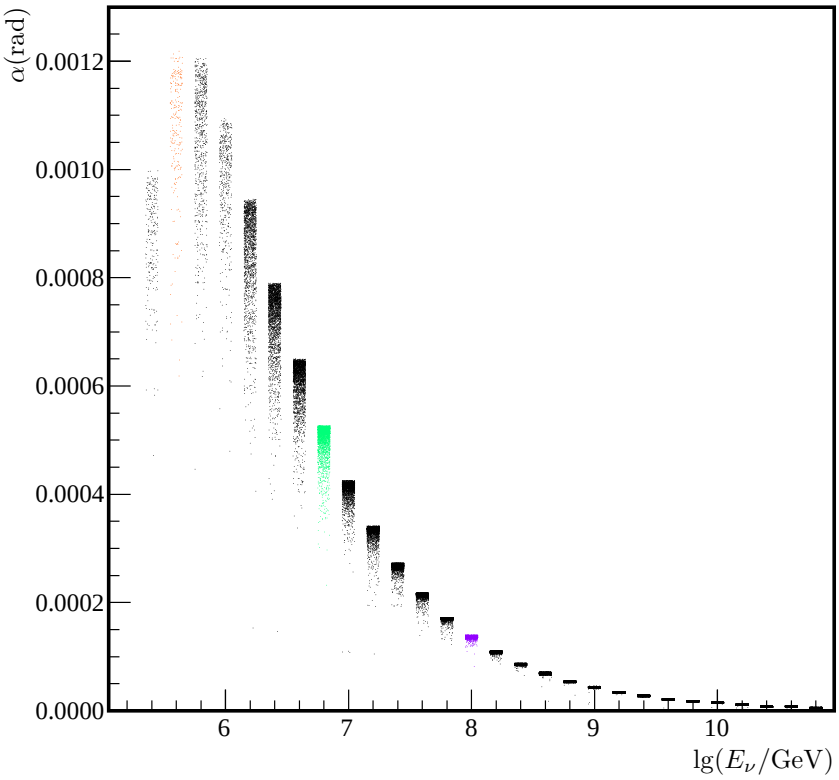

(a)

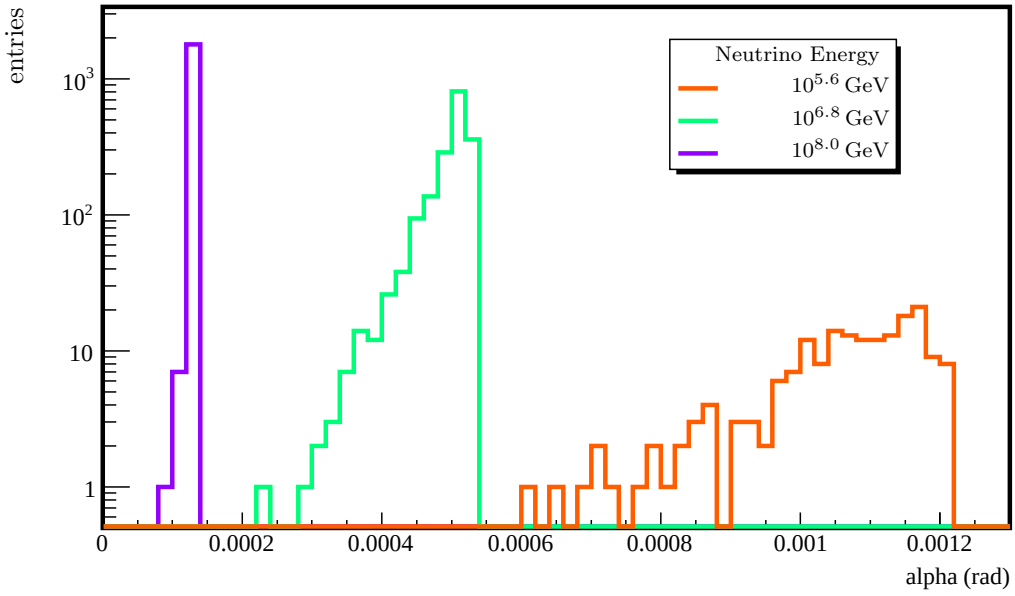

(b)

Fig. C.1: Distribution of the Angle of Beam Spread between two stau trajectories created considering the generation of a squark and a left-handed slepton, the the nucleon structure and the decay of the produced primary particles. Data from [Alb08b]. (a) The incident neutrino energies are varied between $10^{5.4}$ GeV and $10^{10.8}$ GeV. (b) 1D histograms for a sample of three different incident neutrino energies.

Appendix D

stau Generation Modules

In this chapter, all modules used for the production of a complete double stau track data set are described. Parts of the simulation are grouped in independent scripts, written in the scripting language "Python". The following sections always describe the (important) modules used within one of those scripts. Modules only handling the input/output operations, offering additional information or providing services will be skipped. The IceTray software package used is "simulation" in the version V02-03-00.

The IceCube geometry for all data is the IceCube-40 configuration of 2008 consisting of 40 strings supporting 2400 DOMs.

D.1 stau Generation

I3SUSYGen		
parameter	**value**	**description**
Dist0Plane	1000.0 m	Distance of generation plane E2 (Fig. 7.1(a)) to the detector center.
EPrimMin	1.0 GeV	Minimum energy of the primary neutrino (if too small, it will be set to the minimum energy for stau generation).
EPrimMax	10^{12} GeV	Maximum energy of the primary neutrino (if too small, it will be set to the minimum energy).
EIndex	2.0	Spectral index of the neutrino energy distribution.
AlphaMax	0.0 rad	Maximum angle of beam spread between the staus (disabled if 0).
SUSYMass	150.0 GeV	Mass of one stau.
MinSUSYEnergy	3.16×10^4 GeV	Minimum energy of a stau arriving at the detector for being accepted.

cont. on next page

I3SUSYGen (cont.)		
parameter	**value**	**description**
nParticlesEnergy	2	Minimum number of staus with energy larger than MinSUSYEnergy to have a valid event.
nParticlesInside	2	Minimum number of staus traversing the detector volume to have a valid event.
IceCubeRange	500.0 m	Neutrino track vector has to have an intersection point with a sphere having this radius around the detector origin. This equals to the demand of hitting plane P described in Fig. 7.3(b)
ParticleType	"STauMinus"	Type of simulated particle.
Verbose	0	Verbose output.
Start[X-Z]	0	If set to a value $\neq 0$ all stau tracks start here

The resulting file of the first script includes the data of the primary neutrino and the two generated staus. The latter information is available independently and within a data structure, which is used by the modules following in the simulation chain. For the I3SUSYGen module, which is the central module of the first script, only parameters that have not become unused are explained.

D.2 Detector Response

In the second script, all modules handling the detector response are combined. Only parameters differing from the default values are described.

I3PropagatorMMC		
parameter	**value**	**description**
rerr	"/dev/null"	File for stderr redirection.
mode	1	MMC propagation/generation mode (1 propagates the wanted particles).
opts	"-seed=1 -radius=1000 -length=1200"	MMC configuration options.
PropagatePrimary	*true*	Flag to tell MMC whether to propagate primaries or not.
ExoticParticleType	−9132	Type of exotic particle to propagate ($-9132 \hat{=} \tilde{\tau}^-$).
ExoticMass	150.0 GeV	Mass of the exotic particle (stau) to propagate.

The MMC module propagates the staus and handles secondary particles [CR04]. The module has not been able to propagate staus before the work on stau filtering has started. It was enhanced by this feature [Oli08].

I3HitMakerModule		
parameter	**value**	**description**
DetectorMode	1	Decision whether to use IceCube and AMANDA information. 1 =IceCube only.
EnableBinning	*true*	Compute hits bin-wise for tracks, where the number of photo-electrons exceeds a maximum number.
MaxPEs	500000	Maximum number of photo-electrons allowed for each DOM.
MCHitSeriesName	"MCHitSeriesMap"	Map with hits produced in the Monte Carlo calculations.
MCTreeName	"I3MCTree"	Name of Monte Carlo tree with particle information to be used as input.
NBins	587	Width of the bins used for the bin-wise computation of hits.
UsingAmandaTables	*false*	Using AMANDA photonics tables for scaling the amplitude.

The HitMaker is used to generate the hits at the DOMs. It is using the Monte Carlo simulation information of the MMC module.

I3NoiseGeneratorModule		
parameter	**value**	**description**
EndWindow	10000	Time after Monte Carlo hits to be filled with noise.
IceTop	*false*	Generate noise for IceTop.
InIce	*true*	Generate noise for InIce.
InputHitSeriesMapName	"MCHitSeriesMap"	Map with hits produced in the Monte Carlo calculations.
Rate	$6.5e-07$	Average number of events per second.
StartWindow	10000	Time before Monte Carlo hits to be filled with noise.
TWR	*false*	Generate noise for TWR.

The NoiseGenerator produces random Monte Carlo hits like all DOMs produce PMT noise induced hit information. This makes the simulation more realistic.

I3PMTSimulator

The response of the PMT inside a DOM to a Monte Carlo generated hit from the HitConstructor is simulated by the PMTSimulator. For the double stau simulation, it is used with default parameters only.

I3DOMsimulator

The influence of the complicated electronics in the PMT signal inside the DOM is simulated by the DOMsimulator. Also this module is used with default parameters, only.

I3SMTrigger		
parameter	**value**	**description**
TriggerName	"I3Triggers"	Name of the container with trigger information.

SMTrigger is the module calculating the simple majority trigger conditions from the hit DOMs.

I3GlobalTriggerSim		
parameter	**value**	**description**
FilterMode	$false$	If set to $true$, only triggered events will be stored.
I3TriggerName	"I3Triggers"	Name of the container with trigger information.
GlobalTriggerName	"I3TriggerHierarchy"	Name of the container with all trigger information.

The GlobalTriggerSim module is handling the triggers from all trigger modules. For the double stau simulation, only the simple majority trigger is used.

Appendix E

stau Filtering Modules

E.1 Data Cleaning

After the generation of the raw hit and trigger information, the influence of the detector state on the resulting data has to be considered. On the one hand, the real detector does not consist only of working modules, but also of modules not behaving normally and delivering inaccurate data. On the other hand in a real detector also noise signals and hits not belonging to the current event are recognized. These parts of the data stream have to be cleaned out.

I3DOMLaunchCleaning		
parameter	**value**	**description**
InIceInput	"InIceRawData"	Source of the simulated DOM raw data.
InIceOutput	"CleanInIceRawData"	Name of the container for clean DOM raw data.
FirstLaunchCleaning	*true*	If *true*, the first DOM hit information will not be cleaned.
CleanedKeys	[OMKey(String, OM), ...]	Keys for the optical modules to be removed from the raw data.

The DOMLaunchCleaning removes DOMs from the raw data. The DOMs considered "bad" are

OMKey(38,59) "Blackberry",
OMKey(39,61) "Hydrogen",
OMKey(39,21) "Aspudden",
OMKey(39,22) "Liljeholmen",
OMKey(40,51) "Juneberry",
OMKey(40,52) "Alfa_Romeo_Spider",

OMKey(44,25) “Mirkwood”,
OMKey(44,26) “Pink”,
OMKey(44,47) “Homeopatix”,
OMKey(44,48) “Mad_Hatter”,
OMKey(44,55) “Gaston”,
OMKey(44,56) “Ermolai”,
OMKey(46,49) “Gerbil”,
OMKey(46,50) “Ringkobben”,
OMKey(47,55) “Kemps_Card”,
OMKey(47,56) “Ensta”,
OMKey(53,17) “Bryozoan”,
OMKey(53,18) “Fa”,
OMKey(66,33) “New_York”,
OMKey(66,34) “Dou_Mu”,
OMKey(66,45) “Alpaca”,
OMKey(66,46) “Tallahassee”,
OMKey(69,23) “Black”,
OMKey(69,24) “Magenta”,
OMKey(72,37) “Hundgrundet”,
OMKey(72,38) “Buttercup”,
OMKey(77,47) “Hamster” and
OMKey(77,48) “Meldii”.

I3LCCleaning		
parameter	**value**	**description**
InIceInput	“CleanInIceRawData”	Source of the simulated DOM raw data.
InIceOutput	“HLCInIceRawData”	Name of the container for clean DOM raw data.

Local coincidences are an IceCube detector feature to improve data reduction. This module removes a simulated software local coincidence variant, which has not been used for the real detector configuration of 2008.

I3DOMcalibrator		
parameter	**value**	**description**
InputRawDataName	“HLCInIceRawData”	Source of the simulated DOM raw data.
CorrectPedestalDroopDualTau	*true*	Correction of a specific wave form feature.

The DOMcalibrator delivers the data for the correct treatment of the raw data. This is necessary to translate the raw data wave form samples to physical values like voltages or charges. One of the beneficiaries is the FeatureExtractor.

I3TimeWindowCleaning		
parameter	**value**	**description**
InputResponse	"FEPulses"	Source of the simulated DOM data.
OutputResponse	"TWCleanPulses"	Output cleaned data.
TimeWindow	6000 ns	The time window that is used for cleaning out DOMs.

The TimeWindowCleaning is using data already processed by the FeatureExtractor. It removes hits lying outside a specific time window. It is assumed that these time outliers do not contribute to the triggered event.

E.2 FeatureExtractor

Another module, not really fitting to any of the already mentioned categories, is doing a data preprocessing. The so called *FeatureExtractor* is calibrating the sampled waveforms. It is calculating the real voltages of the sample values using calibration data for every DOM and also delivers a charge information for every hit.

I3FeatureExtractor		
parameter	**value**	**description**
InitialHitSeriesReco	"FEHits"	Name for the output data container.
InitialPulseSeriesReco	"FEPulses"	Name for the output data container containing a different set of information.
CalibratedFADCWaveforms	"CalibratedFADC"	FADC information of the DOMcalibrator.
CalibratedATWDWaveforms	"CalibratedATWD"	ATWD information of the DOMcalibrator.
RawReadoutName	"HLCInIceRawData"	Name of the container with raw data.
MaxNumHits	0	Maximum number of peaks to find. (0 = disabled)
FastPeakUnfolding	0	Parameter for peak unfolding.
FastFirstPeak	11	Parameter for choice of peak fitting method.
ADCThreshold	0.4	ADC threshold in terms of single photo-electron discriminator threshold.
PMTTransit	2	If 1 or 2, add PMT transit time to extracted hit times.

E.3 SUSYFilter

The SUSYFilter is used with these settings according to the corresponding analyses done in Sec. 8 for every filter feature.

I3FilterModule<I3SUSYFilter>		
parameter	**value**	**description**
PulseSeriesMap	"TWCleanPulses"	Map with the pulse series from the FeatureExtractor cleaned by the TimeWindowCleaning module.
LaunchSeriesMap	"InIceRawData"	Fallback Map with DOM raw data.
DecisionName	"SUSYFilter"	Name of the variable carrying the final filter decision.
FilterFlagName	"SUSYFilterFlag"	Name of the variable carrying the final filter decision (deprecated).
StatusBitmaskName	"SUSYFilterMask"	Bitmask documenting the passing of the several filtering and cleaning algorithms.
DisplayParticles	1	Put particles into the data stream to display the eigenvectors.
MinDOMs	8	Minimum number of hit DOMs.
MinStrings	3	Minimum number of hit strings.
SingleHits	0	Use only the n first hits of every hit DOM (0=off).
AmpWeight	1.0	The charge C of the hit is used for the ToI calculation as $C^{\mathrm{AmpWeight}}$.
MinEVRatio	1.15	Minimum ratio of $r_\lambda = \lambda_3/\lambda_2$.
MinRMSRatio	2.5	Minimum ratio of $r_\sigma = \sigma_2/\sigma_3$.
MinTimeSlope	0.0	Minimum time slope along the eigenvector with the largest σ (0=off).
zAxisTimeSlope	-3.0	Minimum time slope along the z-axis.
MinThickness	4.0	Minimum value for σ_3.
Sphericity	0.0	Value for reducing "round" events (0=off).
MinMaxStringDist	150.0	Minimum value of the maximum string distance in every event.
UseEV	*True*	Use the ratio $r_\lambda = \lambda_3/\lambda_2$ as filter decision.
UseRMS	*True*	Use the ratio $r_\sigma = \sigma_2/\sigma_3$ as filter decision.
UseCombination	1	If set to one the filter only passes events with r_λ AND r_σ being valid.

Bibliography

[Aug97] The Auger Collaboration (Ed.): *The Pierre Auger Observatory Design Report*. Website. http://www.auger.org/admin/DesignReport/. Version: 2, 14^{th} March 1997

[Aug08] Abraham, J. et al. Pierre Auger collaboration: Observation of the suppression of the flux of cosmic rays above 4×10^{19}eV. In: *Phys. Rev. Lett.* 101 (2008), p. 061101. arXiv:0806.4302 [astro-ph]

[Fly94] Bird, D. J. et al.: The cosmic-ray energy spectrum observed by the Fly's Eye. In: *Astrophys. J.* 424 (1994), March, pp. 491–502

[HiR08] Abbasi, R. et al. HiRes collaboration: Observation of the GZK cutoff by the HiRes experiment. In: *Phys. Rev. Lett.* 100 (2008), p. 101101. arXiv:astro-ph/0703099

[Ice01] The IceCube Collaboration (Ed.): *IceCube Preliminary Design Document*. Website. http://www.icecube.wisc.edu/science/publications/pdd/. Version: 1.24, 11^{th} October 2001

[Nie81] van Nieuwenhuizen, P.: Supergravity. In: *Physics Reports* 68 (1981), No 4, 189-398. http://www.sciencedirect.com/science/article/B6TVP-46TYPH8-3/2/5996de464f28f4657c205fb2c01ad5f3

[PDG08] Amsler, C. et al. (Particle Data Group): Review of particle physics. In: *Phys. Lett. B* 667 (2008), September, No 1-5, pp. 1–1340

[A+95a] Askebjer, P. et al. AMANDA collaboration: On the age versus depth and optical clarity of deep ice at South Pole. (1995). arXiv:astro-ph/9501072

[A+95b] Askebjer, P. et al. AMANDA collaboration: Optical properties of the South Pole ice at depths between 0.8-km and 1-km. In: *Science* 267 (1995), pp. 1147–1150. arXiv:astro-ph/9412028

[A+00] Andres, E. et al.: The AMANDA neutrino telescope: principle of operation and first results. In: *Astropart. Phys.* 13 (2000), March, No 1, pp. 1–20. – ISSN 0927–6505. arXiv:astro-ph/9906203

[A+02] Ahrens, J. et al.: Observation of high energy atmospheric neutrinos with the Antarctic muon and neutrino detector array. In: *Phys. Rev. D* 66 (2002), Jul, No 1, p. 012005

[A+06a] Ackermann, M. et al.: Optical properties of deep glacial ice at the South Pole. In: *J. Geophys. Res.* 111 (2006), July, p. D13203

[A+06b] Ackermann, M. et al. AMANDA collaboration: The ICECUBE prototype string in AMANDA. In: *Nucl. Instrum. Meth.* A556 (2006), January, pp. 169–181. arXiv:astro-ph/0601397

[A+07a] Abraham, J. et al. Pierre Auger collaboration: Correlation of the highest energy cosmic rays with nearby extragalactic objects. In: *Science* 318 (2007), November, pp. 938–943. arXiv:0711.2256 [astro-ph]

[A+07b] Achterberg, A. et al. IceCube collaboration: Five years of searches for point sources of astrophysical neutrinos with the AMANDA-II neutrino telescope. In: *Physical Review D* 75 (2007), No 10, p. 102001

[A+08] Abraham, J. et al. Pierre Auger Collaboration collaboration: Observation of the Suppression of the Flux of Cosmic Rays above 4×10^{19} eV. In: *Phys. Rev. Lett.* 101 (2008), No 6, p. 061101

[A+09a] Abbasi, R. et al. IceCube collaboration: The IceCube data acquisition system: Signal capture, digitization, and timestamping. In: *Nuclear Instruments and Methods in Physics Research Section A: Accelerators, Spectrometers, Detectors and Associated Equipment* 601 (2009), No 3, 294-316. http://dx.doi.org/DOI:10.1016/j.nima.2009.01.001. – DOI DOI: 10.1016/j.nima.2009.01.001. – ISSN 0168–9002

[A+09b] Abbasi, R. et al. IceCube collaboration: Search for Point Sources of High Energy Neutrinos with Final Data from AMANDA-II. In: *Phys. Rev.* D79 (2009), p. 062001. arXiv:0809.1646 [astro-ph]

[ABC07] Albuquerque, Ivone Freire M. ; Burdman, Gustavo ; Chacko, Zackaria: Direct detection of supersymmetric particles in neutrino telescopes. In: *Phys. Rev. D* 75 (2007), No 3, 035006.
http://link.aps.org/abstract/PRD/v75/e035006

[Ait07] Aitchinson, Ian J. R.: *Supersymmetry in Particle Physics.* The Edinburgh Building, Cambridge CB2 8RU, UK : Cambridge University Press, 2007

[Alb08a] Albuquerque, Ivone Freire M.: *private conversation.* November 2008

[Alb08b] Albuquerque, Ivone Freire M.: *private conversation.* December 2008

[B+89] Berger, Ch. et al.: Experimental study of muon bundles observed in the Fréjus detector. In: *Phys. Rev. D* 40 (1989), Oct, No 7, pp. 2163–2171

[B+93] Band, D. et al.: BATSE observations of gamma-ray burst spectra. 1. Spectral diversity. In: *Astrophys. J.* 413 (1993), pp. 281–292

[B+03] Bennett, C. L. et al. WMAP collaboration: First Year Wilkinson Microwave Anisotropy Probe (WMAP) Observations: Preliminary Maps and Basic Results. In: *Astrophys. J. Suppl.* 148 (2003), pp. 1–43. arXiv:astro-ph/0302207

[BDdS09] Boyanovsky, D. ; Destri, C. ; de Vega, H. J. ; Sanchez, N. G.: The Effective Theory of Inflation in the Standard Model of the Universe and the CMB+LSS data analysis. (2009). arXiv:0901.0549 [astro-ph]

[BE87] Blandford, Roger ; Eichler, David: Particle acceleration at astrophysical shocks: A theory of cosmic ray origin. In: *Physics Reports* 154 (1987), No 1, 1-75. http://www.sciencedirect.com/science/article/B6TVP-46T3DRC-20/2/b322fd6f60e7af3d417b030dce38771d. – ISSN 0370–1573

[Bec04] Becker, Julia K.: *Calculation of the AGN Neutrino Flux and of Event Rates for Large Volume Neutrino Telescopes*. Gaußstraße 20, 42119 Wuppertal, Germany, Bergische Universität Wuppertal, Diplomarbeit, March 2004. http://icecube.berkeley.edu/manuscripts/20040302xx-diplom.ps.gz

[Ber09] Berghaus, P. IceCube collaboration: Muons in IceCube. In: *ArXiv e-prints* (2009), January. arXiv:0902.0021

[BGG06] Berezinsky, V. ; Gazizov, A. Z. ; Grigorieva, S. I.: On astrophysical solution to ultra high energy cosmic rays. In: *Phys. Rev. D* 74 (2006), No 4, p. 043005. arXiv:hep-ph/0204357

[B:I07] *30th International Cosmic Ray Conference*. Mérida Yucatán, México : Universidad Nacional Autónoma de México, July 2007 . – ISBN 978–970–32–4216–0

[BMPZ97] Bagger, Jonathan A. ; Matchev, Konstantin T. ; Pierce, Damien M. ; Zhang, Ren-Jie: Weak-scale phenomenology of models with gauge-mediated supersymmetry breaking. In: *Phys. Rev. D* 55 (1997), March, No 5, pp. 3188–3200

[BS99] Bromm, Volker ; Schaefer, Bradley E.: The Spectrum of GRB 930131 ("Superbowl Burst") from 20 keV to 200 MeV. (1999). arXiv:astro-ph/9904129

[BW01] Bahcall, John N. ; Waxman, Eli: High energy astrophysical neutrinos: The upper bound is robust. In: *Phys. Rev. D* 64 (2001), June, No 2, p. 023002. arXiv:hep-ph/9902383

[CH81] Cavallo, G. ; Horstman, H. M.: Spectrum of cosmic fireballs. In: *Astrophysics and Space Science* 75 (1981), March, No 1, pp. 117–123. http://dx.doi.org/10.1007/BF00651388. – DOI 10.1007/BF00651388. – ISSN 0004–640X (Print) 1572–946X (Online)

[CH01] Cowen, D. ; Hanson, K.: Time calibration of the AMANDA neutrino telescope with cosmic ray muons. In: *International Cosmic Ray Conference* Bd. 3, 2001 (International Cosmic Ray Conference), 1133-1136

[Cha08] Chacko, Zackaria: *private conversation*. November 2008

[CM67] Coleman, Sidney ; Mandula, Jeffrey: All Possible Symmetries of the S Matrix. In: *Phys. Rev.* 159 (1967), Jul, No 5, pp. 1251–1256

[CR04] Chirkin, Dmitry ; Rhode, Wolfgang: Muon Monte Carlo: A high-precision tool for muon propagation throughmatter. (2004). arXiv:hep-ph/0407075

[D+00] Dickinson, J. E. et al.: The new South Pole air shower experiment: SPASE-2. In: *Nucl. Instrum. Meth.* A440 (2000), pp. 95–113

[DDRT96] Dimopoulos, Savas ; Dine, Michael ; Raby, Stuart ; Thomas, Scott: Experimental Signatures of Low Energy Gauge-Mediated Supersymmetry Breaking. In: *Phys. Rev. Lett.* 76 (1996), May, No 19, pp. 3494–3497

[DHS+02] Dolgov, A. D. ; Hansen, S. H. ; S., Pastor ; Petcov, S. T. ; Raffelt, G. G. ; V., Semikoz D. et al.: Cosmological bounds on neutrino degeneracy improved by flavor oscillations. In: *Nucl. Phys.* B632 (2002), pp. 363–382. arXiv:hep-ph/0201287

[DPRW65] Dicke, R. H. ; Peebles, P. J. E. ; Roll, P. G. ; Wilkinson, D. T.: Cosmic Black-Body Radiation. In: *Astrophys. J.* 142 (1965), July, 414-419. http://adsabs.harvard.edu/abs/1965ApJ...142..414D. – Provided by the SAO/NASA Astrophysics Data System

[Dzi98] Dziewonski, Adam: Earth Structure, Global. In: James, D. E.: *Encyclopedia of Solid Earth Geophysics*. 1. Springer US, November 1998 (Encyclopedia of Earth Sciences Series). – ISBN 978–0–387–33563–6

[ESS01] Engel, Ralph ; Seckel, David ; Stanev, Todor: Neutrinos from propagation of ultrahigh energy protons. In: *Phys. Rev. D* 64 (2001), November, No 9, p. 093010. arXiv:astro-ph/0101216

[FCG+96] Fixsen, D. J. ; Cheng, E. S. ; Gales, J. M. ; Mather, J. C. ; Shafer, R. A. ; Wright, E. L.: The Cosmic Microwave Background Spectrum from the Full COBE FIRAS Data Set. In: *Astrophys. J.* 473 (1996), December, pp. 576–587. arXiv:astro-ph/9605054

[Fer49] Fermi, Enrico: On the Origin of the Cosmic Radiation. In: *Phys. Rev.* 75 (1949), April, No 8, pp. 1169–1174

[Fis97] Fisher, Gerd: *Lineare Algebra*. 11. Braunschweig/Wiesbaden, Germany : Vieweg, 1997

[FM02] Fixsen, D. J. ; Mather, J. C.: The Spectral Results of the Far-Infrared Absolute Spectrophotometer Instrument on COBE. In: *Astrophys. J.* 581 (2002), December, pp. 817–822

[FT37] Frank, I. M. ; Tamm, I.: Coherent visible radiation of fast electrons passing through matter. In: *C. R. Acad. Sci. URSS* 14 (1937), S. 109–114

[Gam48] Gamow, Georgi A.: The Evolution of the Universe. In: *nature* 162 (1948), October, pp. 680–682

[Gan03] Gangui, Alejandro: Cosmology from Topological Defects. Mangaratiba, Rio de Janeiro (Brazil) : AIP Conf. Proc., 2003, 226-262

[Gee02] Geenen, Heiko: *Energy reconstruction and spectral unfolding of atmospheric leptons with the AMANDA detector*. 42119 Wuppertal, Germany, Bergische Universität Wuppertal, Diplomarbeit, November 2002

[Gee03] Geenen, Heiko for the AMANDA collaboration: Atmospheric Neutrino and Muon Spectra Measured with the AMANDA-II Detector. In: *28th International Cosmic Ray Conference* Bd. 3, 2003 (International Cosmic Ray Conference), pp. 1313–1316

[GHR+07] Gross, Andreas ; Ha, Chang H. ; Rott, Carsten ; Tluczykont, Martin ; Resconi, Elisa ; DeYoung, Tyce ; Wikström, Gustav for the IceCube collaboration: The combined AMANDA and IceCube Neutrino Telescope. In: *30*th International Cosmic Ray Conference[B:I07], pp. 11 – 14. arXiv:0711.0353 [astro-ph]

[GK07] Giunti, Carlo ; Kim, Chung W.: *Fundamentals of Neutrino Physics and Astrophysics*. Great Clarendon Street, Oxford OX2 6DP, UK : Oxford University Press, 2007. – ISBN 978–0–19–850871–1

[GQRS96] Gandhi, Raj ; Quigg, Chris ; Reno, Mary H. ; Sarcevic, Ina: Ultrahigh-energy neutrino interactions. In: *Astropart. Phys.* 5 (1996), No 2, pp. 81–110. arXiv:hep-ph/9512364

[GQRS98] Gandhi, Raj ; Quigg, Chris ; Reno, Mary H. ; Sarcevic, Ina: Neutrino interactions at ultrahigh energies. In: *Phys. Rev. D* 58 (1998), September, No 9, p. 093009. arXiv:hep-ph/9807264

[GR99] Giudice, G. F. ; Rattazzi, R.: Theories with gauge-mediated supersymmetry breaking. In: *Physics Reports* 322 (1999), No 6, 419-499. http://www.sciencedirect.com/science/article/B6TVP-3XWYXKP-2/2/16a18faf206cc1bbf6abc99f02badd14

[Gre66] Greisen, Kenneth: End to the Cosmic-Ray Spectrum? . In: *Phys. Rev. Lett.* 16 (1966), April, No 17, pp. 748–750

[GS85] Gaisser, T. K. ; Stanev, Todor: Muon bundles in underground detectors. In: *Nucl. Instrum. Meth.* 235 (1985), No 1, pp. 183–192

[Ham] Hamamatsu Photonics: *PMT Description*. http://jp.hamamatsu.com/resources/products/etd/eng/html/pmt_001.html

[Hel09] Helbing, Klaus: *private conversation*. February 2009

[HLS75] Haag, Rudolf ; Lopuszanski, Jan T. ; Sohnius, Martin: All possible generators of supersymmetries of the S-matrix. In: *Nuclear Physics B* 88 (1975), No 2, 257-274. http://www.sciencedirect.com/science/article/B6TVC-4718W97-YF/2/5b929365c64c0c0b36bf5a37c91c17f0

[Hoy65] Hoyle, F.: Origin of Cosmic X Rays. In: *Phys. Rev. Lett.* 15 (1965), July, No 4, pp. 131–132

[HZ97] Halzen, F. ; Zas, E.: Neutrino fluxes from active galaxies: A model-independent estimate. In: *Astrophys. J.* 488 (1997), pp. 669–674. arXiv:astro-ph/9702193

[IH83] Irvine, J. m. ; Humphreys, R.: Neutrino Masses and the Cosmic Neutrino Background. In: *J. Phys.* G9 (1983), pp. 847–852

[JERF99] Janka, H.-Thomas ; Eberl, Thomas ; Ruffert, Maximilian ; Fryer, Chris L.: Black Hole – Neutron Star Mergers as Central Engines of Gamma-Ray Bursts. In: *Astrophys. J. Lett.* 527 (1999), pp. L39–L42. arXiv:astro-ph/9908290

[KC07] Klein, Spencer R. ; Chirkin, Dmitry for the IceCube collaboration: Study of high p(T) muons in air showers with IceCube. In: *30*th International Cosmic Ray Conference[B:I07], pp. 35–38. arXiv:0711.0353 [astro-ph]

[Kel09] Kelley, J. L. IceCube collaboration: Determination of the Atmospheric Neutrino Flux and Searches for New Physics with AMANDA-II. (2009). arXiv:0902.0675 [astro-ph.HE]

[KGH01] Klose, Sylvio ; Greiner, Jochen ; Hartmann, Dieter H.: Gamma-Ray Bursts. In: *Physikalische Blätter* 57 (2001), Nr. 12

[KHL+09] Keller, L.M. ; Hill, K.A. ; Lazzara, M.A. ; Gallagher, J. ; Amundsen-Scott South Pole Station CLIMAT Message Project: A comparison of meteorological observations from South Pole Station before and after installation of a new instrument suite. In: *J.Tech.* (2009). http://amrc.ssec.wisc.edu/. – in press

[Kle08] Klein, Spencer R.: Studying High p_T Muons in Cosmic-Ray Air Showers. In: *Nuclear Physics B - Proceedings Supplements* 175-176 (2008), pp. 346–349. – Proceedings of the XIV International Symposium on Very High Energy Cosmic Ray Interactions

[KM82] Kaul, Romesh K. ; Majumdar, Parthasarathi: Cancellation of quadratically divergent mass corrections in globally supersymmetric spontaneously broken gauge theories. In: *Nuclear Physics B* 199 (1982), No 1, 36 - 58. http://www.sciencedirect.com/science/article/B6TVC-472T2D9-186/2/7fc295a156156d9beff9aeb4e60ad82b

[KMC+97] Karle, A. ; Mikolajski, T. ; Cichos, S. ; Hundertmark, S. ; Pandel, D. ; Spiering, C. ; Streicher, O. ; Thon, T. ; Wiebusch, C. ; Wischnewski, R.: Analog optical transmission of fast photomultiplier pulses over distances of 2 km. In: *Nucl. Instrum. Meth.* A387 (1997), No 1-2, pp. 274–277. – ISSN 0168–9002

[Kol07] Kolanoski, Hermann: *Einführung in die Astroteilchenphysik*. Lecture (Website). http://www-zeuthen.desy.de/~kolanosk/astro0607/skript.html. Version: 2007

[KSO73] Klebesadel, R. W. ; Strong, I. B. ; Olson, R. A.: Observations of Gamma-Ray Bursts of Cosmic Origin. In: *Astrophys. J.* 182 (1973), June, L85-L88. http://adsabs.harvard.edu/abs/1973ApJ...182L..85K

[Lai07] Laihem, Karim: *Front Pannel TMB Board*. Aachen University, III Physikalisches Institut B, Otto-Blumenthal Strasse, 52074 Aachen, February 2007. http://astro.uni-wuppertal.de/~atepe/dateien/TMB_AMANDA.pdf. – Description of the front pannel connectors

[Lei03] Leich, Holger: *GPS2VME: User's Guide*, January 2003. http://www.amanda.uci.edu/GPS2VME.ps

[Lei07] Leich, Holger: *GPS4TWR: User's Guide*, February 2007. http://www-zeuthen.desy.de/~leichh/amanda/GPS4TWR/GPS4TWR.doc

[LM00] Learned, John G. ; Mannheim, Karl: High-Energy Neutrino Astrophysics. In: *Annu. Rev. Nucl. Part.* 50 (2000), No 1, 679-749. http://dx.doi.org/10.1146/annurev.nucl.50.1.679

[Mar01] Marciniewski, Pawel: *Fast Digital Trigger Systems for Experiments in High Energy Physics*. Uppsala, Uppsala University, Dissertation, 2001

[Mar08] Martin, Stephen P.: A Supersymmetry Primer. (2008). arXiv:hep-ph/9709356. – version 5

[Més01] Mészáros, P.: Gamma-Ray Bursts: Accumulating Afterglow Implications, Progenitor Clues, and Prospects. In: *Science* 291 (2001), January, pp. 79–84. arXiv:astro-ph/0102255

[Mes06] Messarius, Timo: *Entwurf und Realisierung des AMANDA-Softwaretriggers fÃ¼r das TWR-Datenauslese-System*. Dortmund/Wuppertal, Universität Dortmund, Dissertation, August 2006

[MFS+99] Mather, J. C. ; Fixsen, D. J. ; Shafer, R. A. ; Mosier, C. ; Wilkinson, D. T.: Calibrator Design for the COBE Far Infrared Absolute Spectrophotometer (FIRAS). In: *Astrophys. J.* 512 (1999), February, pp. 511–520. arXiv:astro-ph/9810373

[MMP+05] Mangano, Gianpiero ; Miele, Gennaro ; Pastor, Sergio ; Pinto, Teguayco ; Pisanti, Ofelia ; Serpico, Pasquale D. et al.: Relic neutrino decoupling including flavour oscillations. In: *Nucl. Phys.* B729 (2005), pp. 221–234. arXiv:hep-ph/0506164

[MR93] Meszaros, P ; Rees, M. J.: Relativistic fireballs and their impact on external matter – Models for cosmological gamma-ray bursts. In: *Astrophys. J.* 405 (1993), pp. 278–284

[Mül02] Müller, Katharina: *Einführung Supersymmetrie*. www.physik.unizh.ch/~kmueller/text/vorlesung/susy.pdf. Version: June 2002

[MW99] MacFadyen, A. ; Woosley, S. E.: Collapsars - Gamma-Ray Bursts and Explosions in "Failed Supernovae". In: *Astrophys. J.* 524 (1999), p. 262. arXiv:astro-ph/9810274

[NJMC66] Nelson, Walter R. ; Jenkins, Theodore M. ; McCall, Richard C. ; Cobb, Joseph K.: Electron-Induced Cascade Showers in Copper and Lead at 1 GeV. In: *Phys. Rev.* 149 (1966), September, No 1, pp. 201–208

[Oli08] Olivas, Alexander R.: *private conversation*. May 2008

[Pir99] Piran, T.: Gamma-Ray Bursts and the Fireball Model. In: *Phys. Rept.* 314 (1999), pp. 575–667. arXiv:astro-ph/9810256

[PRSZ97] Povh, Bogdan ; Rith, Klaus ; Scholz, Christoph ; Zetsche, Frank: *Teilchen und Kerne*. 4. Berlin, Heidelberg : Springer, 1997. – ISBN 3–540–61737–X

[Ptu01] Ptuskin, Vladimir S.: Propagation, Confinement Models, and Large-Scale Dynamical Effects of Galactic Cosmic Rays. In: *Space Science Reviews* 99 (2001), pp. 281–293

[PW65] Penzias, Arnold A. ; Wilson, Robert W.: A Measurement of Excess Antenna Temperature at 4080 Mc/s. In: *Astrophys. J.* 142 (1965), July, 419-421. http://adsabs.harvard.edu/abs/1965ApJ...142..419P. – Provided by the SAO/NASA Astrophysics Data System

[PW01] Price, P. B. ; Woschnagg, K.: Role of group and phase velocity in high-energy neutrino observatories. In: *Astropart. Phys.* 15 (2001), No 1, 97-100. http://www.sciencedirect.com/science/article/B6TJ1-429XWT3-8/2/996d5c7e15a2e069bfce495f993e2b81. – ISSN 0927–6505

[PWC00] Price, P. B. ; Woschnagg, K. ; Chirkin, D.: Age vs depth of glacial ice at South Pole. In: *Geophys. Res. Lett.* 27 (2000), July, pp. 2129–2132

[Res09] Resconi, E. IceCube collaboration: Status and prospects of the IceCube neutrino telescope. In: *Nucl. Instrum. Meth.* A602 (2009), April, No 1, pp. 7–13

[RGO+09] Roucelle, Cécile ; Gross, Andreas ; Odrowski, Sirin ; Resconi, Elisa ; Sestayo, Yolanda: IceCube/AMANDA combined analyses for the search of neutrino sources. In: *Proceedings of the 31st ICRC*. Łódź, 2009 (International Cosmic Ray Conference)

[RM92] Rees, M. J. ; Mészáros, P.: Relativistic fireballs - Energy conversion and time-scales. In: *Mon. Not. R. astr. Soc.* 258 (1992), September, 41P-43P. http://adsabs.harvard.edu/abs/1992MNRAS.258P..41R. – Provided by the SAO/NASA Astrophysics Data System

[Rou93] Roulet, Esteban: Ultrahigh energy neutrino absorption by neutrino dark matter. In: *Phys. Rev. D* 47 (1993), June, No 12, 5247–5252. http://adsabs.harvard.edu/abs/1993PhRvD..47.5247R

[Sch02] Schmidt, Torsten: *Aufbau und Funktionsnachweis eines Optischen Moduls mit optisch-analoger Pulsübertragung für den AMANDA-II- und ICECUBE-Detektor*. Berlin, Humboldt-Universität zu Berlin, Dissertation, Juni 2002

[SDSS92] Stecker, F. W. ; Done, C. ; Salamon, M. H. ; Sommers, P.: Erratum: "High-energy neutrinos from active galactic nuclei" [Phys. Rev. Lett. 66, 2697 (1991)]. In: *Phys. Rev. Lett.* 69 (1992), November, No 18, p. 2738

[Seo05a] Seo, Seon-Hee: *AMANDA/IceCube Integration: Trigger*. http://glacier.lbl.gov/icecube/meetings/2005/marchmeeting/UPLOADS/FILE120.3MxuKc_Integration_collab_Mar2005.pdf. Version: March 2005. – Presentation at the IceCube Collaboration Meeting

[Seo05b] Seo, Seon-Hee: *IceCube Trigger System: Structure, Current Status & To Do*. http://glacier.lbl.gov/icecube/meetings/2005/marchmeeting/UPLOADS/FILE121.32Yndl_I3TrigSystem_collab_Mar2005.pdf. Version: March 2005. – Presentation at the IceCube Collaboration Meeting

[SGB01] Severinghaus, J. P. ; Grachev, A. ; Battle, M.: Thermal fractionation of air in polar firn by seasonal temperature gradients. In: *Geochem. Geophys. Geosyst.* 2 (2001). http://dx.doi.org/10.1029/2000GC000146. – Paper no. 2000GC000146

[Sta06] Stanford Research Systems, Inc.: *MODEL DG535 Digital Delay / Pulse Generator OPERATION AND SERVICE MANUAL*. 1290-D Reamwood Avenue, Sunnyvale, CA 94089 U.S.A., February 2006. http://www.thinksrs.com/downloads/man.htm

[Str01] Struck Innovative Systems: *SIS 1100 PCI Gigabit card*. website. http://struck.de/sis1100.htm. Version: June 2001

[Str06] Struck Innovative Systems: *PCI/cPCI-VME link/interface (SIS1100/3100)*. website. http://struck.de/pcivme.htm. Version: September 2006

[Str07] Struck Innovative Systems: *SIS3300 8 Channel 100 MHz 12-bit ADC*. website. http://struck.de/sis3300.htm. Version: January 2007

[Swo97] Swordy, Simon: *Astroparticle Physics at Chicago*. Website. http://astroparticle.uchicago.edu/. Version: 1997

[TCQ04] Thompson, Todd A. ; Chang, Philip ; Quataert, Eliot: Magnetar Spindown, Hyper-Energetic Supernovae, and Gamma Ray Bursts. In: *Astrophys. J.* 611 (2004), pp. 380–393. arXiv:astro-ph/0401555

[UP95] Urry, C. M. ; Padovani, Paolo: Unified Schemes for Radio-Loud Active Galactic Nuclei. In: *Publ. Astron. Soc. Pac.* 107 (1995), p. 803. arXiv:astro-ph/9506063

[Vie95] Vietri, Mario: On the acceleration of ultrahigh-energy cosmic rays in gamma-ray bursts. In: *Astrophys. J.* 453 (1995), pp. 883–889. arXiv:astro-ph/9506081

[W+05] Wischnewski, Ralf et al. Baikal collaboration: The Baikal neutrino telescope: Results and plans. In: *Int. J. Mod. Phys.* A20 (2005), pp. 6932–6936. arXiv:astro-ph/0507698

[Wag03] Wagner, Wolfgang for the AMANDA collaboration: New Capabilities of the AMANDA-II High Energy Neutrino Detector. In: *28th International Cosmic Ray Conference* Bd. 3, 2003 (International Cosmic Ray Conference), pp. 1365–1368

[Wag04] Wagner, Wolfgang: *Design and Realisation of a new AMANDA Data Acquisition System with Transient Waveform Recorders*. Dortmund/Wuppertal, Universität Dortmund, Dissertation, October 2004

[Wax95] Waxman, Eli: Cosmological origin for cosmic rays above 10^{19} eV. In: *Astrophys. J.* 452 (1995), pp. L1–L4. arXiv:astro-ph/9508037

[WB97] Waxman, Eli ; Bahcall, John N.: High energy neutrinos from cosmological gamma-ray burst fireballs. In: *Phys. Rev. Lett.* 78 (1997), pp. 2292–2295. arXiv:astro-ph/9701231

[WB99] Waxman, Eli ; Bahcall, John N.: High energy neutrinos from astrophysical sources: An upper bound. In: *Phys. Rev. D* 59 (1999), December, No 2, p. 023002. arXiv:hep-ph/9807282

[Web83] Webb, Gary M.: First order and second order Fermi acceleration of energetic charged particles by shock waves. In: *Astrophys. J.* 270 (1983), July, pp. 319–338

[Wei82] Weiler, Thomas J.: Resonant Absorption of Cosmic Ray Neutrinos by the Relic Neutrino Background. In: *Phys. Rev. Lett.* 49 (1982), July, p. 234

[Wis99] Wischnewski, R.: Supernova Burst Analysis with the Amanda Neutrino Telescope. In: *International Cosmic Ray Conference* Bd. 2, 1999 (International Cosmic Ray Conference), 229-232

[Woo93] Woosley, S. E.: Gamma-ray bursts from stellar mass accretion disks around black holes. In: *Astrophys. J.* 405 (1993), p. 273

[YDJS97] Yoshida, Shigeru ; Dai, Hongyue ; Jui, Charles C. H. ; Sommers, Paul: Extremely High Energy Neutrinos and Their Detection. In: *Astrophys. J.* 479 (1997), No 2, 547-559. http://dx.doi.org/10.1086/303923. – DOI 10.1086/303923

[YSL98] Yoshida, Shigeru ; Sigl, Gunter ; Lee, Sang-jin: Extremely high energy neutrinos, neutrino hot dark matter, and the highest energy cosmic rays. In: *Phys. Rev. Lett.* 81 (1998), pp. 5505–5508. arXiv:hep-ph/9808324

[ZK66] Zatsepin, G. T. ; Kuzmin, V. A.: Upper limit of the spectrum of cosmic rays. In: *JETP Lett.* 4 (1966), pp. 78–80

[Zub04] Zuber, Kai: *Neutrino Physics*. Dirac House, Temple Back, Bristol BS1 6BE, UK : Institute of Physics Publishing, 2004. – ISBN 0–7503–0750–1

List of Figures

Index

F

G

H

I

J

K

L

M

N

O

P

Acknowledgment

During the whole time working in Wuppertal for AMANDA and IceCube, I never felt alone. All the people of my work group in Wuppertal, but also the IceCube collaboration have become a part of the present thesis and I owe all those people so much. Over the years, many of the former colleagues have become my friends. Of course, I cannot mention all people here. To all those I forgot, I have to apologize in advance.*

From my work group in Wuppertal, I have to mention the two professors, Prof. Karl-Heinz Kampert and Prof. Klaus Helbing, first. They gave me to opportunity to work for AMANDA and IceCube and gave me the subjects for my thesis. They have always been open for my questions. Christopher Wiebush, who invited me to Wuppertal, is the person who changed my picture of doing a doctorate from something diffuse in the future to reality. He always cares for his Ph.D. students and I'm very thankful for his supervision.

Especially for the hardware, there is one name in the work group: Karl-Heinz Becker. He knows a great deal about programming DSP software, installing VME modules, but also about traveling to the South Pole. Without him, many problems, which have occurred during my work for AMANDA, could not have been solved.

Many other members of the work group in Wuppertal have to be mentioned. Timo Karg, who helped with all my trouble with IceTray and who read and corrected this complete thesis, made several challenges manageable. Many happy hours in my office, at the Pole or during conferences, have been the result of Benjamin Semburg's presence. His humor made me feel at home in Wuppertal. He also found many errors in my thesis and improved its quality significantly. The theoretical parts of this work have passed the critical eyes of Daniel Kruppke-Hansen. Ms. Schaarwächter, our secretary, easily solved all non-physics problems and was always a great friendly help whenever I asked her a favor. I also have to thank all those colleagues and friends who made Wuppertal not only a working place, but a city, I felt being welcome in: Heiko Geenen, Viviana Scherini, Lars Linden, Anna Frankowiak, Jan-Patrick Hülß, Simon Robbins, Maria Gurtner, Nils Nierstenhöfer, Oana Tascau (the kind-hearted soul of our group), Nils Potthoff, Steffen Hartmann, Julian Rautenberg, Jahangir Pouryamout, Jan Auffenberg, Markus Risse, Nicole Krohm, but also all the new people, I learned to know in the last few months.

But my work has not been limited to Wuppertal. I was always looking forward to visit DESY in Zeuthen. All its IceCubers gave me a warm welcome. Christian Spiering, Stefan Schlenstedt, Bernhard Voigt or Robert Franke are only a few names to mention. Holger Leich, who developed nearly all hardware modules for the AMANDA/IceCube integration has become a very special person for me. Without his advice while working together at the Pole, in Wuppertal, in Zeuthen or via telephone conferences, the integration would surely have failed, and I always enjoyed working with him.

Working at the South Pole is never a business done by one person. I have to thank Wolfgang Wagner, Carsten Rott, Steve Movit and all other people who have joined and helped me during

*Perhaps we can handle this with a beer...

my voyages to the Pole. Carsten and Steve additionally answered every mail and every question at any time and always had an open ear for all of my troubles regarding AMANDA and IceCube hard and software. Never before have I met a person as kind and helpful as Wolfgang. He presented a whole bunch of improvements for my thesis, reprogrammed DSPs with me, joined me for a short trip to Zeuthen for solving many hardware problems, survived the ride back through the night and is still answering my mails.

I also have to thank the Winterovers for the work they put into the synchronization hardware and I have to thank the whole AMANDA/IceCube collaboration for supporting my work.

My family deserves many thanks. Especially to my mother, Regina Tepe, who offered me a friendly home at the weekends, where I could relax from many hard days, I'm very grateful. She also supported the writing of this thesis with a lot of good food and sympathy.

For the time Svenja Elbers stayed at my side and bearing me during writing, I owe her many thanks. Her language support has caused a great linguistic refinement of this thesis. Having her at my side kept me up through the last weeks.

Selbständigkeitserklärung

Hiermit versichere ich, daß ich diese Arbeit nur unter Zuhilfenahme der angegebenen Quellen und Hilfsmittel selbständig angefertigt habe.

Ort, Datum

Andreas Tepe